École doctorale 352 : Physique et Science de la Matière

THÈSE

pour obtenir le grade de docteur délivré par

l'Université d'Aix-Marseille

Spécialité doctorale "Matière condensée et nanosciences"

Discipline: Physique

présentée et soutenue publiquement par

Martin S. TALLA NOUTACK

le 18 Octobre 2019

First-principles study of the effect of americium content in mixed oxide fuels

Jury

Pär Olsson	Professeur KTH	Rapporteur
Fabien Bruneval	Chercheur CEA	Rapporteur
Andres Saul	Directeur de recherche CNRS	Examinateur
Nathalie Vast	Chercheuse CEA	Examinateur
Grégory Geneste	Chercheur CEA	Directeur
Michel Freyss	Chercheur CEA	Co-Directeur

CEA, CADARACHE
DEN/DEC/SESC/LM2C
13108 Saint-Paul-Lez-Durance, France

THÈSE

Acknowledgements

I would like to express, through these weak words, my deep gratitude to several people who have contributed enormously to the success of this thesis work.

First, I want to thank the members of the jury of my PhD defence, Pär Olsson, Fabien Bruneval, Andres Saul and Nathalie Vast, for having found the time to read my manuscript and for their precious insights on this work.

My thanks go immediately to two main people without whom this work would never have been possible: Michel Freyss and Grégory Geneste.

Michel it was a real pleasure working with you. I have learnt and improved a lot of things necessary for my PhD study as well as my future career especially, reports writing, communication skills including the answer to the questions, etc. You were always available to help me, to give all important documents and to give me precious advices when I was need. Thank you for your suggestions and the corrections that made me grow up during these three years.

Grégory despite the distance, you were fully involved in this thesis work and you have brought me all the elements (which you had) required for the success of this thesis. You always spent time to answer my concerns as numerous as they were. With you, I learned the scientific rigor and a fine interpretation of the results. I have greatly appreciated our meetings and interactions by email.

I thank Gérald Jomard, the head of "Laboratoire de Modélisation Multi-échelles du Combustible" (LM2C). You participated to the success of this work. I benefited of your experience about ABINIT code. You helped me in writing scientific reports and in preparing presentations. I have greatly appreciated working in your laboratory and in particular with you.

I want also to thank all the people of the LM2C lab of CEA Cadarache for their constant support. Thank you Marjorie for your advices and for being interested to my post-thesis; Emeric thank you for your constructive suggestions during my presentation and thank you for having help me (accompanying me to the football stadium) with your car when it was possible; Renaud thank you for being interested to my work; Jacques thank you for all the scientific discussions we had; Rivo thank you for your help especially concerning python or unix scripts.

My gratitude goes to my PhD student colleagues, I have really enjoyed all time spent with you. Thank you, Ibrahim, Cyrille, Didier for our fruitful scientific discussions and all the help you brought me. Allan, Julien, Mourad, Vincent, Akram, Nadia, Cyrille

and Didier I have really enjoyed every moment (jokes, funny discussions, scientific) spent with you.

I thank "Atomic team": Mourad, Ibrahim, Piotr, Cyrille, Akram, Julien, Allan ..., playing football with you was a great pleasure for me.

I cannot end without acknowledge DEN (Direction de l'Énergie Nucléaire), DEC (Département d'Étude du Combustible), SESC (Service d'Etude et de Simulation du Comportement du Combustible), RCOMB project and INSPYRE European project, for their support and for giving me the opportunity to pursue a PhD.

Régine I thank you for your kindness, your availability to address with pleasure all my administrative concerns.

Carole Valot I want to thank you for your constructive comments during all my presentations.

Finally, I want to thank all my friends and my family, whose support was fundamental during these three years.

I have maybe forgotten someone, in all of the cases, thank you to all of you.

Contents

List of Figures

List of Tables

First-principles study of the effect of americium content in mixed oxide fuels

Martin S. TALLA NOUTACK

18 Octobre 2019

Résumé étendu

L'oxyde mixte d'uranium-plutonium (MOX) avec une teneur en plutonium d'environ 25% est le combustible de référence prévu pour les réacteurs nucléaires français du futur. Il s'agit de la filière des réacteurs à neutrons rapides (RNR) dits de Génération IV. Ce combustible sera fabriqué à partir du combustible usé issu dans un premier temps des réacteurs à eau pressurisée (REP) actuellement en fonctionnement en France et, par conséquent, contiendra de l'américium en faible pourcentage. En effet, lors de l'irradiation en réacteur du combustible nucléaire, la fission de l'uranium (U) et du plutonium (Pu) conduit à la formation des produits de fission, mais aussi à la formation par captures neutroniques successives de noyaux lourds en faible quantité ($\sim$ 1% de l'inventaire en REP) appelés actinides mineurs (AMs) tels que l'américium (Am), le neptunium (Np) et le curium (Cm). Parmi les actinides mineurs, l'américium est le plus abondant et ses différents isotopes possèdent des activités élevées par rapport aux autres AMs et donc présentent une radiotoxicité importante lorsqu'ils sont relâchés dans l'environnement. De plus, le plutonium issu du retraitement est susceptible de subir une désexcitation de type $\beta-$ conduisant aussi à la formation d'américium. La question qui émerge est celle de savoir si la présence de l'américium affectera la performance et la sûreté du combustible MOX. Il faut noter que le multirecyclage étant envisagé dans le cas des REP utilisant le MOX (% Pu $\sim$ 10) comme combustible, la même problématique se pose également pour les REP. Ainsi, une meilleure mise en évidence des effets induits par la présence de l'américium sur les propriétés de l'oxyde mixte d'uranium-plutonium est donc nécessaire pour maîtriser les conséquences de la présence de cet élément sur la sûreté et la performance des combustibles.

L'OCDE [27] a publié en 2014 un rapport résumant les résultats d'expériences portant sur l'étude du combustible MOX contenant des actinides mineurs en concept homogène ($\sim$1 à 5%) et hétérogène ($\sim$10 à 20%). Dans le but d'évaluer les performances sous-irradiation de ces combustibles, plusieurs expériences ont été effectuées dans des réacteurs de recherche. Il s'agit notamment des irradiations SUPERFACT dans le réacteur PHENIX, AM1 dans JOYO et AFC-2C et 2D dans ATR. Des propriétés matériaux telles que la conductivité thermique et la température de fusion ont été évaluées dans ces études. Ces études soulignent une forte production d'hélium en fonction de la teneur en américium ainsi qu'une baisse de la conductivité thermique et de la température de fusion. Il ressort de ce rapport que la présence d'actinides mineurs à de faibles teneurs aurait un effet négligeable sur les propriétés matériaux et sous-irradiation du combustible MOX. Cependant, en raison de données insuffisantes sur les mécanismes élémentaires régissant le comportement sous-irradiation du combustible tels que le transport atomique, le piégeage et relâchement des gaz de fission ainsi que la méconnaissance de l'influence des actinides mineurs sur les propriétés mécaniques, élastiques et structurales du combustible (U,Pu)O_2, une telle conclusion nécessite d'être

mieux justifiée. Ainsi, des études supplémentaires visant à étudier l'influence des actinides mineurs, en particulier celle de l'américium, sur les propriétés de transport atomique, la stabilité des défauts ponctuels, les propriétés en températures finies et les propriétés mécaniques, élastiques et structurales du combustible MOX sont nécessaires.

Le CEA co-développe avec EDF une plate-forme logicielle (PLEIADES) contenant le code GERMINAL pour la simulation du comportement du combustible RNR sous irradiation. Cette plate-forme nécessite une base de données sur les propriétés des matériaux pouvant provenir directement des études expérimentales. Cependant, les données expérimentales sont parfois inexistantes ou difficiles à obtenir en raison du coût élevé ou de la radiotoxicité de certains radioéléments comme le plutonium ou l'américium. Ainsi, la modélisation à travers ses différentes échelles allant de l'échelle de l'atome à l'échelle de la pastille combustible se présente comme une alternative. Les différentes techniques de modélisation mises en œuvre (potentiels empiriques, dynamique d'amas, modèles CALPHAD, thermocinétique, thermomécanique, etc.) sont interdépendantes et nécessitent à leur tour des données provenant des échelles plus petites. Les calculs de structure électronique répondent parfaitement à ces préoccupations en fournissant non seulement des données matériaux aux méthodes basées sur des potentiels empiriques, à la dynamique d'amas, aux modèles CALPHAD ou encore aux modèles thermocinétiques et thermomécaniques mais aussi constituent un véritable soutien aux expériences à effets séparés. En effet, les calculs de structure électronique constituent une aide précieuse pour l'interprétation des résultats issus des spectres EXAFS ou XANES mais aussi pour l'identification des pièges et mécanismes de diffusion des gaz de fission.

L'introduction de la méthode de calcul de structure électronique DFT+U (dénomination récemment généralisée pour LDA+U ou GGA+U) en 1992 [28], qui est une approximation au-delà de la théorie de la fonctionnelle de la densité (DFT) standard, optimisée pour prendre en compte les fortes corrélations des électrons des orbitales localisées dont les *5f* dans les oxydes d'actinides, a largement contribué à la réalisation d'études plus précises sur les combustibles nucléaires oxydes. La méthode DFT+U permet de déterminer l'évolution des propriétés physico-chimiques et thermodynamiques d'un oxyde mixte en fonction de sa composition et de sa stœchiométrie [29, 30]. Elle permet de caractériser les défauts ponctuels les plus stables, crées par l'irradiation ou par l'écart à la stœchiométrie et de déterminer l'effet des défauts sur les propriétés structurales, électroniques et thermodynamiques du matériau. Elle permet également d'appréhender les propriétés de transport atomique via la détermination des mécanismes de migration des atomes et des barrières d'énergie associées. Toutefois il n'existe dans la littérature aucune étude utilisant la DFT pour étudier les propriétés matériaux d'oxydes contenant de l'américium.

En résumé, les études réalisées dans la littérature sur le combustible (U,Pu)O_2 contenant de l'Am montrent que l'américium induit une légère diminution de la conductivité thermique, de la température de fusion ainsi qu'une augmentation du potentiel d'oxygène. Cependant, en raison de données insuffisantes ou inexistantes notamment sur les mécanismes élémentaires régissant le comportement du combustible sous irradiation (stabilité des défauts ponctuels, transport atomique, comportement des gaz de fission) ainsi que sur les propriétés en températures finies, mécaniques, structurales et

élastiques, il est impossible de conclure sur l'influence de l'américium. D'autre part, les études expérimentales sur ce composé sont coûteuses et difficiles à mettre en œuvre en raison de la radiotoxicité du plutonium et de l'américium. La théorie de la fonctionnelle de la densité (DFT)+U à travers un schéma de modélisation multi-échelle du combustible se présente donc comme une excellente alternative sachant qu'elle a largement été utilisée dans le cas des autres oxydes d'actinides tels que UO_2 et PuO_2.

C'est dans ce contexte que s'inscrit ce travail de thèse. Il consiste à quantifier et qualifier l'influence d'une faible teneur d'américium sur les propriétés en températures finies, de défauts ponctuels (stabilité et transport atomique), élastiques, structurales et électronique de l'oxyde mixte d'uranium-plutonium en adaptant les calculs de structure électroniques. Pour ce faire, nous avons défini une démarche visant à terme à fournir des données matériaux fiables sur ces oxydes. Nous avons commencé par l'étude des oxydes purs d'américium (AmO_2 et Am_2O_3) afin d'adapter la méthode DFT+U aux oxydes contenant de l'américium. L'idée était ensuite d'appliquer la DFT+U à (U,Pu,Am)O_2 mais vu la complexité du système quaternaire U-Pu-Am-O et les données très rares sur ce composé, nous avons fait le choix de commencer par l'étude de (U,Am)O_2 sachant que le (U,Pu)O_2 a fait l'objet de la thèse d'Ibrahim Cheik Njifon [29] et de quelques études expérimentales. Ce travail de thèse est divisé en six principaux chapitres :

Nous présentons tout d'abord dans le chapitre 1 les méthodes indispensables au calcul des propriétés d'intérêt des oxydes d'actinides. On note dans ce chapitre que les fonctionnelles standard de la DFT sont inefficaces dans la description des oxydes d'actinides en raison du fait qu'elles ne prennent pas en compte les fortes répulsions (fortes corrélations) entre les électrons *5f* des actinides. La méthode DFT+U apparaît clairement comme la solution de l'état de l'art la plus en vue pour la description des matériaux contenant des électrons fortement corrélés.

Dans le chapitre 2 nous présentons la revue scientifique de la littérature sur les oxydes contenant de l'américium. Plus particulièrement nous avons résumé l'essentiel des études existantes sur les propriétés matériaux. Force nous a été donnée de constater que les propriétés élémentaires régissant le comportement du combustible sous irradiation (formation et migration des défauts, gaz de fission) des combustibles nucléaires contenant de l'américium restent jusqu'à présent inconnues. De plus, plusieurs propriétés d'oxydes contenant de l'américium restent jusqu'à présent mal connues ou présentent des contradictions d'une étude à l'autre. Par exemple, les diagrammes de phase binaire Am-O, ternaire U-Am-O ne sont pas complètement établis et pour le système quaternaire U-Pu-Am-O le diagramme est inexistant en raison d'un nombre très limité de données matériaux. Ces remarques tirées de la littérature justifient la nécessité de cette étude.

L'objectif du chapitre 3 est de mettre en œuvre la méthode DFT+U dans le cas des oxydes contenant de l'américium. En effet, l'utilisation de la méthode DFT+U nécessite au préalable la connaissance de deux paramètres clés à savoir les paramètres de Hubbard U et J. Pour cela, l'idée est avant tout d'étudier les états métastables inhérents à la méthode DFT+U afin de rechercher les configurations électroniques des orbitales *5f* de l'Am dans AmO_2 qui conduisent à l'état fondamental du système. Pour cela, nous avons déterminé les matrices d'occupation des électrons *5f* de Am dans AmO_2 en utilisant la méthode de contrôle des matrices d'occupation parfaitement maîtrisée au LM2C (Laboratoire de Modélisation Multi-échelle du Combustible) et

déjà mis en œuvre pour PuO_2 [31] et UO_2 [32]. L'objectif ensuite est de déterminer les paramètres optimums U et J permettant de prendre en compte les fortes corrélations entre les électrons *5f* de l'américium dans AmO_2 et Am_2O_3. Pour cela nous avons calculé plusieurs propriétés matériaux de AmO_2 en fonction des paramètres U et J et par comparaison aux résultats expérimentaux disponibles dans la littérature, nous avons déterminé les paramètres qui permettent de décrire au mieux les propriétés de AmO_2. Enfin, nous avons utilisé ces paramètres dans la méthode DFT+U pour prédire plusieurs propriétés de AmO_2 et Am_2O_3 mal connues ou non connues. Ces études ont fait l'objet d'un article publié dans Phys. Rev. Materials [33].

Nous soulignons dans ce chapitre que la présence d'états métastables inhérents à la méthode DFT+U peut expliquer les controverses rencontrées dans la littérature pour AmO_2 au regard des constantes élastiques ainsi que l'évolution du gap (bande interdite) en fonction du paramètre U de la DFT+U. Nous montrons par la suite que l'état fondamental peut être atteint en imposant les matrices d'occupation des électrons *5f* au début des calculs. Nous observons une légère différence entre les paramètres de maille ($a \neq b \neq c$) lorsque la symétrie cristalline n'est pas prise en compte mais le volume reste très proche du cas où la symétrie cristalline est prise en compte. De plus, dans les deux cas, les moments magnétiques de Am^{4+} sont très proches, ainsi que les gaps (1.1 ± 0.2 eV). Enfin, la densité d'états électroniques et les contributions isotropes des propriétés diélectriques (trace des charges effectives de Born et tenseurs diélectriques) ne sont pas modifiées par la perte de symétrie cristalline.

Nous calculons plusieurs propriétés matériaux de AmO_2 et Am_2O_3, telles que des propriétés structurales, élastiques, énergétiques, électroniques et magnétiques, en fonction des paramètres U et J, ainsi que propriétés diélectriques et les propriétés en température finie. Nos résultats montrent un bon accord avec les données disponibles (expérimentales et calculées). Pour AmO_2, les valeurs (U, J) = (6.00 eV, 0.75 eV) sont celles qui fournissent la meilleure description des propriétés matériaux par comparaison aux données expérimentales disponibles dans littérature. Nous fournissons pour la première fois plusieurs propriétés matériaux telles que les propriétés magnétiques et élastiques (constantes élastiques) ainsi que la constante statique diélectrique du dioxyde d'américium, inconnues jusqu'à présent.

En ce qui concerne les sesquioxydes d'américium, nous montrons que la structure hexagonale de type A (A-Am_2O_3) est la structure la plus stable à basse température. Ce résultat est la première confirmation théorique (en accord avec les calculs CALPHAD rapportés par Gotcu-Freis *et al.* [13]) de la stabilité à basse température de la structure hexagonale de type A de Am_2O_3, dont le diagramme de phase est encore sujet aux controverses. De plus, les propriétés structurales calculées dans cette étude sont très proches des résultats expérimentaux. Nous fournissons pour la première fois les paramètres structuraux internes de la structure hexagonale, qui peuvent servir de référence pour les futurs travaux de modélisation. Nous prédisons également le module d'incompressibilité des structures hexagonale et cubique de type A et C respectivement, ainsi que le gap et l'enthalpie de formation de la structure de type C. Nous soulignons que les valeurs $U = 6$ eV et $J = 0.75$ eV déterminées pour AmO_2 ont tendance à surestimer le gap sans toutefois affecter les autres propriétés matériaux.

L'étude par calcul de structure électronique proposée dans ce chapitre ouvre la voie à une utilisation optimale de l'approximation DFT+U pour l'étude des supercellules AmO_2 fautées (voir Chap. 4) car les propriétés de défauts ponctuels dans AmO_2

n'ont jamais été étudiées. De plus, cette méthode mise en œuvre dans les oxydes purs d'américium peut être étendue aux matériaux plus complexes comme les oxydes mixtes (U, Am)O_2 et (U,Pu,Am)O_2 (voir Chap. 5 et 6).

L'objectif du chapitre 4 est d'étudier les défauts ponctuels atomiques et électroniques dans AmO_2 en utilisant la DFT+U. En effet, la littérature est vierge en ce qui concerne les propriétés de défauts ponctuels dans AmO_2. Or ces propriétés, en particulier les propriétés de transport atomique, contrôlent l'évolution de la microstructure d'un matériau. L'idée dans un premier temps est d'étudier les défauts ponctuels donneurs d'électrons tels que les lacunes d'oxygène et interstitiels d'américium. Nous avons uniquement considéré les défauts donneurs d'électrons car, d'après la littérature [12], Am possède un état d'oxydation maximal de +IV et donc ne peut que se réduire (i.e. capter les électrons). L'objectif est ensuite d'étudier la stabilité et la migration des petits polarons électroniques car puisque les polarons participent à l'équilibre thermodynamique du matériau, ils doivent nécessairement être pris en compte dans les modèles thermodynamiques de défauts. Ces études ont fait l'objet d'un article soumis à Physical Review B.

Il a été montré que les oxydes d'américium sont soumis aux effets d'auto-irradiation, à savoir la désintégration α. Cette auto-irradiation induit des effets balistiques et des collisions élastiques associées qui entraînent des déplacements atomiques et donc des dommages tels que l'augmentation du paramètre de maille [34–36] et la formation de défauts [37]. Dans les oxydes isolants tels que les oxydes d'américium, tout défaut ponctuel (lacune, interstitiel, etc.) peut généralement être décrit soit comme accepteur d'électrons/trous, soit comme donneur. Plus explicitement, ces défauts libèrent des trous ou des électrons, qui peuvent se localiser sur un seul atome, conduisant à une entité appelée petit polaron. La localisation des électrons libérés par les défauts est un degré de liberté physique supplémentaire qui doit être pris en compte afin d'atteindre l'état fondamental réel du système fauté. Dans ce chapitre, nous nous concentrons sur les lacunes d'oxygène et les interstitiels d'américium dans AmO_2, ainsi que les petits polarons associés. Nous montrons que quelles que soient les conditions stœchiométriques considérées, les lacunes d'oxygène sont les défauts dominants dans l'AmO_2. De plus, nous observons que l'énergie de transition (qui est une quantité ne dépendant pas du potentiel chimique des espèces) de la lacune partiellement ionisée $V_O^{\bullet}$ vers la lacune neutre V_O^X est située dans les niveaux d'énergies profonds du gap ($\sim$ 0.3 eV au dessus de la bande de valence), indiquant que les lacunes d'oxygène dans AmO_2 sont des défauts dits "donneurs profonds". Ensuite, nous montrons que les polarons électroniques dans AmO_2 sont stables sous forme isolée au lieu d'être liés au défaut (c'est-à-dire aux lacunes d'oxygène en particulier) et présentent une faible énergie de migration d'environ 0.6 eV.

L'objectif du chapitre 5 a été d'appliquer la DFT+U au dioxyde d'uranium UO_2 contenant de l'américium dans des proportions allant de 0 à 100% afin d'étudier l'influence de l'américium sur les propriétés électroniques, structurales, énergétiques et de défauts ponctuels mais aussi de compléter les expériences à effets séparés menées au CEA. L'un des défis rencontrés a été de construire des supercellules qui décrivent au mieux le désordre chimique des cations U et Am dans les sites cubiques faces centrées (cfc) pour différentes teneurs en Am. Pour cela nous avons construit nos boîtes de sim-

ulation en utilisant les configurations SQS proposées par von Pezold [38]. Nous avons ensuite calculé les propriétés électroniques, structurales, énergétique pour différentes teneurs en Am. L'objectif a ensuite été d'étudier la stabilité des lacunes d'oxygène dans (U,Am)O_2 sachant qu'il a été montré dans la littérature que les lacunes d'oxygène sont les défauts majoritaires dans l'UO_2 en conditions réductrices [39, 40]. Pour cela, nous avons considérés divers environnements chimiques en termes de cations premiers voisins de la lacune et nous avons étudié la stabilité thermodynamique des lacunes dans l'environnement chimique le plus énergétiquement favorable. Les résultats obtenus ont été comparés à ceux obtenus dans UO_2 dans le but de déterminer l'effet de l'américium. Les résultats obtenus dans cette partie ont fait l'objet d'un article publié dans Journal of Physics: Condensed Matter.

Nous montrons dans ce chapitre que les oxydes mixtes (U,Am)O_2 présentent un état de valence de cations fondamentalement différent des autres oxydes mixtes tels que (U,Pu)O_2 et (U,Ce)O_2. En effet, dans (U,Am)O_2, les cations Am agissent comme des accepteurs d'électrons tandis que les cations U agissent comme donneurs d'électrons selon la réaction chimique: $Am^{4+} + U^{4+} \longrightarrow Am^{3+} + U^{5+}$. Ces résultats sont en parfait accord avec les premières expériences XANES (limitées à %Am <20), mais aussi, permettent de les compléter en fournissant une description plus détaillée des oxydes contenant de l'américium sur toute la gamme de teneurs en Am. Nous montrons que pour %Am <50, tous les Am(+IV) sont réduits en Am(+III) alors que les cations U présentent une valence mixte (+IV et +V). Par contre, pour %Am> 50, les cations Am(+IV) se réduisent partiellement en Am(+III) alors que tous les cations U(+IV) sont oxydés en U(+V).

Cette étude montre que le paramètre de maille de (U,Am)O_2 en fonction de la teneur en Am suit un comportement linéaire. Cette évolution linéaire ne peut être obtenue expérimentalement en raison de l'écart à la stoechiométrie associée à la présence lacunes et d'interstitiels d'oxygène (renforcés pour de fortes teneurs en Am supérieures à 40%) ainsi que l'auto-irradiation. Il serait intéressant d'examiner plus en détail, dans le cadre de la DFT+U, l'effet des défauts ponctuels ainsi que des amas défauts sur les propriétés structurales des oxydes mixtes (U,Am)O_2, en particulier sur le paramètre de maille. De plus, nous montrons que les distances cristallographiques U-Am et U-U sont identiques, ce qui correspond à la signature d'une distribution aléatoire des cations dans le sous-réseau cationique. Ainsi, notre étude est la première confirmation du comportement de solution solide idéale de (U,Am)O_2 pourvu que le composé soit parfait (sans défauts) et stœchiométrique. En utilisant deux approches (SQS et paramétrique), nous montrons avec un accord satisfaisant entre les deux approches qu'il ne se produit aucune démixtion dans la solution solide (U,Am)O_2 dans toute la plage de teneurs en américium. Cette étude est la première évaluation de l'enthalpie de mélange d'oxydes mixtes contenant l'américium, la valeur minimale étant d'environ -0.45 eV. Cette valeur (en valeur absolue) est 100 fois supérieure à la valeur obtenue pour (U,Pu)O_2. Par ailleurs, nous montrons que plus il y a d'américium dans la première sphère de coordination d'une lacune neutre d'oxygène, plus cette dernière est énergétiquement stable. Cette étude montre que les lacunes d'oxygène se forment plus facilement dans l'oxyde mixte (U,Am)O_2 que dans UO_2.

Les résultats obtenus dans ce chapitre complètent les études expérimentales et fournissent des données d'entrées utiles pour les méthodes de calcul thermodynamique telles que CALPHAD.

En somme, nos résultats indiquent que la présence de l'américium dans UO_2 facilite la formation de lacunes neutres d'oxygène. De plus, la présence de Am conduit à l'oxydation de U^{4+} en U^{5+} de manière à ce que $[U^{5+}] = [Am^{3+}]$. Ces résultats sur l'effet de l'américium sur les propriétés matériaux de UO_2 ouvrent la voie à l'étude de l'effet de l'américium sur les propriétés matériaux de l'oxyde mixte d'uranium et de plutonium (U,Pu)O_2.

L'objectif du chapitre 6 est d'étendre les études réalisées au chapitre 5 à (U,Pu,Am)O_2 (25 at.% en Pu) avec des teneurs en Am inférieures à 10%. L'idée ici est tout d'abord de construire des supercellules de (U,Pu,Am)O_2 à partir des supercellules de (U,Pu)O_2. Pour cela, nous avons traité l'Am comme une impureté diluée dans une solution solide de (U,Pu)O_2 car la teneur en Am est considérée comme faible devant celle de U et de Pu. Nous avons ensuite étudié la stabilité relative des supercellules en fonction de l'environnement chimique de l'Am en termes de cations premiers voisins. L'objectif suivant est de calculer les propriétés électroniques, structurales, élastiques, en températures finies et de défauts ponctuels dans la configuration la plus favorable. Enfin, par comparaison aux études disponibles sur (U,Pu)O_2 nous avons déterminé l'influence d'une faible teneur en américium sur les propriétés matériaux de (U,Pu)O_2.

Nous proposons tout d'abord une approximation visant à modéliser (U,Pu,Am)O_2 avec une faible teneur en américium (moins de 10%). Nous montrons, en accord avec le chapitre précédent, que plus il y a d'atomes d'uranium autour d'un atome d'américium donné, plus la configuration résultante est stable. La stabilité d'un atome Am lorqu'il est voisin d'un atome U plutôt que d'un atome Pu peut s'expliquer par le transfert de charge électronique se produisant entre les cations U et Am. En ce qui concerne l'état de valence des cations, nous montrons que les cations Am(+IV) dans (U,Pu)O_2 ont tendance à se réduire facilement en Am(+III): (i) dans les composés stœchiométriques, la réduction de Am (+IV) est compensée par l'oxydation de U (+IV) en U(+V). (ii) l'hypostœchiométrie dans les oxydes d'uranium-plutonium contenant de l'américium est compensée par la réduction de tous les cations Am avant toute réduction des cations Pu. Cela nous permet de souligner que l'oxyde d'américium présente un potentiel d'oxygène plus élevé que les oxydes Pu et U. Ce qui induit ainsi une augmentation du potentiel d'oxygène dans les oxydes mixtes uranium-plutonium.
De plus, ces résultats nous permettent de conclure que le fait que la stabilité du crystal soit influencée par le nombre de cations U autour de l'atome Am résulterait probablement de la différence entre les interactions électrostatiques Am(+III)-U(+IV) et Am(+III)-Pu(+IV). En effet, en fonction du nombre d'atomes de Pu et de U entourant un atome de Am donné, les interactions électrostatiques locales peuvent être fortement affectées, ce qui entraînerait une différence dans l'énergie totale du système.

Nous soulignons une diminution du paramètre de maille de $U_{0.75-z}Pu_{0.25}Am_zO_2$ avec l'augmentation de la teneur en Am, en accord avec les études experimentales disponibles dans la littérature [41]. De plus, l'évolution du paramètre de maille en fonction de la teneur en Am n'est pas linéaire comme dans $U_{1-y}Pu_yO_2$. On observe que la présence de Am (pour les teneurs évaluées) n'a pas d'effet notable sur les distances interatomiques M-M (M = U ou Pu) comparé à la distance M-M dans $U_{0.75}Pu_{0.25}O_2$ ($\sim$3.90Å). Par ailleurs, on observe une très légère diminution de la distance U-O d'environ 0.01 Å pour z = 0.0625. Ce résultat était attendu puisque nous avons montré que la présence de Am entraîne une légère diminution du paramètre de maille des oxydes mixtes $U_{0.75}Pu_{0.25}O_2$.

En ce qui concerne les propriétés de défauts ponctuels, nous montrons que la présence de Am induit une diminution (d'environ 50% quel que soit l'environnement chimique du défaut) de l'énergie de formation des lacunes d'oxygène dans (U,Pu)O_2, ce qui est en accord avec les résultats obtenus dans (U,Am)O_2 comparé à UO_2. Cependant, cette étude ne permet pas de proposer une évolution de l'énergie de formation en fonction de la teneur en américium puisque nous n'avons considéré que deux teneurs en américium (3.125 % et 6.25 %).

Ce manuscrit met en évidence la capacité des calculs de structure électronique et plus particulièrement la DFT à soutenir les expériences à effets séparés et à alimenter les techniques de modélisation à plus grande échelle (mentionnées dans le tableau 6.7 ci-dessous) afin d'accroître la prédictivité des codes de performance développés au CEA. De plus, cette étude montre la capacité des calculs DFT à traiter efficacement des matériaux complexes tels que les oxydes contenant de l'américium, en particulier les systèmes quaternaires tels que les oxydes mixtes uranium-plutonium-américium, qui présentent un désordre chimique cationique, un changement spontané de l'état de valence ansi que des effets de fortes correlations. La méthodologie proposée dans cette étude peut être appliquée à d'autres oxydes contenant les actinides mineurs, tels que les oxydes contenant le Np et le Cm, car les propriétés matériaux de ces oxydes sont mal connues. En effet, bien que Np et Cm soient moins abondants que Am dans le combustible usé (U,Pu)O_2, ils pourraient probablement avoir un effet sur les propriétés matériaux du combustible nucléaire RNR. Malgré la maturité de la methode DFT, il est important de souligner que certaines améliorations restent indispensables. Par exemple, des supercellules à 96 atomes (utilisées dans cette étude) limitent le nombre de configurations (en termes d'atomes U et Pu) autour d'un atome Am (in (U, Pu)O_2) et rend également impossible l'étude de l'effet des deuxième et troisième voisins cations sur la stabilité des défauts ponctuels. L'augmentation de la taille de la supercellule i.e. passer d'une supercellule de 96 atomes à une plus grande supercellule pourrait être une alternative. Cependant, cette solution nécessite un temps de calcul très long en DFT+U. Une étude couplant les calculs DFT et les méthodes basées sur les potentiels empiriques interatomiques est actuellement en cours. L'un des objectifs de cette étude est d'utiliser des méthodes basées sur les potentiels empiriques pour explorer plusieurs configurations chimiques autour d'un défaut ponctuel donné ainsi que de nombreux mécanismes de migration afin d'identifier les plus probables. Ensuite, la DFT sera appliquée en tenant compte des configurations/mécanismes les plus probables pour calculer avec une plus grande précision les propriétés de défauts ponctuels et les propriétés énergétiques de transport atomique.

Table 1: Valorisation à travers le schéma de modélisation multi-échelles (développé au CEA) des résultats obtenus dans cette thèse. Nous présentons également les techniques expérimentales complémentaires à la DFT. EELS=Electron Energy Loss Spectroscopy, SIMS=Secondary Ion Mass Spectrometry. DSC= Differential Scanning Calorimetry. KineCluE= Kinetic Cluster expansion.

Propriétés DFT		Techniques expérimentales	Codes, modèles ou techniques à alimenter
Elastiques	Constantes élastiques	Brillouin zone measurements	Thermomechanique Potentiels empiriques
Structurales	Dilatation, thermique	XRD	Thermoméchanique, Potentiels empiriques
	Stabilité de phase	XRD	CALPHAD
Electroniques	Valence des cations	XANES	CALPHAD
Energetiques	Enthalpie de mélange		CALPHAD,
	Enthalpie de formation	Calorimétrie à l'oxygène	KinecluE, Potentiels empiriques,
	Propriétés de défauts ponctuels	Pour l'identification: PAS, RAMAN EELS couplée à la DFT	Dynamique d'amas
Transport	Energie de migration	SIMS, TDS (méthode indirecte)	DICTRA, thermocinétique
Thermodynamiques	chaleur spécifique	Calorimétrie de chute, DSC	Thermoméchanique CALPHAD

General introduction

Uranium-plutonium mixed oxide (MOX) with a plutonium content of about 25% is the reference fuel for the future nuclear reactors in France, the Generation IV sodium-cooled fast reactors (SFR). This nuclear fuel will be fabricated from spent fuel coming out of pressurized water reactors (PWR) currently in operation in France and, as a consequence, will contain a few percent of americium. Indeed, during irradiation in the reactor, the fission of uranium (U) and plutonium (Pu) leads to the formation of fission products, but also to the formation by successive neutron captures of heavy nuclei in small quantities ($\sim$ 1 % of the PWR inventory) called minor actinides (MAs) such as americium (Am), neptunium (Np) and curium (Cm). Out of the minor actinides, americium is the most abundant and its different isotopes have higher activities than other MAs and, therefore have a high radiotoxicity when released into the environment. Furthermore, the plutonium from spent fuel could undergo β-decay, leading also to the formation of americium. The emerging question is whether the presence of americium will affect the performance and safety of the MOX fuel. Note that the multirecycling of spent fuel is now also envisaged for PWR MOX fuel (with Pu content around 10%) and thus, the same issue is raised for PWR since recycled fuel contents a few percent of amercium. A better evidence of the effects induced by the presence of americium on the uranium-plutonium mixed oxide properties is thus necessary to control the consequences of the presence of this element on the safety and the performance of the nuclear fuels.

The OECD [27] published in 2014 a report summarizing the results from the experimental studies of MA-bearing MOX fuel in homogeneous ($\sim$1 to 5% of Am) and heterogeneous ($\sim$10 to 20% of Am) concepts. In order to evaluate the performance of these fuels under irradiation, several experiments were conducted in test reactors. These include the SUPERFACT irradiations in the PHENIX reactor, AM1 in JOYO and AFC-2C and 2D in ATR. Material properties such as thermal conductivity and melting temperature were evaluated in these studies. These studies highlight a high helium production as a function of americium content as well as a decrease in thermal conductivity and melting temperature. According to this report, the presence of MAs in low concentration would have a negligible effect on the material properties and properties under irradiation of the MOX fuel. However, due to insufficient data on the elementary mechanisms governing the fuel behaviour under irradiation such as atomic transport, trapping of fission gases as well as the poor knowledge of the influence of minor actinides on the mechanical, structural, and elastic properties on $(U,Pu)O_2$, such a conclusion needs to be better justified. Thus, additional studies aiming at investigating the influence of minor actinides, particularly americium (since it is the most abundant MA), on atomic transport properties, point defects stability, finite temperature properties, mechanical, structural, and elastic properties of MOX fuel are

required.

CEA is co-developing with EDF a software platform (PLEIADES) containing the GERMINAL code for the simulation of the SFR fuel behaviour under irradiation. This platform requires a database on the material properties that can directly come from the experiments. However, some experimental data are missing or difficult to obtain owing to the cost associated to experiments or radiotoxicity of certain radioelements such as plutonium or americium. Thus, modelling through its various scales ranging from the atom scale to the pellet scale, called multiscale modelling scheme, is an alternative. The various modelling techniques used (empirical potentials, cluster dynamics, CALPHAD models, thermo-kinetics, thermo-mechanics, etc.) are interdependent and also need data often from smaller scales. Electronic structure calculations perfectly address these needs by providing data for methods based on empirical potentials, cluster dynamics, CALPHAD or thermo-kinetic models but also support the separate-effect experiments conducted in CEA. Indeed, electronic structure calculations are a valuable aid for the interpretation of EXAFS or XANES experiments but also for the identification of the traps and mechanisms of fission gas diffusion.

The development of the electronic structure calculation method DFT+U (recently generalized denomination for LDA+U or GGA+U) in 1992 [28], which is an approximation beyond the standard density functional theory (DFT), optimized to take into account the strong correlation effects within the localized orbitals such as the *5f* orbitals in actinide oxides, has largely contributed to the achievement of more precise studies on actinide-based oxides fuel. The DFT+U method enables determining the physicochemical and thermodynamic properties evolution of a mixed oxide as a function of its composition and its stoichiometry [29,30]. It enables characterizing the most stable point defects created by irradiation or by deviation from stoichiometry and determining the effect of these defects on the structural, electronic and thermodynamic properties of the materials. The DFT+U method also allows to apprehend atomic transport properties by determining migration mechanisms of an atom and associated migration energies. However, there are no studies yet in the literature using DFT+U to study the material properties of americium-bearing mixed oxides.

In summary, studies carried out in the literature on (U,Pu)O_2 fuel containing Am show that americium induces a slight decrease in thermal conductivity, melting temperature and an increase in the oxygen potential. However, due to insufficient or missing data, in particular on the elementary mechanisms governing the fuel behaviour under irradiation (stability of point defects, atomic transport, fission gas behaviour) as well as on the finite temperature properties, mechanical, structural and elastic properties, it is impossible to conclude on the influence of americium. On the other hand, experimental studies on this compound are expensive and difficult to implement due to the radiotoxicity of plutonium and americium. The density functional theory (DFT)+U through a multiscale modelling scheme is therefore an excellent alternative, since it has been widely used in the case of other actinide oxides such as UO_2 and PuO_2.

It is in this context that this thesis is conducted. It consists in determining the influence of a low americium content on finite temperature properties, point defects (stability, transport), elastic, structural and electronic properties of uranium-plutonium mixed oxides (U,Pu)O_2 by appropriate electronic structure calculations (DFT+U).

To achieve this, we have defined an approach aimed at providing reliable material data on these oxides. We begin by studying the pure americium oxides (AmO_2 and Am_2O_3) in order to adapt the DFT+U method to americium-bearing oxides and then to provide (to multiscale modelling scheme) some missing properties of interest of AmO_2 and Am_2O_3 oxides. Once the DFT+U method is implemented for pure americium oxides, the next step is to apply it to (U,Pu,Am)O_2 in order to determine the effect of Am. But, given the complexity of the U-Pu-Am-O quaternary system and the very rare data on this compound, we made the choice to first study (U,Am)O_2. Note that experimental data on (U,Am)O_2 are also very scarce and more data are necessary for the CALPHAD modelling of the U-Pu-Am-O system.

The outline of this manuscript is as follows:

After presenting the methods used in this work in Chap. 1, we provide a literature review on material properties, namely structural, elastic, electronic, thermodynamic, point defects properties of Am-bearing oxides in Chap. 2.

The objective of Chap. 3 is to implement the DFT+U method in oxides containing americium. Indeed, the use of the DFT+U method requires the prior knowledge of two key parameters, namely Hubbard U and J parameters. For this, the idea is first of all to study metastable states inherent to the DFT+U method in order to search the electronic configurations of the Am *5f* orbitals in AmO_2 that lead to the ground state of the system. We calculated the Am *5f* electrons occupation matrices in AmO_2 using the well known occupation matrix control method already applied in PuO_2 [31] and UO_2 [32]. The next objective is to determine the optimum U and J parameters allowing to take into account the strong correlations between the Am *5f* electrons in AmO_2. For this, we have calculated several material properties of AmO_2 as a function of the U and J parameters and, by comparison to the experimental results available in the literature, we have determined the parameters which enable a better description of the AmO_2 properties. Finally, we have used these parameters within the DFT+U method to predict several poorly known or missing AmO_2 and Am_2O_3 properties. This part of results has been published in Phys. Rev. Materials [33].

Chap. 4 aims at studying electronic and atomic point defects in AmO_2. Indeed, the literature is blank concerning the properties of point defects in AmO_2. Yet, these properties, in particular the atomic transport properties govern the microstructure evolution of a material. The idea is to first study electron donor point defects such as oxygen vacancies and americium interstitials. Only electron donor defects were considered here because according to the literature [12], the maximum oxidation state of americium is +IV (as in AmO_2) and thus, AmO_2 can only be reduced. The next objective is to study the stability and the hopping of small electronic polarons. Indeed, since the polarons participate in the defect and charge thermodynamic equilibrium of a material, they must necessarily be taken into account in the defect thermodynamic models. Moreover, electron polarons are by products of the formation of oxygen vacancies, which may be present in rather large concentration in AmO_2. The results obtained is this chapter are included in paper submitted to Physical Review B.

Chap. 5 aims at applying DFT+U to UO_2 containing americium in proportions ranging from 0 to 100% in order to study the influence of americium on the electronic, structural, energetic and point defect properties of UO_2, but also to support the separate-effect experiments conducted at CEA on (U,Am)O_2. One of the challenges is to build supercells that better describe the U and Am cations disorder in the face-centered-cubic (cfc) sites for different Am contents. To achieve this, we have constructed our simulation boxes using the SQS configurations proposed by von Pezold [38]. We then calculate electronic, structural, and energetic properties for different Am contents. The next step is to study the stability of the oxygen vacancies in (U,Am)O_2 knowing that, it has been shown in the literature that the oxygen vacancies are the dominant points defects in UO_2 under reducing conditions [39, 40]. For this, we considered various chemical environments in terms of neighboring cations to the vacancy and we studied the thermodynamic stability of the vacancies in the most energetically favourable environment. The results obtained are compared with those obtained in UO_2 to determine the effect of americium. The results obtained in this chapter are published in Journal of Physics: Condensed Matter.

The objective of Chap. 6 is to extend the studies carried out in Chap. 5 to (U,Pu,Am)O_2 (25 atm.% Pu) with Am contents less than 10%. The idea here is first to build supercells of (U,Pu,Am)O_2 from the (U, Pu)O_2 one. For this, we have treated Am as an impurity diluted in a solid solution of (U,Pu)O_2 (in substitution to a given U) because the Am content is considered low compared to that of U and Pu. We then studied the relative stability of supercells according to the Am chemical environment in terms of neighboring cations to the Am atom. The following step is to calculate structural, elastic, energetic, and point defects properties considering the most favourable configuration. Finally, by comparison to the studies available on (U,Pu)O_2 we have determined the influence of a low americium content on the calculated material properties of (U,Pu)O_2.

Chapter 1

Methodological approach

Contents

1.1 Introduction

In this section, we present the Density Functional Theory (DFT), implemented in the electronic structure calculation codes ABINIT and VASP which are used in this study. Actinide based compounds such as americium-bearing oxides have strongly localized *5f* orbitals and therefore their electrons undergo strong Coulomb repulsions. Taking into account these strong correlations requires a deep improvement of the standard DFT functionals through the development of techniques beyond the standard DFT, which are presented in Sec.1.3. These techniques have already been shown to work well in the investigation of actinide compounds. Furthermore, we present some features and

concepts included in the DFT codes which are necessary to obtain the properties of interest of AmO_2, (U, Am)O_2, and (U, Pu, Am)O_2 presented in this PhD work. Namely, spin-orbit coupling, minimun energy path methods, linear response calculations, *ab initio* molecular dynamics.

Note that the energy contribution from the DFT calculations is the internal energy U of the system exclusively. According to the first principle of thermodynamic, U can be connected to the Gibbs free energy G as follows:

$$G = \underbrace{U + pV}_{H} - TS \tag{1.1}$$

where p, V, T, S, H are the pressure, volume, temperature, entropy, enthalpy of the system, respectively. Since in static DFT calculations the equilibrium volume corresponds to a zero pressure and the temperature is zero (the thermal vibrations are not taken into account), $G \approx H \approx U$. Thus, throughout this manuscript, all calculated energies using static DFT relate to the Gibbs free energy G and will be denoted as E.

1.2 Density functional theory

DFT is currently the most popular and efficient method used in the electronic structure calculations of the ground state of solids. Its formulation was developped through the formalism by Hohenberg and Kohn [42] in 1964, and further by Kohn and Sham [43] in 1965. DFT has been largely used since the 1970s for quantum physics and chemistry studies but also more recently and more specifically for the description and prediction of nuclear fuels material properties. Numerous DFT studies already reported in the literature or conducted at CEA highlight the major role played by electronic structure calculations in the complementarity with separate-effect experiments [44–46].

The DFT method aims at simplifying the quantum many-body problem, that we first briefly summurize. The physical properties of a system of S nuclei and N electrons may be obtained by solving the Schrödinger equation:

$$\hat{H}\Psi(\mathbf{r}_1, \mathbf{r}_2, ..., \mathbf{r}_N, \mathbf{R}_1, \mathbf{R}_2, ..., \mathbf{R}_S) = E\Psi(\mathbf{r}_1, \mathbf{r}_2, ..., \mathbf{r}_N, \mathbf{R}_1, \mathbf{R}_2, ..., \mathbf{R}_S) \tag{1.2}$$

H is the total Hamiltonian of the system, $\Psi(\mathbf{r}_1, \mathbf{r}_2, ..., \mathbf{r}_N, \mathbf{R}_1, \mathbf{R}_2, ..., \mathbf{R}_S)$ is the many-body wave function of the system, $\mathbf{r}_i$ (with i from 1 to N) and $\mathbf{R}_p$ (with p from 1 to S) correspond to the coordinates of the electrons and nuclei respectively and E is the total energy which is eigenvalue of the Hamiltonian. The Hamiltonian of Eq.1.2 can be expressed in atomic units in the following form :

$$H = -\frac{1}{2}\sum_{p=1}^{S}\frac{\nabla^2_{\mathbf{R}_p}}{M_p} - \frac{1}{2}\sum_{i=1}^{N}\nabla^2_{\mathbf{r}_i} + \frac{1}{2}\sum_{p=1}^{S}\sum_{q\neq p}^{S}\frac{Z_p Z_q}{|\mathbf{R}_p - \mathbf{R}_q|} + \frac{1}{2}\sum_{i=1}^{N}\sum_{j\neq i}^{N}\frac{1}{|\mathbf{r}_i - \mathbf{r}_j|} - \sum_{p=1}^{S}\sum_{i=1}^{N}\frac{Z_p}{|\mathbf{R}_p - \mathbf{r}_i|} \tag{1.3}$$

The Hamiltonian is formed by five terms: the first and second terms are the kinetic energy related to the nuclei and electrons respectively, the last three terms are the nuclei-nuclei, electron-electron and nuclei-electrons Coulomb interactions respectively. S and N are the total number of nuclei and electrons, M_p and Z are the nuclear mass and nuclear charge.

The analytical resolution of the Hamiltonian defined in Eq.1.3 for a system containing more than one particle is generally impossible. To overcome this issue posed by many-particle systems, several approximations and theorems aiming at simplifing the wave function and therefore the Hamiltonian have been developed (see thesis [29, 40, 47] for more details). The main approximations and theorems are: (i) the Born-Oppenheimer approximation which consists in separating the nuclei motion from the electron motion, justified by the much larger nuclei mass compared to the electron mass, (ii) the Hohenberg and Kohn theorems on which the key principle of the DFT method is based. Indeed, these physicists proved that the ground-state energy of the electronic subsystem is a functional of the electronic density of the ground state. In other words, a given density $n(\mathbf{r})$ can be the ground state density of the electron subsystem for a unique external potential. This completely defines the Hamiltonian, and thus, the ground state energy. Based on these theorems, Kohn and Sham proposed a simpler formulation by introducing an equivalent system of non-interacting electrons, supposed to have the same electron density $n(\mathbf{r})$ in its ground state as that of the real system of interacting electrons. This non-interacting electron gas is described by a set of single-electron wave functions ϕ_i. These progresses lead to reformulate the search of the electronic ground-state energy by the minimization of the density functional:

$$E[n(\mathbf{r})] = -\sum_i \int \phi_i^*(\mathbf{r})\frac{\nabla^2}{2}\phi_i(\mathbf{r})d\mathbf{r} + \int d\mathbf{r} v_{ext}(r)n(\mathbf{r}) + \frac{1}{2}\int\int d\mathbf{r}d\mathbf{r}'\frac{n(\mathbf{r})n(\mathbf{r'})}{|\mathbf{r}-\mathbf{r}'|} + E_{XC}\left[n(\mathbf{r})\right] \tag{1.4}$$

where $v_{ext}(\mathbf{r})$ is the external potential formed by the nuclei-electrons and nuclei-nuclei interactions (which, at fixed atomic positions, is only a constant) of Eq. 1.3 and $\phi_i(\mathbf{r})$ are the Kohn-Sham single-electron wave functions related to $n(\mathbf{r})$ by $n(\mathbf{r}) = \sum_{i=1}^{N} |\phi_i(\mathbf{r})|^2$.

The last term $E_{XC}\left[n(\mathbf{r})\right]$, called exchange-correlation functional, is a key term of DFT since the accuracy of the DFT results depends on the accuracy of the description of this functional. However, its analytical expression as a function of $n(\mathbf{r})$ is unknown and as a consequence, it needs to be approximated.

The minimization of the energy functional (Eq.1.4) with respect to the density (subject to the constraint of orthonormalization of the Kohn and Sham wave functions), leads to a set of one-electron equations, known as the "Kohn-Sham" equation and written as follows:

$$\underbrace{\left[-\frac{1}{2}\nabla^2 + v_{eff}[n(\mathbf{r})]\right]}_{\hat{H}_{KS}[n(\mathbf{r})]}\phi_i(\mathbf{r}) = \epsilon_i\phi_i(\mathbf{r}) \tag{1.5}$$

where $v_{eff}[n(\mathbf{r})]$ is the effective potential given by:

$$v_{eff}[n(\mathbf{r})] = v_{ext}[n(\mathbf{r})] + \int d(\mathbf{r})\frac{n(\mathbf{r}')}{|\mathbf{r}-\mathbf{r}'|} + \frac{\delta E_{XC}[n(\mathbf{r})]}{\delta[n(\mathbf{r})]} \tag{1.6}$$

In practice, $E_{XC}\left[n(\mathbf{r})\right]$ is usually described using two local and semi-local approximations : the Local Density Approximation (LDA) and the Generalized Gradient Approximation (GGA). GGA is a natural progression beyond LDA including the gradient of the electronic density. In many cases, GGA corrects the overestimation of binding energies of molecules and cohesion energies of solids obtained in LDA. This improvement leads to a finer description of structural properties and cohesion energies of materials

especially actinides based materials. On the other hand, GGA is not a perfect approximation owing to the fact that it does not capture the strong correlation effects of the *3d* and *4f-5f* orbitals encountered in transition metal and rare-earth/actinide-bearing materials. Furthermore, GGA as well as LDA fails to describe the non-local van der Waals (vdW) interactions. In particular, taking into account the vdW interactions is required for an accurate modeling of the fission gases such as krypton, xenon, and helium in which the contribution of the vdW interactions is important.

1.3 Approximations beyond standard DFT (LDA/GGA): Suitable methods for actinide-bearing materials

In order to accurately describe strongly correlated materials, several methods beyond the standard DFT exchange-correlation approximations (LDA/GGA) have been developed, among which, the self-interaction correction (SIC) [48], coupling dynamical mean field theory to DFT (DFT+DMFT) [49, 50], hybrid functionals and DFT+U [51, 52]. The SIC method introduces a term allowing to correct the non physical interactions (electron self-interaction) induced by the standard DFT functionals. By cancelling the self-interaction energy, this term contributes to improve the description of the correlated electrons. However, the implementation of this method especially in presence of point defects is very complex. The DFT+DMFT method is very accurate for the description of weakly as well as strongly correlated materials, but it is very time consuming and thus currently limited to fifty-atom supercells. The hybrid functional approach is one of the methods commonly used to describe strongly correlated materials because its implementation is simple. However, this method is also very time consuming and thus, used only for supercells containing no more than a few dozen atoms. The DFT+U method is currently the most used approach to deal with the materials in which the correlation effects among the electrons is important such as actinide-bearing materials. Contrary to the methods presented above, the DFT+U method can be used for systems containing a few hundred atoms and thus, makes it relevant for the investigation of isolated point defects. The DFT+U method is used in this PhD work. In order to test the consistency and reliability of the DFT+U parameters determined in this work, we also performed calculation using the hybrid functional as parametrized by Heyd-Scuseria-Ernzerhof [52]. Indeed, this functional does not require prior knowledge of the onsite Coulomb interaction U and exchange J parameters (see Sec. 1.3.1) but a ratio of the Hartree-Fock exchange term (generally set at 25%) (see Sec. 1.3.2).

1.3.1 DFT+U method

Introduced for the first time by Anisimov [28], the DFT+U method is one of the state-of-the-art approaches extensively and successfully used for correlated materials especially actinide compounds. Moreover, DFT+U can also be used to enforce localization of a charge (hole or electron) on a given orbital of a single atom when studying a mechanism involving charge transfer process.

a) Principle of the DFT+U method

DFT+U consists in adding to the standard DFT functionals (LDA / GGA) an additional Hubbard-like term to take into account the strong correlation effects. The Hubbard term contains two parameters : the U and J (related to an exchange term) parameters taking into account electron-electron interactions within the correlated orbitals. The corrected total energy is the sum of the DFT energy E^{DFT}, the Hubbard interaction energy E_{Hub} and the double counting term E_{dc} (see Eq. 1.7). The double counting term E_{dc} is used to cancel the part of the interactions already taken into account within the standard DFT functionals.

$$E^{DFT+U} = E^{DFT} + E_{Hub} - E_{dc} \tag{1.7}$$

Two types of approaches are usually employed to describe the Hubbard term: the rotationally invariant form by Liechtenstein *et al.* [53] involving the U and J parameters separately, and the form by Dudarev *et al.* [54] rather involving the $U_{eff} = U - J$ difference. However, whatever the approach used, the Hubbard energy is given by:

$$E_{Hub} = \frac{1}{2} \sum_{m\sigma \neq m'\sigma'} W^{\sigma\sigma'}_{mm'} n^{\sigma}_{m} n^{\sigma'}_{m'} \tag{1.8}$$

where n^{σ}_{m} is the number of electrons within the (m, σ) orbital and $W^{\sigma\sigma'}_{mm'}$ is the matrix component of the Coulomb interaction between the electron localized in the orbital m having a spin σ and the electron localized in the orbital m' having the spin σ'. Note that $W^{\sigma\sigma'}_{mm'}$ can be expressed as a function of the Hubbard parameters as $W^{\sigma\sigma'}_{mm'} = U_{mm'} - J_{mm'}\delta_{\sigma\sigma'}$.

As previously mentioned, the use of DFT+U requires prior determination or calculation of the onsite Coulomb interaction U and exchange J parameters related to the Hubbard term.

b) Determination of the DFT+U U and J parameters

In the literature, several manners are used to access the U and J parameters:

(i) *Fit on the available experimental data*: the U and J Coulomb parameters can be determined by a fit based on the experimental data. For instance, properties such as lattice parameter, band gap, bulk modulus, elastic constants, formation enthalpy etc... can be calculated as a function of the U and J parameters and then the values of the parameters allowing to provide the best description of these properties compared to the experimental data can be determined. This method is applied in this study to the americium oxides as presented in Chap. 3.

(ii) *Experimental determination*: By analyzing X-ray photoemission spectra and X-ray absorption spectra of actinide dioxide compounds with the impurity Anderson model, Kotani and Ogasawara [23] extracted the values the U and J parameters for *5f* electrons of actinide atoms. For instance (U, J) = (4.50, 0.54) eV for U atom in UO_2; (5.50, 0.68) eV for Pu atom in PuO_2 and (6.00; 0.75) eV for Am atom in AmO_2.

(iii) *Ab initio calculations*: several methods have been developped to compute the Coulomb parameters in the framework of *ab initio* calculations among which, the con-

straint Random Phase Approximation method by Aryasetiawan *et al.* [55, 56] and the one by Cococcioni *et al.* [57]. In the case of uranium dioxide, Amadon *et al.* [58] applied the constraint Random Phase Approximation method to calculate the U and J parameters. They found $U = 5.7$ eV and $J = 0.4$ eV.

The use of the DFT+U thus allows to correct the DFT in the case of strongly correlated materials. However the DFT+U approximation promotes integer occupations of the correlated orbitals and thereby, creates an anisotropy of the electronic density and thus of the crystal cell. This induces an increase in the number of metastable states as pointed out in numerous DFT+U studies [31, 47, 59]. The metastable states originate from the fact that depending on the initial electronic configuration of the correlated orbitals, the electronic system is sometimes trapped in a local minimum (different from the ground state) during calculations and the energy barrier to jump to the global minimum is too high. In order to provide a reliable and accurate description of the correlated materials, it is necessary to use relevant methods to ensure convergence to the ground state during calculations.

c) Control of the convergence to the ground state

Several techniques have been developed in the literature to avoid metastable states in DFT+U calculations. These are the *U-ramping* method by Meredig *et al.* [60], the *quasi-annealing* method by Geng *et al.* [61], the *controlled symmetry reduction* method by Gryaznov *et al.* [62], and the *occupation matrix control* (OMC) scheme by Amadon *et al.* [59] and Jomard *et al.* [31] applied on UO_2 by Dorado *et al.* [47]. This latter method is the least time consuming and easy to use. We will only present this method since it is the one used in this manuscript.

The principle of the OMC method is to test many electronic filling (occupation matrix) of the correlated orbitals of a perfect crystal and then, determine the occupation matrix leading to the lowest energy (see Chap.3 for more details). The matrix is fixed at the begining of subsequent calculations in order to pre-condition the convergence to the ground state.

The OMC method has been already used to successfully study strongly correlated materials such as PuO_2 [63], UO_2 [64]. This method has been extended to the investigation of point defects in UO_2 in the framework of Dorado's and Vathonne's PhDs [39, 47] as well as to the investigation of uranium-plutonium mixed oxides in the framework of Cheik Njifon's PhD [29].

1.3.2 Hybrid functionals

The principle of hybrid functionals is to increase the localization of correlated electrons by using a linear combination of the Hatree-Fock exact non-local exchange functional and the standard DFT exchange functional (GGA or LDA). The most used formulations are those by Heyd-Scuseria-Ernzerhof (HSE) and the one derived from Perdew-Burke-Ernzerhof (PBE0) functional [51].

Concerning the PBE0 functional, the resulting expression for the exchange and

correlation energy is given as follows:

$$E_{xc}^{PBE0} = \alpha E_x^{HF} + (1-\alpha)E_x^{DFT} + E_c^{DFT} \tag{1.9}$$

E_x^{HF} is the exact non-local exchange term of Hartree-Fock. E_x^{DFT} is the local exchange term as used in the PBE functional. α is a parameter expressing the proportion of the DFT functional replaced by the Hartree-Fock functional. It is usually equal to 0.25. E_c^{DFT} is the correlation term.

The HSE functional is less time consumming than the PBE0 functional because of the separation of short-range (SR) and long-range (LR) electron-electron interactions included in the HSE functional. The resulting expression for the exchange-correlation energy is given by:

$$E_{xc}^{HSE} = \alpha E_x{}^{(HF,SR)}(\mu) + (1-\alpha)E_x^{(DFT,SR)}(\mu) + E_x^{(DFT,LR)}(\mu) + E_c^{DFT} \tag{1.10}$$

In this equation, the separation of short- and long-range electron-electron interactions is only performed on the exchange functional (not on the correlation functional) by introducing an additional parameter μ. The electronic correlations are represented by the standard DFT functional E_c^{DFT}. μ is a parameter having the dimension of a distance and defining the range (long or short) of the separation.

1.4 Representation of the wave functions

After writing Kohn-Sham's single-electron equation (Eq. 1.4), the next challenge is to adequately represent the electron wave functions and to find an adequate basis set that can effectively describe the Kohn-Sham's single-electron wave functions. Indeed, in the interatomic region, the Kohn-Sham single-electron wave functions $\phi_i(\mathbf{r})$ take a relatively smooth form while near the nucleus they oscillate rapidly owing to the attractive potential of the nucleus. Two solutions are commonly used to describe the single-electron Kohn-Sham wave functions. The first solution is to decompose the wave function over a localized orbital basis and the second solution is to decompose the wave function on a plane-wave basis. The decomposition over a localized orbitals basis has the advantage of easily describing the strong oscillations of the wave functions near the nucleus. However, this basis depends on the position of the atoms. Therefore, one should necessarily move the basis each time the positions of the atoms change. The second solution has enormous advantages owing to the fact that this plane wave basis is mathematically simple, and simplifies the calculation of the forces acting on the atoms. In addition, the errors related to the truncation of the basis can be easily controlled by increasing the number of plane waves.

1.4.1 Plane wave representation

In a periodic solid (crystal), the Kohn-Sham wave functions are assumed to take the form imposed by Bloch's theorem. First, the quantum number denoted so far as i in the Kohn-Sham equations (Eq. 1.5) becomes a wave vector $\mathbf{k}$ (that can be restricted to the First Brillouin Zone of the crystal) and a band index n. Then $\phi_{n\mathbf{k}}$ writes as

the product of a plane wave $\exp(i\mathbf{k}.\mathbf{r})$ and a function $u_{n\mathbf{k}}$ having the periodicity of the lattice:

$$\phi_{n\mathbf{k}}(\mathbf{r}) = u_{n\mathbf{k}}(\mathbf{r}) \exp\left[i\mathbf{k}.\mathbf{r}\right] \tag{1.11}$$

Since $u_{n\mathbf{k}}$ is a periodic function, it is possible to expand it as a series of plane waves $\exp(i\mathbf{G}.\mathbf{r})$, with $\mathbf{G}$ being a vector of the reciprocal lattice:

$$u_{n\mathbf{k}}(\mathbf{r}) = \Omega^{-1/2} \sum_{\mathbf{G}} C_{n\mathbf{k}}(\mathbf{G}) \exp\left[i\mathbf{G}.\mathbf{r}\right] \tag{1.12}$$

where Ω is the unit cell volume, $\mathbf{G}$ a wave vector, $C_{n\mathbf{k}}(\mathbf{G})$ are the expansion coefficients in the plane wave basis, and i the complex number defined by $i^2 = -1$.

Finally, the Kohn-Sham wave function itself writes :

$$\phi_{n\mathbf{k}}(\mathbf{r}) = \Omega^{-1/2} \sum_{\mathbf{G}} C_{n\mathbf{k}}(\mathbf{G}) \exp\left[i(\mathbf{G}+\mathbf{k}).\mathbf{r}\right] \tag{1.13}$$

In practice, a truncation in the expansion of the wave function is required. This is done by imposing a cut-off energy E_{cut} to the wave function. Therefore, the $\mathbf{G}$ vectors in Eq.1.13 are those that satisfy the following criterion:

$$\frac{\hbar^2(\mathbf{G}+\mathbf{k})^2}{2m} \leq E_{cut} \tag{1.14}$$

Note that, it is important to choose E_{cut} through convergence tests in such a manner that the energy, energy differences or any other physical observable as a function of E_{cut} satisfies a required accuracy criterion on the properties of interest. On the other hand, it is difficult to use plane waves to reproduce the wave function near the nucleus because of the strong oscillations in this region. Indeed, the description of the strong oscillations of the wave function requires a very large number of plane waves. To overcome this issue, two methods are usually used within the DFT method: (i) the pseudopotential method which is very efficient but its main limitation is the possible non-transferability of the pseudopotential and (ii) the Projector Augmented Wave (PAW) method which will be briefly presented in the following section.

1.4.2 Projector Augmented Wave method (PAW)

The PAW [65, 66] formalism is an efficient and accurate method for the description of complex phases in which atomic relaxations are important. The main idea of the PAW formalism is to divide the wave function into two complementary parts:

(i) A partial wave expansion within an atom-centered sphere called PAW sphere. Within the PAW sphere, the wave function oscillates rapidly.
(ii) An envelope function outside the PAW sphere where the wave function is fairly smooth. The envelope function is expanded onto a plane wave basis set, as presented in the previous section (Sec. 1.4.1).

The PAW method is based on a linear transformation linking the AE (all electron) wavefunctions $\Psi_{nk}$to the corresponding PS (pseudo) wavefunctions $\tilde{\Psi}_{nk}$.

$$|\Psi_{nk}>=|\tilde{\Psi}_{nk}>+\sum_i\left(|\psi_i>-|\tilde{\psi}_i>\right)<\tilde{p}_i|\tilde{\Psi}_{nk}> \tag{1.15}$$

The AE ψ_i and PS $\tilde{\psi}_i$ partial waves are atomic functions and $\tilde{p}_i$ are the the projector fonctions.

All calculations done in this manuscript are based on this formalism, which is implemented in both the VASP and ABINIT codes.

Note that as within the pseudopotential method, the PAW method considers the core electrons as "frozen" since their charge density is assumed not to be affected by a variation of the chemical environment. However, the PAW method has the advantage to also take into account explicitely the charge density of the core electrons. This allows not only to describe the valence electrons but also the "frozen" core in a consistent manner.

1.5 Spin-orbit coupling (SOC)

Spin-orbit coupling (SOC) is the interaction between the particle spin and its motion around the nucleus. This interaction is weaker than the Coulomb interaction. SOC causes a significant change corresponding to a shift in energy levels due to a partial lifting of the degeneracy within orbitals. Fig.1.1 illustrates the fine structure induced by the effect of SOC in materials containing f orbitals. Let us focus on an actinide oxide. Under the effect of SOC, the *5f* level of the actinide atom is split into two sublevels that differ by the quantum number j (j=5/2 or j=7/2). j is the quantum number that quantizes the values of J^2, where J is the total angular momentum. Then, in cubic symmetry (that relevant to the fluorite structure), under the effect of the crystal field, each of these two sublevels is split again in different levels, as illustrated on Fig. 1.1.

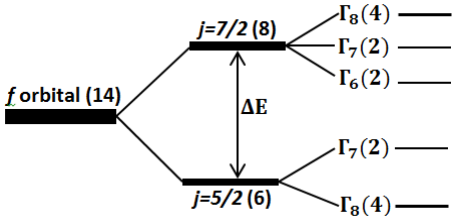

Figure 1.1: Schematic description of the energy splitting induced by spin-orbit coupling. The numbers in parenthesis represent the degree of degeneracy. The Γ_i levels are due to the lifting of the degeneracy by the crystal field in cubic symmetry (that relevant to the fluorite structure) [1].

Based on the Larmor and Thomas approximations the energy perturbation due to SOC can be evaluated as a function of the spin angular momentum $\mathbf{S}$, the angular momentum $\mathbf{L}$, and the total angular momentum $\mathbf{J}$ as follows:

$$\Delta E=\frac{a}{2}\left[\mathbf{J}^2-\mathbf{S}^2-\mathbf{L}^2\right] \tag{1.16}$$

with $a\propto\frac{Z^4}{n^3l\left(l+\frac{1}{2}\right)(l+1)}$, Z is the atomic number and l and n are the quantum numbers that quantize the energy levels of the atom. In the case of the *5f* orbital, the values

taken by J^2 are $j(j+1)\hbar^2$ with j=5/2 or 7/2, the value taken by S^2 is $s(s+1)\hbar^2$ with s=1/2, and the value taken by L^2 is $l(l+1)\hbar^2$ with l=3. The parameter a is proportional to the atomic number Z^4, indicating that the heavier the atom, the greater the effect of the SOC. Since this thesis focuses exclusively on actinide compounds which are heavy materials, we are interested in the effect of SOC in this work.

1.6 Computation of minimum energy path (MEP)

The understanding and the prediction of the nuclear fuel behaviour under irradiation or in storage conditions passes through an accurate modelling of the atomic transport properties such as diffusion coefficients and diffusion mechanisms. The diffusion coefficient D is often given through an Arrhenius law:

$$D = D_0 exp\left(-\frac{E_a}{k_B T}\right) \tag{1.17}$$

in which E_a is the activation energy associated to the diffusion, D_0 the diffusion prefactor. In the case of diffusion through intrinsic point defects such as vacancies, the activation energy E_a is generally identified as the sum of the migration energy E_m and the defect formation energy E_f.

Several techniques such as classical and *ab initio* molecular dynamics may be used to directly access D and then, to determine D_0 and E_a. However, the simulation time in these latter techniques do not allow on to observe diffusion events that are too rare and involve a large energy barrier. Instead of dynamical simulations, static calculations can be used for the study of transport properties in materials. The purpose of static migration calculations is to determine the energy barrier E_m that the migrating atom has to overcome in order to hop from one position in the crystal to the next. The challenge for static migration calculations is to find the most favorable migration mechanism i.e. the minimum energy path (MEP), which is starting from a local energy minimum and leading to another local energy minimum, passing through a saddle point. The energy of the saddle point relative to the local energy minimum is defined as the migration energy E_m. The determination of the MEP between two optimized configurations of a given system can be achieved using methods such as the "Nudged Elastic Band" method or the "String Method".

1.6.1 Nudge elastic band (NEB)

The NEB is a method to find a MEP between a known pair of stable atomic configurations constituted by an initial and a final atomic configuration, both of which are local minima on the potential energy surface. An initial migration path is interpolated and discretized into a set of images between the known initial and final atomic configurations. The MEP has the property that any point on the path is at an energy minimum in all directions perpendicular to the path. This path passes through at least one first-order saddle point. The NEB [67, 68] method is based on a spring interaction between adjacent images which is added to ensure continuity of the path, thus mimicking an elastic band. Each image moves in a force field which is a combination of the

normal component of the potential force and the tangential component of the spring force connecting the adjacent images. The MEP can then be obtained by minimizing (from the saddle point) the forces (physical and spring) acting on the images.

1.6.2 String method

The String Method is very similar in spirit to the NEB, at the exception that the spring forces of the NEB are replaced by a reparametrization procedure [69]. In this method, as in the NEB method, a number of *images* discretizing the path joining the initial and final configurations are first defined using a linear interpolation. The method is iterative, and each iteration consists of two steps: (i) an evolution step, (ii) a reparametrization step. In the evolution step, the same projections of the physical forces as in the NEB are used to direct the images distributed along the string to the MEP. The difference between the string and NEB methods is that, at the reparametrization step, the images are redistributed in order to be kept equally spaced along the pathway. In the NEB method, spring forces are introduced between images along the band. In the string method, no spring forces are used. Instead, the images are equally redistributed along the path after each iteration so that the distance between image p and $p+1$ is constant along the "string". Despite these different approaches for distributing images along the path, there is no significant difference in the final path or the rate at which the methods converge [70].

Note that, since two consecutive images along the path are equidistant, the image index along the final path can be used as relevant reaction coordinate for the considered process.

1.7 Linear response calculations

The methods used to determine electronic dielectric tensor and Born effective charges in this PhD are based on the Density Functional Perturbation Theory (DFPT) [71,72]. DFPT is a variational approach that allows computing the second derivatives of the total energy with respect to various perturbations, such as an external homogeneous electric field.

In an insulator, the Born effective charge tensor $Z^*_{K,\alpha\beta}$ of atom K is the first derivative of the polarization component along direction β with respect to the displacement of atom K along direction α. It can also be written as a mixed second derivative of the total energy with respect to such displacement and to the macroscopic electric field.

The static dielectric tensor connects, at linear order, the macroscopic displacement field to the macroscopic electric field; it describes how an insulator is able to polarize under the application of an external electric field. The static dielectric tensor can be written as the second derivative of the total energy with respect to the electric field components. The so-called relaxed-ion dielectric tensor contains two parts: first, the electronic dielectric tensor, which is the contribution due to the polarization of the electrons at fixed atomic positions; second, a sum of contributions due to atomic displacements, which can be here obtained from the knowledge of the phonon modes at the Γ point. In this work, the phonon modes at Γ are obtained by using a frozen-phonon

methodology (see Sec. 3.4.2).

1.8 *Ab initio* molecular dynamics method

Proposed by Car and Parrinello [73] in 1985, *ab initio* molecular dynamics has been applied for the first time to the actinide mixed oxide compounds by Cheik Njifon in its PhD thesis [29]. Molecular dynamics (MD) calculations are able to predict equilibrium and to some extent non-equilibrium properties of condensed-matter systems. However, large practical applications of MD calculations usually employed empirical pair-potentials. These calculations, while appropriate for many types of systems, require the prior parametrization of the empirical interatomic potential used. Indeed, the parameters of a given empirical interatomic potential may strongly vary from one system to another and, even for one system, they can vary from one atomic configuration to another (for instance, different empirical potentials can be required to describe a material in the bulk state, at surface, with charged point defects, with dislocations). On the other hand, although DFT calculations provide an accurate description of chemical bonds in a large variety of systems, they are computational demanding, especially for large and/ or disordered systems. Thanks to supercomputers, it is now possible, to some extent, to perform so-called "*ab initio* molecular dynamics" (AIMD), a technique that only differs from what has just been described by the fact that the forces are calculated, at each time step, as a result of a complete self-consistent DFT calculation of the current atomic configuration. The computational cost of such technique is, of course, much larger than when an empirical potentials are used and only rather small systems can be treated by AIMD (typically a few tens or at most a few hundreds of atoms). In many cases however, AIMD is able to provide accurate trends about the effect of thermal fluctuations or phase transitions.

Note that AIMD assumes the atoms as being classical point particles. Thus, although the electrons are treated at the quantum level by DFT, the atoms remain a classical system. The electron gas is supposed to adjust instantaneously its state to that of the nuclei: AIMD is thus performed in the framework of the Born-Oppenheimer approximation.

It is possible to impose the temperature or the pressure in a MD simulation, by using a "thermostat" or "barostat". For equilibrium MD, this corresponds to perform the MD in a given statistical ensemble: using only a thermostat corresponds to a simulation in the canonical (NVT) ensemble and using a thermostat and a barostat corresponds to a simulation in the isothermal-isobaric (NPT) ensemble. A thermostat in MD is a set of additional degrees of freedom coupled to the dynamics of the atoms, and which exchange energy with them, playing the role of a reservoir. The most popular thermostats are the Nose thermostat, the Nose-Hoover thermostat and the Langevin thermostat. Practically, there is a supplement of forces in the Newton equations of motion, which pump or add the kinetic energy necessary to make the temperature oscillate around the desired value. When a barostat is used, the simulation cell is allowed to deform in order to match, on average, the desired pressure. The time-evolution of the cell vectors is coupled to the dynamics of the atoms. One very popular barostat is the Parrinello-Rahman barostat. Thermostat and barostat can be used together to control both the temperature and the pressure.

1.9 Basic concepts on small polarons

We study in detail small electron polarons which result from the presence of the oxygen vacancies (see Chap.4). Therefore, in order to avoid redundancy, we choose to present basic concepts about small polarons (self-trapping and its hopping) in Chap.4.

The state-of-the-art methods presented in this chapter will be used in this work to accurately calculate the missing or poorly known properties of americium-bearing oxides in order to provide reliable data to multi-scale fuel modelling scheme developed in CEA.

Chapter 2

State of the art

State of the art on AmO_2, Am_2O_3 oxides, and (U, Am)O_2 and (U, Pu, Am)O_2 mixed oxides

Contents

2.1 Introduction

As mentioned in the general introduction, the investigation of pure americium oxides properties is an important step toward the determination of the effect of americium on

the uranium-plutonium mixed oxides properties using electronic structure calculations. The main idea is to rely on the available data on americium dioxide to implement the DFT+U method in americium-bearing oxides. The methodology defined is then also used to predict missing properties of interest of pure americium oxides. Thus, in the first and second sections, the available data on structural, elastic, magnetic, electronic, and thermodynamic properties on AmO_2 and Am_2O_3 are presented. In the third section, the available studies on the effect of americium in uranium oxide are reviewed. More precisely, valence state of cations, thermodynamic, and structural properties of (U,Am)O_2 are reported. Finally, we report the very few data available on (U,Pu,Am)O_2. In order to evaluate the under-irradiation performance of americium-bearing uranium-plutonium mixed oxide fuels, several experiments have been carried out [27] as mentioned in the general introduction: SUPERFACT irradiations in the PHENIX reactor, AM1 in JOYO and AFC-2C and 2D in ATR. These results point out a high helium production, a slight decrease in the thermal conductivity and the melting temperature, as a function of americium content. However, the elementary mechanisms occurring under reactor operating conditions or resulting of the self-irradiation, such as formation of point defects and atomic diffusion, remain unknown. Nonetheless, in order to refine the prediction of the behaviour of fuel under irradiation, the study of defect properties, atomic transport, and fission gases behaviour is required. We compare when possible the results obtained by calculation (electronic structure calculations) with the experimental ones in order to highlight the reliability of the results yielded by electronic structure calculations.

2.2 Available studies on AmO_2

We have highlighted in Sec.1.3 that the DFT+U approximation is well adapted to the description of the properties of actinide oxides. However, the DFT+U Coulomb U and J parameters are well established only for very few actinide oxides. In the case of AmO_2, the literature does not agree on any value for these parameters (U and J) since they vary from one author to another. Based on the X-ray photoemission spectra and Anderson impurity model, Kotani *et al.* [23] have proposed the DFT+U parameters for some actinide oxides, like UO_2, PuO_2 or AmO_2 (see Table 2.1). The investigation by Kotani *et al.* [23] gives values of $U = 6.00$ eV and $J = 0.75$ eV for Am in AmO_2. However, due to the lack of additional studies aiming at validating these values, further investigation is needed to confirm that these values are indeed the ones that best reproduce the properties of americium dioxide.

Table 2.1: Coulomb U and J parameters between the *5f* electrons extracted from the experiments according to Kotani *et al.* [23] investigations.

	Th	**U**	**Np**	**Pu**	**Am**	**Cm**	**Bk**
U (eV)	4.00	4.50	5.00	5.50	6.00	6.70	7.28
J (eV)	0.40	0.54	0.61	0.68	0.75	0.82	0.89

2.2.1 Structural properties

The face centered cubic (*fcc*) fluorite-type CaF_2 (N° 225 $Fm\bar{3}m$ space group) structure of americium dioxide was identified for the first time by Zachariasen in 1949 [74] and confirmed by Dancausse *et al.* [2] in 2002. Moreover, the X-ray diffraction (XRD) experiments carried out by Dancausse *et al.* [2] show that at low temperature, americium dioxide undergoes a structural transition to the cotunnite phase $PbCl_2$ (Pnma space group) at high pressure (around 40 GPa) (Fig. 2.1). This phase transition to the cotunnite phase is common to most actinide oxides. Note that throughout this manuscript, AmO_2 refers to the *fcc* fluorite-type.

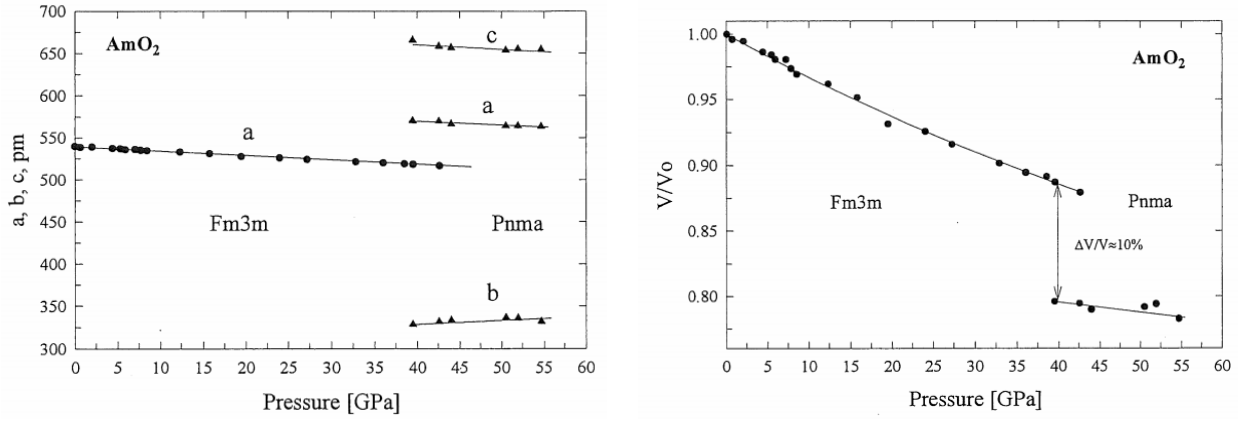

Figure 2.1: Evolution of the lattice parameter (left panel) and relative volume (right panel) as a function of the pressure [2].

Stoichiometric AmO_2 consists of tetravalent Am^{4+} cations and O^{2-} ions. The AmO_2 fluorite structure is formed by two sublattices: (i) the *fcc* sublattice in which the Am^{4+} cations occupy the positions (reduced coordinates in the conventional unit cell) $0,0,0; \frac{1}{2},\frac{1}{2},0; \frac{1}{2},0,\frac{1}{2}$; and $0,\frac{1}{2},\frac{1}{2}$ and (ii) the sublattice formed by the tetrahedral sites in which the O^{2-} anions occupy the positions $\frac{1}{4},\frac{1}{4},\frac{1}{4}$ and its equivalent ones. The coordination numbers of americium and oxygen are respectively 8 and 4.

From Table 2.2, we can clearly see that the values of the lattice parameter of americium dioxide from experiments are relatively scattered because the X-ray diffraction experiments are known to lead to a precision of the order of 10^{-3}. This scatter could result from the self-irradiation (α decay) of americium which induces a large amount of helium bubbles and thus, structural swelling. In order to explain this lattice expansion in AmO_2, several X-ray diffraction studies were performed [3, 4, 6, 75]. All the investigations carried out point out to an exponential evolution of the lattice parameter with time, with an analytical expression described by Eq. 2.1; the maximum relative lattice parameter increase being comprised between 0.22 and 0.325 %.

$$\frac{a_t - a_0}{a_0} = A\left(1 - e^{-Bt}\right) \tag{2.1}$$

where a_t is the lattice parameter value at a generic time t, a_0 is the undamaged lattice parameter and A and B are two constants, depending on the particular sample.

The experimental data and the corresponding fitting curves (by Eq. 2.1) are shown in Fig. 2.2 and were extracted from the Epifano [16] PhD manuscript. In this figure, the lattice expansion evolution as a function of time is consistent between the different studies, with a saturation achieved in about three months.

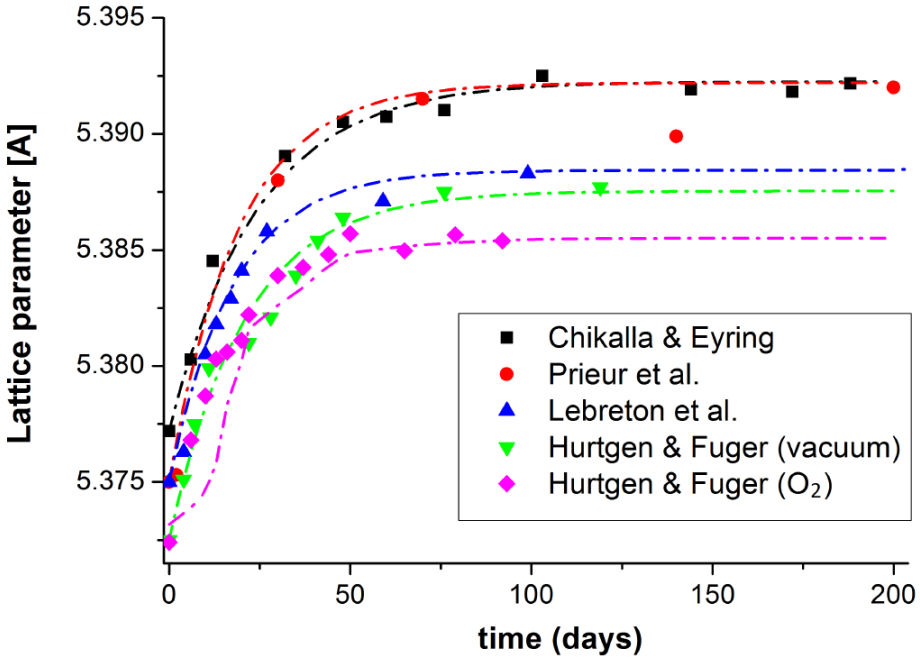

Figure 2.2: Lattice parameter expansion of AmO_2 as a function of time according to Hurtgen and Fuger [3], Chikalla and Eyring [4] , Prieur *et al.* [5] and Lebreton *et al.* [6]. This figure is extracted from Epifano's PhD thesis.

Moreover, the investigations by Hurtgen and Fuger show that the atmosphere can have a great importance [3]. Indeed they show that the relative lattice expansion at saturation is larger in vacuum than in a pure oxygen atmosphere. They relate this difference in behaviour to the tendency for the sample under vacuum to lose small quantities of oxygen under self-irradiation effect with an O/Am ratio at saturation estimated to 1.991. However, a recent investigation by Prieur *et al.* [75] contradicts this hypothesis. Indeed, Prieur *et al.* investigated 40 years old and fresh AmO_2 samples (annealed before measurements) and showed no difference in the valence state of Am and therefore, on the O/Am ratio. By applying the correction proposed in Eq. 2.1, one can therefore retain as reference value of the experimental lattice parameter of americium dioxide the value $a_0 = 5.373$Å.

Very few theoretical investigations on structural properties of AmO_2 are available in the literature. The lattice parameter values obtained in these studies are reported in Table 2.2. The value of the lattice parameter calculated using the HSE hybrid functional is very close to the experimental values. On the other hand, the values of the lattice parameter are underestimated by roughly 1% in LDA+U and overestimated by roughly 1% in GGA+U using the same U and J values. These remarks (underestimation/overestimation of the lattice parameter) confirm one of the trends in DFT+U which is well known. However, appropriate and validated values of the DFT+U U and J parameters need to be used for a good description of the structural properties.

Table 2.2: Experimental and calculated values of the lattice parameter of the AmO_2 fluorite phase.

Method	a_o (Å)	Ref.
DRX	5.383	[76]
Neutron diffraction	5.380	[77]
DRX	5.373	[3]
DRX	5.378	[4]
GGA+U+SOC, U_{eff}=6.5 eV	5.484	[7]
GGA+U, U=4 eV	5.351	[7]
LDA+U, U= 4 eV	5.311	[78]
GGA+U	5.441	[14]
PBE+U, U_{eff}=4 eV	5.425	[79]
HSE	5.375	[79]
HSE+SOC	5.357	[79]
SIC	5.420	[80]

2.2.2 Elastic properties

The bulk modulus was experimentally determined for the first time by Dancausse *et al.* [2] in 2002 using XRD experiments. In this study, the bulk modulus deduced from the Murnaghan equation is 280 GPa. Two years later, the Energy-Dispersive X-ray Diffraction (EDXRD) measurements performed by Idiri *et al.* [81] establish the bulk modulus value at 205 GPa. This value points out a large difference with the value obtained earlier by Dancausse *et al.* [2]. This large gap is also observed for other actinide oxides, such as plutonium dioxide and thorium dioxide. In order to explain this discrepancy, Idiri *et al.* [81] performed further analysis from the low pressure XRD data. By taking into account the overestimation of the pressure due to the solidification of the pressure-transmitter liquid (i.e. silicone oil generally used in the under-pressure experiments) in the reprocessing of the XRD data, the new value obtained is about 200 GPa. This value is consistent with the above EDXRD value (205 GPa) by Idiri *et al.* The same correction applied to plutonium dioxide leads to the same conclusion. The value 205 GPa is therefore the reference value of the bulk modulus of AmO_2.

Table 2.3 shows the calculated values of the bulk modulus. The values obtained through LDA+U (U=4 eV), GGA+U (U=6.5 eV) + SOC as well as by the SIC method are in good agreement with the experimental value.

Table 2.3: Bulk modulus of AmO_2 from the literature.

Method	B_0 (GPa)	References
GGA+U, U=4 eV	140	[7]
LDA+U, U=4 eV	187	[7]
GGA+U+SOC, U_{eff}=6.5 eV	204	[78]
SIC	209	[80]
Exp.	205	[81]

Note that no experimental reference of the elastic constants (other than the bulk

modulus) of americium dioxide exists to our knowledge. The only study on elastic constants reported in the literature was recently published by Yong *et al.* [7] within the GGA+U method. Yong *et al.* found C_{11}=204 GPa, C_{12}=87 GPa, C_{44}=55.3 GPa. These results confirm the mechanical stability of the AmO_2 fluorite-type. The elastic constants values are found to satisfy the following mechanical stability criterion:

$$C_{11} > 0,\ C_{44} > 0,\ C_{11} > |C_{12}|,\ (C_{11} + C_{12}) > 0 \tag{2.2}$$

However, the values obtained by Yong *et al.* [7] show a significant difference compared to those of other actinide oxides (UO_2, PuO_2, NpO_2), whereas the contrary is expected. Indeed, for UO_2, C_{11}= 364 GPa, C_{12}=118 GPa, C_{44}=58 GPa, for PuO_2, C_{11}=374 GPa, C_{12}=111 GPa, C_{44}=70 GPa. Moreover, the bulk modulus (126 GPa) obtained from these (those by Yong et *al.*) values (through the expression $B = \frac{1}{3}(C_{11} + 2C_{12})$) largely differs from the experimental value (205 GPa). Therefore, the reliability of these elastic constants needs to be confirmed (this will be addressed in Sec. 3.4.2).

2.2.3 Magnetic properties

Magnetic properties of AmO_2 were assessed for the first time using Mössbauer spectroscopy [82]. No magnetic transition was observed in these studies. Contrary to the Mössbauer measurements, the susceptibility measurements performed later by Karraker [83], in 1975, reveal an antiferromagnetic transition (AFM) around 8.5 K with a magnetic moment for Am^{4+} ion comprised between 1.32-1.52 μ_B. In order to explain this controversy, Boeuf *et al.* [77] carried out small-angle neutron scattering measurements in a temperature range including 8.5 K. These studies also do not reveal any AFM transition, even below 8.5 K, confirming the Mössbauer measurements. Neutron diffraction and Mössbauer results, however, remain contradictory compared to the susceptibility measurements. A similar situation also occurs with NpO_2, i.e. no AFM transition is observed in the neutron diffraction and Mössbauer experiments while specific heat [84] and susceptibility measurements [85] evidence a magnetic transition at T_N= 25 K. The absence of definite magnetic effects on NpO_2 is interpreted by a small ordered magnetic moment for the Np^{4+} ion in NpO_2. A small ordered magnetic moment for Am^{4+} in AmO_2 may similarly be responsible for the absence of magnetic transition in the AmO_2 Mössbauer spectrum.

Table 2.4: Magnetic moments per Am cation in AmO_2 expressed in Bohr magneton μ_B.

Method	$\mu_{Am^{4+}}$ (μ_B)	**Reference**
GGA+U, U= 4 eV	4.77	[7]
LDA+U, U= 4 eV	5.26	[7]
GGA+U+SOC, U_{eff} = 6.5 eV	5.04	[78]
HSE+SOC	4.96	[79]
HSE	4.99	[79]
Exp.	1.32-1.38	[83, 86]

Few years later, the investigation by Tokunaga *et al.* [86,87] using ^{17}O nuclear magnetic resonance (NMR) points out an AFM transition around 8.5 K with a magnetic moment for Am^{4+} ion of 1.38 μ_B. Furthermore, from the frequency curve with respect to temperature, they observe a NMR line broadening and they supposed that this NMR line broadening could arise from oxygen sublattice distortion. Nevertheless, further investigations are needed to confirm the oxygen sublattice distortion but also to provide additional information as regard the type (collinear or non-collinear) of the AFM order.

Several theoretical studies agree that the most stable magnetic order in americium dioxide is the AFM order. This is the case of the investigations by Wen *et al.* [79] using hybrid functional HSE and HSE+SOC. Suzuki *et al.* [14] also show that AmO_2 is AFM using GGA/LDA+U calculations. These studies are in perfect agreement with recent work by Bendjedid *et al.* [78]. We report some magnetic moment values from the literature in Table 2.4. Although the calculated magnetic moments are in agreement, they show a large discrepancy with the experimental magnetic moments. Further investigations are required to explain this difference. This issue will be addressed in Sec. 3.4.1.

2.2.4 Electronic properties

Up to now, there is only one experimental measurement of the electronic properties of americium dioxide aiming at measuring the band gap (energy gap between the conduction band minimum and the valence band maximum). From the absorption spectroscopy experiments, Suzuki *et al.* [14] find a band gap equal to 1.3 eV. This value is up to now the only experimental reference of the band gap of the AmO_2 fluorite phase.

Table 2.5: Band gap values in AmO_2 from the literature.

Method	Band gap (eV)	Reference
GGA+U, U= 4 eV	1.0	[7]
LDA+U, U= 4 eV	0.7	[7]
GGA+U+SOC, U_{eff} = 6.5 eV	1.3	[78]
HSE+SOC	1.5	[79]
HSE	1.5	[79]
SIC-LSD	0.8	[80]
Exp.	1.3	[14]

The band structure of the AmO_2 fluorite phase has been the subject of very few modelling studies in the literature [7, 78–80]. It is important to highlight that calculations performed within the standard DFT (GGA / LDA) fail to describe the electronic and even magnetic properties of AmO_2 (Fig. 2.3). Indeed, the standard DFT predicts AmO_2 to be a conductor. Moreover LDA predicts AmO_2 to be ferromagnetic. Knowing that AmO_2 is AFM and has a band gap of 1.3 eV, these results are in contradiction with the experimental observations. On the other hand, DFT+U describes AmO_2 as

an insulator [7,80]. One can observe through the calculated electronic density of states (see Fig. 2.3) that the band gap is mostly formed between the oxygen $2p$ occupied bands and the americium $5f$ unoccupied bands. This observation therefore suggests that AmO_2 would be rather a charge transfer insulator. However, no confirmation exits up to now.

The band gap values from the literature are summarized in Table 2.5. Comparing the values of the band gap respectively calculated using hybrid functionals HSE and HSE+SOC, one can clearly see that taking into account the effect of spin-orbit coupling has no influence on the band gap value of AmO_2. On the contrary, the investigations by Bendjedid *et al.* [78] show that without taking spin-orbit coupling into account, the electronic properties remain wrongly described, especially the band gap. This result by Bendjedid *et al.* remains contradictory to the HSE calculations and has been never confirmed, hence the need for additional studies including spin-orbit coupling. We discuss this issue in Chap. 3.

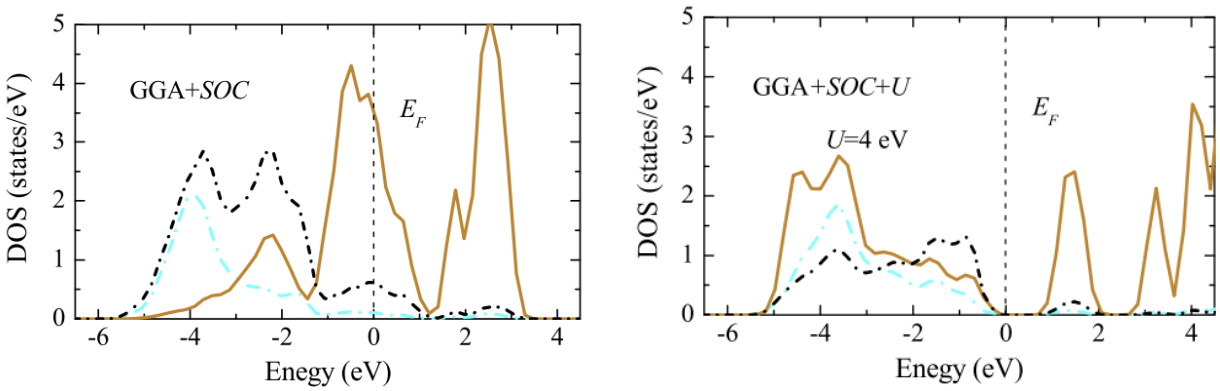

Figure 2.3: Density of states (DOS) of AFM AmO_2 calculated using DFT (left panel) and DFT+U (right panel) and taking into account the effect of spin-orbit coupling [7]. Black and blue dotted lines are $O-p$ and $Am-d$ components and orange line are $Am-f$ components.

2.2.5 Thermodynamic properties

Thermodynamic properties are quantities of interest for nuclear fuel allowing to describe their behaviour with respect to the temperature. Out of these properties we can mention the thermal expansion, the heat capacity, the thermal diffusivity, and the thermal conductivity. Here, we present thermodynamic data available in the literature on the properties cited above.

a) Thermal expansion

The thermal expansion data are essential to evaluate fuel performance aspects like pellet and cladding mechanical interaction. An increase of the temperature generally induces an expansion of the lattice crystal. In addition, a temperature increase can also produces indirect effects on the lattice parameter by changing the oxygen stoichiometry.

The thermal expansion in AmO_2 was measured by Minato *et al.* [9] on flowing air, up to 1500 K and by Fahey *et al.* [8], under oxygen up to 1230 K. Epifano *et al.* [19]

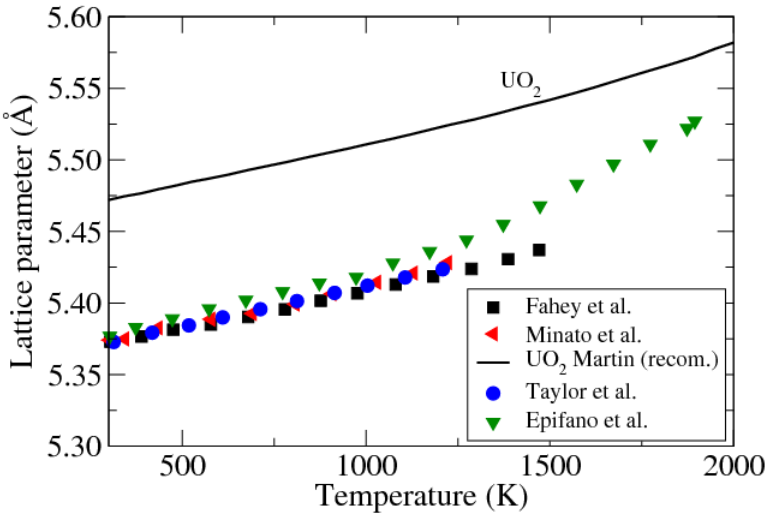

Figure 2.4: Thermal expansion of AmO_2 according to Hurtgen and Fahey *et al.* [8], Minato *et al.* [9], and Taylor *et al.* [10] compared to Martin's recommendation for UO_2 [11].

have extended investigations under pure oxygen up to 1900 K. The results obtained in these studies are shown in Fig 2.4. Due to the lack of sufficient data for americium dioxide AmO_2 especially for the high temperatures (higher than 1300 K), no relevant analytical expression fitting the behaviour of the thermal expansion of this compound (commonly called recommendation) is proposed in the literature. Foccusing on the direct effect of the temperature, Fahey *et al.* [8] proposed a comparative study of the thermal expansion behaviour of different actinide dioxides from thorium to berkelium. According to the latter, the thermal expansion of the lattice parameter as a function of the temperature can be fitted to a second or third order polynomial. Based on the several data available for uranium dioxide, Martin [11] proposed a third order polynomial expression fitting the behaviour of the thermal expansion of UO_2 as well as PuO_2. In order to evaluate the applicability of the third order polynomial fit to AmO_2, we also display in Fig. 2.4 the thermal expansion for UO_2 according to Martin's recommendation [11], expressed as follows:

$$a = a_{273K}(9.9734.10^{-1} + 9.802.10^{-6}T - 2.705.10^{-10}T^2 + 4.391.10^{-13}T^3 \quad (2.3)$$

valid for $273K \leq T \leq 923K$, and

$$a = a_{273K}(9.9672.10^{-1} + 1.179.10^{-5}T - 2.429.10^{-9}T^2 + 1.219.10^{-12}T^3 \quad (2.4)$$

valid for $923K \leq T \leq 3120K$. In these equations a and a_{273K} are the lattice parameter at a given temperature T and at $T = 273\ K$.

For temperatures less than 1200 K the results by Epifano *et al.* [19] show a small difference with other experimental results in Fig. 2.4. The authors explain this difference by a slight residual hypo-stoichiometry during cooling in the 473 K $<$ T $<$ 1173 K range, due to a possibly slow re-oxidation rate. On the other hand, at 1200K these results show a change in the slope of the thermal expansion. According to the authors, this behaviour can be attributed to the reaching below 1200 K of the stoichiometric

O/Am ratio (i.e. O/M=2), whereas the sample was reduced at higher temperature. Based on these results, we can conclude that the third order polynomial like Martin's recommendation is not sufficient to fit the thermal expansion of AmO_2.

b) Heat capacity

The heat capacity of a given material is the energy required to increase the temperature of one mole of this material by one degree Kelvin. The heat capacity is obtained by derivation of the enthalpy increment function with respect to the temperature at constant pressure:

$$C_p = \left(\frac{\partial H}{\partial T}\right)_P \tag{2.5}$$

The enthalpy increment of AmO_2 as a function of the temperature was measured between 365 to 1086 K by Nishi *et al.* [20] using drop calorimetry. In Fig. 2.5 (left panel) we report data from the study by Epifano [16], the fit of Gotcu-Freis *et al.* [13] and the measurements of Nishi *et al.* [20] compared to the enthalpy function of UO_2. All these studies provide a similar description of the stoichiometric AmO_2 from room temperature to 1200 K. The two dioxides (AmO_2 and UO_2) present a very similar trend in the investigated temperature range.

Using the least square minimization, Nishi *et al.* [20] fitted the enthalpy data and found the following expression:

$$H(T) - H(298.15K) = -37.847 + 0.088240T - 6.5749.10^{-7}T^2 + 3422.7T^{-1} \tag{2.6}$$

where the enthalpy is in $kJ.mol^{-1}$.

By derivation of this equation, the heat capacity function was evaluated by Nishi *et al.* [20] (see Fig. 2.5). Konings *et al.* [21] highlight that this fit by Nishi *et al.* [20] yielded too low values near room temperature because of high uncertainty of the experimental points. They thus re-fitted the data of Nishi *et al.* [20] constraining the $C_p(298.15K)$ to 64.8 $J.K^{-1}mol^{-1}$. The heat capacity function obtained in this way is also shown in Fig. 2.5 (black line). Although the description of the enthalpy increment of AmO_2 is similar to the one of UO_2, we observe however a large difference on the heat capacity, especially for high temperature range ($T > 1000K$). This could result from the lack of data for AmO_2 at high temperatures because the enthalpy experimental data are available only for temperatures less than 1200 K.

We can also see that the results by Yong *et al.* [7] based on the calculated phonon dispersion curves of AmO_2 are underestimated, especially for T > 600 K compared to the experimental results. The non-taking into account of the anharmonic effects (enhanced for high temperatures) in phonon dispersion curves, can account for this underestimation. Nevertheless, further data on a larger temperature range are still needed. *Ab initio* molecular dynamics is therefore a good way to explore high temperatures in order to valid and/or refine the recommendations.

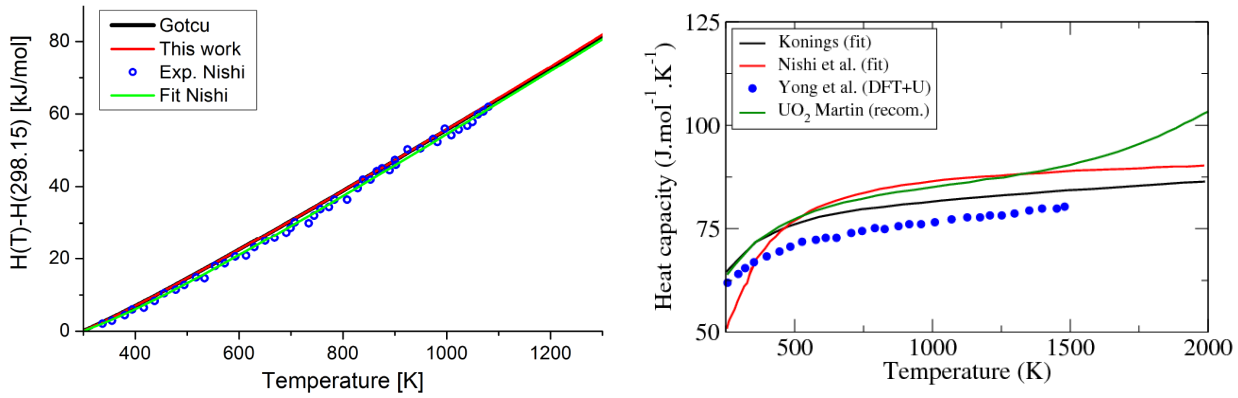

Figure 2.5: Enthalpy increment as a function of temperature : "this work" refers to Epifano's PhD work. Martin's recommendation for UO_2 is similar to Nishi's fit for AmO_2 (left panel) and heat capacity derived from recommendations as well as the DFT+U results by Yong *et al.* [7] (right panel).

c) Thermal conductivity

The thermal conductivity commonly noted λ is an important data for nuclear fuel performance. It quantifies the ability to evacuate the heat from the pellet central part to the coolant during operation in the nuclear reactors. The thermal conductivity is generally obtained indirectly by measuring the thermal diffusivity α, heat capacity C_p, and density ρ and by using the following expression:

$$\lambda = \alpha \rho C_p \tag{2.7}$$

The only available values for the thermal conductivity of americium dioxide directly measured were obtained by Schmidt [88]. Using a method based on the measurement of heat flux, he finds 0.69 and 0.82 $W.m^{-1}.K^{-1}$ for AmO_2 and Am_2O_3 at 333 K respectively. These values are, however, very low compared to those of other actinide oxides [89, 90].

In Fig. 2.6, we show the experimental studies by Nishi *et al.* [20] using the laser method flash method, the results by Yong *et al.* [7] from DFT+U studies and the results by Uchida *et al.* [91] and Kurosaki *et al.* [92] yielded by classical molecular dynamics. All these results point out a decrease of the thermal conductivity with the increase of the temperature.

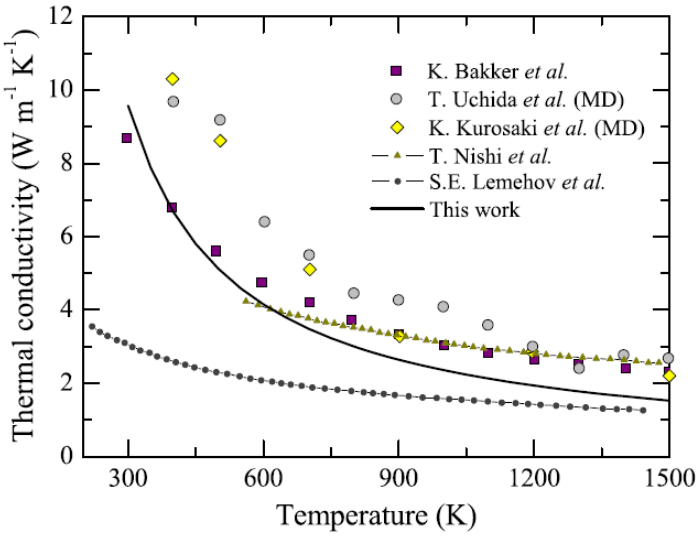

Figure 2.6: Thermal conductivity as a function of temperature : "this work" refers to Yong *et al.* work. MD means classical molecular dynamics. This figure is extracted from the paper by Yong *et al.* [7].

2.3 Available studies on Am_2O_3

We report in this part thermodynamic aspects, structural properties, electronic and magnetic properties of Am_2O_3. Note that the literature remains blank as regards the elastic properties of Am_2O_3.

Americium sesquioxide crystallographic structures were indexed by Templeton and Dauben [76] few years after the identification of the americium dioxide structure. These latter reported: (i) C-$AmO_{1.5+x}$ obtained by heating AmO_2 at 873 K under 1/3 atm of hydrogen. This form was found to be iso-structural with the *bcc* $Ia\bar{3}$ C-type rare earth sesquixode (prototype Mn_2O_3). (ii) A-Am_2O_3 which is hexagonal $P\bar{3}m1$ (prototype La_2O_3), obtained by reduction under 1/6 atm of hydrogen at 1073 K. A monoclinic $C2/m$ sesquioxide, called B-type structure, was observed by Chikalla and Eyring [4] in AmO_{2-x} samples reduced at 1200 K, under a hydrogen-containing atmosphere and then quenched.

2.3.1 Thermodynamics aspects

The Am-O system is less well known than the U-O system because of the lack of thermodynamic data. First attempts to define the Am-O phase diagram date back to the 1960s [4]. Various representations were then proposed in the literature without being completely satisfying.

Despite the similarities between UO_2 and AmO_2, this latter only exists for O/Am ratios less than (or equal to) 2.0. The first Am-O phase diagram reported in the literature was proposed by Sari and Zamorani [12] on the basis of differential thermal analysis (DTA) (see Fig. 2.7). From the shape of the DTA peaks as a function of composition and by comparison with other lanthanide and actinide systems (Ce-O,

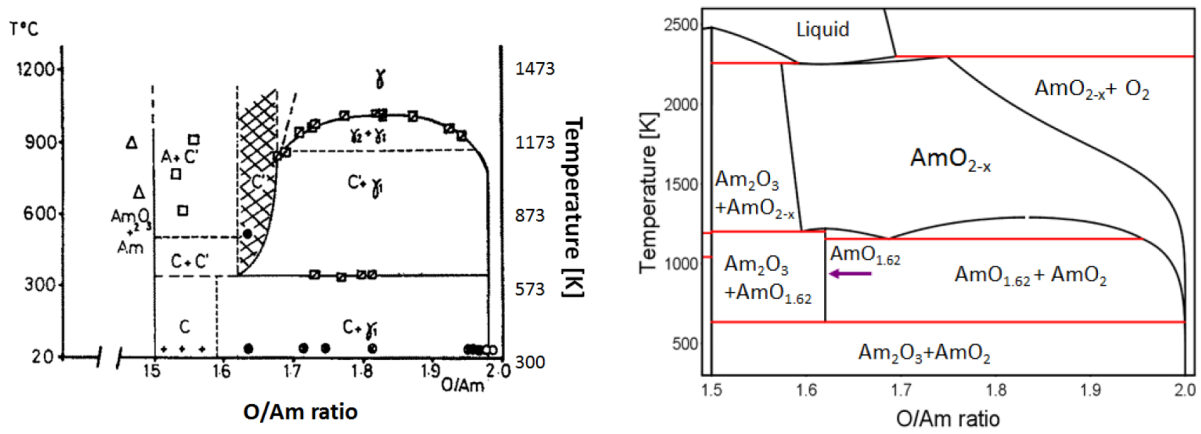

Figure 2.7: Am-O phase diagrams at P= 1 atm according to Sari and Zamorani [12] (left panel) and Gotcu-Freis *et al.* yielded by the CALPHAD method [13] (right panel).

Pr-O, and Pu-O), Sari and Zamorani point out a miscibility gap. According to this study, AmO_{2-x} exhibits a miscibility gap for $1.7 \leq O/Am \leq 1.96$, with a critical temperature around 1300 K. C-$AmO_{1.5+x}$ is considered as the stable sesquioxide form at room temperature. Furthermore, the stoichiometric phase A-Am_2O_3 appears at $T > 500$ K. The Am-O phase diagram as proposed by Sari and Zamorani was later updated by Thiriet and Konings [93]. These latter extended the representation of the phase diagram to higher temperatures, up to the liquid region. Recently, Gotcu-Freis *et al.* [13] reported an Am-O phase diagram based on a CALculation of PHAse Diagram (CALPHAD) assessment (see Fig. 2.7). Because of the lack of data for the high-temperature domains of the liquid and gas phases, this phase diagram focused only on the solid domain established in the $1.5 < O/Am < 2.0$ range. Moreover, the lack of data for the C-type phases made a complete CALPHAD assessment of all phases reported in the previous phase diagrams impossible.

On the other hand, the existence of a miscibility gap for $O/Am > 1.7$ and $1100 < T < 1300$ K as pointed out by Sari and Zamorani, has never been confirmed. Moreover, no further confirmation of the thermodynamic stability of A-Am_2O_3 at room temperature has been reported. According to the recent studies carried out by Epifano *et al.* using as the starting point the CALPHAD assessment by Gotcu-Freis *et al.*, [13] the miscibility gap pointed out by Sari and Zamorani is still controversial.

Finally, due to the lack of sufficient data on AmO_{2-x}, the most stable Am sesquioxide crystallographic structure at room temperature is not well established. Thanks to their predictive capability, electronic structure calculations are thus a good way to answer this question (see Sec. 3.7).

2.3.2 Structural properties

In this section, a summary of the room temperature crystallographic data for americium sesquoixides is provided in Table 2.6.

Table 2.6: Crystallographic data at room temperature for americium oxides.

Phases	s.g.	a_0(Å)	b_0(Å)	c_0(Å)	α(°)	β(°)	γ(°)	**Ref.**
		3.805	3.805	5.960	90.00	90.00	120.00	[4]
A-Am_2O_3	$P\bar{3}m1$	3.812	3.812	5.975	90.00	90.00	120.00	[3]
		3.818	3.818	5.980	90.00	90.00	120.00	[94]
B-Am_2O_3	$C2/m$	14.340	3.520	8.920	90.00	100.40	90.00	[4]
		14.300	3.640	8.920	90.00	100.39	90.00	[3]
C-$AmO_{1.5+x}$	$Ia\bar{3}$	11.013	11.013	11.013	90.00	90.00	90.00	[4]
		11.023	11.023	11.023	90.00	90.00	90.00	[3]
C-$AmO_{1.6+x}$	$Ia\bar{3}$	10.966	10.966	10.966	90.00	90.00	90.00	[4]

a) A-Am_2O_3 hexagonal phase

The first studies on the hexagonal A-type phase were carried out by Chikalla [4] in 1968. Using XRD the author finds $a_0 = 3.805$ Å and $c_0 = 5.960$ Å as lattice parameters. These values are in agreement with those found by Hurtgen and Fuger [3] in XRD nine years later, namely $a_0 = 3.812$ Å and $c_0 = 5.975$ Å. The most recent experimental studies are those of Nishi *et al.* [94] on the basis of the XRD. They reported as lattice parameters $a_0 = 3.818$ Å and $c_0 = 5.980$ Å. The slight difference observed in the above values results from the self-irradiation effect. At present, no value calculated by DFT of the lattice parameter of the hexagonal phase has been reported in the literature.

b) B-Am_2O_3 monoclinic phase

The lattice parameters of the metastable B-Am_2O_3 phase were first determined by Chikalla [4] in 1968 using XRD. The author finds: $a_0 = 14.34$Å, $b_0 = 3.52$Å, $c_0 = 8.92$Å, and $\beta = 100.40°$. These studies are in agreement with those of Hurtgen and Fuger [3] whose reported parameters are $a_0 = 14.30$ Å, $b_0 = 3.64$ Å, $c_0 = 8.92$ Å, and $\beta = 100.39°$.

c) C-$AmO_{1.5+x}$ and C-$AmO_{1.6+x}$ cubic phases

The intermediate phases C-$AmO_{1.5+x}$ and C-$AmO_{1.6+x}$ have the bcc C-type. These phases are closely related to the hypostoichiometric fluorite structure, where an increase of oxygen vacancies leads to their ordering into a C-type structure. Indeed, two oxygen atoms in the conventional unit cell are replaced by two vacancies, leading to a displacement of the cations located at the center of the faces in the fluorite cell to 24*d* Wyckoff sites. The reorganisation gives rise to a new unit cell which is formed by 2x2x2 modified fluorite-type sub-cells. The lattice constants reported in the literature on the basis of the XRD experiments by Chikalla [4] are 11.013 Å for $AmO_{1.5+x}$ and 10.966 Å for $AmO_{1.6+x}$.

2.3.3 Electronic and magnetic properties

Recent calculations by Suzuki *et al.* [14] within the DFT+U approach describe the hexagonal Am_2O_3 phase as a AFM material at low temperature. However, no experimental evidence exists up to now. The comparison between the electronic DOS of AmO_2 and that of A-Am_2O_3 (see Fig. 2.8) obtained in LDA+U(U=3.7 eV) shows that Am_2O_3 is also insulating and has a band gap about twice as wide as AmO_2, i.e. 2.6 eV. This result is good in agreement with the studies of Petit *et al.* [80]. Unlike AmO_2, the band gap of A-Am_2O_3 sesquioxide is formed between the *5f* states of americium. This makes A-Am_2O_3 a Mott insulator, like UO_2.

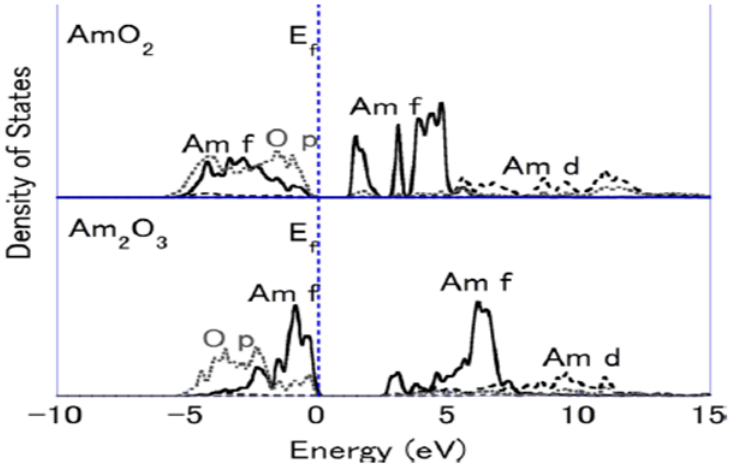

Figure 2.8: Electronic density of states of fluorite americium dioxide AmO_2 and hexagonal americium sesquioxide (Am_2O_3) calculated using LDA+U [14].

2.4 Available studies on (U, Am)O_2

In this section, we report the available studies (experiments and calculations) on thermodynamic and structural properties of (U, Am)O_2, and on the valence state of the U and Am cations. We compare when possible the results obtained by electronic structure calculations with the experimental results in order to highlight the reliability of the electronic structure calculation results. Elastic and magnetic properties as well as atomic transport properties (and stability of point defects) will not be presented in this section because the literature is blank to the best of our knowledge with regard to these properties.

2.4.1 Thermodynamic properties

a) Representation of the U-Am-O system

The U-Am-O system is poorly known up to now. A first attempt to define the phase diagram of this system has been recently proposed by Guéneau and Lebreton [15] on the basis of the CALPHAD method. In this study, the starting point was the

interpolation of the CALPHAD models of the binary systems U-O [95] and Am-O [13]. We report in Fig. 2.9 the phase diagrams for different temperatures extracted from Lebreton's PhD manuscript [96]. The phase diagrams reported include a miscibility gap for O/M<2 and $Am/(Am+U) \geq 0.5$. However this model of phase diagram is still not accurate because only few experimental data were available to optimize the interaction parameters, in particular taking into account the valence states of U and Am cations in (U,Am)O_2 which can be different from their values in the pure oxides UO_2 and AmO_2.

On the basis of the above computations of Lebreton, Epifano [13] performed new experimental investigations by in-situ HT-XRD. The author confirms the existence of a miscibility gap in the oxygen hypostoichiometric, americium-rich domain of the (U,Am)$O_{2\pm x}$ compounds. On the other hand, according to the author, further measurements would be necessary to better define the limits of this biphasic domain and, in particular, to determine the minimum Am/(Am+U) ratio for which the phase separation can occur.

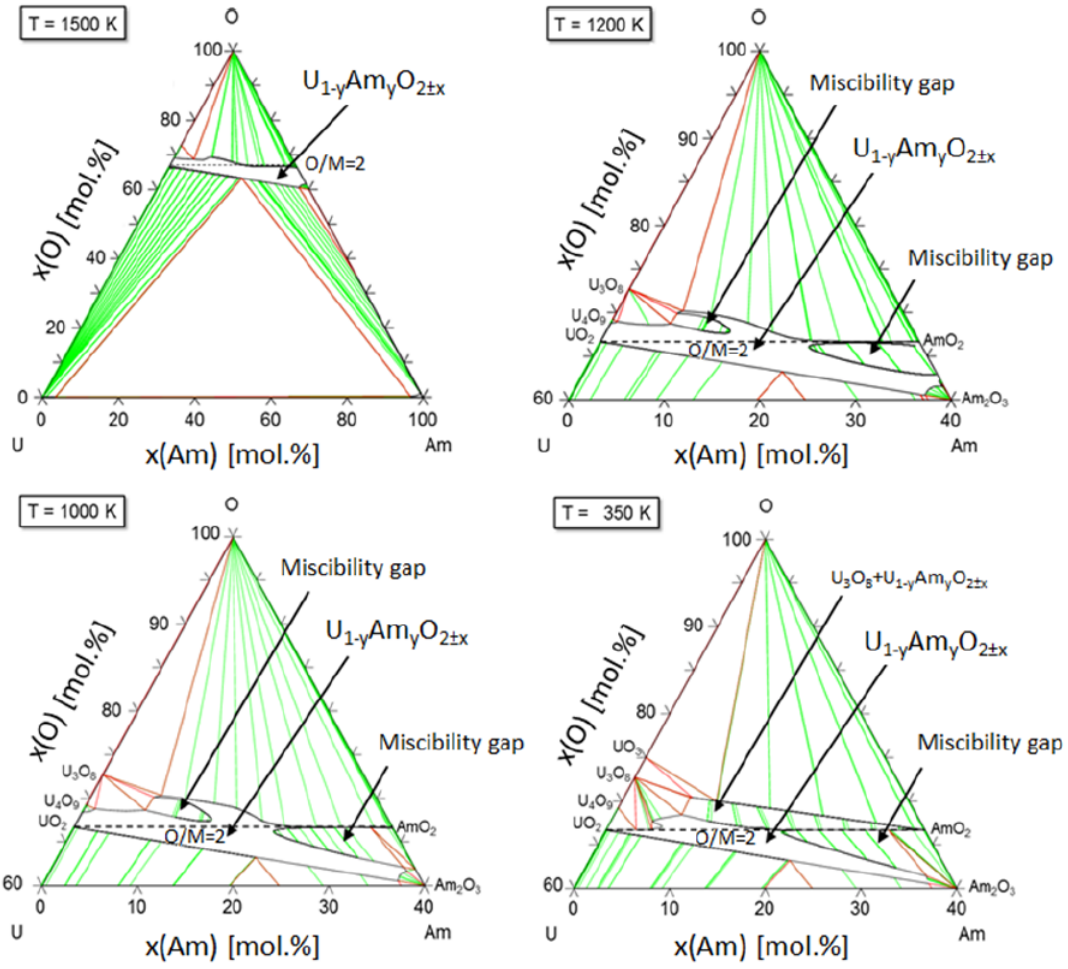

Figure 2.9: The U-Am-O phase diagram at four different temperatures according to Lebreton [15]. This figure is extracted from Lebreton's PhD thesis [16].

b) Heat capacity

Although the first studies on the U-Am-O system date from 1983, it is only very recently that the first results on thermodynamic properties have been published [97]. The authors (Valu et *al.*) investigated $U_{1-y}Am_yO_{2\pm x}$ compounds with y = 0.09 and 0.19 in the temperature range from 425-1790 K by drop calorimetry. The enthalpy increment functions of the system obtained follow the same evolution as in UO_2 and AmO_2. These authors therefore conclude that the Neumann-Kopp additivity rule is valid for $U_{1-y}Am_yO_{2\pm x}$ with y = 0.09 and 0.19.

Epifano [16] has extended the investigations for higher Am contents, namely Am/(Am+U)= 30, 40, 50, 60, and 70% based on the drop calorimetry technique. These studies show that, for Am/(Am+U) > 40% and T > 1100 K, the enthalpy increment functions are rather higher than those of UO_2 and AmO_2 and therefore, the Kopp-Neumann additivity rule is not valid in this case. However, the available experimental data for AmO_2 are limited to 1080 K and the enthalpy function was extrapolated above this temperature. This extrapolation is not appropriate for this case because it does not take into account the effect of the oxygen vacancy formation that occurs in AmO_{2-x} for $T > 1100K$ even under pure O_2 atmosphere. The author concludes that the oxygen vacancy formation is likely responsible for the high enthalpy values measured for the compositions with high Am content. For further improvement of the interpretation of the results, the effect of O vacancies on the heat capacity would need to be further quantified.

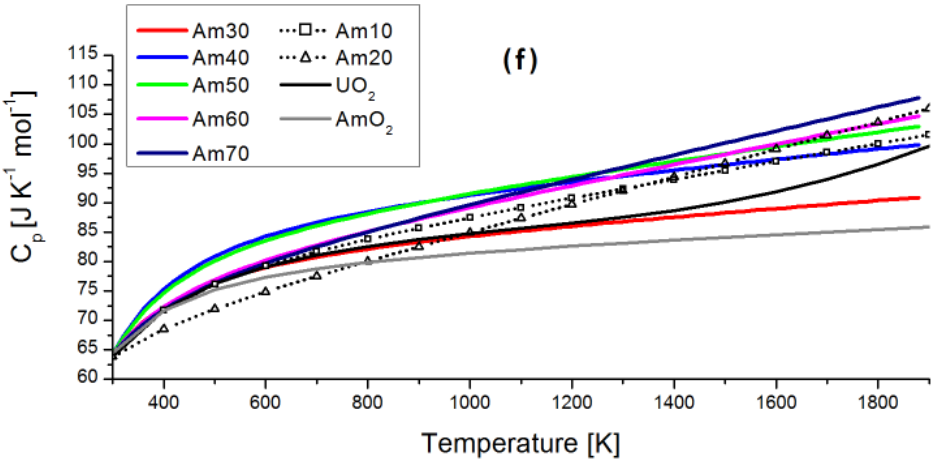

Figure 2.10: Heat capacity of $(U,Am)O_{2\pm x}$ for various Am contents derived from the enthalpy increments obtained by drop calorimetry. This figure is extracted from Epifano's PhD thesis [16].

By constraining the heat capacity value (using the value from the Kopp-Neumann rule) at room temperature in the fit, Valu *et al.* [97] obtained the following heat capacity functions:

$$Cp(J.K^{-1}.mol^{-1}) = 74.172 + 14.601.10^{-3}T - 1.321384.10^{6}T^{-2},\ y = 0.09 \quad (2.8)$$

$$Cp(J.K^{-1}.mol^{-1}) = 62.367 + 23.054.10^{-3}T - 0.489837.10^{6}T^{-2},\ y = 0.19 \quad (2.9)$$

These functions are represented in Fig. 2.10.
The heat capacity functions of the (U, Am)O_2 oxides were also investigated by Epifano by deriving a linear regression of all the enthalpy data. For the fit, the author used a Maier-Kelley polynomial relation [98] given by:

$$Cp(J.K^{-1}.mol^{-1}) = a + bT + cT^{-2} \tag{2.10}$$

where T is the temperature in Kelvin and a, b and c are the parameters to optimize. The above constrain used by Valu *et al.* [97] was also applied to $C_p(298.15K)$. We have also reported the latter results in Fig. 2.10.

2.4.2 Valence state of cations

The first studies on uranium-americium mixed oxide, especially on $U_{0.5}Am_{0.5}O_2$, were reported in the literature in 1983 by Bartscher and Sari [99].These studies are based on the oxygen potential measurements as a function of temperature and the O/M ratio. The O/M ratios were determined by thermogravimetry using as a reference point a value of the O/M ratio determined by dissolving a sample fragment followed by titration of the U(+IV) content of the sample obtained by potentiostatic coulometry [99,100]. According to these studies, in hypostoichiometric conditions, americium has a mixed oxidation state (+III/+IV) while uranium has an oxidation state of +IV. These conclusions based only on the transposition of valence states in uranium-plutonium or uranium-cerium mixed oxides, however, are not directly linked on any experimental data.

Table 2.7: Radii of U and Am ions (coordination 8) [24]

Ions	**U(+IV)**	**U(+V)**	**Am(+III)**	**Am(+IV)**
Radius (Å)	1.00	0.89	1.09	0.95

Ten years later, the results published by Mayer *et al.* [101] on the same compound are in contradiction with the previous results obtained by Bartscher and Sari [99]. Indeed, Mayer *et al.* [101] , using X-ray photoemission spectroscopy, reveal the presence of americium only with an oxidation state of +III, while suggesting an oxidation state for some uranium cations higher than +IV. These results therefore highlight a significant difference with similar systems such as uranium-cerium or uranium-plutonium mixed oxides in which all cations have an oxidation state +IV in stoichiometric conditions. Investigations by Prieur *et al.* [24] by X-ray Absorption Near Edge Structure (XANES) on compounds with low Am contents confirmed that americium has an oxidation state of +III whereas uranium has mixed oxidation states (+IV and +V) in uranium-americium mixed oxides. These studies were performed on compounds with Am/(U+Am)=10, 15 and 20 mol.% ratios. Moreover, from the average oxidation states of cations, the O/M ratios of the investigated samples could be determined. It was found that, for almost stoichiometric compounds (i.e. O/M $\sim$ 2.00), the U(+V) fraction was very close to the trivalent Am (+III) content, suggesting a charge compensation mechanism. Although the fluorite structure is preserved for all Am compositions investigated, the Extended X-Ray Absorption Fine Structure (EXAFS) experiments highlighted some effects on the local structure due to the charge distribution. The reported Am-O distance is about

2.42 Å, which is significantly longer than that in AmO_2 (2.32 Å). This is consistent with the trivalent oxidation state of Am, since the cation radius of Am(+III) is larger than that of Am(+IV) (see Table 2.7). The reported first U-O distance is about 2.34 Å, in agreement with the partial oxidation of U(+V). A slightly oxidized $U_{0.85}Am_{0.15}O_{2.04}$ sample exhibited an U(+V) fraction around 0.23 (instead of ∼0.15), indicating an additional contribution due to the accommodation of oxygen in interstitial positions.

Table 2.8: Crystallographic data at room temperature for uranium and americium dioxides as well as uranium-americum mixed oxides from refinement of the EXAFS spectra. (*) indicates two numbers: the first relates to the normal fluorite site and the second relates to the cuboctahedral sites.

	Distance(Å)			**coord. number**		**O/M**	**Ref.**
Compd.	d_{M-M}	d_{U-O}	d_{Am-O}	M-M	M-O		
UO_2	3.866	2.355		11.9	7.9	2.00	[102]
	3.867	2.357		11.9	8.0	2.00	[103]
AmO_2	3.803		2.318	11.7	8.1	2.00	[94]
Am_2O_3	3.676		2.999	3.0	3.0	1.50	[16]
$U_{0.85}Am_{0.45}O_{2\pm x}$	3.966	2.355	2.427	11.9	7.9	2.01	[24]
	3.866	2.342	2.427	11.6	7.9	2.00	[16]
$U_{0.7}Am_{0.3}O_{2\pm x}$	3.859	2.330	2.438	11.9	8.0	2.02	[16]
$U_{0.5}Am_{0.5}O_{2\pm x}$	3.853	2.18/2.359*	2.433	12.0	8.0/6.9*	1.97	[16]
$U_{0.3}Am_{0.7}O_{2\pm x}$	3.844	2.17/2.29*	2.404	12.0	7.3/7.1*	1.90	[16]

As part of his thesis, Lebreton [15] shows from the XANES experiments on almost stoichiometric compounds with Am/(U+Am) ratios ranging from 0.1 to 0.49 that americium cations have only an oxidation state of + III and U (+IV) coexists with U(+V). These results are in good agreement with the previous ones.

The most recent studies were performed by Epifano in the framework of her PhD thesis. The author extended the investigations up to Am/(Am+U) = 70 mol%. For Am/(Am+U) < 0.4, these studies reveal, in agreement with the previous studies, an oxidation state of (+III) for Am and mixed oxidation state (+IV/+V) for U with U(+V) and Am(+III) having the same concentration. Moreover, all the sample investigated in this composition were stable for O/M ∼ 2. A good agreement was also found as regards the interatomic distances (see Table 2.8). For Am/(Am+U)=0.4 and 0.5, EXAFS experiments point out important changes in the oxygen sublattice around uranium, including both vacancies in the normal fluorite sites and interstitials in cuboctahedral positions. Despite these arrangements, all investigated samples with Am/(Am+U)=0.4 and 0.5 were slightly hypostoichiometric (i.e. O/M < 2.00). Epifano concludes that for these compositions, the $(U,Am)O_2$ solid solution is stable in hypostoichiometric conditions. This conclusion was confirmed also for Am/(Am+U)=0.6 and 0.7. For these compositions, the O/M ratio is respectively equal to 1.93 ± 0.02 and 1.90 ± 0.02. Furthermore, the author highlighted the appearance for the first time of Am(+IV) in the mixed oxide, but also the preservation of the fluorite symmetry.

The oxidation state of cations from different studies in the literature are reported in Table 2.9. Although Epifano points out the co-existence of oxygen vacancies (around Am atom) and oxygen interstitials in cuboctahedral sites, the coordination number of U is less than 8.0 (instead of > 8.0) and the one of Am equals to 8.0 (instead of < 8.0), except for Am/(Am+U)=0.7 (see Table 2.8). According to Epifano, this

could result from the high uncertainties (>0.5) affecting the determination of the atom coordination, especially light atoms as oxygen.

Table 2.9: Valence state of U and Am cations obtained by XANES experiments.

	Am content (mol. %)				O/M	Ref.
Target Am/M	Am(+III)	Am(+IV)	U(+IV)	U(+V)		
10	10	0	81	9	2.00	[16]
15	15	0	71	14	2.00	[24]
	15	0	62	23	2.04	[24]
	15	0	67	18	2.02	[16]
20	20	0	63	17	1.99	[16]
30	28	0	40	32	2.02	[16]
50	48	0	10	42	1.97	[16]
60	50	7	8	35	1.93	[16]
70	49	18	4	29	1.90	[16]

Despite the above studies, it remains difficult to explain why for Am-content larger than 40% several uranium are found in high oxidation state (> +IV) and why O/M < 2.00, given the compensation mechanism related to both oxygen vacancies and interstitials. Moreover, we can see in Table 2.8 that the manufacturing of (U,Am)O_2 with O/M=2.00 is very challenging, forcing the authors to assume O/M non exactly equal to 2.00 when stoichiometric conditions are targetted. As it stands, only electronic structure calculations can provide additional investigations for O/M=2.00 and then provide the effect of oxygen defects (vacancies and interstitials) on the valence states of cations (see Chap. 5).

2.4.3 Structural properties

According to the results reported in the literature (on the basis of XRD or XAS experiments), all the $U_{1-y}Am_yO_2$ compounds are single-phase and isostructural to UO_2 and AmO_2 [24, 104–106]. We report in Table 2.10 the crystallographic data available in the literature. We can see that all lattice parameters differ from those given by the theoretical Vegard's law, when calculated from UO_2 and AmO_2 experimental data (see Fig. 2.12). According to Lebreton *et al.*, this is due to the peculiar cationic charge distribution in these mixed oxides as mentioned above (Sec. 2.4.2). We can observe that lattice parameter values are scattered since the precision of XRD is the order of 10^{-3}. Lattice expansion under self-irradiation effects known to occur in ^{241}Am-bearing oxides as presented in Fig. 2.11, is thus the main explanation for the discrepancy between the experimental values. The relative evolutions of the lattice parameters as a function of time for the various compositions are reported in Fig. 2.11. In all the cases, an exponential behaviour of the type described by Eq. 2.1 is observed.

Since the EXAFS experiments (see Sec. 2.4.2) show a compensation distance mechanism (i.e. shortening of the U-O and strengthening of the Am-O distances) in the uranium-americium mixed oxides for O/M $\sim$ 2, one could expect to obtain the lattice parameter as a linear combination of UO_2 and AmO_2 lattice parameters. Thus, the peculiar evolution of the lattice parameter as a function of Am content (for compo-

Table 2.10: Lattice parameter values as well as the age of the samples. These studies are carried out using XRD.

Am/(Am+U) (mol.%)	a(Å)	Age(days)[a]	a(Å)	Age(days)[b]	a(Å)	Age(days)[c]
7.5	5.467	6.0	5.466	6.0		
10	5.466	5.0			5.469	0.0
15	5.462	5.0	5.461	5.0	5.467	0.0
20	5.460	4.0			5.466	0.0
30	5.455	5.0	5.454	5.0		
40	5.466	90.0	5.464	90.0		
50	5.456	4.0	5.454	4.0		
60	5.459	95.0	5.459	95.0		
70	5.450	100.0	5.454	100.0		

[a]Ref. [16] [b]Ref. [102] [c]Ref. [24]

sitions in which O/M =2 i.e. %Am <0.4) as shown in Fig 2.12 remains difficult to understand. We will address this issue in Chap. 5.

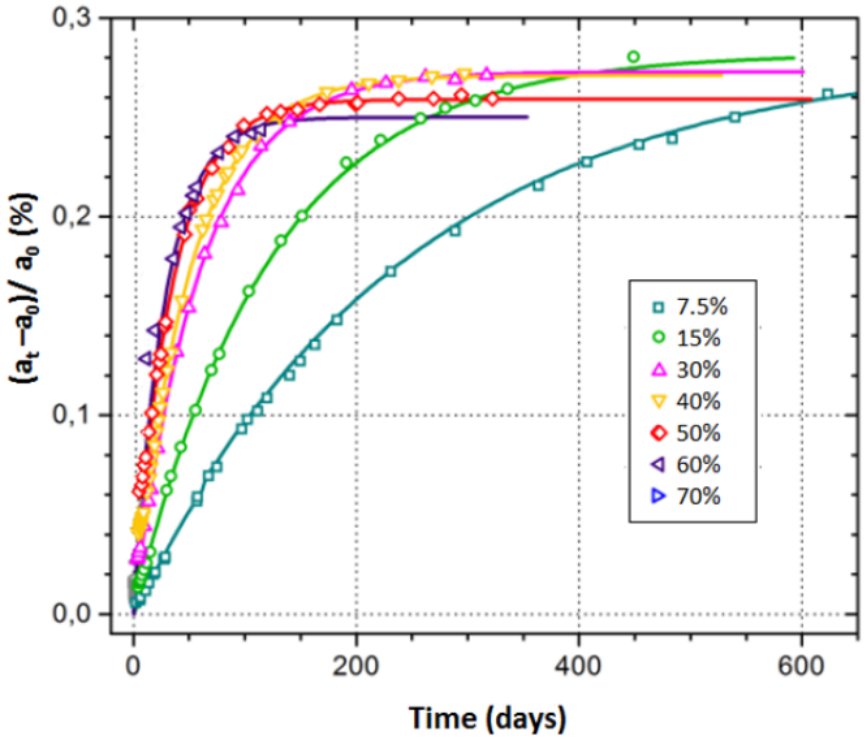

Figure 2.11: Self-irradiation induced absolute and relative evolution of the lattice parameter for (U,Am)$O_{2\pm x}$ with Am/(U+Am) = 7.5, 15, 30, 40, 50, 60 and 70 mol.% [15, 17].

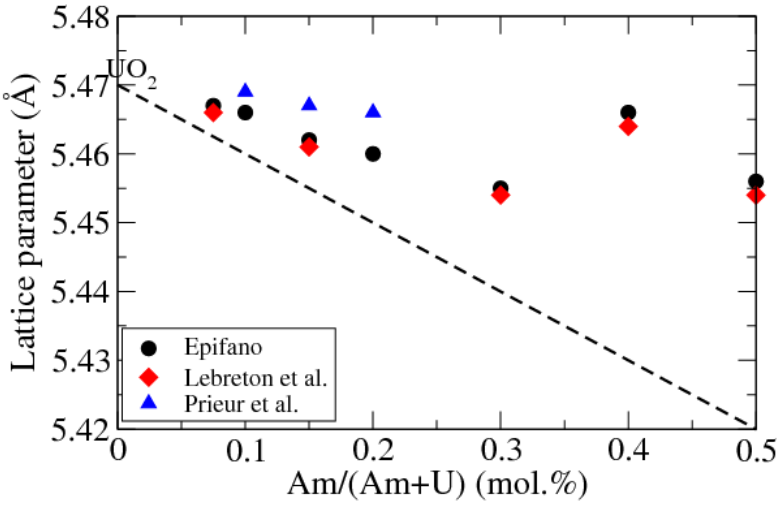

Figure 2.12: Evolution of the lattice parameter of (U,Am)O_2 as a function of Am/(U+Am) [15,16]. The dotted line is obtained by a linear combination between the UO_2 and AmO_2 experimental lattice parameters. Lebreton and Epifano used the same samples for the composition range shown here.

2.5 Available studies on (U, Pu, Am)O_2

Investigations on (U,Pu,Am)O_2 compounds are very scarce up to now. The first studies reported in the literature were performed by Osaka *et al.* [107] in 2005. The latter studies concern more particularly the $U_{0.685}Pu_{0.270}Am_{0.045}O_{2\pm x}$ compound. Using thermogravimetric analyzes, the authors measured the oxygen potential of this compound as a function of the O/M ratio at 1273 K. These studies show that the presence of americium increases the oxygen potential, which is in good agreement with the studies contained in the report published by the OECD in 2014 [27]. Moreover, the latter studies show that the presence of americium induces a decrease in the thermal conductivity as well as in the melting temperature of (U,Pu)O_2. These studies are in agreement with the investigations by Morimoto *et al.* [18]. Indeed the latter measured the thermal conductivities of $U_{0.7-z}Pu_{0.3}Am_zO_2$ solid solution (z =0.007-0.03) using the laser flash method in the temperature range from 900 to 1713 K. The authors show that the thermal conductivities of MOX fuels containing a few percent of Am decrease slightly with increasing Am-content (see Fig. 2.13). The thermal conductivities up to about 1500 K satisfied the classical phonon transport model :

$$\lambda_0 = \frac{1}{A + BT} \tag{2.11}$$

The coefficient A increases linearly while the coefficient B hardly varies with the increase of Am-content. Assuming that the chemical formula of (U,Pu,Am)O_2 was $U^{4+}_{0.7-2y}U^{5+}_{y}Pu^{4+}_{0.3}Am^{3+}_{y}O^{2-}_{2}$, the authors determined the coefficient A and B. They found:

$A = 0.90y + 0.014(mK/W)$ and $B = 2.40.10^{-4}(m/W)$

Using classical molecular dynamics simulation, Weiwei *et al.* [108] investigated the lattice parameter expansion and thermal conductivities of $U_{0.7-x}Pu_{0.3}Am_xO_2$ (x=0, 0.03, 0.05, 0.10, 0.15, 0.20, 0.25) in the temperature range from 300 to 3000 K. According to the authors, the lattice parameters follow the Vegard's law. Furthermore, the

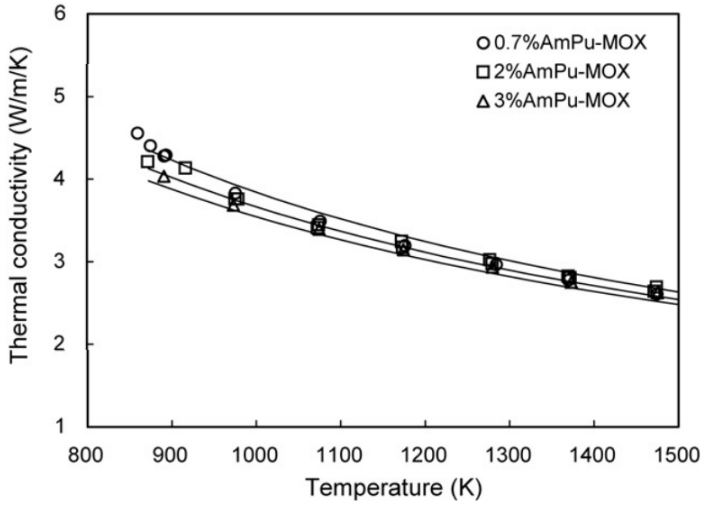

Figure 2.13: Comparison between the experimental and calculated thermal conductivities. Open symbols are the thermal conductivities evaluated from the experimental data. Solid lines are the thermal conductivities calculated from the phonon scattering model [18].

Am content barely influences the thermal conductivities of $U_{0.7-x}Pu_{0.3}Am_xO_2$. However, these studies do not take into account the possible electronic charge transfer between U and Am as in $U_{1-y}Am_yO_2$. Moreover, the previous studies on $U_{1-y}Am_yO_2$ show that the presence of americium induces an increase in the formation of point defects namely for temperatures higher than 1200 K, which causes the change in the slope of lattice parameter expansion. Further studies are still needed to accurately describe the thermodynamic properties of (U,Pu,Am)O_2 mixed oxides.

The structural properties of (U,Pu,Am)O_2 with low Am-content (0-7%) and O/M=2 were evaluated by Kato *et al.* [109]. The authors showed that for a plutonium content equal to ∼20%, the lattice parameters are a = 5.456 Å and a = 5.454 Å for Am-contents of 0.4 and 1.5 % respectively. It is clear that the lattice parameter slightly decreases with increasing Am-content. However, this decrease is not linear as in the case of (U,Pu)O_2. Moreover, these studies assume Am to have an oxidation state of +IV in the (U, Pu)O_2 compound. In the absence of additional experimental data, it is impossible to conclude on the linear evolution of the lattice parameter as a function of americium content. This compound remains open to experimental studies as well as modelling.

2.6 Conclusion

We presented a review of the scientific literature on AmO_2, Am_2O_3, (U,Am)O_2, and (U,Pu,Am)O_2 compounds. Several properties of interest for nuclear fuels containing americium as stability of point defects, atomic transport properties, fission gas behaviour remain unknown. Yet, these properties are essential for the determination of the elementary mechanisms governing the behaviour of the fuel under irradiation.

The DFT results on structural, elastic, and electronic properties of the AmO_2 and Am_2O_3 compounds reported in the literature show a good agreement with the experi-

mental results. However, because of the unavailability of a sufficient number of experimental and modelling data on these compounds, it was very challenging to suggest the most reliable reference data in most of the cases. For instance, in the case of Am_2O_3, although its various structures are quite easily identified, the stable structure at low temperature is far from established. Therefore, we suggest that electronic structure calculations be conducted to complement the experimental results. We also highlight that in the case of AmO_2 and Am_2O_3, there are no experimental studies providing the values of the elastic constants. In the case of AmO_2, only one theoretical study was done using the DFT+U method to calculate these elastic constants. However, because of the large difference between the bulk modulus obtained from these elastic constant values and the experimental value, the reliability of these results is questioned. Moreover, even if the literature points out an antiferromagnetic order for AmO_2, the type of magnetic order (collinear or non-collinear) remains unclear. Yet, the knowledge of the type of magnetic order is essential for electronic structure calculations. Finally, it emerges from the literature that the DFT+U U and J Coulomb parameters are not well established since they vary from one author to another.

Although the valence state of cation in (U,Am)O_2 solid solution is well established for Am-content less than 40 mol.%, further investigation for high Am-content are still necessary. Indeed the XANES experiments evidenced for Am/(Am+U) $> 50\%$ a charge compensation mechanism related to the co-existence of oxygen vacancies and oxygen interstitials, but some U cations however had a high oxidation state (+V) even for low O/M ratio. Moreover, the presence of atomic point defects in (U,Am)O_2 compounds especially oxygen vacancies and interstitials make the investigation of the lattice parameter as a function of Am-content very challenging.

Concerning (U,Pu,Am)O_2, no reliable theoretical investigation is reported in the literature and the experimental studies are very scarce, highlighting the need of additional investigations.

In general, the literature review shows that several properties of Am-bearing oxides are missing or poorly known. Thus, this PhD work, through electronic structure calculations, is expected to address in detail these issues, the main objective being to investigate thermodynamic, elastic, structural, electronic and atomic transport properties as well as point defects stability of (U,Pu,Am)O_2. Then by comparing these results to the ones obtained in (U,Pu)O_2 by Cheik in his PhD work [29], the effect of americium can be determined. A preliminary step towards this objective is the better knowledge of the properties of americium oxides (AmO_2 and Am_2O_3) and (U, Am) mixed oxides (see Chap. 3 and 5).

Chapter 3

Implementation of the DFT+U method in americium dioxide and sesquioxide

The goal of this chapter is to first implement the DFT+U method in americium oxides by determining the optimal U and J values of the DFT+U method allowing to describe the strongly correlated Am *5f* electrons. Then, the next step is to use these U and J values within the DFT+U to predict some missing or poorly known properties of interest in americium oxides.

Contents

3.1 Introduction

A better knowledge of the americium oxide systems is a required step toward the investigation of the effect of americium on (U,Pu)O_2 properties using DFT+U. Indeed, this step allows implementing the DFT+U method to americium bearing oxides but also provides some of the data allowing to calculate the phase diagram of the U-Pu-Am-O system. However, theoretical or experimental data on the properties of americium oxides are very scarce, giving rise to several open questions as shown in the critical review of Chap. 2.

Whereas the onsite Coulomb interaction U and exchange J are well known for UO_2 [23,32], this is not the case for americium oxides for which the literature does not agree on any value since these values strongly vary from one author to another [1,7,78,79]. Thus, in this study we purpose to provide the optimal values of the U and J parameters for americium oxides, which will be used in a subsequent study to evaluate the effect of americium in mixed actinide oxides. In this context, we also perform calculations using an hybrid functional to test the reliability of our U and J parameters.

Despite some studies reported in the literature, the knowledge of most bulk properties of americium oxides remains limited. To our knowledge, dielectric properties of americium oxides remain unknown. For instance, the static dielectric constant has never been neither measured nor calculated. Moreover, most of the temperature-dependent properties in AmO_2 are limited to temperatures lower than 1200 K. Although the magnetic ground state of UO_2 is identified as a transverse 3k antiferromagnetic (AFM) state below 30 K [110], the literature does not provide detailed information concerning AmO_2. As regards americium sesquioxides Am_2O_3, the stable crystal structure at low temperature is not fully established [21]. In addition the only available studies on americium sesquioxides reported in the literature aims at determining the lattice constants [3,14,94] and the band gap [14]. Thus, the Am_2O_3 compounds require a deeper study.

Furthermore, the literature reports only one study carried out by Yong *et al.* [7] aimed at computing the elastic constants of AmO_2 using the DFT+U approximation. However, the bulk modulus obtained in this study largely deviates from the experimental value. In addition, in a recent study published by Pegg and co-workers [1] using DFT+U calculation, one can see that the evolution of the band gap as a function of the U parameter is not smooth. The reason for these discrepancies is likely related to the fact that the system is trapped into metastable states during the calculations [31,59]. Indeed, it is now established that the DFT+U induces (electronic) metastable states, in relation with the symmetry-lowering associated to this method. Dorado *et al.* [111] showed that in UO_2 the presence of metastable states induces large differences in bulk properties and the formation energy of point defects.

In this chapter we address the above concerns. Particularly, by correctly treating the issue of the metastable states, and by computing several bulk properties of AmO_2 as a function of the U and J parameters and comparing to the available experimental data, we determine the U and J values that can be used to provide a good description of AmO_2. We then use these values through the DFT+U method to predict some unknown or poorly known properties of interest (finite temperature properties, energetic, elastic properties) of americium oxides.

3.2 Computational details

The exchange and correlation effects are described by the Generalized Gradient Approximation (GGA) parameterized by Perdew, Burke and Ernzerhof [112]. The "Full Localized Limit" (FLL) [28, 113] is chosen to describe the double counting correction of DFT+U (Eq. 1.7) because the ground state of americium oxides is insulating and thus, orbital occupations of *5f* electrons is close to one or zero.

Results are obtained using a plane-wave cutoff energy equals to 500 eV using VASP code and 871 eV using ABINIT code. According to our convergence tests, these input values lead to a precision (in term of total energy differences corresponding to physical quantities) lower than 1 meV per atom. Unit cells containing 2 f.u. (6 atoms) as well as 4 f.u. (12 atoms) are used. For the 6-atom cell, one lattice vector (c) is along one axis of the cubic fluorite structure, while the two others are turned by 45° with respect to the cubic directions, and have lengths corresponding to $\sqrt{2}/2$ times the cubic lattice constant. Using VASP, the calculations are done on a 6×6×6 k-points mesh generated by the Monkhorst-Pack [114] method, which is sufficient for an energy convergence smaller than 0.3 meV per atom. With ABINIT, we used a 6×64 k-point mesh. We performed full relaxation of the cell until the pressure acting on the system becomes lower than 0.01 kbar (VASP) and 5.10^{-7} Ha/bohr^3 ($\sim$ 0.15 kbar) (ABINIT), until the convergence on energy becomes smaller than 10^{-5} eV per atom (VASP), and until the convergence on forces for the structural optimization becomes smaller than 5.10^{-5} Ha/bohr ($\sim$2.5 meV/Å) (ABINIT). In order to ensure the convergence of calculations to the ground state, a practical occupation matrix control scheme for the *5f* correlated orbitals is used [32]. Note that either VASP or ABINIT codes are used in the whole study (except in Sec. 3.7 in which VASP has been exclusively used) and we ensured that the results obtained with both codes are in agreement. Sometimes, either the ABINIT or VASP code does not offer the possibility to compute certain properties. In this case we clearly indicate which one is used.

3.3 Ground state and metastable states in AmO_2

The use of the DFT+U approximation induces an increase in the number of electronic metastable states having high energy barriers separating each other, making the convergence to the ground state difficult. Such metastable states have been already reported in other compounds such as γ and β cerium [59], plutonium dioxide PuO_2 [31] and uranium dioxide UO_2 [32]. It has been shown in UO_2 that the presence of metastable states induces large differences in calculated properties, for instance in the formation energy of point defects [111]. Indeed, the DFT+U approximation promotes the integer occupation of the correlated orbitals and thereby, creates an anisotropy of the electron density and thus of the crystal cell after structural optimization. The investigations by Jomard *et al.* [31] on plutonium oxides provided a practical scheme which consists in calculating and comparing the energies of all filling configurations of *5f* orbitals and therefore allows one to determine the ground state. Metastable states could be also expected in AmO_2 using DFT+U since it is a compound with strongly correlated *5f* orbitals. This section is dedicated to the calculation of the ground state of AmO_2, considering collinear magnetism (i.e. the magnetization is a scalar quan-

tity). An antiferromagnetic order similar to the 1k collinear order is imposed in the calculations (see Fig. 3.2 (a)).

3.3.1 Calculation taking symmetries into account

In metallic americium the electronic configuration of the valence orbitals is $5f^7 6s^2$ and in americium dioxide, the oxidation state of americium atoms is +IV with five electrons in the *5f* orbitals. There are C_7^5=21 different manners, called electronic configurations, to fill the seven *5f* orbitals of a given spin channel with five electrons, i.e., assuming for Am^{4+} a high-spin electronic configuration. As a consequence, only two *f* orbitals of a given americium atom should be not filled. Our purpose in this section is to determine the ground-state occupation matrix of Am atoms in AmO_2 using the occupation matrix control scheme.

Twenty-one diagonal matrices expressed in the basis of the real spherical harmonics, ordered as in Ref. [115] i.e. by increasing m, with the x,y, and z directions being those of the conventional cell of the cubic fluorite structure, have been imposed at the beginning of each calculation. Each matrix corresponds to one particular electronic configuration of *5f* orbitals. Referring to the cubic crystal field, *f*-levels are partially degenerated. This suggests that some initial states should lead to the same final states. However, in order to check the efficiency of the method on the AmO_2 system, we use these 21 occupation matrices as the starting point. We adopted the following notation for the occupation matrix:

$$[1111100] = \begin{pmatrix} 1 & 0 & 0 & 0 & 0 & 0 & 0 \\ 0 & 1 & 0 & 0 & 0 & 0 & 0 \\ 0 & 0 & 1 & 0 & 0 & 0 & 0 \\ 0 & 0 & 0 & 1 & 0 & 0 & 0 \\ 0 & 0 & 0 & 0 & 1 & 0 & 0 \\ 0 & 0 & 0 & 0 & 0 & 0 & 0 \\ 0 & 0 & 0 & 0 & 0 & 0 & 0 \end{pmatrix}.$$

Each diagonal occupation matrix configuration is imposed during the first steps of the first self-consistent cycle. We firstly impose the crystal symmetry in our calculations (density, forces, stress) starting from an undistorted unit cell. Note that the use here of a 1k antiferromagnetic order changes the cubic $Fm\bar{3}m$ space group to the tetragonal $P4/mmm$ space group. We used several values of the U parameter in the range of 4.00-8.00 eV and two values of the J parameter (0.50 eV and 0.75 eV). Depending on the initial matrix, several different states are reached. We present our results in Table 3.1, setting the lowest energy to 0 eV. We decide to display in this table only the case in which the U parameter equals 6 eV and J=0.75 eV. Indeed, for any value of U, the initial matrices leading to the lowest energy remain the same although the number of final states slowly increases when U increases. The J parameter does not have a significant influence on the final state.

We observe from Table 3.1 five different final states reached by the self-consistent procedure, which strongly depend on the initial occupation matrix. Actually, depending on the orbitals filled, the system is sometimes trapped in a local minimum and going

Table 3.1: Relative energies per AmO_2, lattice constant, magnetic moment per Am^{+4} and band gap of the states obtained starting from the 21 initial diagonal occupation matrices. The energy of the lowest state is set to zero. The results are given for U=6 and J=0.75 eV. The lattice constant given corresponds to that of a cubic crystal that would have the same volume. The calculations were performed taking the symmetry of the crystal into account.

Initial matrix	$(E - E_{min})$/Am (meV)	a (Å)	μ_{mag} (μ_B)	Band gap (eV)
[0011111]	207.86	5.53	5.9	0.0
[0101111]	207.86	5.53	5.9	0.0
[0110111]	0.00	5.44	5.3	1.1
[0111011]	207.86	5.53	5.9	0.0
[0111101]	370.48	5.48	5.5	0.2
[0111110]	572.06	5.44	5.2	0.4
[1001111]	207.86	5.53	5.9	0.0
[1010111]	0.00	5.44	5.3	1.1
[1011011]	207.86	5.53	5.9	0.0
[1011101]	370.48	5.48	5.5	0.2
[1011110]	207.86	5.53	5.9	0.0
[1100111]	0.00	5.44	5.3	1.1
[1101011]	982.33	5.45	5.2	0.2
[1101101]	370.48	5.48	5.5	0.2
[1101110]	207.86	5.53	5.9	0.0
[1110011]	0.00	5.44	5.3	1.1
[1110101]	207.86	5.53	5.9	0.0
[1110110]	0.00	5.44	5.3	1.1
[1111001]	370.48	5.48	5.5	0.2
[1111010]	207.86	5.53	5.9	0.0
[1111100]	370.48	5.48	5.5	0.2

to another minimum would require too much energy since the path from one minimum to another would involve partial occupancies. Out of these five states we have two metallic states and three insulating ones. Concerning the lowest-energy state, there are five initial matrices that finally lead to that state, so we can clearly conclude that we have five initial electronic configurations which allow us to reach the ground state. For this ground state, the occupation matrix for correlated electrons of the majority spin channel is given by:

$$M^{sym} = \begin{pmatrix} 1.02 & 0.00 & 0.00 & 0.00 & 0.00 & 0.00 & 0.00 \\ 0.00 & 0.32 & 0.00 & 0.00 & 0.00 & 0.00 & 0.00 \\ 0.00 & 0.00 & 1.03 & 0.00 & 0.00 & 0.00 & 0.00 \\ 0.00 & 0.00 & 0.00 & 0.10 & 0.00 & 0.00 & 0.00 \\ 0.00 & 0.00 & 0.00 & 0.00 & 1.03 & 0.00 & 0.00 \\ 0.00 & 0.00 & 0.00 & 0.00 & 0.00 & 1.02 & 0.00 \\ 0.00 & 0.00 & 0.00 & 0.00 & 0.00 & 0.00 & 1.02 \end{pmatrix}.$$

3.3.2 Calculation without taking symmetries into account

In this section, we are now interested in the influence of the crystal symmetries on the ground state. DFT+U is likely to break the cubic symmetry (or more precisely the tetragonal symmetry resulting from the AFM order) and then may induce after structural relaxation a slight difference between the lattice constants a, b and c. It is then important to evaluate the effect of the reduction of the symmetry on the ground-state properties of AmO_2. Thus, we perform our calculations without taking any symmetry into account using the ABINIT code. We use U=6 eV and J=0.75 eV. We have performed two searches.

(1) The lattice constants and atomic positions are fixed (in the perfect cubic geometry) and the 21 matrices are tested (imposed over the 20 first steps of the electronic loop). The final matrix corresponding to the lowest energy is then

$$M_1^{no\ sym} = \begin{pmatrix} 0.44 & 0.00 & -0.42 & 0.00 & 0.00 & 0.00 & 0.00 \\ 0.00 & 0.25 & 0.00 & 0.00 & 0.00 & 0.00 & 0.00 \\ -0.42 & 0.00 & 0.66 & 0.00 & 0.00 & 0.00 & 0.00 \\ 0.00 & 0.00 & 0.00 & 0.99 & 0.00 & 0.00 & 0.00 \\ 0.00 & 0.00 & 0.00 & 0.00 & 0.99 & 0.00 & 0.00 \\ 0.00 & 0.00 & 0.00 & 0.00 & 0.00 & 0.99 & 0.00 \\ 0.00 & 0.00 & 0.00 & 0.00 & 0.00 & 0.00 & 0.99 \end{pmatrix}.$$

Another state has an energy only 1 meV above, with a matrix $M_2^{no\ sym}$ very close to that found in the symmetric case:

$$M_2^{no\ sym} = \begin{pmatrix} 0.99 & 0.00 & 0.00 & 0.00 & 0.00 & 0.00 & 0.00 \\ 0.00 & 0.25 & 0.00 & 0.00 & 0.00 & 0.00 & 0.00 \\ 0.00 & 0.00 & 0.99 & 0.00 & 0.00 & 0.00 & 0.00 \\ 0.00 & 0.00 & 0.00 & 0.12 & 0.00 & 0.00 & 0.00 \\ 0.00 & 0.00 & 0.00 & 0.00 & 0.99 & 0.00 & 0.00 \\ 0.00 & 0.00 & 0.00 & 0.00 & 0.00 & 0.99 & 0.00 \\ 0.00 & 0.00 & 0.00 & 0.00 & 0.00 & 0.00 & 0.99 \end{pmatrix}.$$

(2) The previous calculations are continued by a full structural optimization (cell and atomic positions). At the end, the configurations corresponding to $M_1^{no\ sym}$ and $M_2^{no\ sym}$ have their energy slightly lowered, but the matrices are preserved all along the relaxation. However, we observe that another configuration jumps during the relaxation onto a different electronic state, leading to a final configuration that is more stable than the ones corresponding to $M_1^{no\ sym}$ and $M_2^{no\ sym}$ by $\sim$ 0.08-0.09 eV/AmO_2. The final matrix of that case is:

$$M_3^{no\ sym} = \begin{pmatrix} 0.80 & 0.01 & -0.15 & 0.22 & -0.15 & 0.00 & 0.19 \\ 0.01 & 0.25 & 0.01 & -0.00 & 0.01 & -0.00 & -0.01 \\ -0.15 & 0.01 & 0.88 & 0.17 & -0.11 & 0.00 & 0.15 \\ 0.22 & -0.00 & 0.17 & 0.73 & 0.17 & 0.00 & -0.22 \\ -0.15 & 0.00 & -0.11 & 0.17 & 0.88 & -0.01 & 0.15 \\ 0.00 & -0.00 & 0.01 & 0.00 & -0.00 & 0.99 & 0.00 \\ 0.19 & -0.00 & 0.15 & -0.22 & 0.15 & 0.00 & 0.80 \end{pmatrix}.$$

Table 3.2: Relative energies per AmO_2, lattice constant, Am^{4+} magnetic moment of the states obtained starting from the 21 initial diagonal occupation matrices. The energy of the lowest state is set to zero. The lattice constant given corresponds to that of a cubic crystal that would have the same volume. The calculations were performed without taking any symmetry into account.

Initial matrix	$(E - E_{min})$/Am (eV)	a (Å)	μ_{mag} (μ_B)	occupation matrix
[0011111]	0.08	5.44	5.2	$M_1^{no\ sym}$
[0101111]	0.85	5.49	5.2	
[0110111]	0.76	5.46	5.1	
[0111011]	0.00	5.44	5.2	$M_3^{no\ sym}$
[0111101]	0.95	5.46	5.9	
[0111110]	0.32	5.49	5.6	
[1001111]	0.08	5.44	5.2	$M_1^{no\ sym}$
[1010111]	0.09	5.44	5.2	$M_2^{no\ sym} \sim M^{sym}$
[1011011]	0.08	5.44	5.2	
[1011101]	0.64	5.47	5.4	
[1011110]	0.08	5.44	5.2	$M_1^{no\ sym}$
[1100111]	0.75	5.47	5.1	
[1101011]	1.24	5.48	5.1	
[1101101]	0.95	5.46	5.9	
[1101110]	0.77	5.48	5.2	
[1110011]	0.75	5.47	5.2	
[1110101]	0.66	5.48		
[1110110]	0.76	5.46	5.1	
[1111001]	0.47	5.45		
[1111010]	0.61	5.50	5.4	
[1111100]	0.95	5.46	5.9	

Table 3.2 displays the results obtained at the end of the structural optimization. We have 15 different final states: the number of metastable states has significantly increased with respect to the search of the previous section in which symmetries are accounted for. This is probably a consequence of symmetry breaking by DFT+U. Furthermore, the lowest energy obtained is roughly 90 meV lower than the one obtained when the symmetries are taken into account. Moreover, the matrix very close to that of the symmetric case (M^{sym}), corresponds here to the third metastable state. It is clear that the reduction of the number of symmetries increases the probability of the system to be trapped into a metastable state during the calculation.

Finally, we observe that, for $M_1^{no\ sym}$, $M_2^{no\ sym}$, and $M_3^{no\ sym}$, the Am^{4+} magnetic moment is almost the same as in the symmetric case. Nevertheless, we observe a slight

difference between the lattice constants ($a \neq b \neq c$) but the cell volume remains in the three cases very close to the case where crystal symmetry is taken into account. Finally, the band gaps are in the three cases rather close to each other around 1.1 ($\pm$ 0.2) eV. Therefore, the calculations taking into account crystal symmetry are expected not to have a significant effect on the bulk properties.

3.4 Bulk properties of AmO_2

Having identified the *5f* occupation matrix of the ground state of the AmO_2 system, it is now possible to correctly model bulk properties. In order to evaluate these properties using DFT+U, it is essential to determine the values of the onsite Coulomb interaction U and the exchange J parameters for AmO_2. Kotani *et al.* [23] proposed a systematic analysis of actinide *4f* core X-ray photo-emission spectra in the actinide dioxide series using the Anderson impurity model. Based on the electronic states of these materials they determined the U and J parameters. For AmO_2, they find U=6.00 eV and J=0.75 eV. At present, there is no explicit calculation of these parameters in order to validate the Kotani values. As a result, the literature does not agree on any value of U and J, since the values used in the early first-principles studies strongly vary from one author to another [1, 7, 78, 79].

Our investigation in this section aims at determining the values of onsite Coulomb parameters allowing to correctly describe the bulk properties of americium oxides using the GGA+U approximation as parametrized by PBE [112]. We evaluate structural properties, electronic properties, elastic properties, enthalpy of formation, magnetic properties including or not spin-orbit coupling (SOC) as a function of U and J parameters as well as dielectric and some thermodynamic properties. U varies in the range of 0.0-8.0 eV and J varies in the range of 0.0-0.75 eV. For simplicity, the present investigation of the U and J values is performed by taking into account symmetries. The *5f* electron occupation matrix (M^{sym}) for the symmetric case obtained in the Sec. 3.3.1 has thus been used to avoid the metastable states. Finally, we determine the parameters that best reproduce experimentally known properties. In order to test the consistency and reliability of our studies, we also perform calculation using the hybrid functional approximation as parametrized by Heyd-Scuseria-Ernzerhof [52]. Indeed, this functional does not require prior knowledge of onsite Coulomb interaction U and exchange J parameters but the ratio of Hartree-Fock exchange (generally set at 25%) used in this approximation. However, the computing time is extremely large compared to DFT+U calculations. Our results have been compared to other available HSE results as well as experimental results.

3.4.1 Magnetic structure

According to the experimental results [83, 87], the magnetic ground state of AmO_2 is known to be antiferromagnetic. Furthermore, our calculation using the HSE functional shows that the antiferromagnetic order (1k AFM) is more stable than the ferromagnetic (1k FM) order. In fact, we find the relative energy $E_{AFM} - E_{FM}$ equals to -0.03 eV per AmO_2 formula (see 3.5). In order to model AmO_2 using GGA+U calculation, we compute the energies of the ferromagnetic and antiferromagnetic orders (considering

the 1k order) for several U values. We plot in Fig. 3.1(a) the total energy of AFM and FM ordering per unit formula as a function of the U parameter. This figure is completed by displaying the energy difference between these magnetic orders (see Fig. 3.1(b)). We can see that the values of the U parameter larger than 4 eV lead to negative values of the $E_{AFM} - E_{FM}$ difference and thus, give the correct antiferromagnetic ground state.

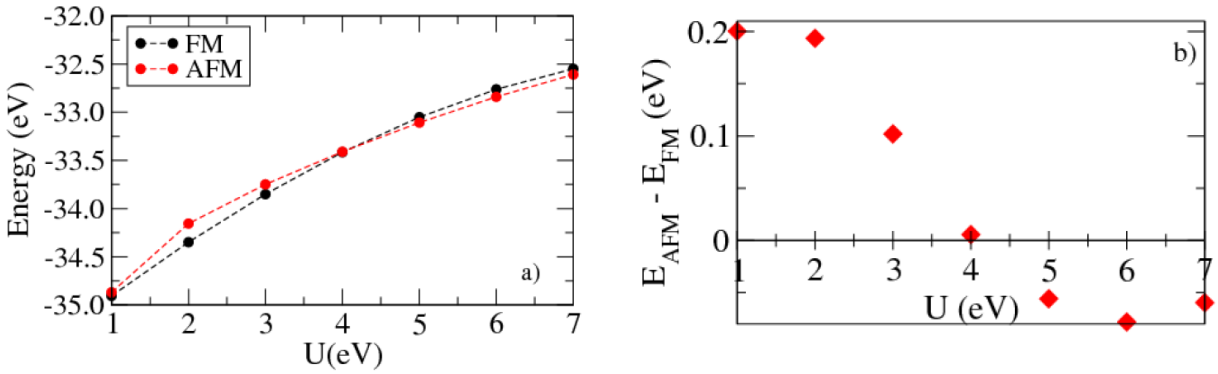

Figure 3.1: a) Total energy as a function of the U parameter. Black circles correspond to the ferromagnetic (FM) order while red circles to the 1k antiferromagnetic (AFM) order. b) Energy difference between 1k AFM and 1k FM ordering with respect to U. The VASP code was used here.

Although the magnetic ground state of AmO_2 is known to be an antiferromagnetic state, the literature does not provide any explicit investigation on the type (collinear or non-collinear) of the AFM order (see Fig. 3.2. Table. 3.3 provides the orientation of the magnetic moments carried by an actinide (Am, U or Pu) atom in the 3k AFM order). In UO_2 the magnetic ground state is identified as a transverse 3k AFM state [110]. We here study the relative stability between longitudinal 1k and transverse 3k AFM orders including the spin-orbit coupling and thus, performing non-collinear magnetism (i.e. the magnetization is a vector field) and we present our results in Fig. 3.3 and Table 3.4. For comparison, we also study the relative stability between longitudinal 1k and transverse 3k AFM orders including the spin-orbit coupling in UO_2 and PuO_2 for the fixed values of U and J parameters, (U=4.50,J=0.51) eV and (U=4.00,J=0.70) eV respectively (see Table 3.4).

Results for AmO_2: Fig. 3.3(a) shows that the 1k AFM order is the most stable order starting from the value U=4 eV when the SOC is not included in the calculations. Conversely, Fig. 3.3(b) shows that the 3k AFM order is more stable than the 1k order with an energy difference equals to 0.1 eV per unit formula when the contribution of the SOC is added.

The investigation by Tokunaga *et al.* [86] on $Pu_{0.91}Am_{0.09}O_2$ using ^{17}O nuclear magnetic resonance (NMR) shows an effective magnetic moment of 1.38 μ_B/Am^{4+} ion around 8.5 K in accordance with the magnetic susceptibility studies by Karraker *et al.* [83]. Our computed magnetic moment (2.2 *or* 2.4 μ_B) when spin orbit coupling is included is not close to this experimental result but is nevertheless much closer than the one obtained without taking SOC into account. In addition, we observe that the 3k AFM order tends to increase the cell volume (Table 3.4). This can be attributed to the distortion occurring in the oxygen sublattice. In fact, we observe an oxygen sublattice distortion of roughly 0.17 Å along the crystallographic directions <111>.

Table 3.3: Orientation of magnetic moment vectors carried by actinide cations in a 12-atom supercell with a non-collinear 3k magnetic order.

Magnetic moments Orientation[xyz]	Reduced coordinates
[111]	(0.00;0.00;0.00)
$[1\bar{1}\bar{1}]$	(0.50;0.50;0.00)
$[\bar{1}\bar{1}1]$	(0.50;0.00;0.50)
$[\bar{1}1\bar{1}]$	(0.00;0.50;0.50)

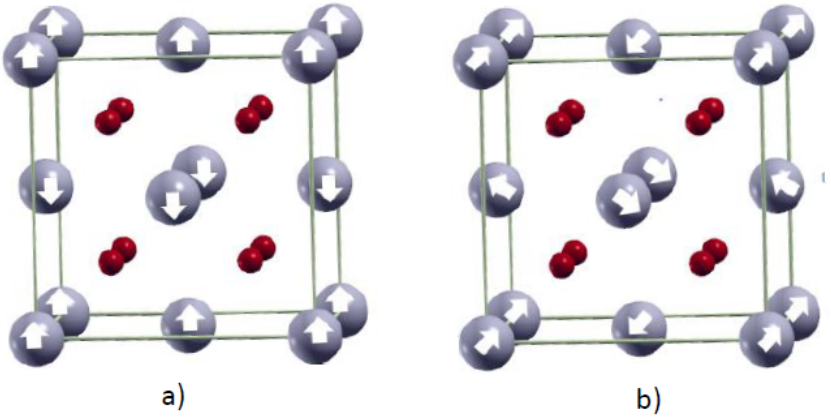

Figure 3.2: AmO_2 fluorite structure (12-atom cell): a) longitudinal 1k collinear order and b) transverse 3k non-collinear order. Arrows illustrate the 1k and 3k orientations of spin magnetic moments carried by the americium atoms. Red atoms are oxygen atoms. 1k = [001] and 3k = [111].

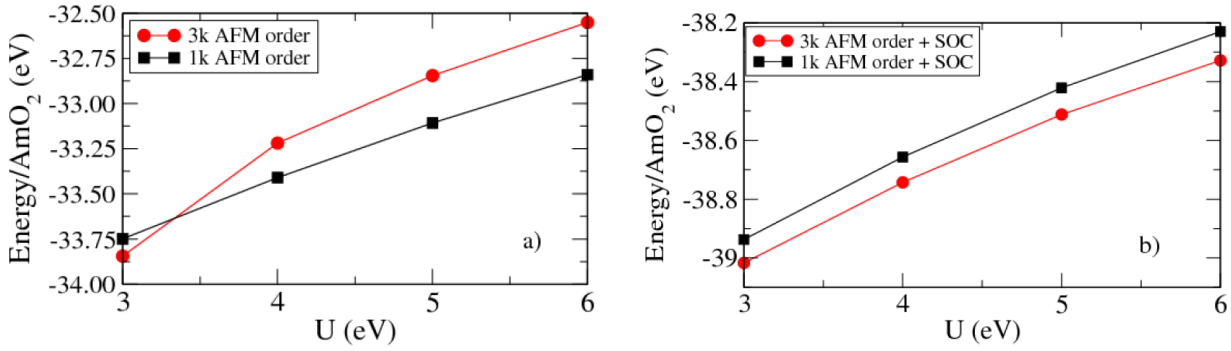

Figure 3.3: Total energy per americium atom as a function of the U parameter. Red line corresponds to 3k antiferromagnetic order while black line to 1k antiferromagnetic order. a) SOC is not included and b) SOC is included. Calculations were performed on the AmO_2 fluorite structure (12-atoms cell) using VASP code.

Our result confirms the observations made by Tokunaga *et al.* [86]. Indeed, from the frequency curve with respect to temperature, they observe a NMR line broadening and they supposed that this NMR line broadening could arise from oxygen sub-lattice distortions. Based on these results, we suggest that the AmO_2 magnetic ground state is a transverse 3k AFM order with a oxygen sub-lattice distortion of roughly 0.17 Å. However, the longitudinal 1k AFM order without SOC remains a reasonable approximation of the magnetic ground state of AmO_2 (3k AFM order) for the computing of bulk properties although the magnetic moment is poorly described (5.3 μ_B instead of

1.4 μ_B).

Results for UO_2: As in AmO_2, we study the relative stability between longitudinal 1k and transverse 3k AFM orders including the spin-orbit coupling. Table 3.4 shows that, without taking the contribution of the spin-orbit coupling, the 3k AFM order is more stable than 1k AFM order, which is in agreement with the experimental results as well as with the one reported in the investigation by Laskowski *et al.* [116]. In contrary, when the SOC is added, the 3k order is no longer the most stable, which is still in agreement with the first-principles investigation by Laskowski *et al.* [116]. Indeed, using the fully localized limit (FLL) for double counting correction (DCC) within the DFT+U method, they show that 1k order is the most stable order. However, they show that using the "around mean field" (AMF) approximation for DCC, the non-collinear AFM 3k order is more stable than the 1k order. Nevertheless, the use of AMF-DCC should be less adequate for strongly localized *5f* electrons.

Table 3.4: Lattice parameter, c/a ratio, difference between the energies of 1k AFM order and 3k AFM order and spin magnetic moment in AmO_2, PuO_2, and UO_2 depending on different orientations of spin magnetic moments (1k and 3k) without and with SOC. We used U=6 eV and J=0.75 eV for AmO_2, U=4.00 eV and J=0.70 eV for PuO_2, and U=4.50 eV and J=0.51 eV for UO_2 in DFT+U calculations. The occupation matrix used is the one determined in Sec.3.3.1.

		a(Å)	c/a	$\mu_{mag}(\mu_B)$	$\Delta E = E - E_{1k\ or\ 1k+SOC}$(eV)
AmO_2	1k order	5.44	0.99	5.3	0.00
	1k order+SOC	5.46	1.00	2.2	0.00
	3k order	5.51	1.00	5.8	0.29
	3k order+SOC	5.50	1.00	2.4	-0.10
	Exp.	5.37 [a]	1.00	1.4 [b]	0.00
PuO_2	1k order	5.46	1.02	4.1	0.00
	1k order +SOC	5.46	1.00	2.9	0.00
	3k order	5.46	1.00	4.0	0.00
	3k order+SOC	5.46	1.00	3.0	-0.10
	Exp.	5.40 [c]	1.00		
UO_2	1k order	5.56	0.99	2.0	0.00
	1k order+SOC	5.57	1.00	0.7	0.00
	3k order	5.57	1.00	2.1	-0.01
	3k order+SOC	5.57	1.00	0.6	0.01
	Exp.	5.47 [d]	1.00	1.7 [d]	

[a]Ref · [3] [c]Ref · [41]
[b]Ref · [83] [d]Ref · [117]

Results for PuO_2: We observe that in PuO_2, the 3k AFM order becomes more stable than 1k AFM order when the contribution of SOC is added as in AmO_2. Up to now, the magnetic behaviour in PuO_2 is not clearly established from experiments.

Overall, our calculations highlight that the energy correction related to the spin-orbit coupling decrease across the actinide series when the number of electron decreases (5.2 eV for AmO_2, 4.5 eV for PuO_2 and 3.5 eV for UO_2), which was expected since the effect of SOC increase with increasing atomic number.

3.4.2 Other bulk properties

Modelling the 3k AFM order including SOC requires a considerable computing time. Moreover, another challenge here would be to determine the ground-state occupation matrix allowing modelling of the 3k AFM order including SOC. We thus come back to collinear magnetism and use longitudinal 1k AFM order without taking into account SOC to model AmO_2 since we showed in Sec. 3.4.1 that, without including SOC, the 1k AFM order is more stable than the transverse 3k AFM order and can be used as an approximation of the AmO_2 magnetic ground state. The investigations in AmO_2 (using the hybrid functional) by Wen *et al.* [79] or in UO_2 [32, 39] and in PuO_2 [31] also show that 1k AFM order can be used as an approximation of the 3k AFM order to successfully compute several bulk properties. Nevertheless, it is important to note that 1k AFM approximation changes the point group O_h to D_{4h}. For instance one can clearly see (Table 3.4) that the c/a ratio differs from 1.00. In this case, the crystal field splits the *5f* orbitals in two twofold-degenerate levels ($2\times E_u$) and three non degenerate levels (A_{1u}, B_{1u} and B_{2u}). Except when explicitly mentioned, the calculations are now performed using the matrix obtained by taking into account symmetries (for the bulk quantities considered herebelow, taking into account symmetries or not is not expected to significantly change results).

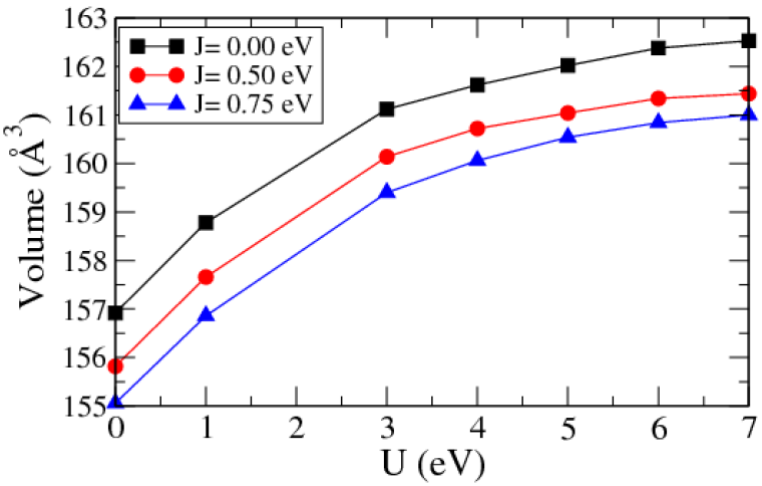

Figure 3.4: Evolution of the cell volume (12 atoms) as a function of the U and J parameters.

a) Structural properties

In this part, we calculate the lattice constant using different values of the U and J parameters. We then evaluate the influence of the J parameter on the cell volume in order to choose the J value that allows to obtain the volume closest to the experimental one (∼155 Å^3). We observe a slight decrease of the volume when the J parameter increases (see Fig. 3.4). The value J=0.75 eV leads to the smallest volume, and thus we keep it in all the rest of our calculations. From Table 3.5, we can see that the computed lattice constant (a=5.36 Å) obtained with HSE approximation is very close both to the experimental value (a=5.37 Å) and to other calculated values like the one obtained by Wen *et al.* [79] using HSE (a=5.38 Å). Our GGA+U computed value (a=5.44 Å, using U=6 eV) is slightly above the experimental data (1.3%) but is still

in a reasonable agreement. The same trend is observed for other computed values available in the literature (see Fig. 3.5). Note that J=0.75 eV is now fixed in all the following calculations.

b) Electronic properties

The only uncertainty is on the value of the U parameter. We have already seen that U must be larger than 4 eV for a correct description of the magnetism. Here, we now precise the value of U based on the value of the band gap.

In Fig. 3.5(a), we present the band gap calculated as a function of the U parameter. The calculated band gap (1.1 eV) using GGA+U (6 eV) is close to the experimental one (1.3 eV) though it is slightly underestimated (see Table 3.5). We see that the band gap obtained with the HSE06 functional (1.6 eV) is overestimated but is in agreement with the one obtained by Wen *et al.* [79] using the same functional.

We also present in Fig. 3.5(b) the electronic density of states (DOS) projected onto the Am-f spin-up and spin-down states and the O-p orbitals (using U= 6 eV and J= 0.75 eV) in order to provide a more detailed description of the electronics properties of AmO_2 (the calculation is performed here without symmetry, using the $M_3^{no\ sym}$ matrix). We set the top of the valence band maximum as the energy reference. The results obtained show that the band gap of AmO_2 is formed between the O-p occupied bands and the Am-f unoccupied bands. We can conclude that AmO_2 rather behaves as a charge-transfer insulator. This behaviour is close to that of PuO_2 but very different from that of UO_2 which is a Mott insulator i.e. with a U-f U-f band gap.

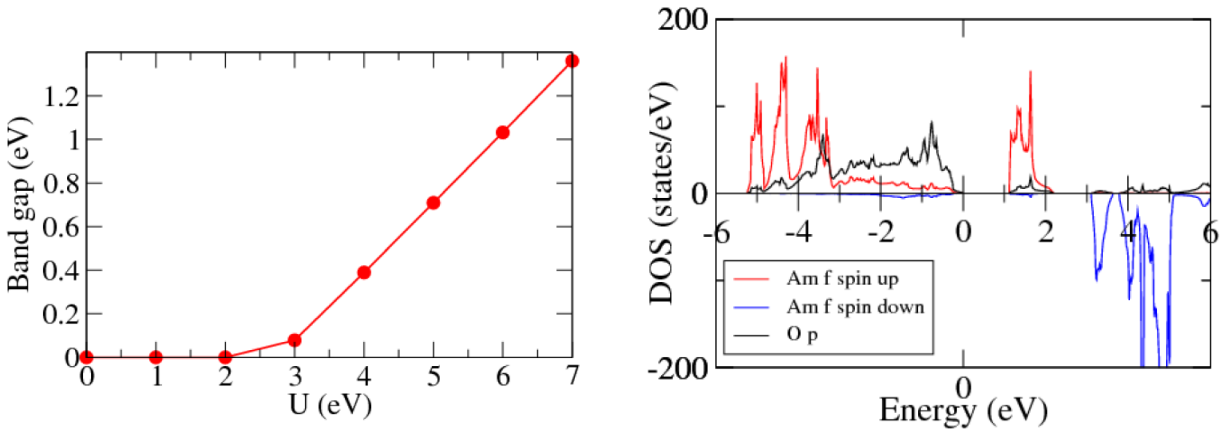

Figure 3.5: (a) Evolution the band gap as a function of the U parameter. (b) Electronic density of states (DOS) projected onto the Am-f (spin-up and spin-down) and O-p orbitals in AmO_2.

We showed that the values U= 6 eV and J= 0.75 eV provide a correct description of the band gap, the lattice parameter as well as the magnetism of AmO_2 compared to the early studies in the literature. The next objective is confirm this value of U= 6 eV by assessing the elastic properties and formation enthalpy.

c) Elastic properties

Up to now, no experimental study aimed at determining the elastic constants of AmO_2 exists to our knowledge and the theoretical studies are scarce. Only the bulk modulus has been measured. The only available first-principles study in the literature has been performed by Yong *et al.* [7] using the GGA+U approximation. However, the bulk modulus obtained from the elastic constants in this study largely deviates from the experimental value. The metastable states could explain the origin of the discrepancies observed in the results obtained by Yong *et al.* [7].

Fig. 3.6 displays the evolution of the elastic constants as a function of the U parameter as obtained from our calculations. The results show the same trend as those obtained in UO_2, NpO_2 and PuO_2 (see Table 3.5) and can be regarded as reference values. We observe that C_{11} and C_{12} remain almost constant with the increase of U while C_{44} slightly decreases. The bulk moduli obtained from these values are smaller than 10% off the experimental value [81] (Table 3.5), which is acceptable. This small underestimation is within the error expected for the computational method (GGA+U). Our calculated value (210 GPa) using the HSE06 functional is close to the experimental value (205 GPa) [81] and the one obtained by Petit *et al.* [80] (209 GPa) using the SIC method.

Although the results (lattice constant and bulk modulus) obtained with the HSE06 functional are closer to the experimental results than the GGA+U ones, the HSE06 functional requires much longer computing time compared to the GGA+U method. Nevertheless, a reasonable agreement with the experimental results as well as other HSE06 results allows us to conclude on the reliability of our study.

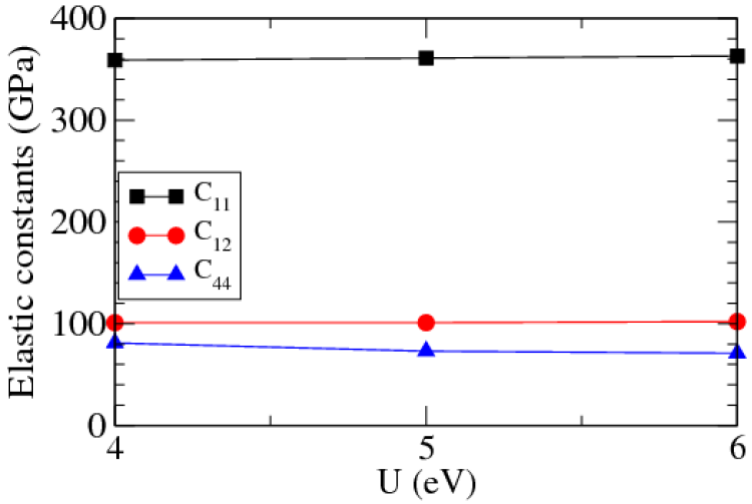

Figure 3.6: Evolution of the elastic constants with respect to the U parameter. The calculations were performed on the AmO_2 fluorite structure (12-atom cell) using the VASP code.

d) Dielectric properties

To our knowledge, dielectric properties of americium oxides remain unknown. For instance, the static dielectric constant has never been either measured or calculated.

Using Density Functional Perturbation Theory as implemented in the ABINIT code, we have performed response function calculations to obtain the electronic dielectric tensor and the Born effective charges. The calculations are performed using the 6-atom unit cell, (i) taking into account the symmetries (case 1), and (ii) without symmetry (case 2). The occupation matrix and cell vectors are the ones corresponding to the M^{sym} matrix in the first case, and to the M_3^{nosym} matrix in the second case. In this section, U is now fixed to 6.00 eV and J to 0.75 eV.

The phonon modes at the Γ point of the First Brillouin Zone have been obtained using a finite-difference (frozen-phonon) scheme: the atoms are displaced one by one along each direction, by $+\delta$ and $-\delta$ (with $\delta = 0.0025\, a.u.$), and the total energy and atomic forces of the distorted configuration are recomputed, which allows to construct the force constant matrix and then the dynamical matrix at Γ. The latter is diagonalized, providing the phonon pulsations ω_i^2, and phonon eigenvectors, from which the mode effective charge and the oscillator strength tensor are constructed for each of the 18 modes. Each mode possessing a non-zero effective charge contributes to the static dielectric constant [118]. These contributions are then computed, and added to the electronic dielectric tensor to obtain the (relaxed-ion) static dielectric tensor. Convergence with δ is checked by doing the same calculation using 2δ (which provides the same dielectric constant with a precision of 0.01).

We obtain the following results, where small deviations from diagonal tensors (in case 2) are only due to the loss of symmetry caused by DFT+U:

a. *Born effective charges.* In case 1,

$$\mathrm{Z}^*_{\mathrm{Am}} = \begin{pmatrix} 5.14 & 0.00 & 0.00 \\ 0.00 & 5.14 & 0.00 \\ 0.00 & 0.00 & 4.58 \end{pmatrix} \quad \mathrm{Z}^*_{\mathrm{o}} = \begin{pmatrix} -2.57 & 0.00 & 0.00 \\ 0.00 & -2.57 & 0.00 \\ 0.00 & 0.00 & -2.29 \end{pmatrix}.$$

In case 2,

$$\mathrm{Z}^*_{\mathrm{Am}} = \begin{pmatrix} 4.92 & 0.19 & 0.18 \\ 0.19 & 4.92 & 0.18 \\ 0.19 & 0.19 & 4.91 \end{pmatrix} \quad \mathrm{Z}^*_{\mathrm{o}} = \begin{pmatrix} -2.46 & -0.10 & -0.09 \\ -0.10 & -2.46 & -0.09 \\ -0.09 & -0.09 & -2.46 \end{pmatrix}.$$

Small differences do exist between the two cases, due to different symmetries, but the tensors have the same trace : $1/3\mathrm{Tr}(Z^*_{Am})$=4.95 (case 1) and 4.92 (case 2); $1/3\mathrm{Tr}(Z^*_O)$=-2.48 (case 1) and -2.46 (case 2).

b. *Electronic dielectric tensor.* In case 1,

$$\epsilon^\infty = \begin{pmatrix} 6.15 & 0.00 & 0.00 \\ 0.00 & 6.15 & 0.00 \\ 0.00 & 0.00 & 5.91 \end{pmatrix}.$$

In case 2,

$$\epsilon^\infty = \begin{pmatrix} 6.31 & 0.25 & 0.23 \\ 0.25 & 6.31 & 0.00 \\ 0.23 & 0.23 & 6.19 \end{pmatrix}.$$

Here again, both tensors have a very close trace: 1/3Tr(ϵ)=6.17 (case 1) and 6.16 (case 2).

c. *(Relaxed-ion) static dielectric tensor (thus including ionic contributions).* In case 1,

$$\epsilon_S = \begin{pmatrix} 19.18 & 0.00 & 0.00 \\ 0.00 & 18.19 & 0.00 \\ 0.00 & 0.00 & 13.83 \end{pmatrix}.$$

In case 2,

$$\epsilon_S = \begin{pmatrix} 16.83 & 1.35 & 1.42 \\ 1.35 & 16.82 & 1.42 \\ 1.42 & 1.42 & 16.81 \end{pmatrix}.$$

The static dielectric constant is thus 1/3Tr(ϵ_D)=17.40 (case 1) / 16.82 (case 2).

Knowing the experimental static dielectric constants of UO_2 (23.8) [119] and PuO_2 (18.9) [120], our value for AmO_2 can be regarded as a reference since it follows the same trend.

We observe that the loss of symmetry caused by DFT+U induces an anisotropy in the dielectric properties, and this anisotropy may be different from one occupation matrix to another. But it is satisfactory to see that the tensors obtained by the two occupation matrices have almost the same trace, that is to say, the dielectric properties averaged over the Cartesian directions are preserved from one occupation matrix to another.

e) Formation enthalpy

Finally, we also compute the formation enthalpy ΔH_f of AmO_2 with respect to molecular oxygen and metallic Am-α (computed using GGA+U with the same U and J parameters in order to keep the same energy reference). This energy, related to the $Am + O_2 \longrightarrow AmO_2$ reaction, can be written as follows:

$$\Delta H_f^{Amo_2} = E_{tot}^{AmO_2} - E_{tot}^{Am} - E_{tot}^{O_2} \tag{3.1}$$

where $E_{tot}^{AmO_2}$, E_{tot}^{Am}, and $E_{tot}^{O_2}$ are the total energy of the AmO_2 compound, of molecular oxygen, and of Am-α. To our knowledge, there is only one experimental study [21] aimed at evaluating the formation enthalpy of AmO_2. Our computed values (-8.56 and -8.29 eV with U=5 and 6 eV respectively) deviate from the experimental value (-9.51 eV) by roughly 10%. A part of the contribution of this 10% disagreement with the experiment could arise from the use of the Hubbard term to describe metallic americium. The GGA approximation overestimates the cohesion energy of O_2 molecule (-6.01 eV instead of -5.21 eV as in Ref [121]), which could explain another part of the error obtained calculating cohesion and formation energies of oxide compounds within GGA+U approximation. We then performed a correction in the energy of the oxygen

molecule using the following approximation: $2E_{tot}(O) + E_{bind}(O_2)$, where $E_{tot}(O)$ is the total energy of the O atom (spin-polarized, no symmetry) and $E_{bind}(O_2)$ is the experimental [121] binding energy of the O_2 molecule. This contributes to improve the formation enthalpy, the new values being: -9.42 and -9.15 eV with U=5 and U=6 eV respectively. One observes that the error with respect to the experimental value has decreased from 10% to ∼1-3%.

Note that it has been showed [122] in the case of UO_2 and PuO_2 that by taking into account the van der Waal (vdW) interactions, the error of 10% (compared to the experiment) can be minimized up to smaller than 0.1%. Thus, we tested the use of vdW-optPBE instead of using only PBE to describe the exchange and correlation functional. However, this correction of correlation functional has not improved the formation enthalpy of AmO_2, since we obtained -8.21 eV (i.e. the relative error is still ∼10%).

3.5 Discussion of the onsite Coulomb parameters (U,J)

We summarize in Table 3.5 all our computed results obtained on the bulk properties of AmO_2. Regarding Sec. 3.4.1, the values of U smaller than 5 eV do not offer a good description of the magnetic ground state as experimentally known.

Table 3.5: Calculated lattice parameter, band gap, bulk modulus, elastic constants, formation enthalpy, Am^{4+} magnetic moment, and relative stability of magnetic order. For comparisons, previous experimental results as well as other theoretical results are listed. Since there is no experimental value of elastic constants, the ones of UO_2 and PuO_2 are also listed in order to show a trend. In parenthesis: formation enthalpy estimated using a total energy for O_2 equal to $2E_{tot}(O) + E_{bind}(O_2)$, where $E_{tot}(O)$ is the total energy of the O atom (spin-polarized, no symmetry) and $E_{bind}(O_2)$ the experimental binding energy of the O_2 molecule.

Comp.	Method	a (Å)	Gap (eV)	C_{11} (GPa)	C_{12} (GPa)	C_{44} (GPa)	B_0 GPa	ΔH_f (eV)	μ_{mag} (μ_B)	$E_{AFM} - E_{FM}/Am$ (eV)
	GGA+U (5 eV)	5.44	0.7	361	101	73	187	-8.56 (-9.42)	5.3	0.05
	GGA+U (6 eV)	5.44	1.1	363	102	71	189	-8.29 (-9.15)	5.3	-0.06
AmO_2	HSE06	5.36	1.6	-	-	-	210	-	5.1	-0.08
	GGA+U^a	5.44	-	-	-	-	-	-	-	-0.03
	GGA+U^b (eV)	5.43	0.0	-	-	-	-	-	-	-
	GGA+U^c (eV)	5.35	1.0	204	87	55	126	-	4.77	-
	SIC[d]	5.42	0.8	-	-	-	209	-	-	-
	HSE[b]	5.38	1.5	-	-	-	-	-	-	-
	Exp.	5.37[c]	1.3[a]		-	-	205[f]	-9.51[g]	-	AFM[h]
UO_2	Exp.	-	-	389[i]	119[i]	60[i]	207[f]	-	-	-
PuO_2	GGA+U^j	-	-	375	111	70	178	-	-	-

[a]Ref. [14];[b]Ref. [79];[c]Ref. [7];[d]Ref. [80];[e]Ref. [3];[f]Ref. [81]; [g]Ref. [21];[h]Ref. [83, 87];[i]Ref. [123];[j]Ref. [29]

The comparison of our results obtained with GGA+U(6 eV) to other computed values on the one hand, and to the experimental results on the other hand shows a good agreement. Thus, we can clearly conclude that (U, J) = (6 eV, 0.75 eV) can be used to correctly model AmO_2 using GGA+U with the PBE parametrization. This result is in line with the values determined from experiments by Kotani *et al.* [23]. Indeed, the Kotani values have never been used in previous studies. To our knowledge, the current study is the first one providing the onsite Coulomb interaction U and

exchange J by fitting on several bulk properties of AmO_2. These values can be used to further study properties like formation and migration energies of point defect in a large defective supercell using GGA+U calculations. Such properties are extremely important for nuclear application and other domains such as semiconductor physics.

3.6 Finite temperature properties

Throughout this manuscript, the temperature dependent properties are calculated on the basis of *ab initio* molecular dynamics (MD). The Verlet algorithm [124] is used to numerically integrate Newton's equations of motion. The Verlet algorithm is very stable (in particular, more stable than the simpler Euler method). Also, it is a time-reversible algorithm. For this reason it is well adapted to the simulation of conservative systems such as the ones studied here.

The position at time $t + \Delta t$ is given by:

$$\mathbf{r}_i(t + \Delta t) = \mathbf{r}_i(t) + \frac{d\mathbf{r}_i(t)}{dt}\Delta t + \frac{1}{2}\frac{\mathbf{F}_i}{m_i}\Delta t^2 + O(\Delta t^3) \tag{3.2}$$

The position at time $t - \Delta t$ is given by:

$$\mathbf{r}_i(t - \Delta t) = \mathbf{r}_i(t) - \frac{d\mathbf{r}_i(t)}{dt}\Delta t + \frac{1}{2}\frac{\mathbf{F}_i}{m_i}\Delta t^2 - O(\Delta t^3) \tag{3.3}$$

where $\mathbf{r}_i$ and m_i are the position and mass of particle i. $\mathbf{F}_i$ is the force acting on the particle i calculated in our case within DFT+U calculations. The sum of the Eq. 3.2 and Eq. 3.3 gives the propagation position :

$$\mathbf{r}_i(t + \Delta t) = 2\mathbf{r}_i(t) - \mathbf{r}_i(t - \Delta t) + \frac{1}{m_i}\mathbf{F}_i\Delta t^2 + O(\Delta t^4) \tag{3.4}$$

and the velocity

$$\mathbf{v}_i(t) = \frac{d\mathbf{r}_i(t)}{dt} = \frac{\mathbf{r}_i(t + \Delta t) - \mathbf{r}_i(t - \Delta t)}{2\Delta t} + O(\Delta t^3) \tag{3.5}$$

The Verlet algorithm uses Eq 3.4 to obtain the next position vector from the previous one with $\Delta t = 2\ fs$ in our simulations. At each time step of the molecular dynamics trajectory, it is possible to calculate some instantaneous quantities such as :
(i) The temperature
(ii) The pressure
(iii) The energy and the enthalpy

The instantaneous temperature is obtained from the instantaneous kinetic energy E_k, as:

$$E_k = \frac{3}{2}Nk_BT(t) = \sum_i \frac{1}{2}m_i\mathbf{v}_i(t)^2 \tag{3.6}$$

The pressure contains a contribution from the potential energy and a contribution from the kinetic energy. The potential part, in *ab initio* MD, is obtained directly from the

DFT calculation (using Hellman-Feynman theorem, as for the atomic forces). Let us call it P_{DFT}. The kinetic part is equal to NK_BT/V:

$$P(t) = \frac{Nk_BT(t)}{V} + P_{DFT}(t) \tag{3.7}$$

The instantaneous energy is the sum of the instantaneous kinetic energy, $\frac{3}{2}Nk_BT(t)$, and of the instantaneous potential energy, directly given by the DFT calculation. The instantaneous enthalpy is obtained by adding to the instantaneous energy the term $P(t)V(t)$.

The temperature, pressure and energy/enthalpy of the simulation are obtained by time-averaging these instantaneous quantities over the equilibrated part of the trajectory.

Ab initio MD in this work is performed within the (NPT) isothermal-isobaric ensemble i.e. the number of particles N, the pressure P, and temperature T are kept fixed. The temperature and pressure are controlled by using the Langevin thermostat (to fix the temperature) together with the Parrinello-Rahman barostat (to fix the pressure). VASP code is used.

The parameters associated with the thermostat and barostat are:
(i) 10 ps^{-1} for the friction coefficient related to atomic degrees of freedom, (ii) 20 ps^{-1} for the friction coefficients related to lattice degrees of freedom and 1000 amu for the fictitious mass related to lattice degree of freedom.

The molecular dynamics simulations are performed over 12 to 15 *ps*. The first 5 *ps* are considered as the time needed for the system to reach the equilibrium at a given temperature. Therefore, the statistical averaging is made over 7 to 10 last picoseconds. A 96-atom supercell is used and the calculations are performed at Γ point of the Brouillon zone. All symmetries are switch off and the convergence criterion over self-consistent cycles is set at 10^{-5} eV per atom. The pressure is fixed to 0 kbar.

Note that the average pressure was not exactly equal to 0 kbar despite the use of the barostat. This could result from the size of our system (96-atom supercell). Indeed, *ab initio* MD is very time consuming especially for the strongly correlated materials and thus are still limited to a few hundred atoms and few picoseconds. Therefore, it is necessary to perform a small correction on the average volume and energy of the system in order to cancel the contribution related to the non-zero pressure (see appendix A).

3.6.1 Lattice thermal expansion

The linear thermal expansion is obtained through the following equation:

$$\frac{\Delta a}{a_0} = \frac{a_T - a_0}{a_0} \tag{3.8}$$

where a_T is the lattice parameter at temperature T and a_0 corresponds to the lattice constant at room temperature.

The thermal expansion of AmO_2 calculated in this work is shown in Fig. 3.7 together with the experimental ones. For comparison we also report the thermal expansion of

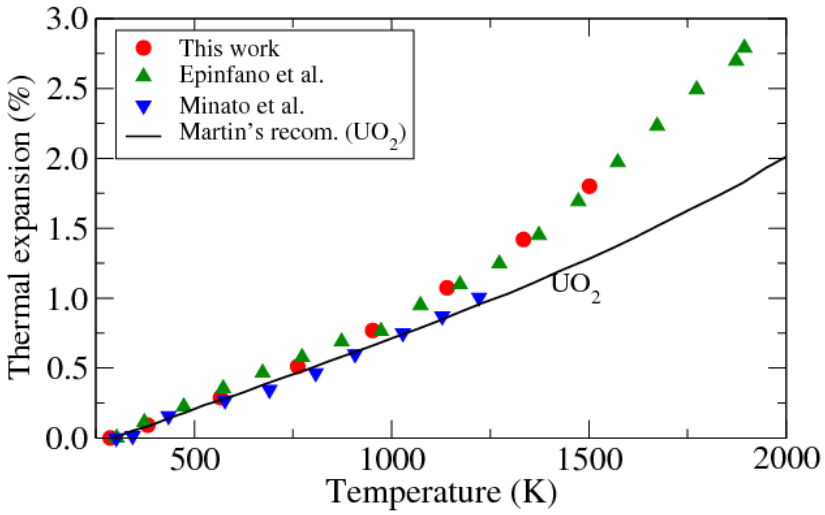

Figure 3.7: Thermal expansion of AmO_2 as a function of temperature compared to the experimental ones [9, 19] and Martin's recommendation for UO_2 [11].

UO_2 given by the Martin's recommendation [11]. All the thermal expansion data calculated in this work are displayed in Table 3.6.

Our calculated thermal expansion is consistent with the experimental result by Minato *et al.* [9] and in good agreement with the one by Epifano *et al.* [19]. We observe a quasi-linear behaviour for temperatures lower than 1200 K whereas at 1200 K, one highlights a change in the slope. This behaviour shows a noticeable difference with UO_2 (see Martin's recommendation). The origin of this change in the slope is not clearly identified. Epifano *et al.* point out the presence of the oxygen point defects. However, this conclusion is still controversial since, no defect is introduced in our system (i.e. O/M remains equal to 2.00)or formed for these temperatures but we obtain the same description of the lattice expansion. Further investigations including oxygen vacancies are needed to unequivocally conclude.

3.6.2 Enthalpy increment

The calculated enthalpy increments for AmO_2 as a function of T is shown in Fig 3.8 and numerical data are reported in Tab.3.6. For comparison, we also plot the measurement by Nishi *et al.* [20] using the drop calorimetry method as well as the calculated values by Epifano [16] on the basis of the CALPHAD model (solid line).

Our *ab initio* MD enthalpy increment as a function of temperature is in good agreement with the experimental measurements by Nishi *et al.* [20]. Moreover, our results contribute to confirm the CALPHAD results by Epifano [16] especially for temperatures higher than 1200 K. Indeed, the CALPHAD model prior needs data to optimize the Gibbs energy parameters included in this model. However we can see in Fig. 3.8 that the few data available before this work were limited at temperatures smaller than 1200 K.

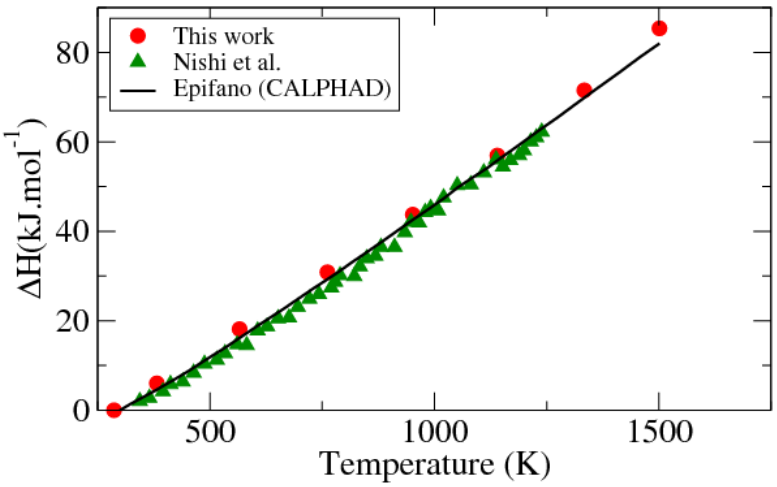

Figure 3.8: Enthalpy increment of AmO_2 as a function of temprature: red points represent this work, green triangles experimental study by Nishi *et al.* [20] and solid line, modeling studies by Epifano [16].

Table 3.6: Linear thermal expansion values as a function of temperature calculated in this work.

T(K)	$\Delta a/a_0(\%)$	ΔH(kJ.mol^{-1})
286.58	0.000	0.00
381.74	0.091	6.00
566.21	0.288	18.14
761.79	0.512	30.84
951.94	0.769	43.72
1140.39	1.074	56.93
1334.04	1.420	71.51
1501.29	1.801	85.35

3.7 Investigation of bulk properties of americium sesquioxides Am_2O_3

According to the experimental results, americium can be reduced to Am^{3+} within mixed oxides such as (U,Am)O_2 and (U,Pu,Am)O_2 [20, 24, 96]. In order to investigate the mixed oxides containing americium atoms, it is important to know some bulk properties of Am_2O_3 in which all americium atoms have a +III valence. The investigation of americium sesquioxides remains up to now very scarce and the only available studies on americium sesquioxides reported in literature aim at determining the lattice constants [3, 14, 94] and the band gap [14]. In this part, we first investigate the stable crystal structure at low temperature, then we predict several bulk properties such as band gap, bulk modulus, structural parameters, formation enthalpy and spin magnetic moment.

3.7.1 Stable crystal structure Am_2O_3 low temperature

From plutonium, the actinide sesquioxides (and also many other sesquioxides) crystallize into three different crystalline phases. These are the bcc C-type, monoclinic B-type and hexagonal A-type. The stable crystal structure of americium sesquioxide at room temperature is not fully established. Early studies [12, 93] report Am_2O_3 as a bcc C-type structure at room temperature. However, since Pu_2O_3 has a hexagonal A-type at room temperature and Cm_2O_3 a monoclinic B-type structure, the bcc C-type structure at room temperature for Am_2O_3 is unlikely according to Konings *et al.* [21]. Furthermore, no oxygen potential measurements are fully consistent with the data of Sari and Zamorani previously mentioned [12] in the literature. Our purpose here is to investigate the americium sesquioxide namely bcc C-type and hexagonal A-type and determine the stable structure of the crystal at low temperature. All experimental studies on the B-type are in agreement with the fact that it is stable only at high temperature [12, 19, 93] and, as a result, we will not investigate this phase.

Since Am_2O_3 contains correlated *5f* orbitals, it is essential to monitor the electronic occupations of these orbitals using DFT+U as shown for AmO_2. In Am_2O_3, Am^{3+} ions have six electrons in the *5f* orbitals. There are C_7^6=7 different configurations (still assuming high-spin electronic configurations) and therefore seven possible initial diagonal occupation matrices. We imposed these seven occupation matrices at the beginning of each calculation. We used 1k antiferromagnetic order [21] and (U,J) = (6 eV, 0.75 eV) as well as (5 eV, 0.75 eV). The symmetries have been taken into account. We display our results in Table 3.7. For the hexagonal structure four different states are reached including one metallic state.

As regards the cubic structure, five different final states depending of the initial matrix are reached with two metallic states (See Table 3.7).

Table 3.7: Relative energies obtained starting from the 7 initial diagonal occupation matrices. The energy of the lowest state is set to zero. For bcc C-type, the 80-atom conventional unit cell is used and a 5-atom primitive cell for the hexagonal A-type.

	(E-E_{min})/Am (eV)	
Initial matrix	A-type	C-type
[0111111]	0.00	0.00
[1011111]	0.00	0.00
[1101111]	0.00	0.53
[1110111]	0.00	0.00
[1111011]	1.25	0.33
[1111101]	0.66	0.23
[1111110]	0.31	0.21

Knowing the ground states of bcc C-type and hexagonal A-type, we can now compare the total energy of these structures. The relative energy per Am_2O_3 formula unit is $E_{Cub} - E_{Hex} = 0.86$ eV (using U= 6 eV) and 0.80 eV (using U= 5 eV), indicating that the hexagonal A-type is the most stable crystal structure of americium sesquioxide at low temperature. This result is not in agreement with the first thermodynamic phase diagram of the Am-O system reported by Sari and Zamorani [12] using differential

thermal enthalpy (DTA). However, it is in agreement with the one reported by Gotcu-Freis *et al.* [13] using the CALPHAD method [125], though this CALPHAD phase diagram is not completely established owing to the lack of experimental data on the stoichiometric C-type phase. More specifically, the existence of another stoichiometric sesquioxide phase with bcc structure reported by Sari and Zamorani [12] is still controversial. Furthermore, most experimental [120] and theoretical [21] studies on Am_2O_3 have been made on the hexagonal structure. Therefore, further experimental work is required to fully establish the thermodynamic description of the Am-O system.

3.7.2 Bulk properties

Several bulk properties such as lattice parameters, band gap, magnetic moment, bulk modulus and formation enthalpy of A-type and C-type structures have been calculated in this section. The computed internal structural parameters for A-type obtained after relaxation of all the degrees of freedom are z_{am}=0.2448 and z_0=0.6504. These parameters are found not to depend on the value of U and are required to model the hexagonal Am_2O_3 structure. Since there are neither experimental nor theoretical values up to now, our values can be used as reference. Table 3.8 presents the results computed in this work compared to the experimental results as well as the theoretical ones. Regarding the hexagonal Am_2O_3 A-type, we can see that our computed lattice parameters show a good agreement with the experimental results yielded by Nishi *et al.* [94]. The lattice parameters of bcc C-type obtained in this study are slightly overestimated (1.4%) compared to the experimental results obtained by Hurtgen and Fuger [3] but are nevertheless within the error expected for the computational method (GGA+U).

Our computed band gap (2.85 eV) using GGA+U (5 eV) is close to the only available theoretical result [14](2.60 eV) whereas the one computed using GGA+U (6 eV) shows a large discrepancy. Since the value obtained using the HSE functional (2.2 eV) is close to one obtained with GGA+U (5 eV), it is likely that the U= 6 eV value is not an appropriate value for A-Am_2O_3. However, we cannot conclude because of the lack of additional data. For bcc C-type, the evolution of the U value does not have a significant influence on the band gap.

Concerning the bulk modulus, our calculated values, 135 GPa for C-type and 139 GPa for B-type follow the same trend as the ones obtained in Pu_2O_3 (137 – 164 GPa) using DFT+U [29]. Concerning the A-type structure the bulk modulus remains the same when U varies. The bulk moduli have never been neither calculated nor experimentally determined in Am_2O_3 C-type or A-type structures and our values are then a first prediction of Am_2O_3 bulk moduli. Indeed, owing to the good agreement of our computed lattice constants with the experimental data we are also confident on the reliability of the calculated bulk moduli.

Like for AmO_2, we compute the Am_2O_3 formation enthalpies of both A-type and C-type structures i.e. the energy related to the $2\,Am + \frac{3}{2}\,O_2 \longrightarrow Am_2O_3$ reaction (see Table 3.8). For the A-type, we observe that the correction applied in the energy of the O_2 molecule allows to obtain an energy roughly smaller than 5% off the experimental data [21]. For C-type structure, our computed value -16.53 eV±1% constitutes a prediction as it is the first determination to the best of our knowledge (where

Table 3.8: Calculated lattice parameters, band gap, magnetic moment and bulk modulus (B_0) of both hexagonal A-type and bcc C-type Am_2O_3 structure. These properties are compared to experimental available data as well as theoretical ones. In parenthesis: formation enthalpy estimated using a total energy for O_2 equal to $2E_{tot}(O) + E_{bind}(O_2)$, where E_{tot}(O) is the total energy of the O atom (spin-polarized, no symmetry) and $E_{bind}(O_2)$ the experimental binding energy of the O_2 molecule.

Comp.	Method	a(Å)	b(Å)	c(Å)	Gap (eV)	$\mu_{mag}(\mu_B)$	B_0(GPa)	ΔH_f (eV)
	GGA+U (5 eV)	3.87	3.87	5.96	2.85	6.1	139	-16.04(-17.35)
	GGA+U (6 eV)	3.87	3.87	5.98	3.29		139	-15.91(-17.20)
A-type	HSE06	3.77	3.77	6.04	2.20	6.2		
	GGA+U^a				2.60	5.9		
	Exp.[c]	3.82	3.82	5.98				-17.52[d]
	GGA+U (5 eV)	11.17	11.71	11.21	1.17	6.1	100	-15.24(-16.53)
C-type	GGA+U (6 eV)	11.17	11.17	11.21	1.25	6.2	135	-15.06(-16.35)
	Exp.[c]	11.02	11.02	11.02				

[a]Reference [14].
[b]Reference [94].
[c]Reference [3].
[d]Reference [21].

1% represents the relative error attributed to the GGA+U method compared to the experimental data, assuming that this error is almost the same as in A-Am_2O_3 or AmO_2). This value is one of the data on the C-type structure needed for the CALPHAD method [19] to better refine the phase diagram of the Am-O system. Indeed, for the moment, this phase is not included in the CALPHAD model of the Am-O system due to the lack of data [19].

3.8 Conclusion

In this chapter, we report results yielded by DFT+U calculations on the ground-state properties of americium dioxide and its sesquioxides. Our study contributes to establish fundamental bulk properties of americium oxides either unknown up to now or poorly known. We highlight that the presence of metastable states in DFT+U calculations can account for the discrepancies observed in the literature for AmO_2 regarding the elastic constants as well as the evolution of the band gap as a function of the U parameter of the DFT+U. We show that the ground state can be reached by imposing occupation matrices at the beginning of calculations. We observe a slight difference between the lattice constants ($a \neq b \neq c$) when crystal symmetry is not imposed but the cell volume remains very close to the case in which the crystal symmetry is taken into account. Moreover, in both cases, the Am^{4+} magnetic moments are very close to each other, as are the band gaps (1.1±0.2 eV). Finally, the density of states and the isotropic contributions to the dielectric properties (trace of Born effective charge and dielectric tensors) are unchanged by the loss of symmetry.

We calculate several bulk properties of AmO_2 and Am_2O_3 such as structural, elastic, energetic, electronic and magnetic properties as a function of U and J parameters, as well as dielectric and temperature dependant properties. Our results show a good agreement with the available data (experimental and computed). For AmO_2, the values (U,J) = (6.00 eV,0.75 eV) are those providing the best description of bulk properties

by comparison to the available experimental data. We provide for the first time several bulk properties such as magnetic and elastic (elastic constants) properties as well as the static dielectric constant of americium dioxide, which were unknown up to now.

Concerning americium sesquioxides, we find the hexagonal A-type to be the most stable structure at low temperature. This result is the first theoretical confirmation (in agreement with the CALPHAD calculations reported by Gotcu-Freis *et al.* [13]) of the stability at low temperature of the hexagonal A-type structure of Am_2O_3, the phase diagram of which is still controversial. Furthermore, the structural properties computed in this study are very close to the experimental results. We provide for the first time the internal structural parameters for the hexagonal structure, which can be used as reference for future works. We also predict the bulk modulus of both bcc C-type cubic and A-type hexagonal structures as well as the band gap and the formation enthalpy of the bcc C-type. We highlight that the U=6 eV and J=0.75 eV values probably tend to overestimate the band gap of the sesquioxide but do not affect other bulk properties.

The first-principles study proposed in this chapter paves the way for an optimal use of the GGA+U approximation to study AmO_2 defective supercells (see Chap. 4) since the defect properties in AmO_2 have been never investigated and can be extended to study more complex materials like (U,Am)O_2 mixed oxides (see Chap. 5).

Chapter 4

Study of atomic and electronic point defects in AmO_2

After implementing the DFT+U method for americium oxides, the main goal of this chapter is to investigate the stability and migration mechanisms of electronic and atomic point defects in americium dioxide. Note that literature is blank concerning defect properties in AmO_2.

Contents

4.1 Introduction

As mentioned is Chap. 3, AmO_2 is an insulating oxide with a fluorite structure (like PuO_2 and UO_2), having a bandgap of 1.3 eV [14]. This material is known to be submitted to self irradiation effects, namely α-decay. Self-irradiation induces ballistic effects and associated elastic collisions which lead to atomic displacements and thus damage such as defect formation [37], and lattice parameter expansion [34–36]. Self-irradiation damage in AmO_2 were the subject of very few study in the literature. For instance, some authors have investigated the self-irradiation effect on structural properties of Am-bearing oxides using X-Ray Diffraction [75]. Furthermore, other authors have carried out studies on He bubbles and the nature of the defects induced by α-decay in AmO_2 using Transmission Electronic Microscopy (TEM) [126]. However, no study to our knowledge has been conducted on elementary mechanisms occurring under self-irradiation such as formation and migration of electronic and atomic point defects. Yet, these properties are also essential to understand the microstructure evolution of a material.

Beside the possible creation of point defects by self-irradiation effects (which is a non-equilibrium phenomenon), we note that the Am-O phase diagram has been shown to be rather complex. Americium oxides are mixed valence compounds, in which Am may exist in the two charge states +III (in Am_2O_3) and +IV (in AmO_2). There is however a strong tendency for AmO_2 to the departure from stoichiometry, and the possibility of intermediate phase between AmO_2 and Am_2O_3 (see the phase diagrams shown in Chap. 2). AmO_2 is thus a system that may easily deviate from the nominal O/Am ratio = 2, and in which oxygen vacancies are easily formed at equilibrium (thus independently from self-irradiation effects).

In an ionocovalent insulator, any point defect (vacancy, interstitial, etc ..) can generally be described either as an acceptor or as a donor. More explicitly, a defect releases holes or electrons, which can possibly be localized on one single atom (especially in the case of mixed valence), leading to a so-called small polaron. It is therefore strongly probable that oxygen vacancies in AmO_2 are associated with small electron polarons.

In this chapter, we investigate the chemistry of point defects in AmO_2. However, since AmO_2 is the most oxidized form of americum, which has rather the tendency to lose oxygen, and since in most real conditions, americium in mixed oxides exhibits the tendency to be reduced to Am^{3+}, the study of acceptor defects is not a relevant issue. We therefore restrict our investigations to native donor point defects, i.e. oxygen vacancies and americium interstitials, and to the behaviour of excess electrons released in the lattice. Our computational approach is described in Sec. 4.2. Sec. 4.3 presents the results on oxygen vacancies and americium interstitials. Some basic concepts about small polarons in insulators are briefly reviewed in Sec. 4.4 before presenting the results about the electron polarons in AmO_2 in Sec. 4.5. Sec. 4.6 sets up a simple defect model to discuss how our *ab initio* results can be used to predict defect concentrations in AmO_2.

4.2 Computational scheme

4.2.1 Defect formation energies

The formation energy of a point defect X in charge state q in AmO_2 is given by:

$$E_f(X,q) = E_{tot}(X,q) + E_{corr} - E_{tot}(AmO_2) - \sum_i \Delta n_i \mu_i + q\mu_e \tag{4.1}$$

where E_{tot}(X,q) is the total energy of the AmO_2 supercell containing the defect X with charge q and $E_{tot}(AmO_2)$ is the energy of the supercell without defects (perfect system). $\Delta n_i = n_i$(in defective system) - n_i(in perfect system) denotes the change in the number of atomic species i upon the defect formation. μ_i is the chemical potential of species i. It is a variable that reflects the fact that the materials can be grown in i-rich or i-poor external conditions. μ_e is the electron chemical potential and E_{corr} denotes the set of corrections used for charged supercells [127].

The chemical potentials of Am and O cannot be completely determined through first-principles calculations because they depend on the external conditions (e.g. μ_O depends on temperature and oxygen partial pressure P_{O_2}), but knowledge of the stability domain of the AmO_2 oxide (with respect to other phases and pure elements) provides an accessible range for these chemical potentials compatible with existence of bulk AmO_2. The formation enthalpy of AmO_2 can be obtained as:

$$\Delta H_f^{Amo_2} = \mu_{AmO_2}^{bulk} - \mu_{Am}^{Am_{met}} - 2\mu_O^{O_2} \tag{4.2}$$

with

$$\mu_{AmO_2}^{bulk} = \mu_{Am} + 2\mu_O \tag{4.3}$$

where $\mu_{Am}^{Am_{met}}$ is the Am chemical potential in its standard state (metallic α-americium), and $\mu_O^{O_2}$ is the O chemical potential in its standard oxygen gas state. We will now consider the chemical potentials of the elements with respect to their standard state:

$$\begin{cases} \Delta\mu_{Am} = \mu_{Am} - \mu_{Am}^{Am_{met}} \\ \Delta\mu_O = \mu_O - \mu_O^{O_2} \end{cases} \tag{4.4}$$

Our purpose here is to find the relative stability domain of AmO_2 with respect to O_2, α-Am and americium sesquioxide Am_2O_3. The conditions of stability of AmO_2 are :

$$\begin{cases} \Delta\mu_O < 0 \\ \Delta\mu_{Am} < 0 \\ \Delta H_f^{AmO_2} = \Delta\mu_{Am} + 2\Delta\mu_O \\ \Delta H_f^{Am_2O_3} \geq 2\Delta\mu_{Am} + 3\Delta\mu_O \end{cases} \tag{4.5}$$

Here, for consistency, we take the GGA+U formation enthalpies computed in Chap. 3 $\Delta H_f^{Amo_2}$ = -9.15 eV and $\Delta H_f^{Am_2O_3}$ = -17.20 eV. The graphic solution of this set of

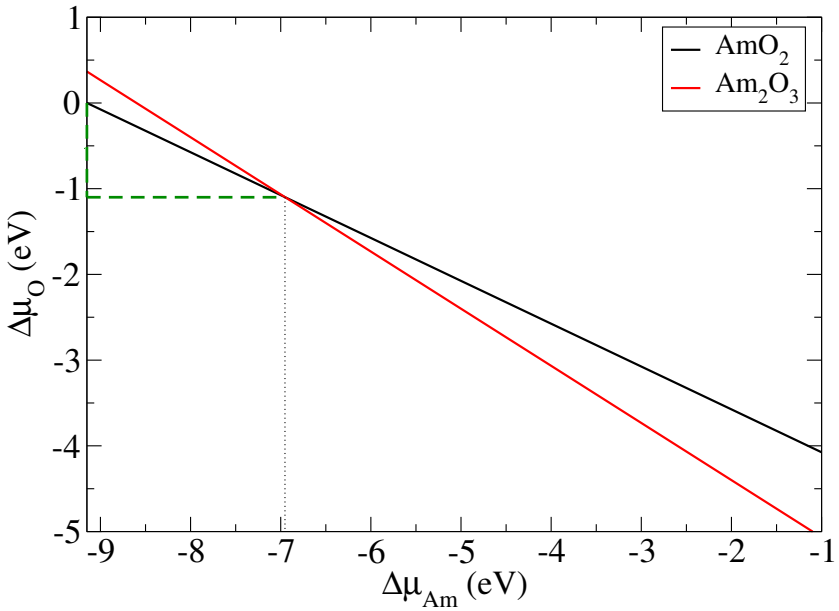

Figure 4.1: $\Delta\mu_O$ as a function of $\Delta\mu_{Am}$ for different phases of the Am-O system. This figure is obtained by solving the set of Eqs. 4.5. For AmO_2, ΔH_f is -9.15 eV [21] and for Am_2O_3 -17.20 eV [21] which are values obtained in Chap. 3 (see Tab. 4.2.2).

equations is plotted on Fig. 4.1. From this figure, the accessible range for $\Delta\mu_{Am}$ and $\Delta\mu_O$ (in eV) regarding the stability of AmO_2 relative to Am_2O_3 and the pure elements, can be given by:

$$-1.10 \leq \Delta\mu_O \leq 0 \tag{4.6}$$

$$-9.15 \leq \Delta\mu_{Am} \leq -6.95 \tag{4.7}$$

Assuming $\Delta\mu_{Am}$ and $\Delta\mu_O$ are imposed by the external conditions, we can now access to μ_{Am} and μ_O using Eq. 4.4. DFT total energies are used to estimate μ_i for O and Am in their standard state i.e. $2\mu_O^{O_2} = E_{O_2}^{tot}$ and $\mu_{Am}^{Am_{met}} = E_{\alpha-Am}^{tot}$. However, the Generalized Gradient Approximation, which is used in this work, is known to overbind the O_2 molecule by about 1 eV. To overcome this problem, the total energy of the oxygen atom is used instead, and combined with the experimental value for the binding energy $E_{O_2}^{coh}$ as follows:

$$\mu_O^{O_2} = 2E_O^{tot} + E_{O_2}^{coh} \tag{4.8}$$

where $E_{O_2}^{coh}$ (< 0) is the experimental binding energy of O_2 (-5.21 eV) [128]. Note that for consistency, the formation enthalpies used for AmO_2 and Am_2O_3 also include this correction [33].

In this study, we will consider two limiting cases, depending on the external conditions and corresponding to O-rich and O-poor conditions. The maximal value allowed

Table 4.1: conditions (O-poor and O-rich) considered in the present work.

	O-poor	O-rich
$\Delta\mu_O$	-0.75	-0.29
$\Delta\mu_{Am}$	-7.65	-8.56

for $\Delta\mu_O$ is 0. However, this oxygen chemical potential is in practise unreachable, since it corresponds to extremely high oxygen pressure or very low temperatures: using ideal gas law [129], we find that $\Delta\mu_O = 0$ corresponds to T=300 K and $P_{O_2} \sim 1.0\times10^9$ atm or T $\sim$ a few K and $P_{O_2} = 1.0$ atm. Thus, we use instead the ambient conditions T=300 K and $P_{O_2} = 0.2$ atm to define our O-rich conditions. This corresponds to $\Delta\mu_O$ = -0.29 eV.

From Eq. 4.6, the minimal value allowed for $\Delta\mu_O$ is -1.10 eV. However, we cannot use this value to define the O-poor conditions because it leads to formation energies of neutral vacancies very close to zero ($\sim$ 0.04 eV). Combined with the formation energies of the electron polaron presented below, this leads to an inconsistency because there is no region of the band gap over which all the defect formation energies would be positive. Consistency is recovered only for $\Delta\mu_O \gtrsim$ -0.93 eV. In clear, there is a small interval of the chemical potential [-1.10; -0.93]eV over which oxygen vacancies and electron polarons form in very large quantity (i.e. AmO_2 does not exist any more), and yet AmO_2 should be more stable than Am_2O_3. An explanation for this gap could be the possible existence of a phase with intermediate stoichiometry between AmO_2 and Am_2O_3, in relation with the easy departure from stoichiometry in AmO_2. As noticed in the introduction, the Am-O phase diagram as determined experimentally is rather complex [13, 16]. In particular a phase with stoichiometry $AmO_{1.62}$ is reported in the literature above 620 K, with a complex cubic structure [4,16], probably isostructural to C-type Am_2O_3. The existence of this phase for oxygen chemical potentials intermediate between those that stabilize Am_2O_3 and AmO_2 could explain why oxygen vacancies and electron polarons are found to form in very large concentration for $\Delta\mu_O \in$ [-1.10 eV; -0.93 eV].

As O-poor conditions, we will thus consider the following conditions: $\Delta\mu_O$ = -0.75 eV, which corresponds to T $\sim$ 680 K and $P_{O_2} = 0.2$ atm. The external conditions chosen to plot the defect formation energies in this work are summarized in Tab. 4.1.

The formation energy of the electron polaron is defined as:

$$\Delta E_f(e',\,-1) = E_{tot}(AmO_2 + e',\, q=-1) - E_{tot}(AmO_2) - \mu_e \tag{4.9}$$

where $E_{tot}(AmO_2 + e',\, q=-1)$ is the total energy of the supercell containing one self-trapped electron polaron with the charge q=-1.

The calculation of defect formation energies according to Eq. 4.1 involves a correction term E_{corr}, which is the sum of the monopole part of the Makov-Payne correction [130] (using the static dielectric constant calculated in Chap. 3, see Tab. 4.2.2) and of a band alignment performed using the *6s* semicore levels of americium, as in Refs. [131, 132].

The electron chemical potential μ_e is referenced to the valence band maximum (VBM), E_{VBM}, and is written as $\mu_e = E_{VBM} + \epsilon_F$. The GGA+$U$ Kohn-Sham band

gap from Chap. 3 is used (1.1 eV, see Tab. 4.2.2).

The energy of the VBM is calculated by [133] $E_{VBM} = E_{tot}(AmO_2) - E_{tot}(AmO_2, +1)$, with $E_{tot}(AmO_2, +1)$ being the energy of a perfect supercell in which an electron has been removed (thus emptying a delocalized Kohn-Sham state at the VBM). Also, we can estimate the energy of the conduction band minimum (CBM) in the same way, $E_{VBM} = E_{tot}(AmO_2, -1) - E_{tot}(AmO_2)$, with $E_{tot}(AmO_2, -1)$ being the energy of a perfect supercell in which an electron has been added (thus filling a delocalized Kohn-Sham state at the CBM). The band gap may then be obtained as $E_{CBM} - E_{VBM}$ and is found here to be 1.10 eV, thus similar to the Kohn-Sham band gap.

4.2.2 Density-Functional Theory calculations

A. DFT functionals

Our DFT calculations are carried out using ABINIT package [134, 135]. The exchange and correlation effects are described by the Generalized Gradient Approximation (GGA) parameterized by Perdew, Burke and Ernzerhof [112]. The rotationally invariant form by Liechtenstein *et al* [53] is used for the electron interaction energy related to the Hubbard term (E_{Hub}). For the double counting expression, we have chosen the "full localized limit" (FLL) [28, 59, 113], because the ground state of americium oxides is insulating and thus, orbitals occupation of *5f* electrons is close to one or zero.

B. Numerical parameters

The onsite Coulomb terms U and J used for Am *5f* orbitals are (6.00 ; 0.75) eV. Indeed, in Chap. 3 by computing several bulk properties of AmO_2 as a function of the U and J parameters and comparing with available experimental data, we showed that ($U = 6.00$; $J = 0.75$) eV can be used to provide a good description of AmO_2. Results are obtained using a plane-wave cutoff energy of 871 eV. According to our convergence tests, this parameter leads to a precision lower than 1 meV per atom on physical energies (total energy differences). A 96-atom supercell ($2 \times 2 \times 2$ in terms of the conventional *fcc* fluorite unit cell of AmO_2) is used, with various point defects inserted inside: oxygen vacancy, americium interstitial and electron polaron.

The calculations are done using a $2{\times}2{\times}2$ k-point mesh to sample the Brillouin Zone associated with the supercell, generated by the Monkhorst-Pack [114] method, which is sufficient for an energy convergence much better than 0.3 meV per atom on the insulating supercells. In the case of the metallic supercells (delocalized electron, delocalized hole), however, the k-point mesh is increased to $4{\times}4{\times}4$. We performed structural optimizations keeping fixed the lattice vectors (equal to the theorical values yielded by GGA+U) of the cell, until the forces acting on the atoms become smaller than $2.0{\times}10^{-4}$ Ha/bohr ($\sim$ 0.01 eV/Å). In other words, only atomic positions are relaxed.

The supercell is constructed by doubling in the three directions the unit cell from Chap. 3, after full structural relaxation without accounting for symmetries. Accordingly, the $5f$ occupation matrix denoted as M_3^{nosym} inChap. 3 is used throughout

this work to initialize all the supercell calculations. For the simulation of the electron polaron, a specific methodology is applied (see Sec. 4.5).

For the charged supercells, the extra charge is compensated by a uniform background, as usually done for the compensation of charged defects in insulator compounds. Oxygen vacancies are studied in charge states q = 0, +1, +2, americium interstitials in charge states q=0, +1, +2, +3 and +4, and the electron polaron is simulated by adding an extra electron in the supercell (q = -1).

C. Magnetic configuration

In all calculations, we turn on spin polarization and switch off all symmetries. The 1k antiferromagnetic (AFM) state is assumed for AmO_2, since we showed in Chap. 3 that, although the magnetic ground state of AmO_2 is more probably a 3k AFM order below the Néel temperature (8.5 K), 1k AFM order (without taking relativistic effets into account) can be used as a good approximation. Thus, we do not include spin-orbit coupling (SOC) in our calculations, and perform all our calculations in the framework of collinear magnetism (i.e. the magnetization is a scalar field). Note that taking SOC into account is computationally demanding and prevents the use of supercells sufficiently large for an accurate enough description of the properties of defective supercells. Furthermore, it has been shown in UO_2 [40] that the spin-orbit coupling results in energy corrections on order of the tenth electron volts, whereas the energies we are dealing with here are on the order of electron volts.

Tab. 4.2.2 gathers important data on AmO_2 and Am_2O_3 compounds obtained in chap. 3 and used throughout the current study.

Table 4.2: Lattice parameter, band gap, formation enthalpy, magnetic moment and static dielectric constant ϵ_S of AmO_2 and Am_2O_3 obtained in Chap. 3 in comparison with other studies. Results were obtained using GGA+U with U = 6 eV and J = 0.75 eV.

		a(Å)	Band gap (eV)	H_f (eV)	μ_{mag} (μ_B)	ϵ_S
AmO_2	GGA+U*	5.44	1.1	-9.15	5.1**	16.8
	Other works	5.42[a] ; 5.37[b]	0.8[a] ; 1.3[c]	-9.66[d]	4.8[e]	-
Am_2O_3	GGA+U*	11.18	1.25	-17.20	6.2	-
	Other works	11.02[b]	-	-17.52[d]	-	-

*Chap. 3

** using 5f occupation matrices and no symmetry (5.2 from integration of electron density inside PAW atomic spheres) [33]

[a]Ref. [80]

[b]Ref. [3]

[c]Ref. [14]

[d]Ref. [21]

[e]Ref. [7]

4.3 Oxygen vacancies and americium interstitials

We begin by a description of the donor point defects in AmO_2, i.e. oxygen vacancies and Am interstitials.

4.3.1 Oxygen vacancies

The oxygen vacancy is double donor defect. It liberates two electrons. In its charge-neutral state (V_O^X), these two extra electrons are localized on two of the four adjacent Am atoms, giving rise to the formation of two Am^{3+} ions in the close vicinity of the vacancy. If these two electrons unbind from the vacancy and migrate far away in the lattice, they leave behind a charged (ionized) oxygen vacancy $V_O^{\bullet\bullet}$ or at least a partially ionized oxygen vacancy $V_O^{\bullet}$ if one of the electrons remains bonded to the vacancy. Indeed, the calculation of $V_O^{\bullet}$ provides only one Am^{3+}, while the fully ionized oxygen vacancy $V_O^{\bullet\bullet}$ is associated with no Am^{3+} in the supercell. Note that Am^{3+} are easily identified by their spin magnetic moment: our GGA+U calculations provide a moment of $\sim 5.8\ \mu_B$ for Am^{3+}, versus $\sim 5.1\ \mu_B$ for Am^{4+} (in this chapter, the magnetic moments are evaluated using the $5f$ occupation matrices on Am atoms).

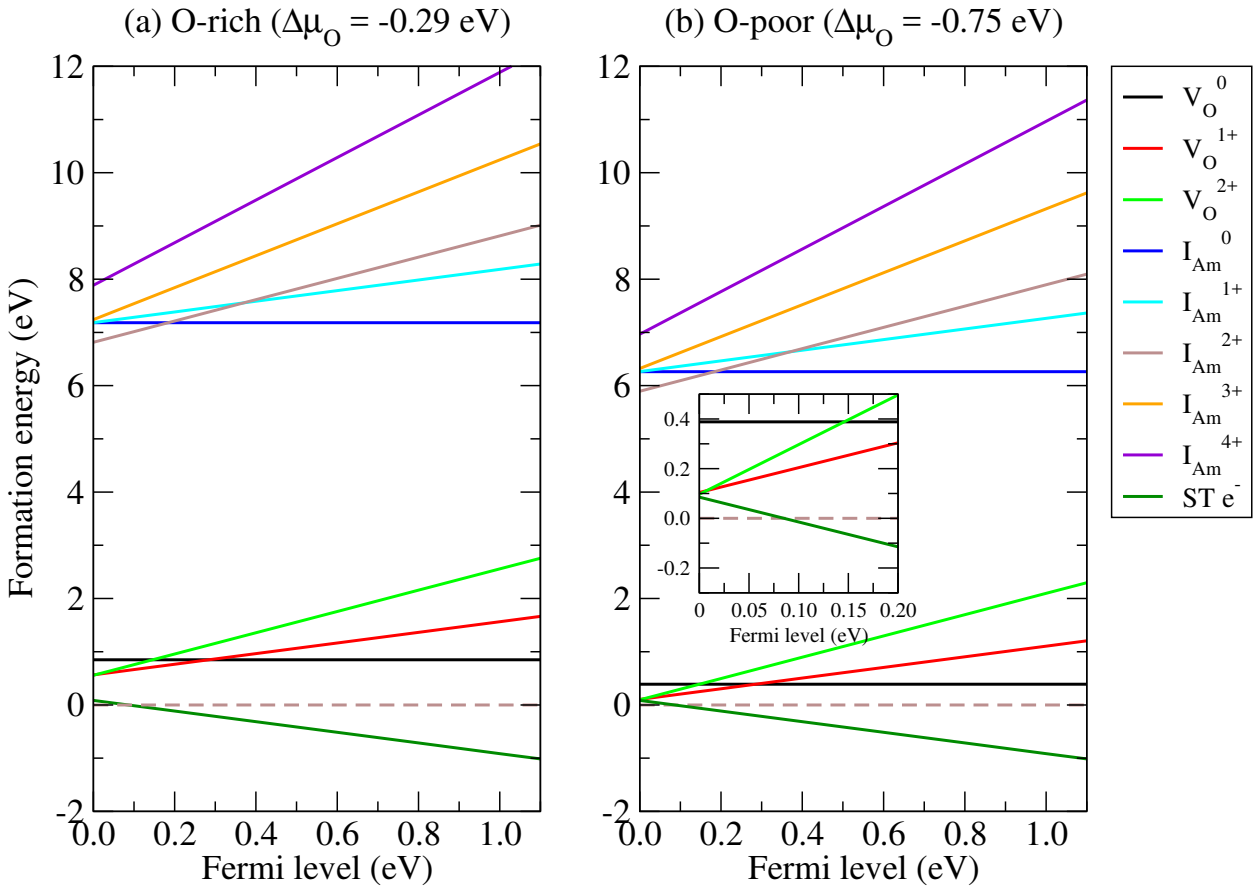

Figure 4.2: Formation energy of the oxygen vacancy, americium interstitial and self-trapped electron polaron in their possible charge states, as a function of the Fermi level in the band gap of AmO_2 for (a) oxygen-rich and (b) oxygen-poor conditions. ST e^- denotes the self-trapped electron polaron. Inset (in right panel): zoom on the VBM region.

Fig. 4.2 displays the formation energies of the oxygen vacancies V_O^X, $V_O^{\bullet}$ and $V_O^{\bullet\bullet}$ as a function of Fermi level in the two external conditions described above: oxidizing (O-rich) and reducing (O-poor). From these formation energies, we can calculate the transition energy level between the O vacancy in charge state q and the same defect in charge state q'. It is defined as:

$$\epsilon_{\mathrm{V_O}}(q/q') = \frac{\Delta E_f(\mathrm{V_O}, q; \epsilon_F = 0) - \Delta E_f(\mathrm{V_O}, q'; \epsilon_F = 0)}{q' - q}, \tag{4.10}$$

where $\Delta E_f(\mathrm{V_O}, q; \epsilon_F = 0)$ is the formation energy of the O vacancy in charge state q, calculated for the Fermi level at the VBM [136] $\epsilon_{\mathrm{V_M}}(q/q')$ corresponds to the Fermi level at which the formation energies of the defect in charge states q and q' cross.

We find here: $\epsilon_{\mathrm{V_O}}(+2/+1) = 0.01$ eV and $\epsilon_{\mathrm{V_O}}(+1/0) = 0.28$ eV. These transition levels are very far from the CBM (~ 1 eV or more), indicating that the oxygen vacancy in AmO_2 is a *deep double donor defect*.

Fig. 4.3 (d)(e)(f) display the electronic density of states (e-DOS) of the supercell containing the charge-neutral oxygen vacancy. Panel (d) plots the total e-DOS. It can be seen that two occupied states with opposite spin appear in the band gap, but at very low energy, close to the VBM (they are spotted with green arrows), which emphasizes the picture of a *deep donor* for the O vacancy in AmO_2. Panel (e) plots the e-DOS projected on the $5f$ orbitals of the two Am^{3+} which are next to the vacancy and that carry the two electrons released by the defect, while panel (f) plots the e-DOS projected on the $5f$ orbitals of two Am^{4+} (with opposite spin) of the supercell (their projected e-DOS are typical of those of the other Am^{4+}). We observe that the occupied $5f$ orbitals of Am^{4+} are localized down in the valence band, a feature that has already been pointed out in Chap. 3. This positionning is noticeably changed for Am^{3+}, since adding one electron in a $5f$ orbital has two effects: first, the energy of the newly occupied state strongly decreases from the CBM down to the VBM and second, at the same time, the energy of the other $5f$ states increases towards the VBM.

Am^{3+} has thus the tendency to accumulate the occupied $5f$ states at the VBM, which can be seen as a precursor to the formation of Am_2O_3, which is a Mott insulator with a band gap $Am\ 5f \rightarrow Am\ 5f$ (in contrast to AmO_2 which rather behaves as a charge-transfer insulator with a band gap $O\ 2p \rightarrow Am\ 5f$), as already explained in Chap. 3.

4.3.2 Americium interstitials

The americium interstitial I_{Am} liberates four electrons and is thus a quadruple donor defect. In the charge-neutral state, I^X_{Am} induces the formation of four trivalent americium Am^{3+} in the crystal. Upon charging the defect, the number of Am^{3+} in the supercell decreases accordingly (3 for $I^{\bullet}_{Am}$, 2 for $I^{\bullet\bullet}_{Am}$, 1 for $I^{\bullet\bullet\bullet}_{Am}$) up to the fully ionized Am interstitial $I^{\bullet\bullet\bullet\bullet}_{Am}$, that does not induce the presence of any Am^{3+}, as expected.

The formation energies of this defect in charges states q from 0 to +4 are plotted as a function of Fermi level on Fig. 4.2, superimposed to those of the oxygen vacancy. Only two of the studied charge states are found stable: $I^{\bullet\bullet}_{Am}$ and I^X_{Am}, with a transition energy level between them equal to $\epsilon_{\mathrm{I_{Am}}}(+2/0) = 0.18$ eV. Once again, this ionization energy is far from the CBM, which indicates that the Am interstitial is a deep donor, as the oxygen vacancy.

On the other hand, one can see (Fig. 4.2) that the formation energies of Am interstitials are several eV higher ($\sim$6 eV at ϵ_F=0.0 eV) than those of the oxygen vacancies, indicating that these defects are unlikely, and will never be present in the

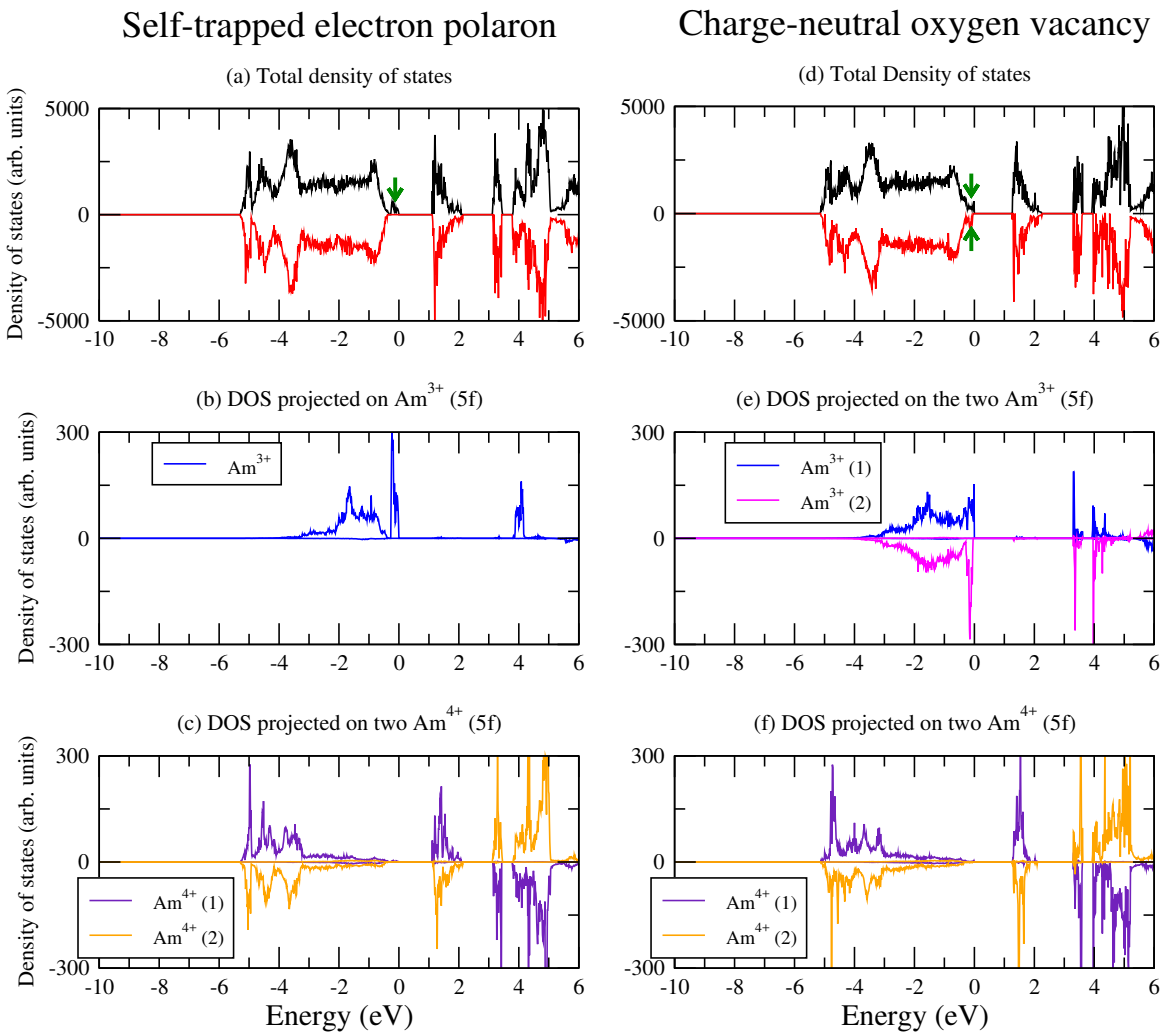

Figure 4.3: Electronic density of states. Left panels: supercell with the self-trapped electron polaron. Right panels: supercell with the charge-neutral oxygen vacancy. Top: total density of states. Middle: density of states projected on f orbitals of the Am^{3+} atoms of the supercell (one single Am^{3+} in the case of the polaron, two in the case of the vacancy). Bottom: density of states projected on f orbitals of two Am^{4+} with opposite spin of the supercell. In panels (a) and (d), the small green arrows spot the defect states (occupied in both cases). The Fermi energy (highest occupied states) is set at 0 eV. Positive values: spin up; negative values: spin down.

AmO_2 matrix. This suggests that the majority of the intrinsic donor defects in AmO_2 are the oxygen vacancies.

4.4 Self-trapped small polarons in insulators: basic concepts

Having described the donor point defects in AmO_2, we now investigate how the electrons released by these defects behave in the lattice, and more precisely, whether they can localize on single Am atoms far from the vacancies, under the form of small polarons. Before, however, we briefly review some basic concepts about small polarons

in insulators.

4.4.1 Self-trapping

A small polaron corresponds to the localization of an extra elementary charge (electron or hole) on a single atom in an insulating crystal, associated with a set of atomic distortions around it. In an insulator, these charges are generally released by some point defect. For example, in most oxide materials, the oxygen vacancy liberates two electrons. These two electrons can either stay localized very close to the vacancy (which is then said to be in the neutral state), or diffuse in the lattice, leaving behind them a doubly charged oxygen vacancy. Whether the vacancy is ionized or not depends on the electronic chemical potential μ_e. If one of these electrons, once released in the lattice, localizes on a single atom, the entity corresponding to this localized electron, with the associated lattice distortion is called a *small polaron*.

The mechanism by which an extra electron localizes on a single atom in the lattice is called *self-trapping*: this is a self-consistent mechanism along which the localization of the electron, and the appearance of distortions around it favor each other. Indeed the localization of the electron on one atom (which corresponds to a change in the oxidation state of the atom) creates a distortion all around, because it breaks the translational periodicity of the lattice. Moreover, this distortion is mostly the result of the electrostatic interaction between the localized electron and the surrounding polarizable matrix. The immediate environment is therefore radially polarized. In return, this polarization field creates on the polaronic site a deep electrostatic potential which favors the localization of the charge. Roughly speaking, the formation of a polaronic state (rather than a delocalized Bloch-like band state) takes place if the energy cost associated with the self-trapping distortion and the quantum confinement of the charge is compensated by the (favorable) interaction between the charge and the polarization field of the self-trapping distortion, a balance which is obviously system-dependent. It is important to understand that the charge localization and the self-trapping distortion are necessary to each other and cannot be dissociated in a small polaron. The formation of the polaronic state is schematically described on Fig. 4.4 (a),(b).

4.4.2 Diffusion

Under the effect of thermal fluctuations, small polarons may jump from an atom onto a nearest one. However, the physical mechanism that underlies this hopping is not the same as the one encountered in the hopping of (heavy enough) atoms. Indeed, atomic hopping is usually considered as resulting from a "thermal over-barrier" process, in which the potential energy barrier that separates one site from the other is overcome thanks to the thermal vibrations of the atoms themselves. But this is usually not the case for a small polaron, simply because a localized electron (or a hole) in its ground state is subject to a strong quantum confinement, associated to a strong quantization of its energy levels. At room or moderate temperatures, the excited states of the localized charge may lie too high, so that the localized charge, in many situations, does not undergo the thermal fluctuations and remains frozen in its ground state. Thus, the notion of "thermal over-barrier" for a localized electron (or hole) does not

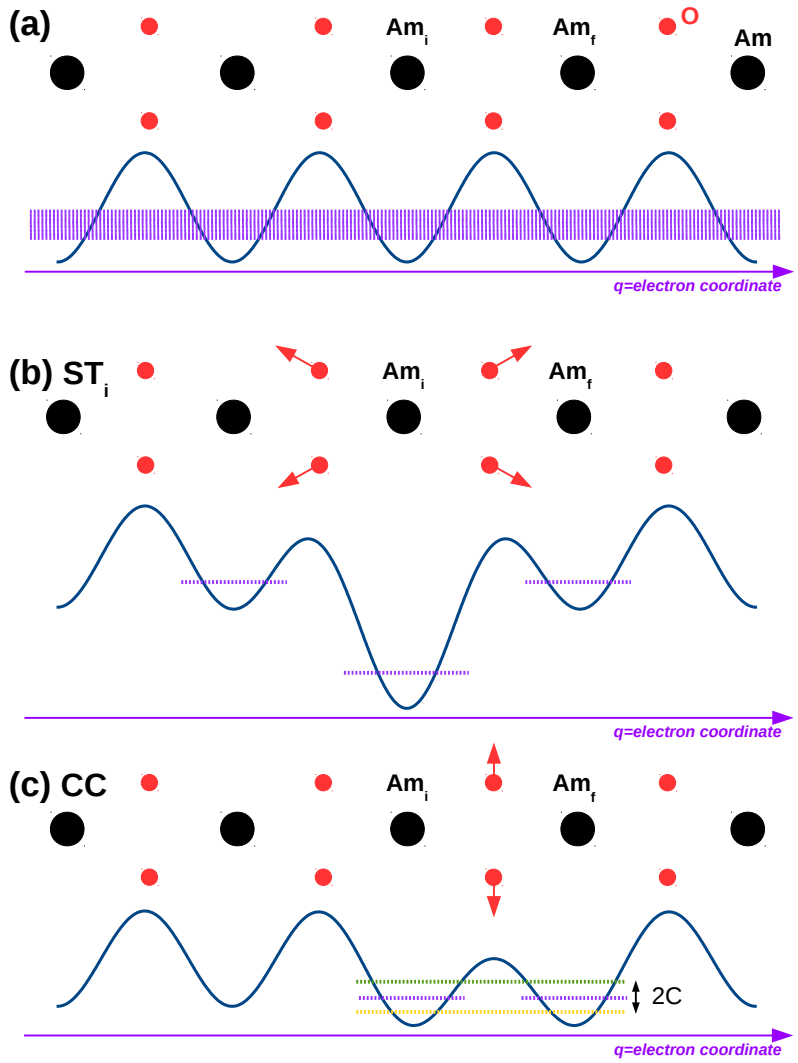

Figure 4.4: Schematic representation of the self-trapping process of an excess electron [22]. The blue line schematically represents the potentiel felt by the electron; (a) periodic undistorted crystal: the electron is delocalized throughout the crystal under the form of a Bloch wave and its eigenstates form a band (purple lines); (b) self-trapped state at site Am_i: the crystal is distorted around the particle (here the 1 st neighbour oxygens are pushed away, which is schematically featured by the red arrows), which makes the Am_i site more stable than the neighboring sites. Note that transfer by tunneling from Am_i site onto the neighboring sites is impossible. The polaron is the association of the particle localized at site Am_i and of the set of surrounding distortions; (c) coincidence configuration (CC) for polaron hopping from site Am_i onto site Am_f: the atomic distortions have been modified so that the electron feels a symmetric potential, the two (diabatic) ground levels in the two wells (Am_i and Am_f) are equalized (purple lines), making transfer by tunneling possible through the remaining barrier. The green/yellow lines represent the ground and 1 st excited adiabatic states of the electron, which are at coincidence separated by $2C$ (electronic coupling).

make sense in such a situation. And yet, small polaron hopping is known as being a thermally activated process, with a hopping rate being proportional to an Arrhenius term e^{-E_c/k_BT}.

In fact, the process by which the small polaron hopping takes place involves thermal fluctuations, but those of the lattice atoms. With temperature, the atomic vibrations occurring around the polaron may, occasionally, lead to specific atomic configurations in which the self-trapping is weakened, and more precisely, confined to a pair of neighboring sites (instead of one), so that the energy of the localized electron is the same

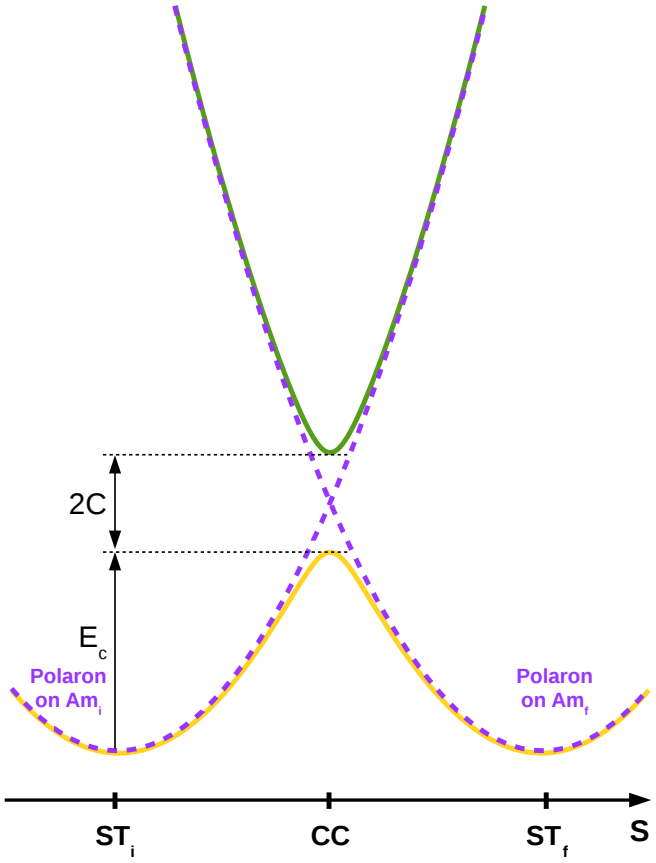

Figure 4.5: Typical energy profile along the hopping path of a small polaron, as a function of the reaction coordinate, denoted here as S. S is an atomic distortion that drives the lattice from the initial self-trapped configuration (ST_i) to the final self-trapped one (ST_f), passing by a coincidence configuration at the transition point (CC). It is important to distinguish this energy profile (function of an atomic coordinate) from the ones drawn on Fig. 4.4(b)(c), which corresponds to the electronic potential (i.e. seen by the excess electron) at fixed lattice configuration (either ST_i or CC). E_c is the coincidence energy, which plays the role of the activation energy for the hopping process of the small polaron.

whether it is localized on the initial site or on the final site (see Fig. 4.4 (c)). Such an atomic configuration, in which the energies of the ground states in the initial well and in the final well are in coincidence, is called a "coincidence configuration" (CC) [137]. These specific lattice configurations are the ones in which the hopping of the excess electron effectively takes place, because they are favorable to a resonant tunneling between the two (diabatic, i.e. considered as constrained to remain localized on one site) ground states (the charge feels a symmetric double well at coincidence). The mechanism by which the electron transfers onto the nearest site is thus intrinsically quantum (tunneling), but this tunneling takes place in a specific configuration created by the thermal fluctuations of the lattice atoms.

There is obviously an infinity of such coincidence configurations, and many of them can play a role in the hopping. However, very often in polaronic hoppings, one single coincidence configuration is relevant (that of lowest energy [137]). It plays the role of the transition state for the polaronic hopping process. Let us call its energy E_c (with respect to the self-trapped state of the polaron). Since this configuration is reached by thermal fluctuations, the rate at which it is visited is therefore proportional to e^{-E_c/k_BT},

which explains the Arrhenius form of the polaronic hopping rate.

The reaction coordinate for the hopping of the polaron consists therefore in the set of atomic distortions that drives the system from the initial self-trapped configuration (denoted as ST_i) up to the final self-trapped one (denoted as ST_f), transiting along the path by the coincidence configuration (CC). Here we denote this (atomic) reaction coordinate as S. The set of atomic distortions along S may follow one or several phonon modes of the lattice. For simplicity, we consider that only one phonon mode, with pulsation ω_S, contributes to the reaction coordinate S. $\frac{\omega_S}{2\pi}$ can therefore be considered as an attempt frequency for the hopping of the small polaron.

The energy of the system as a function of S is schematically plotted on Fig. 4.5. The dashed curves on this figure represent the energy of the system with the excess electron in its ground state, considered as strictly localized on the initial or on the final atom. They are often called *diabatic* curves (or diabatic surfaces) and, as explained above, they cross at CC. However, at coincidence, the two electronic diabatic ground states are usually coupled, and the electronic coupling C breaks the degeneracy, so that the two adiabatic levels (i.e. the true electronic eigenstates within the adiabatic approximation) are split by $2C$. Taking into account the coupling C, the energy of the system as a function of S is represented by the *adiabatic* curves (or adiabatic surfaces, solid lines on Fig. 4.5). Note that the adiabatic curves deviate from the diabatic ones only around the coincidence point

We have said that polaronic hopping takes place in a coincidence configuration, by a tunneling of the charge through the barrier felt at coincidence. Indeed, in a symmetric double well, a quantum particle initially localized in one of the two wells with an energy smaller than the barrier oscillates, through a tunneling motion, with a typical time $\hbar/2C$, where C is the electronic coupling. $2C$ is the energy separation between the ground and 1st excited (adiabatic) states in the double well at coincidence. However, the coincidence event has a certain timescale itself, and obviously, the hopping event does take place only provided the typical time for tunneling through the barrier is smaller than the coincidence timescale. Thus, two opposite limit behaviours may exist:

- If the typical time for tunneling through the barrier at coincidence is much smaller than the coincidence timescale, polaronic hopping is automatic at each coincidence event. In other words, it is as if the polaron had the time to adjust its state to the atomic configurations: the hopping is thus said to be "adiabatic", because the system stays on the adiabatic surface all along the transfer (the adiabatic approximation is always true). The hopping rate in that case takes the form $k = k_0 e^{-E_c/k_B T}$, k_0 being the typical frequency of the phonon mode that drives the system to the coincidence ($\sim 10^{13}$ s^{-1}).

- If, on the contrary, the typical time for tunneling through the barrier at coincidence is much larger than the coincidence timescale, polaronic hopping is not automatic at all, and many occurrences of the coincidence configuration can be necessary before the jump takes place. The prefactor of the jump rate in that case is controlled, not only by the phonons, but also by the probability for the charge to transfer through the barrier at coincidence, which is a typical quantum mechanism, and will involves the coupling C in the expression of the prefactor. The prefactor may in that case be much smaller than the phonon frequencies ($k_0 << 10^{13}$ s^{-1}). In that case, since the polaronic charge is not fast enough to adjust its

state to the atomic configuration and remains on one side of the symmetric barrier at coincidence (instead of adjusting to the true adiabatic ground state which is delocalized over the two wells), the jump is said to be "non-adiabatic", because the system leaves the adiabatic surface around CC (the adiabatic approximation is not true at CC).

In order to know if the transfer takes place adiabatically or not, it is possible to calculate the Landau-Zener adiabaticity criterion:

$$\gamma_{th}(T) = \frac{2\pi}{\hbar\omega_S}\sqrt{\frac{\pi}{E_S k_B T}}C^2, \tag{4.11}$$

in which ω_S is the pulsation of the lattice phonon mode that drives the system from the self-trapped configuration up to the coincidence, and E_S is the reorganization energy, that may be approximated by $4E_c$ in an harmonic model.

$\gamma_{th} >> 1$ corresponds to the adiabatic case, the prefactor of the transfer rate is then $k_0 = \frac{\omega_S}{2\pi}$. In contrast, $\gamma_{th} << 1$ corresponds to the non-adiabatic situation described above.

4.5 Electron polaron

The results of Sec. 4.3 clearly indicate that the donor defects in AmO_2 tend to form Am^{3+} cations thanks to the localization of the electrons released by the defect on single Am atoms. Note that this local change of oxidation state of americium is in agreement with the electronic density of states of AmO_2, for which the CBM has been shown to be formed by Am $5f$ states (see e.g. our Chap. 3): the electrons released by the donor O vacancy thus come to populate these states, forming Am^{3+}.

However, instead of localizing on single atoms in the vicinity of the defect, the excess electrons can escape and diffuse through the crystal. Here two limit behaviours are *a priori* possible: either they are delocalized, under the form of a Bloch wave (conduction electron, Fig. 4.4 (a)), or they remain localized on another single Am atom, which corresponds therefore to a self-trapped electron polaron (Fig. 4.4 (b)).

4.5.1 Computation of the self-trapped electron polaron in AmO_2

It is easy to compute the delocalized state of an excess electron in the supercell (we just add one electron and compute the total energy of the system without performing any structural optimization). But the computation of the self-trapped electron polaron is more complex. We follow the methodology described in Ref. [22] (hereafter recalled). However, we also have to test among the different possible occupation matrices for the $5f$ orbitals of the Am atom that receives the excess electron.

First we select one Am atom in the supercell, that will receive the excess electron (and thus will be reduced from Am^{4+} to Am^{3+}). For each of the possible $5f$ occupation

matrices of Am^{3+} (there are 7 possibilities corresponding to placing 6 electrons among the 7 orbitals of a given spin channel), we use the following two-step procedure:

- We first perform a structural optimization with the *5f* occupation matrices on all the Am atoms kept strictly constant along all the electronic self-consistent cycles. The occupation matrix used here for the Am^{4+} *5f* electrons is the one obtained in Chap. 3, i.e. the matrix called M_3^{nosym}. This imposes that the chosen Am atom carries the charge +3 while all the other Am carry the charge +4, with the good orbitals occupied, and creates around Am^{3+} the appropriate self-trapping distortion. At the end, the lattice around the polaron has relaxed and is characteristic of a self-trapping distortion able to localize the excess electron on the chosen atom (i.e. a potential similar to that of Fig.4.4(b)).

- Then, the system is completely optimized without any constraint, starting from the pre-optimized geometry obtained just above, and the previous occupation matrices for *5f* orbitals (but maintained only over the 20 first electronic iterations of the first ionic step). This way, the system normally relaxes to a polaronic state with the electron localized on the chosen Am atom, and moreover in the chosen $5f$ orbital (provided this state is stable).

The calculations are performed by switching off all the symmetries. This two-step procedure is achieved for the 7 possible occupation matrices of the $5f$ orbitals of the Am^{3+}, and the most stable final configuration is selected as the one that best describes the polaronic state of the excess electron in AmO_2.

In this final configuration, we observe that the added electron indeed becomes localized on the chosen americium atom (as expected). This localization is associated to : (i) an increase of the magnetic moment of the atom on which the electron is localized, from ~ 5.1 up to 5.85 μ_B, and (ii) an expansion of the Am-O bond lengths between the Am^{3+} and its eight oxygens 1st neighbour, by $\sim 3.3\%$. This increase in the Am-O distances, i.e. the O atoms are slightly pushed away from the localized excess electron, corresponds to the self-trapping distortion characteristic of the polaronic state.

4.5.2 Self-trapping energy, formation energy of the electron polaron

The supercell containing the self-trapped electron polaron is 1.01 eV lower in energy than that with a delocalized electron (i.e., at the bottom of the conduction band, in the perfect crystal). The self-trapping energy is thus -1.01 eV. This very large value indicates that electron polarons are extremely stable in AmO_2. This self-trapping energy is larger than the one encoutered, e.g. in some rare-reath titanates (-0.55 eV [138]). However, large self-trapping energies may be found, for instance in $BaCeO_3$, where Swift *et al.* [139] report a self-trapping energy of -0.78 eV for the electron polaron (which locally corresponds to the reduction of Ce^{4+} in Ce^{3+}). In bulk ceria however, electron polaron self-trapping energies are less negative (-0.54 to -0.30 eV [140]).

Fig.4.2 plots the formation energy of the electron polaron as a function of Fermi level, superimposed to the formation energies of oxygen vacancies and Am intersti-

tials. Note that the formation energy of the polaron does not depend on the external conditions.

We observe that, due to its large stability, the formation energy of the electron polaron is positive only over a very small range of the Fermi level near the VBM (between 0 and 0.09 eV). This restricts the accessible range of the Fermi level in AmO_2 to 0-0.09 eV. This is related to the fact that the self-trapping energy of the electron polaron in AmO_2 is very close to the band gap (1.1-1.3 eV [14, 33]). Note that a negative value for the formation energy of small polaron would indicate a spontaneous reduction of Am^{4+} to Am^{3+} and thus, the spontaneous formation of americium sesquioxide Am_2O_3.

The self-trapped electron polaron is therefore a very stable intrinsic defect in AmO_2. In the accessible range of the Fermi level, the dominant atomic point defect is first the fully ionized oxygen vacancy $V_O^{\bullet\bullet}$ (up to ϵ_F=0.01 eV), then the singly ionized oxygen vacancy $V_O^{\bullet}$. Therefore, in the absence of other point defect in AmO_2, the electron polarons are probably, at least partly charge-compensated by fully ionized and partially ionized oxygen vacancies. Note that with a Fermi level so close to the VBM, the AmO_2 matrix can also contain holes, which will be discussed in Sec. 4.6.

4.5.3 Electronic density of states of the polaronic system

Fig. 4.3 (a)(b)(c) display the electronic density of states (e-DOS) of the supercell containing the self-trapped electron polaron. Panel (a) plots the total e-DOS. It can be seen that one occupied state appears in the band gap (it is spotted with a green arrow), at very low energy, close to the VBM, just like the defect states of the neutral oxygen vacancy. Panel (b) plots the e-DOS projected on the $5f$ orbitals of the Am^{3+} which carries the excess electron, while panel (c) plots for comparison the e-DOS projected on the $5f$ orbitals of two Am^{4+} (with opposite spin) of the supercell (their projected e-DOS are typical of those of the other Am^{4+}). Like in the charge-neutral oxygen vacancy, the occupied $5f$ orbitals of Am^{4+} are localized down in the valence band. [33] For Am^{3+}, we also observe exactly the same tendency as for the charge-neutral oxygen vacancy: the energy of the newly occupied $5f$ state of Am^{3+} strongly decreases from the CBM down to the VBM, while the energy of the other (occupied) $5f$ states of Am^{3+} increase towards the VBM. As for the oxygen vacancy, Am^{3+} accumulates the occupied $5f$ states at the VBM.

4.5.4 Association energy between electron polaron and oxygen vacancy

The large stability of the electron polaron in AmO_2 suggests that the electrons released by an oxygen vacancy may have the tendency to spontaneously unbind from their parent defect, in order to be rather in a self-trapped state, far from the defect in the lattice. We examine this possibility in this subsection. Having computed the oxygen vacancy in its different possible charge states and the self-trapped electron polaron, we can indeed calculate the association energy between the electron polaron and the oxygen vacancy.

We consider the following processes:

- Association between an electron polaron and a singly ionized oxygen vacancy, providing a neutral oxygen vacancy:

$$\underbrace{V_O^{\bullet}}_{\substack{partially\ ionized\\ vacancy}} + \underbrace{Am'_{Am}}_{\substack{isolated\ small\\ polaron}} \rightarrow Am_{Am}^{X} + \underbrace{V_O^{X}}_{\substack{neutral\ oxygen\\ vacancy}} \tag{4.12}$$

  We note as E_{a_1} the energy of this process.

- Association between two electron polarons and a fully ionized oxygen vacancy, providing a neutral oxygen vacancy:

$$\underbrace{V_O^{\bullet\bullet}}_{\substack{fully\ ionized\\ vacancy}} + \underbrace{2Am'_{Am}}_{\substack{2\ isolated\\ small\ polarons}} \rightarrow 2Am_{Am}^{X} + \underbrace{V_O^{X}}_{\substack{oxygen\\ vacancy}} \tag{4.13}$$

  We note as E_{a_2} the energy of this process.

-E_{a_1} (resp. -E_{a_2}) is thus the energy required to unbind one (resp. two) electron(s) from the neutral vacancy V_O^X and put it (them) far away in the lattice under the form of an (resp. two) isolated self-trapped electron polaron(s), leaving behind a partially (resp. fully) ionized $V_O^{\bullet}$ (resp. $V_O^{\bullet\bullet}$). We find two positive values $E_{a_1} = 0.20$ eV and $E_{a_2} = 0.12$ eV, confirming the larger stability of the polaronic state, i.e. the electron released by the vacancy is more stable far from the vacancy as a self-trapped polaron, rather than bonded to the vacancy (in its close vicinity).

Other defects are reported in the literature to have the released electrons or holes preferentially localized not on their nearest neighbours: for instance, the electrons liberated by the neutral oxygen vacancy at the CeO_2(111) surface rather localize on next nearest-neighbour Ce atoms rather than nearest neighbours [141, 142]. In bulk ceria however, electron polarons are found to effectively bind to oxygen vacancies, however weakly, with association energies $\sim$ -0.1 eV [140]. In some perovskites such as $BaZrO_3$ or $BaSnO_3$ doped with trivalent elements on their B site (Zr or Sn), the hole liberated by the acceptor dopant is found to localize on one oxygen second-neighbour of the dopant in the case of the largest dopants [22, 143].

4.5.5 Transfer of the electron polaron

We now investigate the possibility for the electron polaron to migrate from an Am atom onto the next nearest one.

We denote as Am_i (resp. Am_f) the americium atom on which the electron polaron is initially (resp. finally) localized. The two atoms chosen are 1st neighbours on the Am sublattice, and carry the same spin (we recall that AmO_2 is modeled as an AFM compound). The basic concepts that underlie the physics of small polaron transfer have been recalled above (Sec. 4.4.2): the hopping of a small polaron is a quantum mechanism taking place in a coincidence configuration, which may appear due to the thermal fluctuations of the lattice atoms. In a coincidence configuration, the ground levels of the excess electron, considered as localized either in the initial or in the final

well, are equalized, making possible a resonant tunneling of the electron from one of these (diabatic) ground states onto the other.

It is generally admitted that, in small polaron transfer, there is mostly one coincidence configuration that contributes to hopping, although in theory, the number of coincidence configurations is infinite, and that this configuration is the lowest-energy one [137]. Its energy E_c (coincidence energy) plays the role of an activation energy for the hopping process of the polaron. It has been proposed to obtain this CC by linear interpolation between the initial and the final self-trapped configurations and plotting the total energy of the system along this path [140]. This, however, should slightly overestimate the coincidence energy. On the other hand, it is possible to use methods such as the "Nudged Elastic Band" (NEB) or the "String Method", which allow computing the Minimum Energy Path (MEP) between the two self-trapped configurations. Note, however, that these techniques assume that the energy evolves smoothly enough along the path: the energy profile must be derivable at the coincidence point, which is the case only if the electronic coupling at coincidence is large enough (see Fig. 4.5). In theory, this excludes the hopping processes in which the electronic coupling is very weak, i.e. the non-adiabatic processes.

It is, however, difficult to predict in advance the nature (adiabatic or not) of the hopping. Thus, we assume the validity of the String Method algorithm for the present problem, and use it to compute the MEP between two self-trapped configurations corresponding to the polaron localized on neighboring Am sites (with same spin). In the String Method, the path between the initial and the final configurations is discretized in a series of intermediate configurations (or images). Initialization is achieved by a linear interpolation, and we use 11 images to make the calculation (including the initial and final ones).

At the end of the calculation, the average difference per image between two successive iterations is $\sim 2.0\times10^{-4}$ Ha ($\sim$ 5 meV). The occupation matrices of the $5f$ orbitals are imposed over 20 electronic steps at the initial iteration of the String Method, using a linear interpolation between the occupation matrices of the two self-trapped configurations.

Fig. 4.6 displays the energy profile obtained, as a function of image index: the energy barrier is $\sim$ 0.55 eV.

Along the hopping path, the spin magnetic moments on the initial and final Am show a discontinuous behaviour, transiting suddenly from their initial value ($\sim$ 5.85 μ_B for Am_i, $\sim$ 5.1 μ_B for Am_f) to their final one ($\sim$ 5.1 μ_B for Am_i, $\sim$ 5.85 μ_B for Am_f), between images 5 and 6. We recall that 5.85 μ_B (resp. 5.1 μ_B) is a magnetic moment characteristic of Am^{3+} (resp. Am^{4+}). This means that the electron itself is *abruptly transfered* from Am_i onto Am_f.

In order to show how the self-trapping distortion is transferred along the hopping path, we now scrutinize the evolution of the Am_i-O and Am_f-O distances (between Am_i/Am_f and the eight first neighbour oxygen atoms of the first coordination shell, averaged over the eight oxygen atoms), and plot these mean distances as a function of image index along the hopping path (Fig. 4.7 (a)): we observe that the system undergoes a progressive weakening of the self-trapping distortion in the initial site, and a progressive strengthening of the self-trapping distortion in the final site: indeed the <Am_i-O> distance progressively decreases from $\sim$ 2.43 Å to the undistorted value

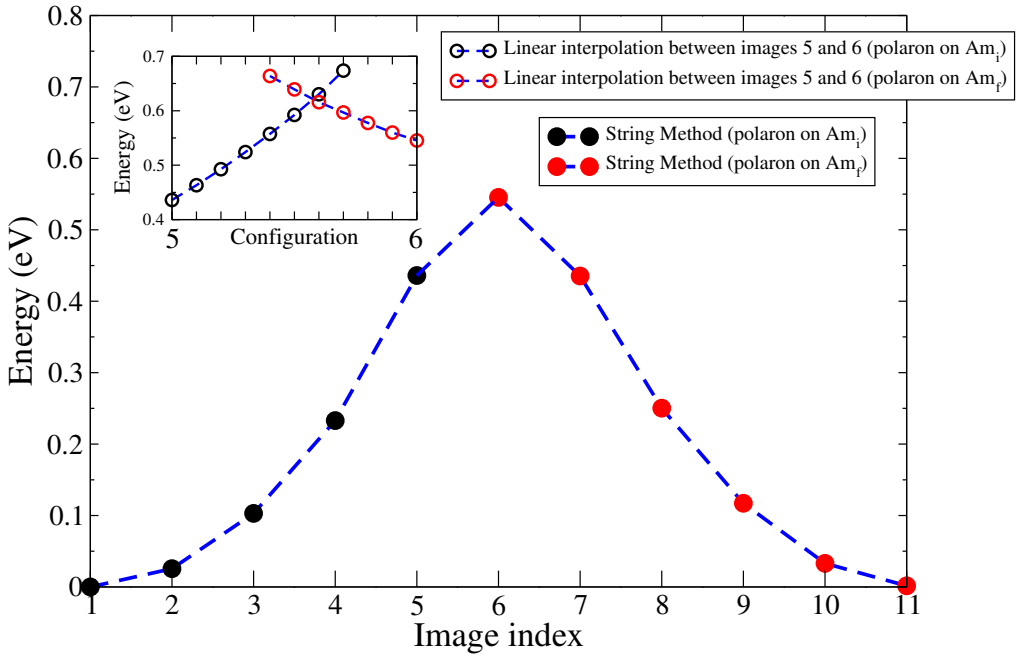

Figure 4.6: Energy along the hopping path of the self-trapped polaron, as provided by the String Method. Hopping is considered here between two 1st neighbours Am atoms. The black (resp. red) part of the curve gathers the configurations in which the polaron is localized on Am_i (resp. Am_f). Inset: energy as a function of configuration linearly interpolated between images 5 and 6 (black symbols: configurations in which the polaron is localized on Am_i; red symbols: configurations in which the polaron is localized on Am_f). Configuration number 1 (resp. 11) is the self-trapped configuration at site Am_i (resp. Am_f).

2.35 Å, while at the same time, there is a progressively increase of this distance in the final site, <Am_f-O>. In the coincidence state that should be reached somewhere between image 5 and 6, the <Am-O> distances should be equal to 2.39-2.40 Å in both sites. This configuration corresponds to a state in which the distortion is equally shared between the two Am atoms. The self-trapping distortion is therefore *continuously transfered* along the hopping path, in contrast to the electron itself.

Finally, we construct a set of atomic configurations to approach as much as possible the coincidence configuration (CC) involved in the hopping path. For that, we take the two configurations of the path which surround the CC (from Fig. 4.7, configurations number 5 and 6), and linearly interpolate these two configurations, building 9 intermediate configurations. Then, two series of calculations are performed: the total energy of each of these configurations is computed, with the $5f$ occupation matrices initialized either to those of image 5, or to those of image 6 (which corresponds to initialize the electronic loop with the polaron either on Am_i or on Am_f).

The results are shown in the inset of Fig. 4.6. The crossing of these two curves provides a better approximation of the CC involved in the hopping. Its energy is ~ 0.6 eV above that of the self-trapped configuration. In all these configurations, intermediate between configurations 5 and 6 and close to the CC, the polaron is always obtained as

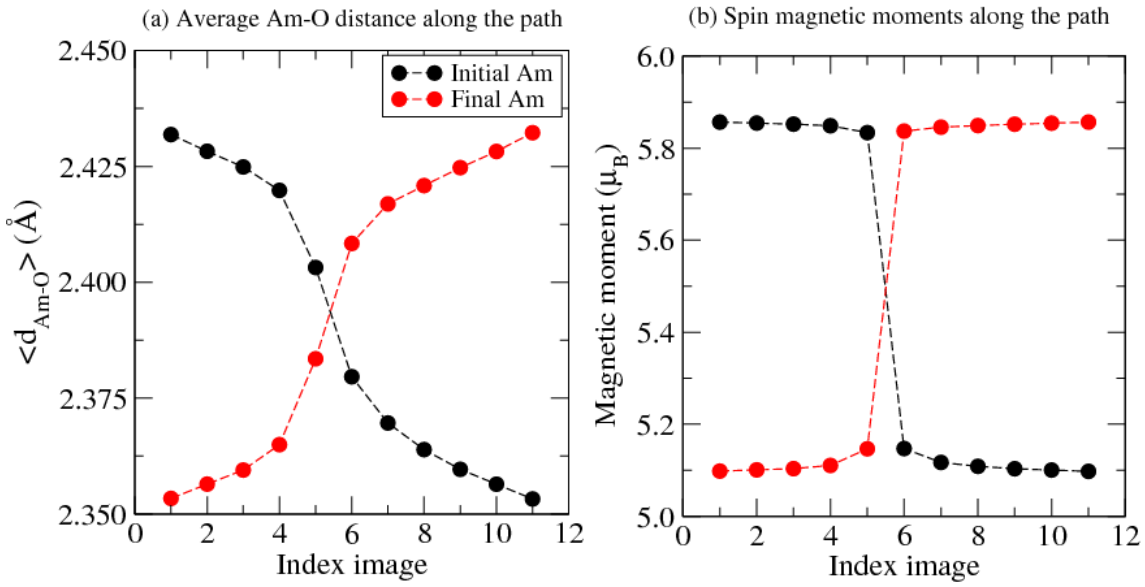

Figure 4.7: (a) Evolution of the average distance between the initial (or final) Am and the eight oxygen atoms of the first coordination shell, as a function of image index along the hopping path onto a 1st neighbour Am atom. The oxygen atoms are pushed away from the Am^{3+} ion by about 0.08 Å (on average) in the self-trapped state, which is a hallmark of the self-trapping distortion. Here we see that the self-trapping distortion is progressively transfered from the initial Am onto the final Am along the hopping path of the polaron. (b) Evolution of the magnetic moments of the initial and final Am atoms along the hopping path. Black (resp. red) circles correspond to configurations in which the polaron is localized on Am_i (resp. Am_f).

strictly localized on one side of the barrier, i.e. either on Am_i or on Am_f, according to how the calculation is initialized. The calculation does never evolve spontaneously to a state in which the excess electron would be equally shared between Am_i and Am_f, as it could be expected in an adiabatic hopping. Only a small decrease (resp. increase) of the magnetic moment on the polaronic (resp. neighboring) site to ~ 5.8 (resp. 5.2) μ_B is observed. The smallest energy difference between the state found localized on Am_i and that found localized on Am_f (reached at the configuration number 7 of the inset of Fig. 4.6) provides an upper limit to the electronic coupling, namely $C < 7.2$ meV, because (unconstrained) DFT is not expected to provide diabatic states, but only adiabatic states. The curves of Fig. 4.6 (with inset) are thus expected to correspond to the solid line curves of Fig. 4.5. The electronic coupling in the CC is thus probably very weak, providing here the picture of a non-adiabatic hopping.

Having an upper limit to the electronic coupling ($C < 7.2$ meV), we can estimate an upper limit to the adiabaticity criterion given by Eq. 4.11. We take as typical phonon energies 0.00086-0.0026 Hartrees (wave numbers $\sim$ 189-570 cm^{-1}) corresponding to the range of the zone-center modes computed in AmO_2 and involving only oxygen displacements. At room temperature, we obtain $\gamma_{th} \lesssim 0.03$-$0.10$, which provides further indication that the hopping probably rather takes place in the non-adiabatic limit.

The transfer barrier of 0.6 eV found here is noticeably larger than polaronic transfer barriers reported in the literature for other oxide compounds, for instance 0.4 eV [144] or 0.12-0.23 eV [140] in CeO_2 and $\sim$ 0.3 eV in $BaCeO_3$ [139] for electron polarons, or $\sim$ 0.1-0.2 eV for oxygen-type hole polarons in several oxides [22, 143, 145], 0.15-0.30 eV for Fe^{3+} holes in $LiFePO_4$ [146–149]. We note that a barrier of 0.5-0.6 eV is reported

for hole polarons in TiO_2 in the case of a non-adiabatic hopping [145, 150]. The high barrier found here is probably related to the large self-trapping energy of the electron polaron in AmO_2.

A posteriori, we can question the validity of the String Method algorithm on such a mechanism, along which the energy appears as not very smooth at the CC. However, the method provides a continuous path (in the sense of the lattice distortions) between the two self-trapped configurations, with an activation energy smaller than what would be provided by a simple linear interpolation between these two configurations (the linear interpolation provides an activation energy of 0.97 eV). It is thus clearly an improvement over this latter approach.

4.6 Discussion

The previous results allow to build the following scenario for AmO_2: the large stability of the electron polaron (which is related to the easiness for Am^{4+} to be reduced into Am^{3+}) restricts the range of possible Fermi levels to a very narrow interval just above the VBM (0-0.09 eV). Electron polarons will be thus in large number in AmO_2, and it is probable that they will be mostly charge-compensated by ionized oxygen vacancies (moreover we have seen that oxygen vacancies spontaneously liberate electron polarons in the lattice). However, since the Fermi level is thus very close to the VBM, we must also consider the possibility to have free holes in addition to the oxygen vacancies to ensure charge compensation of the electron polarons.

We set up a simple and approximate model in order to estimate the concentration in the different defects, charges, and equilibrium Fermi level. [151] The concentration of free holes is assumed to be

$$p = \int_{-\infty}^{E_{VBM}} n_v(E) f_p(E) dE, \tag{4.14}$$

with $n_v(E) = \frac{1}{2\pi^2}\{\frac{2m_h^*}{\hbar^2}\}^{3/2}\sqrt{E_{VBM} - E}$ and $f_p(E) = \frac{1}{1+e^{-(E-\mu_e)/k_BT}}$.

The concentration of free (band) electrons is neglected since electrons in the lattice clearly prefer the polaronic state. For simplicity, we take the effective mass m_h^* equal to the electron mass. The concentration of point defect X in charge state q is

$$[X] = [M] e^{-\frac{\Delta E_f(X,q)}{k_BT}}, \tag{4.15}$$

with $[M]$ being the concentration in possible sites for the defect (e.g. for V_O this is the oxygen concentration in AmO_2). [136] The formation energy of the defect, $\Delta E_f(X, q)$, depends on the oxygen chemical potential $\Delta\mu_O$ (external conditions) and on the Fermi level ϵ_F if $q \neq 0$.

The Fermi level at equilibrium, ϵ_F^{eq}, may be obtained by solving the electroneutrality equation, assuming that oxygen vacancies are the only atomic defects in the system (with possible charge states 2+, 1+, 0):

$$[e^-_{pol}] = p + 2[\mathrm{V}_\mathrm{O}^{2+}] + [\mathrm{V}_\mathrm{O}^{1+}] \tag{4.16}$$

$[e^-_{pol}]$ denotes the concentration of electron polarons. Numerical applications are done here for T=300 K. Note that Eq. 4.16 is solved for a given value of $\Delta\mu_O$ (which acts as a parameter).

Eq. 4.16 admits positive solutions (i.e. ϵ_F^{eq} remains in the band gap) only for oxygen-poor conditions. Using $\Delta\mu_O$ = -0.75 eV, we obtain ϵ_F^{eq} = 0.012314 eV. In these conditions, the concentration of electron polarons is $\sim$ 0.059 per f.u., that of free holes $\sim 5.2 \times 10^{-4}$ per f.u., and that of oxygen vacancies, 0.040 per f.u.. This means that almost 6% of the Am atoms in AmO_2 are spontaneously reduced into Am^{3+} under such external conditions. We see that the electron polarons are mostly compensated by the oxygen vacancies rather than by the holes, and that the concentration of oxygen vacancies is significant, leading for AmO_2 to the picture of a non-stoichiometric compound, with formula $AmO_{1.96}$ (for T=300 K and $\Delta\mu_O$ = -0.75 eV). With an equilibrium Fermi level so close to the VBM, the concentration of free holes is significant, but is dominated by that of electron polarons by about two orders of magnitude, at least for a hole effective mass equal to the free electron mass. If a larger hole mass is assumed, e.g. ten times that of free electron, we have ϵ_F^{eq} = 0.014845 eV and the concentration in oxygen vacancies slightly decreases to $\sim$ 3.5%. Then the concentration in free holes is increased, although remaining $\sim$ 4 times smaller than that of electron polarons. The important loss of oxygen in those oxygen-poor conditions may be seen as precursor for the formation of hypostoichiometric Am oxide.

Note however that the very large concentrations found here (due to very small formation energies) make the present defect model very approximate, since the calculation of the concentration based on the formation energy usually assumes concentrations << 1.

In oxygen-rich conditions ($\Delta\mu_O$=-0.29 eV), the formation energy of the oxygen vacancy becomes too large to allow charge compensation of the electron polarons by $V_O^{\bullet\bullet}$ or $V_O^{\bullet}$, and this role is probably entirely played by free holes. There is probably no important loss of oxygen in those conditions.

4.7 Conclusion

In this chapter, we have studied intrinsic donor point defects and electron polarons in AmO_2, using a first-principles GGA+U framework within which the Am $5f$ orbital occupation matrices are carefully controlled. We have shown that the oxygen vacancy is a deep double donor, with small to moderate formation energies. Am interstitials have prohibitive formation energies and are thus unlikely in AmO_2. The self-trapped electron polaron is extremely stable. This large stability confines the possible values of the Fermi level in AmO_2 to a very narrow interval just above the Valence Band Maximum (0-0.09 eV).

In the oxygen-poor conditions here considered ($\Delta\mu_O$ = -0.75 eV, i.e. T=680 K and P_{O_2}=0.2 atm), oxygen vacancies are easily formed in AmO_2. The liberated electrons have the tendency to move far from the vacancies and localize in the lattice under the form of self-trapped polarons, since this state is found more stable than when the electron is trapped close to the vacancy. In other words, the oxygen vacancies are spontaneously ionized. Electron polarons are probably in rather large number, with

charge compensation mostly ensured by ionized and partially ionized oxygen vacancies. In oxygen-rich conditions, electron polarons may remain in large concentration but should be charge-compensated by free holes rather than by ionized oxygen vacancies.

The self-trapped state of the excess electron in AmO_2 is associated with a self-trapping distortion mostly consisting of an increase of the Am-O distance (between Am carrying the excess electron and the eight 1st neighbour oxygens) by about 0.08 Å. The hopping of the polaron involves a rather large activation barrier of ~ 0.6 eV, and probably takes place by a non-adiabatic mechanism.

Chapter 5

Study of bulk properties and point defects in (U,Am)O_2 mixed oxides and comparison with UO_2 and (U,Pu)O_2

The objective of this chapter is to evaluate the influence of the americium content on the UO_2 bulk and point defect properties in order to pave the way to the study of the influence of Am on (U,Pu)O_2 properties but also to support the experimental studies conducted in CEA.

Contents

5.1 Introduction

The $U_{1-y}Am_yO_2$ solid solution displays a chemical disorder in the cationic sublattice i.e. U and Am cations randomly occupy the face-centered-cubic (fcc) lattice and as a consequence, a very accurate modelling requires a very large supercell (several thousand

atoms) for a good description of the chemical disorder. Since first-principles calculations are currently limited to a few hundred atom supercells especially for actinide oxides, the cationic distribution in the fcc lattice which better reproduces the chemical disorder needs to be approximated. As a first approximation, the U and Am cations can be distributed randomly in the fcc lattice (for a given composition), and a configurational average energy and other properties can be calculated. However, owing to the high computing time (enhanced in actinide coupounds) and given the large number of configurations for a large supercell, such an approach appears impractical. In order to overcome this shortcoming posed by cationic disorder in solid solutions using first-principles calculations, several approaches have been developed and proposed in the past. For instance, (i) the Coherence Potential Approximation (CPA) [152] in which all A atoms and separately all B atoms of a given binary alloys AB are assumed equivalent and each is embedded in a uniform medium, (ii) the Virtual Crystal Approximation (VCA) [153] in which the alloy is assumed to have a single <AB> averaged type atom, (iii) the Special-Quasirandom Structure (SQS) [154] which will be described in Sec. 5.2.1. The CPA as well as the VCA approaches do not take into account the local structure relaxations which impact local properties averaging. The SQS method has been shown to be relevant for transition element alloys [155] and uranium-plutonium mixed oxides [29].

The structural and electronic properties of $U_{1-y}Am_yO_2$ solid solutions have been the subject of very few experimental investigations in the literature. For instance, Mayer *et al.* [101] examined the electronic structure of $U_{1-y}Am_yO_2$ (y=50%) mixed oxide using X-ray photoemission spectra (XPS). More recently, the electronic and structural properties of these oxides have been analysed using Extended X-Ray Absorption Near Edge (XANES) and Extended X-Ray Absorption Fine Structure (EXAFS) [24, 107, 156] as well as X-ray diffraction (XRD) [102] experiments. Despite these investigations, the knowledge of many properties remains limited. For example, the early experiments show a discrepancy regarding the lattice constant as a function of Am content. This can be attributed to the self-irradiation effects which is known to occur in the Am-bearing oxides. In addition, literature does not provide any data on the mixing enthalpy which is one of the quantity required to conclude on the structural stability of the random alloys. Concerning cation electronic valences in $U_{1-y}Am_yO_2$ solid solutions, all available experimental studies do not agree with each other. Up to now, the litterature is blank concerning point defects investigation in $U_{1-y}Am_yO_2$. Thus, DFT+U calculations in combination with the SQS approach are expected to provide information complementary to the available experimental results and, moreover, predict some missing data.

In order to address the above open questions, the present chapter reports results on the structural, electronic and energetic properties as well as oxygen vacancies stability in $U_{1-y}Am_yO_2$ in the framework of DFT+U calculations. In order to have a global insight on the effect of americium, these bulk properties have been studied for americium content in the range of 0 to 100%.

5.2 Computational details

Our DFT calculations in this chapter are carried out using the same code and same functionals as in the previous chapter (Chap. 4).

The onsite Coulomb terms U and J are set in the mixed oxides to the same values as for the end members UO_2 and AmO_2 i.e. $(U\ ;\ J) = (4.50\ ;\ 0.54)$ eV for UO_2 [23] and (6.00 ; 0.75) eV for AmO_2 as mentionned in Chap. 3. This assumption has been already made for (U,Pu)O_2 [29] to successfully compute bulk properties.

In order to search the ground state within the DFT+U method, we applied the occupation matrix control scheme [31,111] on the *5f* orbitals. In UO_2, a given U^{4+} ion has two *5f* electrons and in AmO_2 a given Am^{4+} ion has five *5f* electrons. Therefore, there are 21 possible diagonal matrices for UO_2 and AmO_2 referring to different manners to fill the seven *5f* orbitals of a given spin channel with two electrons (UO_2) or five electrons (AmO_2), thus 21×21 electronic configurations for $U_{1-y}Am_yO_2$ assuming (i) U^{4+} and Am^{4+} in high-spin electronic configuration and (ii) that the occupation matrix is the same for all the atoms of a given chemical species in the supercell. Given the large number of electronic configurations and high computational time, the systematic exploration of these 21×21 occupation matrices is very complex. Moreover, as we will see later, some of the U and Am atoms in the mixed oxide may undergo a change of their oxidation state, involving therefore a change of their occupation matrix, which complexifies the problem. As a starting point for searching the ground state of the mixed oxides, *5f* orbital occupation matrices of the end members UO_2 and AmO_2 can be applied, leaving the possibility to control possible electronic charge tranfers which induces change in the atomic valence states. For Am, the occupation matrix used as a starting point of the calculations is the one previously found, and called $M_3^{no\ sym}$ in Chap. 3.

Note that the modelling of $U_{1-y}Am_yO_2$ mixed oxides required a rigorous methodology. Indeed, in order to model the electronic charge transfer occurring during calculations, we have first to suppress all symmetries to prevent charges (electrons or holes) to remain delocalized over the supercell. Preliminary calculations show that some charge tranfers spontaneously take place in the supercell and may lead to the formation of Am^{3+} and U^{5+}. The atoms undergoing this change of their valence state are thus spotted. However this preliminary step is not sufficient to maintain completely hole localized on a single U atom. Holes can only be completely localized (instead of being delocalized throughout the supercell) in the presence of an initial sufficient structural distortion around the U atoms. We thus proceed in two main steps:

i) Obtain a distortion field by constraining the charge state of the atoms according to the preliminary step mentioned above: this is done by maintaining the *5f* occupation matrices constant (each matrix being related to the valence state of the corresponding cation) during the 20 to 30 first steps of all the self-consistent cycles of this pre-optimization. The aim is to first create the distortion needed to have the charge transfer and then leave the system converge to the correct final state. This pre-optimization step is performed until complete localization of the holes on the U.

ii) Final structural optimization without constraint: the system is completely optimized (atomic positions and supercell vectors) without any constraint, starting from the last geometry and previous occupation matrices, but which are kept fixed (only)

on the 20 to 30 first steps of the first self-consistent cycle.

The 1k antiferromagnetic (AFM) state is generally used as an approximation of the 3k AFM order in UO_2 [110] and AmO_2. Thus, the magnetic state of the mixed uranium-americium oxide is assumed here to be a 1k AFM order.

5.2.1 Modelling of solid solution

The SQS method is a randomness lattice theory consisting at mimicking as closely as possible the spatial correlation functions of an infinite random alloy within a finite size supercell [154]. This theory is based on the minimisation of the error function denoted $\epsilon(\sigma)$ (given in equation 5.1) which quantifies the deviation of the averaged correlation function of a particular structure from the corresponding correlation function of a truly infinite random alloy of the same composition.

$$\epsilon(\sigma) = \sum_f \frac{D_f}{(k\bar{d}_f)^n} \left| \bar{\Pi}_f(\sigma) - \langle \bar{\Pi}_f \rangle_R \right| \tag{5.1}$$

In this equation, σ denotes a configuration of the solid solution A_xB1-x (i.e. a particular distribution of A and B on the different sites of the lattice), $f = (k, m)$ denotes a "figure", i.e. the choice of a way to scrutinize the "state" (A or B) of the atoms (k=2: by pairs, k=3: by triangles, etc) located at maximum distance "m" from each other (m=1: first-neighbor, m=2: second-neighbor, etc). k is also called the number of vertices (i.e. the number of lattice sites taken into account in figure f). D_f is the number of possible figures f at a given site of the lattice, owing to symmetry. To each site is affected a "spin", i.e. +1 if the site is occupied by chemical species A, -1 if the site is occupied by chemical species B. A configuration sigma may thus be completely defined by a set of integers equal either to +1 or to -1. d_f is the average of the distances between two vertices in a given figure f.

$\Pi_f(\sigma)$, with a given $f = (k, m)$, is defined in Ref. [154] as the average over the lattice sites (and possible orientations) of the spin products of the k atoms at m-th distance from each other. This is a spatial k-point correlation function for a maximal distance between the k lattice sites equal to m. It reflects how k lattice sites separated by maximal distance m are correlated with each other concerning the presence of species A or B.

$\langle \Pi_f \rangle_R$ is the corresponding correlation function of an ideal infinite random lattice, which has an analytical expression.

Based on the Eq. 5.1, von Pezold *et al.* [38] proposed the atomic fractional coordinates of SQS structures of 32-atom fcc supercells of binary A-B alloys for all atomic compositions with an increments of 2/32. For more details about the SQS approach see Refs [38,154]. We have used the configurations given by von Pezold *et al.* [38]. The latter configurations are found to efficiently reproduce the elastic constants of Al-Ti alloy with the same precision as simulations performed on 10x10x10 size supercell [38].

5.2.2 Computational parameters

Results are obtained using a plane-wave cutoff energy equal to 871 eV with the ABINIT code. According to our convergence tests, this input parameter lead to a precision lower than 1 meV per atom on physical energies (energy difference). 96-atom supercells (2×2×2) are used. The calculations are done using a 2×2×2 k-points mesh generated by the Monkhorst-Pack [114] method, which is sufficient for an energy convergence smaller than 0.3 meV per atom. We performed full relaxation of the cell until the pressure acting on the system becomes lower than 5×10^{-7} Ha/bohr^3 (∼0.15 kbar) and until the forces, for the structural optimization, become lower than 5.10^{-4} Ha/bohr (∼0.025 eV/Å).

5.3 Electronic properties

In this section, we study the electronic structure and the valence state of cations (U,Am) in the mixed oxides. Note that the knowledge of the valence state of ions in a compound is required to compute its phase diagram. In particular, the thermodynamic computational method CALPHAD [157] uses a sublattice model based on the information on the valence state of species [158]. Furthermore, the knowledge of the cation valence state and electronic structure are needed to subsequently model atomic transport properties, which control the microstructure evolution of materials.

5.3.1 Valence state of (U,Am) in mixed oxides

a) Stoichiometric conditions

We first investigate the oxidation state of Am and U cations in the $U_{1-y}Am_yO_2$ mixed oxides in the stoichiometric conditions (i.e. O/(U+Am) =2) as a function of the Am content in the whole range of Am concentration. Fig. 5.1. The values of Am content (y) for which an *ab initio* calculation has been performed are the ones listed in Table 5.4. Table 6.4 shows the evolution of the cationic species concentration. Depending on the Am content, two different behaviours are observed.

From 0 to 50%, one can see that Am(+IV) cations are all reduced to Am(+III) whereas uranium cations have mixed valence (+IV/+V) with the U(+V) content equals that of Am. We highlight that the U(+V) cations are located as close as possible to the Am(+III) cations i.e. in the first or second coordination shell depending on the possibility offered by the SQS configuration. We can conclude that U(+V) accommodate the formation of Am(+III). These results are the first theoretical confirmation of the XANES experiments (see Refs. [26, 101, 102]). Indeed, these experimental studies (limited to Am content lower than 20%) show by analysing the XANES spectra that U cations have mixed valence states (+IV/+V) in $U_{1-y}Am_yO_2$ whereas americium cations are all trivalent. In summary, all the Am (+IV) cations are reduced to Am(+III) when there are sufficient U (+IV) to be oxidized in U (+V) in order to accommodate charge neutrality and the formation of Am (+III).

On the contrary, for Am/(Am+U)>50%, literature does not provide any investiga-

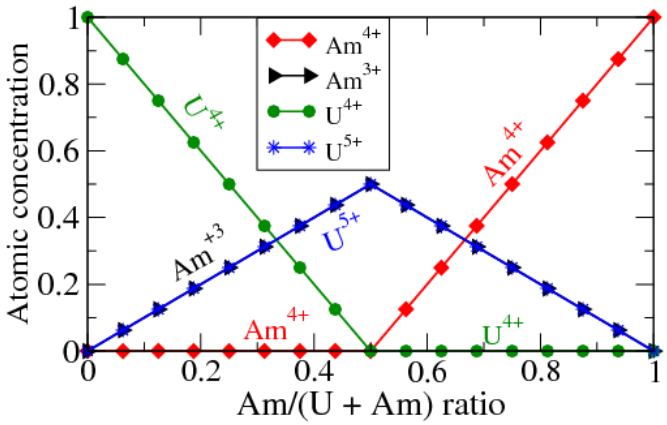

Figure 5.1: Concentration of the cationic species in the crystal as a function of the americium content Am/(Am+U). These evolutions are extrapolated from the calculated points displayed in Tab 5.4.

tion, thus the present study is a prediction regarding the valence state of the cations. Our DFT+U results show that (see Table 6.4, %Am $>$ 50), contrary to the Am content smaller than 50%, U cations are now completely oxidized in U(+V) whereas Am cations are found in mixed valence (+III/+IV). Moreover, our results show a change of behaviour at Am/(Am+U) ratio equals to 50%. This point corresponds to the maximun concentration of trivalent americium and pentavalent uranium.

On the basis of these DFT results, it is possible to propose the evolutions shown in Fig. 5.1 for the concentrations in the different atomic species as a function of Am content.

The valence state of cations in (U,Am)O_2 shows a significant difference with other mixed oxides like (U,Pu)O_2 or (U,Ce)O_2 for which the valence state of cations in stoichiometric conditions remains +IV. In other words, mixing U and Am oxides leads to a chemical reaction which is not the case with (U,Pu)O_2 or (U,Ce)O_2.

Table 5.1: Valence states of cations (Am,U) in $U_{1-y}Am_yO_2$ mixed oxides. The total Am atomic fraction (y) as well as the atomic fractions of all cations in the crystal are displayed. O/M (M=U+Am) is the oxygen/metal ratio. For comparison, the results from the XANES experiments are also displayed.

		Atomic fraction (% at.)					
		y	Am(+III)	Am(+IV)	U(+IV)	U(+V)	O/M
		6.25	6.25	0.00	87.5	6.25	2
%Am<50		18.75	18.75	0.00	62.50	18.75	2
	Exp. [24]	15.00	15.00	0.00	71.00	14.00	2
%Am>50		68.75	31.25	37.50	0.00	31.25	2

b) Hypo-stoichiometric conditions

We have also investigated the valence state of Am and U cations in mixed oxides for hypo-stoichiometric conditions. In order to induce hypo-stoichiometric conditions, a

neutral oxygen vacancy is created in a 96-atom supercell. Table 5.2 displays the valence state of cations obtained in hypo-stoichiometric conditions as well as the results for $U_{1-y}Pu_yO_2$ from XANES experiments [25].

Table 5.2: Valence state of cations (Am,U) in mixed oxides.The total Am atomic fraction (y) as well as the atomic fractions of all cations in the crystal are displayed. O/M is the oxygen/metal ratio. For comparison, the result on (U,Pu)O_2 mixed oxides from the XANES experiments [25] is also displayed.

$U_{1-y}Am_yO_{2-x}$					
Atomic fraction (% at.)					
y	Am(+III)	Am(+IV)	U(+IV)	U(+V)	O/M
6.25	6.25	0.00	93.75	0.00	1.97
$U_{1-y}Pu_yO_{2-x}$ [25]					
Atomic fraction (%)					
y	Pu(+III)	Pu(+IV)	U(+IV)	U(+V)	O/M
30.00	4.00	26.00	70.00	0.00	1.98

Because of the lack of other studies on (U,Am)O_2 in hypo-stoichiometric conditions, only the results of $U_{0.7}Pu_{0.3}O_{2-x}$ from XANES experiments by Vigier *et al.* [25] have been displayed for comparison. Knowing that hypo-stoichiometry in UO_{2-x} is accommodated by the reduction of U(+IV) to U(+III), one could expect to have the same behaviour in $U_{1-y}Am_yO_{2-x}$ mixed oxides. However, we can see from Table 5.2 that the hypo-stoichiometry in $U_{1-y}Am_yO_{2-x}$ is rather accommodated by the reduction of U(+V) to U(+IV) since the U cations have mixed valence states (+IV and +V) in the perfect $U_{1-y}Am_yO_2$ compounds. Actually a neutral oxygen vacancy releases two electrons, therefore leading to the reduction of two U(+V) cations to two U(+IV) cations and the Am atoms cannot be reduced since they are all $AmAm^{+3}$ (for y= 6.25%).

We thus confirm that in $U_{1-y}Am_yO_2$ there is a charge transfer from U(+IV) to Am(+IV), which explains the formation of U(+V) and Am(+III) in equal concentration in the stoichiometric conditions. This result shows a difference with (U,Pu)O_2 in which the hypo-stoichiometry is accommodated by the reduction of Pu(+IV) to Pu(+III) (see Table 5.2).

The electrons released by the neutral oxygen vacancy can diffuse throughout the crystal instead of localizing on a single atom in the vicinity of the vacancy leaving behind a partially ionized $V_O^{\bullet}$ ($q = +1$) or completely ionized $V_O^{\bullet\bullet}$ ($q = +2$) vacancies. When an ionized oxygen vacancy ($q = +2$ for example) is induced in $U_{1-y}Am_yO_2$ as diplayed in Table 5.3, the valence state of cations is identical to what is observed in perfect $U_{1-y}Am_yO_2$ as expected. Note that the calculations using charged supercells are performed with the lattice vectors fixed (only atomic positions are relaxed) as recommended by Bruneval *et al.* [159].

In order to enlight the mechanism of electronic charge transfer occuring in (U,Am)O_2 solid solution, it is important to investigate the electronic structure.

Table 5.3: Valence state of cations (Am,U) in mixed oxides in presence of a charged oxygen vacancy. The total Am atomic fraction (y) as well as the atomic fractions of all cations in the crystal are displayed. O/M is the oxygen/metal ratio. For comparison, the results of the perfect supercell are also plotted.

	$U_{1-y}Am_yO_{2-x}$					
	Atomic fraction (% at.)					
	y	Am(+III)	Am(+IV)	U(+IV)	U(+V)	O/M
$q = 0$	6.250	6.250	0.000	93.750	0.000	1.970
$q = +1$	6.250	6.250	0.000	90.625	3.125	1.970
$q = +2$	6.250	6.250	0.000	87.500	6.250	1.970
	$U_{1-y}Am_yO_2$					
	Atomic fraction (% at.)					
	y	Am(+III)	Am(+IV)	U(+IV)	U(+V)	O/M
Perfect	6.250	6.250	0.000	87.500	6.250	2.000

5.3.2 Electronic structure

To understand the electronic structure of $U_{1-y}Am_yO_2$ mixed oxides and compare it to UO_2 oxide, the density of states (DOS) is calculated for y= 6.25% and y= 0%. The projection of this DOS on different orbitals is plotted in Fig. 5.2. The top of the valence band was set as the reference energy.

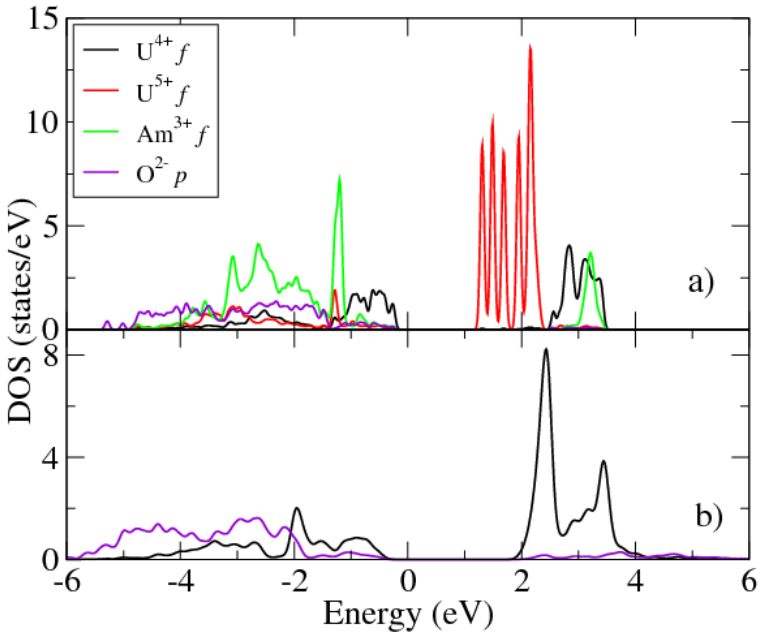

Figure 5.2: Density of states of Am^{4+}-f, Am^{3+}-f, U^{4+}-f, U^{5+}-f and O-p components in (a) $U_{1-y}Am_yO_2$ (with y=6.25%) and (b) UO_2 computed using DFT+U. The density given here is the projected density on a given atom.

We observe in Fig. 5.2 that the band gap of $U_{1-y}Am_yO_2$ is formed between the U *5f* components (U(+IV) and U(+V)) confirming that U(+IV) is partially oxidized to U(+V) in the solid solution. It is known that the band gap of AmO_2 is formed

between the Am f and O p components (as shown in Chap. 3) such that charge is prone to be transferred from O p to Am f components, whereas the gap of UO_2 is formed between the U f components (see Fig. 5.2). In addition, the band gap of AmO_2 (1.1-1.3 eV) is smaller than the UO_2 one, which is 2 eV. These results indicate that the reduction of Am(+IV) to Am(+III) according to the $Am^{4+} + \frac{1}{2}O^{2-} \longrightarrow Am^{3+} + \frac{1}{4}O_2$ reaction is more favourable than the reduction of U(+IV) to U(+III) according to the $U^{4+} + \frac{1}{2}O^{2-} \longrightarrow U^{3+} + \frac{1}{4}O_2$ reaction. The high oxygen potential of AmO_2 compared to that of UO_2 could account for this difference.

The partial oxidation of U(+IV) to U(+V) might be explained as follows: Am^{4+} acts as an electron acceptor and U^{4+} is an electron donor (according to the $U^{4+} + \frac{1}{4}O_2 \longrightarrow U^{5+} + \frac{1}{2}O^{2-}$ reaction) in the solid solution of the (U,Am)O_2 mixed oxide. Thus, the chemical reaction related to this mechanism can be written as $Am^{4+} + U^{4+} \longrightarrow Am^{3+} + U^{5+}$. Such a mechanism has been previously observed in $U_{1-y}Pu_yO_{2\pm x}$ solid solution but only in hypo-stoichiometric conditions using electrical conductivity measurements, where a charge tranfer reaction $Pu^{4+} + U^{4+} \longrightarrow Pu^{3+} + U^{5+}$ was suggested [160].

5.4 Structural properties

In this section, we investigate structural properties of $U_{1-y}Am_yO_2$ namely the lattice parameter as well as the interatomic distances (in the first cordination shell) as a function of Am content Am/(Am+U) in the 0 to 100% range.

5.4.1 Lattice parameter

Assuming a linear behaviour of the lattice parameter as a function of composition in mixed oxides, Kato *et al.* [109] proposed an analytical expression based on the experimental ionic radius of the species in the pure compounds and taking deviation from stoichiometry into account, In particular, ionic radii of Am^{4+},U^{4+} and O^{2-} for $U_{1-y}Am_yO_2$ mixed oxides. However, this analytical expression is not suitable for mixed $U_{1-y}Am_yO_2$ oxides because of various valence states of the species : Am^{3+}, Am^{4+}, U^{4+}, and U^{5+}. We thus calculate (performing a complete optimization of the supercell) the lattice parameter in the whole range of Am concentration and results are reported in Table 5.4.

We emphasized that all the calculations performed on stoichiometric systems are charge-neutral.

Table 5.4: Lattice parameters of $U_{1-y}Am_yO_2$ mixed oxides in the whole Am concentration range.

y(% at.)	0.00	6.25	12.50	18.75	25.00	31.25	50.00	68.75	75.00	93.75	100.00
a(Å)	5.540	5.533	5.527	5.520	5.518	5.511	5.505	5.474	5.469	5.443	5.438

In Fig. 5.3, we display the lattice parameter as a function of Am content together with experimental results from XRD analysis [26,156] for comparison. We also display the results obtained by linear combination of the UO_2 and AmO_2 experimental lattice parameters (dotted lines) given by the following equation:

$$a_{U_{1-y}Am_yO_2} = (1-y)a_{UO_2} + ya_{AmO_2} \tag{5.2}$$

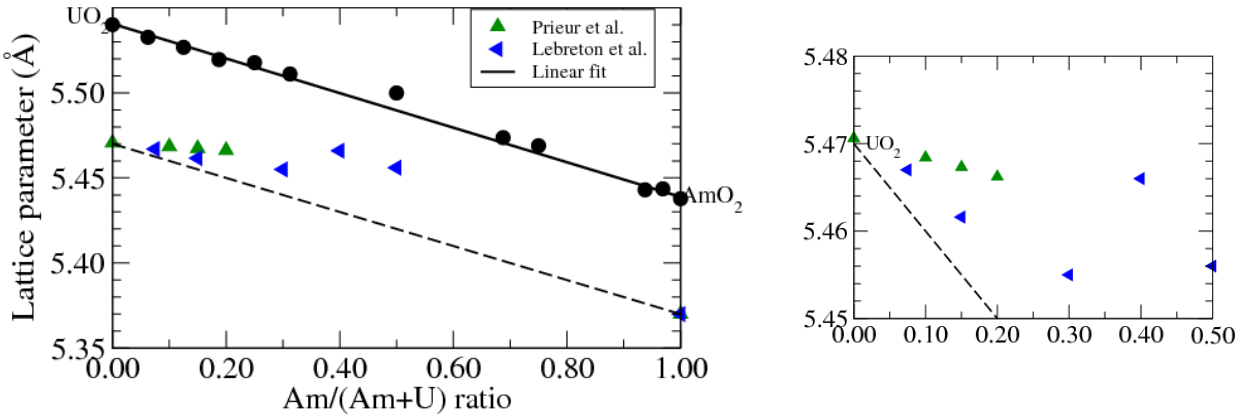

Figure 5.3: Lattice parameter of $U_{1-y}Am_yO_2$ computed using DFT+U compared to the experimental data. The black circles represent the calculated values fitted by a linear expression (black line), the diamonds (blue and green) are the XRD experiments and the dotted line is the evolution of the lattice parameter obtained by a linear combination of the UO_2 and AmO_2 experimental lattice parameters. On the left, zoom of the experimental data over the 0 to 50% Am concentration range.

One can clearly see that the calculated lattice parameter of $U_{1-y}Am_yO_2$ as a function of Am content follows a linear behaviour (black line) expected for a stoichiometric ideal solid solution. We also observe that although our results (black line) show a slight overestimation (∼1.3% which is in the error margin of the GGA+U method) compared to the dotted line which is yielded by linear combination of the experimental data, both lines have the same slope. Note that the change in cation valence does not have a significant effect on the evolution of the lattice parameter as a function of the composition. In other words, the evolution of the lattice parameter remains linear as in the case of (U,Pu)O_2 or (U,Ce)O_2 in which the valence states of cations do not change. The compensation mechanisms between U and Am cations could account for this behaviour. While the reduction of Am (+IV) to Am (+III) is associated to an increase (∼11.5%) in the ionic radius from 0.95 Å to 1.09 Å, the oxidation of U (+IV) to U (+V) is associated to a decrease (∼11.2%) in the ionic radius from 1.01 Å to 0.89 Å. One can also see that the experimental values (blue and green diamonds) are scattered. Lattice expansion under self-irradiation effects, which is known to occur in ^{241}Am-bearing oxides [4, 6, 161] can account for this discrepancy between experiments and our results. Moreover, the evolution of the experimental values as a function of the Am content does not have the same slope as the lines from the linear combination of UO_2 AmO_2 lattice parameters (black and dotted lines) which is the behaviour expected for a stoichiometric ideal solid solution.The deviation from stoichiometric (enhanced for %Am$>$ 30) combined with the oxygen interstitial formation observed by Lebreton *et al.* [6] in the samples they characterized could account for this behaviour.

The comparison between calculated data and the XRD ones is thus impossible due to self-irradiation effects, oxygen vacancies and interstitials as mentioned above. It would be interesting to further investigate in the framework of DFT+U the effect of point defects as well as cluster defects on the structural properties of $U_{1-y}Am_yO_2$ mixed oxides, especially on the lattice parameter in order to support the experimental studies. It will be investigated in near future.

5.4.2 Interatomic distances

In order to provide a deeper unterstanding of the effect of the Am content on the atomic local environment of UO_2 oxide and more details on the structure of $U_{1-y}Am_yO_2$, interatomic distances are analysed and reported in Table 5.5. We also reported in parenthesis the relative variation Δd of the interatomic distances with respect to the experimental (resp. calculated) distances in pure UO_2 defined as :

$$\Delta d = \left| \frac{d - d_{ref}}{d_{ref}} \right| \tag{5.3}$$

where d_{ref} is the U-O interatomic distance in the UO_2 pure oxide.

Though our DFT+U results show a slight overestimation (which is a well known tendency of the DFT+U method as stated previously) of bond lengths compared to the EXAFS results, one can see that our results are in good agreement with the experimental data by Prieur *et al.* [26]. In particular, the calculated variation of U-O distance equals to $\Delta d = \sim 2\%$ is in good agreement with the measured one.

The bond length of the first oxygen atoms surrounding Am(+III) cation is about 2.46 ± 0.02 Å which is in agreement with that obtained for the Am(+III)-O distances in pure Am_2O_3. For Am content equal to 75%, in addition to Am(+III)-O chemical bonds, we also have Am(+IV)-O bonds measuring 2.36 Å. This latter bond length is consistent with Am(+IV)-O distance found (in this study) in AmO_2 pure oxide.

Table 5.5: Interatomic distances of $U_{1-y}Am_yO_2$ in comparison with the EXAFS experiments [26]. In parenthesis are the relative variation Δd defined in Eq 5.3. These distances are the average distance over the first coordination shell of a given species with a statistical error 0.02 Å. (*) corresponds to Am(+III)-O/Am(+IV)-O distances.

	y(%)	**Distances (Å)**			
		$\mathbf{d_{U\text{-}U}}$	$\mathbf{d_{U\text{-}Am}}$	$\mathbf{d_{U\text{-}O}}$	$\mathbf{d_{Am\text{-}O}}$
	0.00	3.89	/	2.40	/
	6.25	3.90	3.90	2.35(0.02)	2.47
	12.50	3.90	3.89	2.34(0.02)	2.47
Exp. [26]	15.00	3.86	3.87	2.33(0.02)	2.43
	50.00	3.90	3.90	2.34(0.02)	2.46
	75.00	3.88	3.90	2.33(0.01)	2.44/2.36*

The first U(+IV)-O distances (2.35 ± 0.02 Å) are slightly shorter than in UO_2 pure oxide 2.40 ± 0.02 Å indicating the structural modification due to the presence of Am. The first U(+IV)-U(+IV) or U(+IV)-Am(+III) bond lengths are 3.90 ± 0.02 Å. The same bond length for both U(+IV)-U(+IV) and U(+IV)-Am(+III) indicates a random distribution in the cationic sublattice which is similar to an ideal solid solution behaviour.

5.5 Energetic properties

To evaluate the stability of alloyed compounds, the free enthalpy of mixing is usually considered [122,155,162]. The Gibbs free energy of mixing refers to the energy difference of a configurationally random alloy where the atomic species randomly occupy lattice positions [163] with respect to the pure compounds.The Gibbs free energy of mixing is given by:

$$\Delta G_{mix} = \Delta H_{mix} - T\Delta S_{mix} \tag{5.4}$$

where ΔH_{mix} is the mixing enthalpy and ΔS_{mix} the mixing entropy. For the zero temperature, $\Delta G_{mix} = \Delta H_{mix}$.
The mixing enthalpy of $U_{1-y}Am_yO_2$ is defined as:

$$\Delta H_{mix}(y) = H^{U_{1-y}Am_yO_2} - (1-y)H^{UO_2} - yH^{AmO_2} \tag{5.5}$$

The mixing enthalpy is computed in the current study using both SQS configurations and a parametric approach introduced by Sluiter [162] and already used for $U_{1-y}Pu_yO_2$ [122]. The parametric approach is based on a polynomial representation of $\Delta H_{mix}(y)$. Assuming a third-order cubic representation and using the limiting conditions $\Delta H_{mix}(0) = \Delta H_{mix}(1) = 0$ corresponding to the pure elements, it can be shown that:

$$\Delta H_{mix}(y) = \Delta H_{sol}^{U \text{ in } AmO_2} y^2(1-y) + \Delta H_{sol}^{Am \text{ in } UO_2} y(1-y)^2 \tag{5.6}$$

where $\Delta H_{sol}^{U \text{ in } AmO_2}$ and $\Delta H_{sol}^{Am \text{ in } UO_2}$ are the solution enthalpies for uranium in the lattice of AmO_2 and vice versa respectively. Fore more details see Refs [122, 155, 162].

The parametric approach has been successfully used in β-Ti with transition elements [155] and in $U_{1-y}Pu_yO_2$ mixed oxides [122].

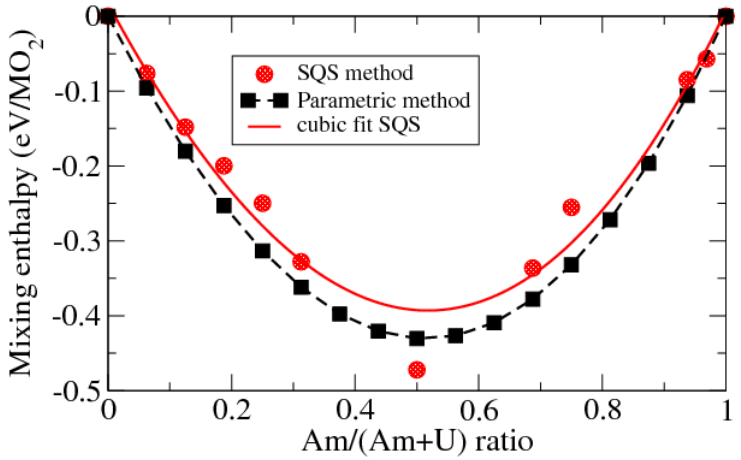

Figure 5.4: Solid solution mixing enthalpy $\Delta H_{mix}^{SQS}(y)$ and $\Delta H_{mix}^{Par}(y)$ of $U_{1-y}Am_yO_2$ calculated using the SQS configurations and the parametric approach.

Fig. 5.4 shows $\Delta H_{mix}^{SQS}(y)$ and $\Delta H_{mix}^{Par}(y)$ over the whole range of composition. The enthalpy of mixing of UO_2 and AmO_2 is found negative in the entire range of Am concentrations whatever the method used indicating that there is no phase separation related to the variation of Am content. Moreover, we can see that all the points lie on, or are very close to the convex hull of the calculated enthalpies, suggesting the absence of demixing into intermediate phases. For a ratio Am/(Am+U) equal to 50%, the

compound is more stable than all the other compositions. However, it is not excluded that it could be possible to find another similar configuration (SQS) with a mixing enthalpy closer to the cubic adjustment (red curve) than that shown in Fig.5.4. Indeed, the configurations resulting from the SQS approach do not systematically lead to the lowest-energy configuration but to a configuration as disordered as possible. Note that the mixing enthalpy absolute values in $U_{1-y}Am_yO_2$ are about 100 times larger than the ones obtained in $U_{1-y}Pu_yO_2$ (using the same SQS configurations) [122] indicating the higher stability of mixed uranium-americium oxides compared to the mixed uranium-plutonium oxides. This larger stability compared to mixed uranium-plutonium oxides is probably related to the charge-tranfer reaction between U^{4+} and Am^{4+} that takes place in (U,Am)O_2 mixed oxide.

$\Delta H_{mix}^{Par}(y)$ and $\Delta H_{mix}^{SQS}(y)$ show a rather good agreement with each other, with the maximum difference of not more than 40 meV per unit cell, suggesting that the parametric approach for for $U_{1-y}Am_yO_2$ solid solution makes sense.

These ΔH_{mix} results are the first prediction and are useful for the CALPHAD method for the computation of the phase diagram of the U-Am-O system since this phase diagram is not fully established yet.

5.6 Oxygen vacancies stability

It has been shown in early studies [39, 40] that oxygen vacancies in UO_2 are the most dominant point defects in accessible range of the Fermi level in the band gap whatever the external conditions. The main objective of this section is to evaluate the influence of the presence of americium on the oxygen vacancy stability in UO_2. We have only considered here an americium content equals to 6.25% corresponding to two atoms in the 96-atom supercell. We recall that an oxygen atom is located in a tetrahedral environment consisting of four actinide cations. For Am/(U+Am)=6.25%, there is three possible initial chemical environments (containing U and/or Am atoms) around an oxygen vacancy as shown in Fig. 5.5. The tetrahedron formed by : (i) two Am^{3+} and two U^{4+} is termed config. 1, (ii) one U^{5+}, one Am^{3+}, and two U^{4+} is termed config. 2 and (iii) four U^{4+} is termed config. 3.

We assess the energetically most favorable configuration for oxygen vacancies and we report our results in Table 5.6. Note that the valence state of cations in the supercell as displayed in Table 5.2 is not affected by the change in chemical environment around the oxygen vacancy. Eq. 4.1 is adapted and used to calculate the formation energies of oxygen vacancies in (U,Am)O_2 :

$$E_f(X,q) = E_{tot}(X,q) + E_{corr} - E_{tot}(bulk) + \mu_O^{(U,Am)O_2} + q\mu_e \tag{5.7}$$

where E_{tot}(X,q) is the total energy of the (U,Am)O_2 supercell containing the defect X with charge q and E_{tot}(bulk) is the energy of the perfect system and E_{corr} are the corrections used for charged supercells. $\mu_O^{(U,Am)O_2}$ is the oxygen chemical potential in (U,Am)O_2 given by $\mu_O^{(U,Am)O_2} = \frac{1}{2}\mu_O^{O_2} + \Delta\mu_O$ (see Sec. 4 for more details about this equation). For comparison with UO_2, we use $\Delta\mu_O = -2.19\,eV$ in oxygen-rich conditions which is the same value used for UO_2 [39].

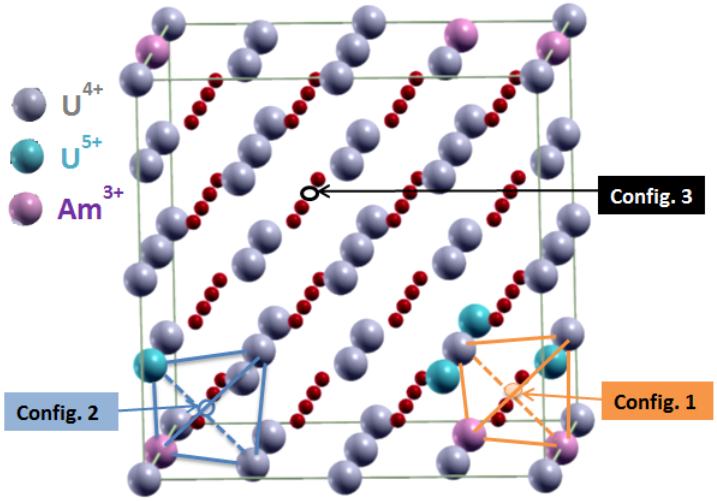

Figure 5.5: 96-atom supercell containing 32 cations (U and Am) in the *fcc* sites and 64 oxygen atoms (red balls) in the tetrahedral sites. Config. *i* is formed by one oxygen vacancy in a tetrahedron environment occupied by : 1) 2 Am^{3+} (pink balls) 2 U^{4+} (gray balls), 2) 1 Am^{3+}, 1 U^{5+} (green balls) and 2 U^{4+}, and 3) 4 U^{4+}.

One can see that the energetically most favorable configuration is the one including two Am^{3+} in the first coordination shell, and thus, two U^{5+} in the second coordination shell of the defect. This results was expected since we showed in Sec. 5.3.1 that an oxygen vacancy in (U,Am)O_2 releases two electrons that localized preferably on two U^{5+}, leading to their reduction to two U^{4+}. Thus, the two electrons liberated by the O vacancy must find easily two U^{5+} in the vicinity of the defect, which is possible only in config. 1. Our result support the only EXAFS result by Epifano [16] which shows that the neutral oxygen vacancy in (U,Am)O_2 are formed in the vicinity of americium cations. The config. 3 is about 0.2∼0.3 eV higher in energy than the config. 1 and 2. This energy difference can be seen as the additional energy required to the localization of the excess electron on U^{5+} atom when the vacancy is far from the second coordination shell of the defect.

The subsequent study of this section is performed considering the config. 1. The stability of oxygen vacancies are evaluated considering possible charge states of the vacancy (V_O^X, $V_O^{\bullet}$, $V_O^{\bullet\bullet}$).

Table 5.6: Formation energies of oxygen vacancies as a function of the chemical environment in terms of the first coordination shell of the vacancy.

Initial chemical environnment	Formation Energy (eV)
2 $Am^{3+}$and 2 U^{4+}	1.1
1 Am^{3+}, U^{5+} and 2 U^{4+}	1.2
4 U^{4+}	1.4

Results are shown in Fig. 5.6 in which external conditions are oxygen-rich conditions. One observes three stability domains over the Fermi level in the band gap: (i)

the partially ionized defects $V_O^{\bullet\bullet}$ (q=2) over the range from 0 to 0.1 eV, (ii) the ionized defects $V_O^{\bullet}$ (q=1) over the range from 0.1 to 0.5 and (iii) the neutral defects V_O^X over the rest of the Fermi level range.

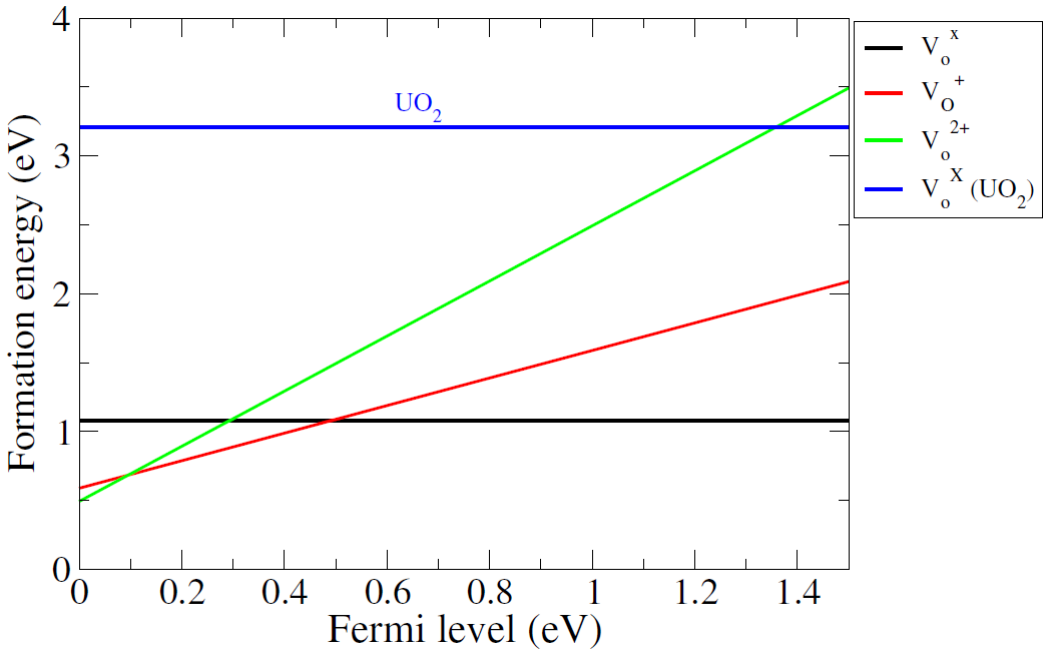

Figure 5.6: Formation energy of the oxygen vacancy in three possible charge states as a function of the Fermi level in the band gap of $U_{0.9375}Am_{0.0625}O_2$. The black line corresponds to the neutral oxygen vacancy (V_O^X), the red one to the +1 charged vacancy ($V_O^{\bullet}$) and the green one to the +2 charged defect ($V_O^{\bullet\bullet}$). The blue line is the neutral oxygen vacancy in UO_2. Oxidizing conditions are considered i.e. oxygen-rich conditions ($\Delta\mu_O = -2.19\,eV$).

In order to evaluate the effect of Am atom on the oxygen vacancy stability in UO_2, we compare the formation energy of the neutral oxygen vacancy in (U,Am)O_2 with the one obtained in UO_2. We use the same external condition for (U,Am)O_2 and UO_2 and results are shown in Fig. 5.6. We can observe that formation energy of a neutral oxygen vacancy in UO_2 is higher than in (U,Am)O_2. This result indicates that the presence of Am in UO_2 facilitates the formation of oxygen vacancies and the formation of hypo-stoichiometric (U,Am)O_2 compounds.

5.7 Conclusion

Electronic structure, structural and energetic properties and oxygen vacancies stability are calculated in this chapter using GGA+U calculations in combination with the SQS approach of chemical disorder.

$U_{1-y}Am_yO_2$ mixed oxides show particular cation valence states which are fundamentally different from other mixed oxides like $U_{1-y}Pu_yO_2$ and $U_{1-y}Ce_yO_2$. Indeed, in $U_{1-y}Am_yO_2$, Am acts as an electron acceptor whereas U acts as an electron donor according to the $Am^{4+} + U^{4+} \longrightarrow Am^{3+} + U^{5+}$ mechanism. These results are in good agreement with early XANES experiments (limited to %Am<20) but also al-

low to complete them by providing a larger description of Am-bearing oxides over the entire range of Am content. We show that for %Am<50, all Am(+IV) are reduced to Am(+III) whereas U has mixed valence (+IV and +V). On the contrary, when %Am>50, Am(+IV) is partially reduced to Am(+III) whereas all U(+IV) cations are oxidized to U(+V). This study shows that the lattice parameter as a function of the Am content follows a rather linear behaviour that cannot be experimentally observed owing to the deviation from stoichiometry combined with the presence of oxygen interstitials (enhanced for the large Am content higher than 40%) observed in samples that have been experimentally characterized in the early studies and subject to self irradiation. It would be interesting to further investigate in the framework of DFT+U the effect of point defects as well as cluster defects on the structural properties of $U_{1-y}Am_yO_2$ mixed oxides, especially on the lattice parameter. In addition, we show that U-Am and U-U bond lengths are identical on average which is the signature of the random distribution of cations in the cation sublattice. Thus, our study is the first confirmation of the ideal solid solution behaviour (from the structural point of view) of $U_{1-y}Am_yO_2$ provided a perfect defectless and stoichiometric compound could be obtained. Using two approaches (SQS and parametric), we show with a satisfactory agreement between both approaches that there is no demixing in $U_{1-y}Am_yO_2$ in the whole range of Am content at low temperature. This study is the first assessment of the mixing enthalpy of Am-bearing oxides, the minimum value being about -0.45 eV which (in absolute value) is 100 times higher than the value obtained for (U,Pu)O_2. Moreover, we show that a larger number of Am cations in the first coordination shell is associated to a more energetically stable oxygen vacancy. (U,Am)O_2 is thus found to more easily form oxygen vacancies than UO_2 and thus, forms more easily hypo-stoichiometry compound.

The results obtained in this chapter support the experimental studies and on the other hand, can be useful for the thermodynamic computational methods like CALPHAD.

Our results indicate that the presence of Am in UO_2 facilitates the formation of neutral oxygen vacancies. In addition, the presence of Am leads to the oxidation of U^{4+} to U^{5+} in such a manner that $[U^{5+}]=[Am^{3+}]$. These results on the effect of Am on UO_2 properties pave the way toward the investigation of the effect of Am on (U,Pu)O_2 material properties.

Chapter 6

Investigation of the effects of a low americium content on properties of $(U,Pu)O_2$

The goal of this chapter is to quantify the effect of a low americium content on electronic, structural, energetic and defect properties of uranium and plutonium mixed oxides.

Contents

6.1 Introduction

In the literature, very few studies have been conducted on Am-bearing uranium-plutonium mixed oxides. Yet, a better knowledge of material properties of these oxides, especially the data and mechanism related to the thermodynamic and atomic transport

properties as well material properties (mixing enthalpy a are necessary, elastic properties) to monitor the consequences of the presence of this element on the safety and the performance of the uranium-plutonium mixed oxide fuels. As preliminary studies in the literature, some authors [18] showed using a flash laser method that americium leads to a decrease in thermal conductivity. They showed that the thermal conductivity up to 1500 K satisfies classical phonon transport. However no confirmation of these studies exists up to now.

Kato and Konashi [109] proposed a model to calculate the lattice parameter as a function of the Pu content, Am content and O/M ratio. However, the authors assume in the model that all cations keep their oxidation state (+IV), although an electron charge transfer (between U and Am cations) is known to occur in Am-bearing mixed oxides as (U,Am)O_2 mixed oxides (see Chap. 5). Regarding the oxidation state of cations in (U,Pu,Am)O_2 mixed oxides, the americium as well as the uranium valence state appears to be still not univocally identified. More recently, Vauchy *et al.* [164] showed that the valence state of Am cations in (U,Pu)O_{2-x} mixed oxides depends on the U-Pu cation distribution. However, there exists up to now no additional confirmation of these studies and thus, electronic structure calculation is expected to address this issue in detail. On the other hand, modelling (U,Pu,Am)O_2 is challenging because we do not know the exact distribution of the americium cations in (U,Pu)O_2 solid solution. Note that the elementary mechanisms (point defect formation, atomic transport, fission gas trapping etc ...) governing the fuel behaviour under irradiation have never been studied yet in the literature.

In this chapter, we first propose an approximation to model (U,Pu,Am)O_2 containing a few percent of americium (smaller than 10%). In the second section, we address the valence state of cation in (U,Pu,Am)O_2 considering stoichiometric and hypostoichiometric conditions. Then we evaluate the effect of americium on the structural, elastic and energetic (mixing enthalpy) properties. Finally, we assess the influence of americium on the point defect properties.

6.2 Computational details

Our DFT calculations in this chapter are carried out using the same code (ABINIT) and same functionals as in the previous chapters (Chap. 4 and Chap. 5).

The onsite Coulomb terms U and J are set in the mixed oxides to the same values as for the pure compounds UO_2, PuO_2, and AmO_2 i.e. $(U\ ;\ J) = (4.50\ ;\ 0.54)$ eV for UO_2, (4.00 ; 0.70) eV for PuO_2, and (6.00 ; 0.75) eV for AmO_2. Based on the approximation mentioned in Chap. 5, Sec. 5.2, we use as starting point for searching the ground state, the *5f* orbital occupation matrices of U in UO_2, Pu in PuO_2 and Am in AmO_2.

For the same reasons as in the previous chapters, we apply the 1k antiferromagnetic order. All crystal symmetries are switched off.

Results are obtained using a plane-wave cutoff energy equal to 871 eV with the ABINIT code. According to our convergence tests, this input parameter lead to a precision lower than 1 meV per atom on physical energies (total energy differences).

96-atom fluorite supercells (2×2×2) are used. The calculations are done on a 2×2×2 k-point mesh generated by the Monkhorst-Pack [114] method, which is sufficient for an energy convergence smaller than 0.3 meV per atom. We performed full relaxation of the cell until the pressure acting on the system becomes lower than 5.10^{-7} Ha/bohr^3 (∼0.15 kbar) and until forces, for the structural optimization, become smaller than 5.10^{-4} Ha/bohr (∼0.025 eV/Å).

6.3 Modelling of (U,Pu,Am)O_2

It is well known that (U,Pu)O_2 forms an ideal solid solution [25, 41] and thus, the simulation boxes required for its modelling can be obtained through the SQS configurations as shown in Ref. [29]. Our purpose in this section is to add a few percent (<10%) of americium to this solid solution with 25% of plutonium. The challenge here is to build the simulation boxes (from the (U,Pu)O_2 one with 25% of Pu) needed for a representative modelling of (U,Pu,Am)O_2. Note that the literature does not propose any investigation on this compound based on electronic structure calculations.

The Am contents considered in this chapter are 3.125% and 6.25% corresponding to one and two cations out of thirty two (thirty two corresponds to the total number of cations in our simulation box). To build the simulation box needed for the modelling of (U,Pu,Am)O_2, we assumed that the Am content (3.125% or 6.25%) considered in this study is sufficiently low compared to the ones of U (71.875% or 68.75%) and Pu (25%) to be treated as an impurity diluted in a solid solution of (U,Pu)O_2. In practice, one or two U atoms are substituted by one or two Am atoms so as to have a $U_{0.75-z}Pu_{0.25}Am_zO_2$ composition. Then, the relative stability of the supercells is studied as a function of the Am chemical environment in terms of the number of U and Pu neighbouring cations. For z= 3.125%, we consider three different chemical environments in terms of U and Pu cations surrounding Am that we term "configuration" in the subsequent study. Indeed, for the $U_{0.75}Pu_{0.25}O_2$ solid solution (obtained from the SQS approach), our simulation box (96 atoms) offers only three possible configurations. These are the configuration formed by: (i) 4 Pu and 8 U termed Conf.1, (ii) 2 Pu and 10 U termed Conf.2, and (iii) 1 Pu and 11 U termed Conf.3 (see Figure 6.1). For each of these configurations we calculate the total energy of the crystal and we display the energy difference in Table 6.1. One can observe that the most energetically favourable configuration is Conf.3 which is 180 meV lower in energy than Conf.1 and 67 meV than Conf.2. This indicates that the more U atoms around the Am atom, the more stable the configuration is.

Now, we want to build the simulation box for z= 6.25% of Am (i.e. 2 Am/32 cations). For this, we retrieve the above Conf.3 (since it is the most stable) and we add another Am atom considering two different chemical environments in terms of U and Pu cations around the Am atom. We term Conf.3.1 the chemical environment containing 1 Pu and 11 U and Conf.3.2, the one containing 2 Pu and 10 U. One observes that Conf.3.1 is slightly more stable (36 meV lower in energy) than Conf.3.2. This result confirms once again that the more U atoms around the Am atom, the more stable the configuration is. The electron charge transfer known to occur between U and Am cations can explain why an Am atom is more stable near an U atom rather than a Pu atom (see Chap. 5). However, the fact that the relative stability of the crystal so depends on the number of U cations surrounding an Am atom is surprising.

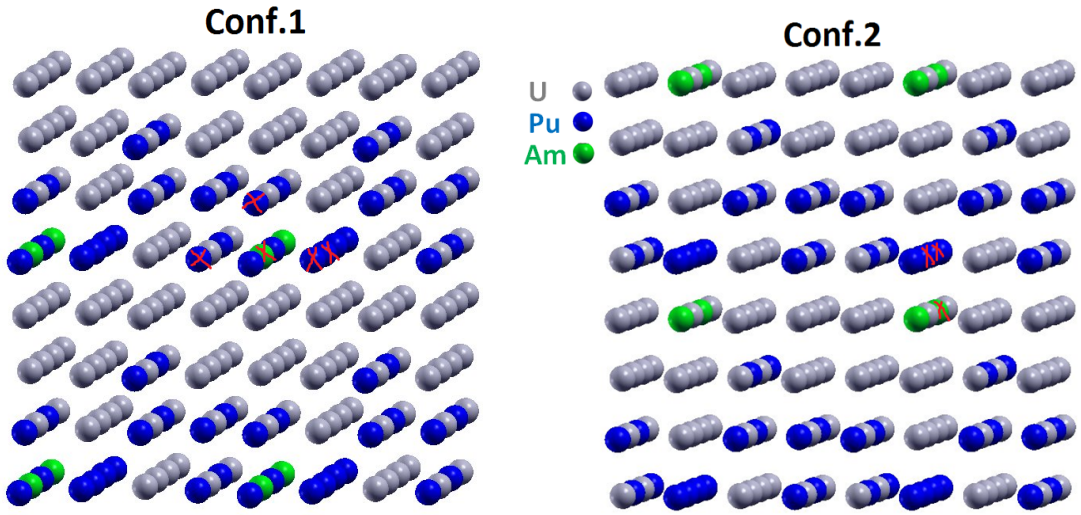

Figure 6.1: 96-atom supercell containing 32 cations (U, Pu, Am) in the *fcc* sites (25% of Pu and 3.125% of Am). To make the figure more visible, the 64 oxygen atoms located in the tetrahedral sites were removed. Periodic boundary conditions are applied in order to easily identify all U (gray balls) and Pu (blue balls) cations surrounding the Am (green balls) atom inserted. The inserted Am atom and its neighbouring Pu are indicated by a red symbol.

Indeed, one could expect to have the same total energy for the configurations having at least one U atom in the vicinity of Am. We will address this issue more in the next section by studying valence state of U, Pu, and Am cations in stoichiometric and hypo-stoichiometric (U,Pu,Am)O_2.

Table 6.1: Energy difference between the crystals with different chemical environment around the Am atom for 3.125% and 6.25% of Am.

	Initial Chemical environment around Am	Energy difference difference meV
%Am= 3.125	Conf.1: 4 Pu and 8 U	180
	Conf.2: 2 Pu and 10 U	67
	Conf.3: 1 Pu and 11 U	0
%Am= 6.25	Conf.3.1: 1 Pu and 11 U	0
	Conf.3.2: 2 Pu and 10 U	36

6.4 Valence state of U,Pu, and Am in mixed oxides

The data on cation valence investigated in this section can make it possible to improve the thermodynamic model describing the uranium-plutonium mixed oxides containing americium and also to support the early experimental studies. In the literature, the americium valence state appears to be still not univocally identified within uranium-plutonium mixed oxides. The first studies by Osaka et *al.* [107] reported only an oxidation state of +III for Am whereas U cations have a mixed valence state (+IV/+V). More recently, Vauchy et *al.* [164] showed that the valence state of Am cations in sub-stoichiometric (U,Pu)O_{2-x} mixed oxides depends on the U-Pu distribution. Indeed,

these latter showed that americium exhibits a mixed valence (+III/+IV) when the mixed oxide shows some U-Pu distribution heterogeneities, whereas it is purely tetravalent when (U,Pu)O_{2-x} is homogeneous. However, the investigations by Vauchy et *al.* remain the only study evidencing this behaviour. Our purpose in this section is to address in detail the valence state of the U, Pu and Am cations within $U_{0.7-z}Pu_{0.25}Am_zO_2$ (stoichiometric and hypo-stoichiometric) mixed oxides using the SQS approach to describe the (U,Pu)O_2 solid solution. This study is the first theoretical study aiming at investigating the valence state of cations in the (U,Pu,Am)O_2 mixed oxides. Note that $U_{0.7-z}Pu_{0.25}Am_zO_2$ obtained from the SQS approach shows a rather heterogeneous U and Pu distribution at the atomic scale (see the structures from Fig. 6.1).

6.4.1 Stoichiometric conditions

We study the oxidation state of the U, Pu and Am cations within $U_{0.7-z}Pu_{0.25}Am_zO_2$ in the stoichiometric conditions (i.e. O/(U+Pu+Am)=2.00) considering z=0.03125 (3.125%) and 0.0625 (6.25%). Table 6.2 displays the evolution of the cationic species concentration. One can see that Am(+IV) cations are all reduced to Am(+III), uranium cations show a mixed valence (+IV/+V) with [U(+V)]=[Am(+III)], whereas plutonium cations keep their oxidation state (i.e. +IV). The chemical formula of the (U,Pu,Am)O_2 mixed oxides in this case can be written as $U^{+IV}_{1-2z}U^{+V}_zPu^{+IV}_{0.25}Am^{+III}_zO_2$, confirming that there is an electronic charge transfer from uranium atoms to americium atoms. This result is not surprising since we pointed out in Chap. 5 an oxidoreduction reaction of type $Am^{+IV} + U^{+IV} \longrightarrow Am^{+III} + U^{+V}$.

The relative stability as a function of the number of U cations around the Am atom (shown in Table 6.1) could likely result from the difference in Am(+III)-U(+IV) and Am(+III)-Pu(+IV) electrostatic interactions. Indeed, depending on the number of Pu and U atoms surrounding a given Am atom, the local electrostatic interactions can be strongly affected, which lead to a difference in the total energy of the system.

Table 6.2: Valence states of cations (U, Pu, Am) in $U_{0.75-z}Pu_{0.25}Am_zO_2$ mixed oxides. The total Am atomic fraction (z) as well as the atomic fractions of all cations in the crystal are displayed. O/M (M=U+Pu+Am) is the oxygen/metal ratio.

	Atomic fraction (%)						O/M
z	U(+IV)	U(+V)	Pu(+III)	Pu(+IV)	Am(+III)	Am(+IV)	
3.125	68.750	3.125	0.000	25.000	3.125	0.000	2.00
6.250	62.500	6.250	0.000	25.000	6.250	0.000	2.00

6.4.2 Hypo-stoichiometric conditions

We also investigate the valence of U, Pu, and Am cations in hypo-stoichiometric $U_{0.75-z}Pu_{0.25}Am_zO_{2-x}$. In order to induce hypo-stoichiometry, an oxygen vacancy is created in Conf.3 (for z= 3.125%) and Conf.3.1 (for z= 6.25%) supercells. Results are displayed in Table 6.3. We can see that in hypo-stoichiometric $U_{0.75-z}Pu_{0.25}Am_zO_{2-x}$ mixed oxides, all Am cations are found to have an oxidation state of +III, whereas uranium cations are found to be tetravalent U(+IV). According to the Am content, Pu cations

have either a mixed valence (+III/+IV) or remain tetravalent (i.e. Pu(+IV)). Indeed, the electrons released by the neutral oxygen vacancy first localize on U(+V) cations (note that the U(+V) cations are found to be the first neighbours of the Am(+III) cations), leading to their reduction to U(+IV). Then, the Pu (+IV) cations can only be reduced to Pu(+III) if all Am(+IV) cations are already reduced to Am(+III) and all U(+V) to U (+IV). This result confirms the one of Vauchy et *al.* [164]. Indeed, these latter showed that, in hypo-stoichiometric $U_{0.750}Pu_{0.246}Am_{0.004}O_{2-x}$ with a heterogeneous distribution of U and Pu cations within the solid solution, the reduction of Am(+IV) to Am(+III) is completed before any reduction of Pu(+IV) cation to Pu(+III).

Table 6.3: Valence states of cations (U, Pu, Am) in $U_{0.75-z}Pu_{0.25}Am_zO_{2-x}$ mixed oxides. The total Am atomic fraction (z) as well as the atomic fractions of all cations in the crystal are displayed. O/M (M=U+Pu+Am) is the oxygen/metal ratio.

	Atomic fraction (%)						O/M
z	U(+IV)	U(+V)	Pu(+III)	Pu(+IV)	Am(+III)	Am(+IV)	
3.125	71.875	0.00	3.125	21.785	3.125	0.000	1.97
6.250	62.750	0.00	0.000	25.000	6.250	0.000	1.97

In summary, Am(+IV) cations in (U,Pu)O_2 mixed oxides tend to easily reduce to Am(+III): (i) in stoichiometric compounds, the reduction of Am(+IV) is compensated by the oxidation of U(+IV) to U(+V). (ii) hypo-stoichiometry in americium-bearing uranium-plutonium oxides is accommodated by the reduction of all U(+V) cations (since all Am(+IV) are completely reduced to Am(+III) in a case of a low Am content) before any reduction of Pu cations. This allows us to highlight that americium exhibits a higher oxygen potential than Pu and U, and thus induces an increase in the oxygen potential in uranium-plutonium mixed oxides.

6.5 Structural, elastic and energetic properties

The aim of this section is to evaluate the effect of americium on lattice parameters, interatomic distances, bulk modulus, and mixing enthalpy of uranium-plutonium mixed oxides with 25% of plutonium.

6.5.1 Lattice parameters

The lattice parameters of $U_{1-y-z}Pu_yAm_zO_2$ compounds were evaluated by Kato and Konashi [109] using XRD. These latter proposed a model to calculate the lattice parameters as functions of Pu content, Am content and O/M ratio:

$$a = 4\sqrt{3}\left[\left((1-y-z)r_{U^{4+}} + yr_{Pu^{4+}} + zr_{Am^{4+}}\right)\left(1 + 0.112x + r_{O^{2-}}\right)\right] \qquad (6.1)$$

where x is the deviation from the stoichiometry and r is the ionic radius of the species.

In this model, the authors considered that Am^{4+} was stable in the stoichiometric (U,Pu)O_2 having a low Am content. On the contrary, we showed in the previous section that Am is more stable under Am^{3+} form in (U,Pu)O_2, leading to a partial oxidation of U^{4+} to U^{5+}. Therefore, for a fine description of the lattice parameters of $U_{1-y-z}Pu_yAm_zO_2$, this model has to be improved.

We calculate the lattice parameters of $U_{0.75-z}Pu_{0.25}Am_zO_2$ (in Conf.3.1) with z=3.125% and 6.125%. Our results are displayed in Table 6.4. It was not possible to compare our values to other ones because the compositions evaluated in this study were never studied in the literature. We can see that the lattice parameters of $U_{0.75-z}Pu_{0.25}Am_zO_2$ decrease with increasing Am content, in agreement with the early studies [41]. Moreover, the evolution of the lattice parameter as a function of Am content (for the compositions evaluated) is not linear as in $U_{1-y}Pu_yO_2$. However, it would be important to extend this study to higher Am contents in order to unequivocally conclude on the evolution of the lattice parameter.

Table 6.4: Lattice parameters, bulk moduli as well as mixing enthalpy of $U_{0.75-z}Pu_{0.25}Am_zO_2$ mixed oxides as a function of Am content.

z(%)	0.000	3.125	6.250
a(Å)	5.514	5.507	5.505
B_0 (GPa)	197*	191	193
ΔH_{mix} (meV)	-4.3	-34	-87

*Ref. [29]

6.5.2 interatomic distances

The objective of this section is to evaluate the effect of Am on U-U, U-Pu, Pu-Pu, O-Pu, and O-U crystallographic distances with respect to their values in $U_{0.75}Pu_{0.25}O_2$. To access these distances, we make an average on all interactomic distances (of the same type) in our simulation box considering periodic boundary conditions.

We still consider two Am contents, z=3.125% and 6.25% and we display our results in Table 6.5. We can observe that the presence of Am has no noticeable effect on the M-M bond length (M= U or Pu) compared to the M-M ones in $U_{0.75}Pu_{0.25}O_2$ (∼3.90 Å). On the other hand, one observes a very slight decrease in U-O bond lengths of the first oxygen atoms surrounding the U cations of about 0.01 Å for z = 0.0625. This result could be expected since we showed in the previous section that the presence of Am leads to a slight decrease in the lattice parameter of $U_{0.75}Pu_{0.25}O_2$ mixed oxides.

It is satisfactory to observe that the Am-O bond length (∼2.45 Å) is not far from its reference value in Am(+III)-O (2.47 Å), confirming the trivalent character of Am cation in (U,Pu,Am)O_2 mixed oxide.

Note that the U-Am and Pu-Am distances (3.89 Å) are almost identical to the M-M (M=Pu or U) distances (about 3.90 Å).

Table 6.5: Interatomic distances in $U_{0.75-z}Pu_{0.25}Am_zO_2$ mixed oxides as a function of Am content.

	Interatomic distances (Å)				
z (%)	d_{U-U}	d_{Pu-Pu}	d_{U-Pu}	d_{U-O}	d_{Pu-O}
0.000	3.90	3.89	3.89	2.393	2.370
3.125	3.90	3.87	3.89	2.390	2.370
6.250	3.90	3.88	3.89	2.386	2.367

6.5.3 Elastic properties

We recall that the bulk modulus characterizes a response of a material to an isotropic pressure. As in Chap. 3, the bulk moduli of $U_{0.75-z}P_{0.25}Am_zO_2$ are calculated by imposing small deformations of the supercell around the equilibrium volume. Then, the Birch-Murnaghan's equation of state (which connects the variation of the energy of the system to the volume and the bulk modulus) is used to fit the calculated values (volume and energy) in order determine the bulk modulus.

Table 6.4 shows the bulk moduli of $U_{0.75-z}P_{0.25}Am_zO_2$ for z= 3.125% and 6.25% in comparison with the value obtained in $U_{0.75}P_{0.25}O_2$ i.e. for z= 0. For both Am contents investigated, we obtained almost the same bulk modulus ($\sim$ 191 GPa). This value does not differ significantly from the one obtained in $U_{0.75}P_{0.25}O_2$ (196 GPa) [29], suggesting that Am in low concentration does not have a significant effect on the bulk modulus of uranium-plutonium mixed oxides.

6.5.4 Energetic properties

In this chapter, we also evaluate the mixing enthalpy of $U_{0.75-z}Pu_{0.25}AmzO_2$ mixed oxides still considering z= 0, 0.03125, and 0.0625. As in Chap. 5, the mixing enthalpy is defined as the energy of the following reaction:

$$(0.75-z)UO_2 + 0.25\,PuO_2 + zAmO_2 \longrightarrow U_{0.75-z}Pu_{0.25}Am_zO_2 \tag{6.2}$$

and thus,

$$\Delta H_{mix} = E_{tot}(U_{0.75-z}Pu_{0.25}Am_zO_2) - (0.75-z)E_{tot}(UO_2) - 0.25E_{tot}(PuO_2) - zE_{tot}(AmO_2) \tag{6.3}$$

were $E_{tot}(i)$ is the total energy from DFT+U calculations.

We recall that the mixing enthalpy (ΔH_{mix}) calculated here is equal to the mixing Gibb free energy (ΔG_{mix}) since calculations are done at zero temperature.

Our results are displayed in Table 6.4. We obtained negatives values for ΔH_{mix}, suggesting that there is no phase separation in $U_{0.75-z}Pu_{0.25}Am_zO_2$ solid solution in low temperature (room temperature) for the compositions evaluated. We can also observe that the presence of Am induces an important increase of ΔH_{mix} (absolute value), from -4.3 meV for %Am = 0 to -87 meV for %Am=6.25, making the reaction described in Eq. 6.2 very exothermic. The electronic charge transfer from U cations to Am cations can account for this behaviour. This result is in agreement with what was observed

in (U,Am)O_2. Indeed, ΔH_{mix} in (U,Am)O_2 (considering the absolute values) is 100 times higher than its value in (U,Pu)O_2 in which there is no electronic charge transfer in stoichiometric conditions.

6.6 Oxygen vacancy stability in (U,Pu,Am)O_2

The objective of this section is to study the influence of a low content of americium on the formation energy of point defects namely oxygen vacancy. For this, calculation are carried out considering the same chemical environments around the defect (number of U and Pu cations surrounding the defect) as in Cheik Njifon's PhD [29]. Then, we compare our result to Cheik Njifon ones to determine the effect of americum.

We consider four type of tetrahedral environment around the oxygen vacancy (knowing that an oxygen atom in (U,Pu,Am)O_2 is located in a tetrahedral occupied by the U, Pu or Am atoms). These are: (i) 0 Pu, 3 U and 1 Am termed 0Pu4U, (ii) 1 Pu, 2 U and 1Am termed 1Pu2U1Am, (iii) 2 Pu and 2 U termed 2Pu3U and (iv) 3 Pu and 1 U termed 3Pu1U (see Fig. 6.2). We do not take into account the potential effect of the geometric configuration i.e. the configurations obtained by changing the positions of the U and Pu cations (located on the tetrahedron). We only focus on the effect of the number of the U and Pu cation neighbours on the formation energy of the neutral oxygen vacancy and we only consider z= 0.03125 (3.125% of Am).

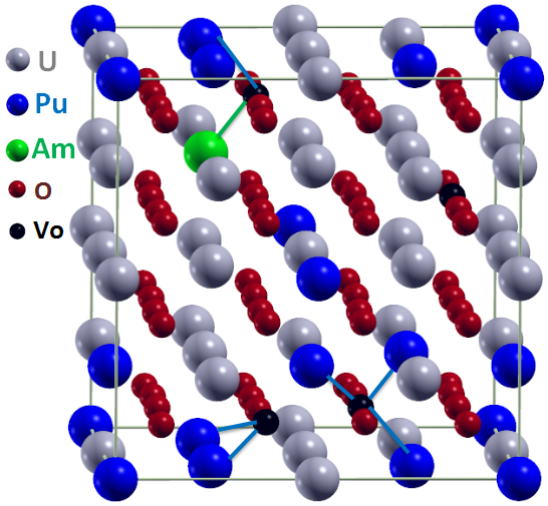

Figure 6.2: 96-atom supercell representing the simulation box used is this chapter showing the different chemical environments considered around an oxygen vacancy . Each oxygen vacancy (black balls) is connected to the surruonding Pu (blue balls) or Am (green balls) atoms by the blue or green lines.

For each configuration, we calculate the formation energies of the neutral oxygen vacancies and we display our results in Table 6.6. We consider here stoichiometric conditions corresponding to $\Delta\mu_O$ = -2.14 eV. This value has been determined for $U_{0.75}P_{0.25}O_2$ by Cheik in its PhD thesis see Ref. [29] and chosen here in order to make possible the comparison of our results to the ones obtained in $U_{0.75}P_{0.25}O_2$.

It has been shown in $U_{0.75}P_{0.25}O_2$ [29] that the chemical environment played a

major role in the stabilization of the oxygen vacancies. Indeed, these studies show that the chemical environment containing at least 2 Pu are the most energetically favorable, the energy difference between the most stable chemical environment and the less stable one being 0.5 eV. The author explains this large variation by the formation of electron polarons which consists in the reduction of the nearest (of the vacancy) Pu (+IV) to Pu (+III) with the local distortion associated.

Table 6.6: Formation energies of neutal oxygen vacancies in $U_{0.75-z}Pu_{0.25}Am_zO_2$ mixed oxides as a function of the chemical environment in terms of the U and Pu cations surrounding the vacancy. *In case of z=0, 1Pu2U1Am becomes 1Pu3U.

Chemical environment	Formation energy (eV)	
	z=0 (0% Am) [29]	z=0.03125 (3.125% Am)
0Pu4U	2.0	1.8
1Pu2U1Am*	1.8	1.9
2Pu2U	1.4	2.0
3Pu1U	1.4	1.9

From Table 6.6, we can see that in contrast to what was observed in $U_{0.75}P_{0.25}O_2$, the formation energy of a neutral oxygen vacancy in Am-doped $U_{0.75}P_{0.25}O_2$ are not affected by the change in the chemical environment: the formation energy remains constant whatever the chemical environment (in terms of Pu and U cations). Results presented in Sec. 6.4 could account for this behaviour. Indeed we have shown in this section that oxygen vacancies in $U_{0.75-z}P_{0.25}Am_zO_2$ induce first the reduction of U(+V) to U(+IV) (when Am are all trivalent) before any reduction of Pu(+IV). One of the perspectives here could be to extend this investigation to a larger Am contents in order to also consider chemical environment (around the oxygen vacancy) containing more than one Am cations. This would also allow evaluating the evolution of the formation energies of the oxygen vacancies as a function of Am content. The achievement of these objectives could need an increase of the size of our simulation box.

We can also observe that the formation energies of neutral oxygen vacancy in (U,Pu,Am)O_2 displayed in Table 6.6 are almost identical to the one of the most stable vacancy configuration in (U,Pu)O_2 whatever the chemical environment of the vacancy (even for the one containing 1Am). This result suggests that the presence of a low Am content in (U,Pu)O_2 does not have a significant effect on the formation energy of oxygen vacancies.

6.7 Conclusion

In this chapter, the effect of a low americium content on the electronic, structural, elastic, energetic and defect properties of uranium-plutonium mixed oxides is evaluated.

We first propose an approximation to model (U,Pu,Am)O_2 containing a few percent of americium (smaller than 10%). We show in agreement with Chap. 3 that the more U atoms around the Am atoms, the more stable the configuration is. The electron charge transfer known to occur between U and Am cations can explain why an Am cation is more stable near an U cation. Concerning the valence state of cations, we show that

Am(+IV) cations in (U,Pu)O_2 mixed oxides tend to easily reduce to Am(+III): (i) in stoichiometric compounds, the reduction of Am(+IV) is compensated by the oxidation of U(+IV) to U(+V). (ii) hypostoichiometry in americium-bearing uranium-plutonium oxides is accommodated by the reduction of all U(+V) cations (which result from the the presence of Am (+III) cation) before any reduction of the Pu cations. This allows us to highlight that americium exhibits a higher oxygen potential than Pu and U, and thus induces an increase in the oxygen potential in uranium-plutonium mixed oxides.

In addition, these results allow us to conclude that the relative stability as a function of the number of U cations around the Am atom could likely result from the difference in Am(+III)-U(+IV) and Am(+III)-Pu(+IV) electrostatic interactions. Indeed, depending on the number of Pu and U atoms surrounding a given Am atom, the local electrostatic interactions can be strongly affected, which lead to a difference in the total energy of the system.

We point out a decrease in the lattice parameters of $U_{0.75-z}Pu_{0.25}Am_zO_2$ with increasing Am content, in agreement with early studies [41]. Moreover, the evolution of the lattice parameter as a function of Am content (for the three compositions assessed) is not linear as in $U_{1-y}Pu_yO_2$. However, it would be important to extend this study to higher Am contents in order to unequivocally conclude on the evolution of the lattice parameter. We can observe that the presence of Am has no noticeable effect on the M-M bond length (M= U or Pu) compared to the M-M ones in $U_{0.75}Pu_{0.25}O_2$ ($\sim$3.90 Å). On the other hand, one observes a very slight decrease in U-O bond lengths of the first oxygen atoms surrounding the U cations of about 0.01 Å for 6.25% of Am. This result could be expected since we showed that the presence of Am leads to a slight decrease in the lattice parameter of $U_{0.75}Pu_{0.25}O_2$ mixed oxides. In addition, we show that the presence of Am in (U,Pu)O_2 has no noticeable effcet on the bulk modulus. In contrast, the mixing enthalpy of (U,Pu)O_2 is strongly affected by the presence of Am. Indeed the presence of Am leads to a rapid increase of the mixing enthalpy (absolute value) from -4 meV for %Am= 0 to -87 meV for %Am= 6.25.

As regards point defect properties, we show that the oxygen vacancies in (U,Pu,Am)O_2 are insensitive to the chemical environment in terms of the U and Pu cations surrounding the vacancy, which is in contrast to what was observed in (U,Pu)O_2. Indeed, in (U,Pu)O_2, the chemical environments containing at least 2 Pu are the most energetically favorable, the energy difference between the most stable chemical environment and the less stable one being 0.5 eV. However, from our study, we cannot propose an evolution of the formation energy with respect to the americium content since we only considered two americium contents (3.125% and 6.25%). Therefore, one of the perspectives here could be to extend this investigation to larger Am contents in order to also consider chemical environments (around the oxygen vacancy) containing Am cations.

Note that finite temperature properties (thermal expension, enthalpy increment and specific heat) in Am-doped uranium-plutonium mixed oxides are important perspectives for this chapter. Indeed the study of this properties have been already initiated in this study but could not yet be completed. These properties control the fuel behaviour under irradiation in reactor.

General conclusion

The goal of this study consists in determining the influence of a low americium content on point defects (stability and atomic transport), elastic, structural, electronic and finite temperature properties of uranium-plutonium mixed oxides $(U,Pu)O_2$ by appropriate electronic structure calculations i.e. DFT+U. To achieve this, we have defined an approach aiming at providing reliable material data on these oxides. We began by studying the pure americium oxides (AmO_2 and Am_2O_3) in order to adapt the DFT+U method to americium-bearing oxides and then to provide (in a multiscale modelling scheme) some missing properties of interest of AmO_2 and Am_2O_3 oxides. Once the DFT+U method implemented in pure americium oxides, the next step was to apply it to $(U,Pu,Am)O_2$ in order to determine the effect of Am. But, given the complexity of the U-Pu-Am-O quaternary system and the very rare data on this compound, we made the choice to first study $(U,Am)O_2$ knowing that the study of $(U,Pu)O_2$ had been the subject of Ibrahim Cheik Njifon's PhD thesis [29]. Note that experimental data on $(U,Am)O_2$ are also very scarce and more data are necessary for the CALPHAD modelling of the U-Pu-Am-O system.

In the first chapter devoted to results, the aim was to determine the optimal U and J values of the DFT+U method in americium oxides allowing to describe the strongly correlated Am *5f* electrons. The issues of metastable states inherent to the DFT+U method were carefully investigated in order to search the electronic configurations of the Am *5f* orbitals in AmO_2 that lead to the ground state of the system. Then, these U and J values have been used within the DFT+U to predict some missing or poorly known properties of interest in americium oxides.

After a careful investigation of metastable states inherent to the DFT+U method, we highlight that the presence of metastable states in DFT+U calculations can account for the discrepancies observed in the literature for AmO_2 regarding the elastic constants as well as the evolution of the band gap as a function of the U parameter of the DFT+U. We show that the ground state can be reached by imposing occupation matrices at the beginning of calculations. We observe a slight difference between the lattice constants ($a \neq b \neq c$) when the crystal symmetries are not imposed but the cell volume remains very close to the case in which the crystal symmetries are imposed. Moreover, in both cases, the Am^{4+} magnetic moments are very close to each other, as are the band gaps (1.1±0.2 eV). Finally, the density of states and the isotropic contributions to the dielectric properties (trace of Born effective charge and dielectric tensors) are unchanged by the loss of symmetry.

In the second part of this results chapter, we calculated several bulk properties of AmO_2 and Am_2O_3 such as structural, elastic, energetic, electronic and magnetic properties as a function of the U and J parameters, as well as dielectric and tempera-

ture dependent properties. Our results show a good agreement with the available data (experimental and computed). For AmO_2, the values (U,J) = (6.00 eV,0.75 eV) are those providing the best description of bulk properties by comparison to the available experimental data. We provide for the first time several bulk properties such as magnetic and elastic (elastic constants) properties as well as the static dielectric constant of americium dioxide, which were unknown up to now. We point out a 3k AFM order for AmO_2 with an oxygen sublattice distortion of 0.17 Å. We highlight that modelling the 3k antiferromagnetic (AFM) order including spin-orbit coupling (SOC) requires a considerable computing time in a large supercell. A rapid development of computational resources will make it possible in a near future to include SOC when studying the defective supercells for a more accurate description of point defect properties.

Concerning americium sesquioxides Am_2O_3, we find the hexagonal A-type to be the most stable structure at low temperature. This result is the first theoretical confirmation (in agreement with the CALPHAD calculations reported by Gotcu-Freis *et al.* [13]) of the stability at low temperature of the hexagonal A-type structure of Am_2O_3, the phase diagram of Am-O which was still controversial. Furthermore, the structural properties computed in this study are very close to the experimental results. We provide for the first time the internal structural parameters for the hexagonal structure, which can be used as reference for future works. We also predict the bulk modulus of both bcc C-type cubic and hexagonal A-type structures as well as the band gap and the formation enthalpy of the bcc C-type. We highlight that the U=6 eV and J =0.75 eV values fitted on AmO_2 properties probably tend to overestimate the band gap but do not affect other bulk properties.

The thermal expansion of AmO_2, calculated using *ab initio* molecular dynamics, is consistent with the experimental result by Minato *et al.* [9] and in good agreement with the one by Epifano *et al.* [19]. We observe a quasi-linear behaviour for temperatures lower than 1200 K whereas at 1200 K, we highlight a change in the slope. This behaviour shows a noticeable difference with UO_2. The origin of this change in the slope is not clearly identified. Epifano *et al.* [19] point out the presence of the oxygen point defects. However, this conclusion is still controversial since no defect is introduced in our system (i.e. O/M remains equal to 2.00) but we obtain the same description of the lattice expansion. Further investigations including oxygen vacancies are needed to unequivocally conclude.

The first-principles study proposed in this first results chapter paves the way for an optimal use of the DFT+U approximation to study AmO_2 defective supercells (see Chap. 4) since the defect properties in AmO_2 have never been investigated. In addition, this methodology can be applied to other minor actinide oxides like NpO_2 and CmO_2 since the material properties of these oxides are poorly known. Indeed, although Np and Cm are less abundant than Am within the $(U,Pu)O_2$ spent fuel, it is not excluded to expect a non negligeable effect on SFR-Na nuclear fuel properties.

In the second chapter devoted to the results, the main goal was to investigate the stability and migration mechanisms of atomic and electronic point defects in americium dioxide using the DFT+U method implemented in the previous chapter. More precisely, we have studied intrinsic donor point defects and electron polarons in AmO_2, using a first-principles DFT+U framework within which the Am *5f* orbital occupation matrices are carefully controlled.

We show that the oxygen vacancy is a deep double donor, with small to moderate formation energies (less than 1 eV for the neutral vacancies). Am interstitials have a prohibitive formation energy and are thus unlikely in AmO_2. The self-trapped electron polaron is extremely stable. This large stability confines the possible values of the Fermi level in AmO_2 to a very narrow interval just above the Valence Band Maximum (0-0.09 eV). In oxygen-poor conditions ($\Delta\mu_O$= -0.75 eV), oxygen vacancies are easily formed in AmO_2. The liberated electrons have the tendency to move far from the vacancies and localize in the lattice under the form of self-trapped polarons, since this state is found more stable than when the electron is trapped close to the vacancy. In other words, the oxygen vacancies are spontaneously ionized. Electron polarons are probably in rather large number, with a charge compensation mostly ensured by ionized oxygen vacancies. In oxygen-rich conditions, electron polarons may remain in rather large concentration but should be charge-compensated by free holes rather than by ionized oxygen vacancies. The self-trapped state of the excess electron in AmO_2 is associated to a self-trapping distortion mostly consisting of an increase of the Am-O distance (between the Am atoms carrying the excess electron and the eight 1 st neighbour oxygen atoms) by about 0.08 Å. The hopping of the polaron involves a large activation barrier of ∼0.6 eV, and probably takes place by a non-adiabatic mechanism.

In the third results chapter, the objective was to evaluate the influence of the americium content on the UO_2 bulk and point defect properties in order to pave the way to the study of the influence of Am on $(U,Pu)O_2$ properties but also to support the experimental studies conducted in CEA on $(U,Am)O_2$.

$(U,Am)O_2$ mixed oxides show a particular valence state of cations which is fundamentally different from other mixed oxides like $(U,Pu)O_2$ and $(U,Ce)O_2$. Indeed, in $(U,Am)O_2$, Am acts as an electron acceptor whereas U acts as an electron donor, according to the $Am^{4+} + U^{4+} \longrightarrow Am^{3+} + U^{5+}$ mechanism. These results are in good agreement with early XANES experiments (limited to %Am<20) but also complete them by providing a broader description of Am-bearing oxides over the entire range of the Am content. We show that for %Am<50, all Am(+IV) are reduced to Am(+III) whereas U has mixed valence (+IV and +V). On the contrary, when %Am>50, Am(+IV) is partially reduced to Am(+III) whereas all U(+IV) cations are oxidized to U(+V). This study shows that the lattice parameter as a function of the Am content follows a linear behaviour that cannot be experimentally observed owing to the deviation from stoichiometry combined with the presence of oxygen interstitials (enhanced for the large Am contents higher than 40%) observed in samples that have been experimentally characterized in the early studies and subject to self irradiation. It would be interesting to further investigate in the framework of DFT+U the effect of point defects as well as defect clusters on the structural properties of $U_{1-y}Am_yO_2$ mixed oxides, especially on the lattice parameter. In addition, we show that U-Am and U-U bond lengths are identical on average, which is the signature of the random distribution of cations in the cation sublattice. Thus, our study is the first confirmation of the ideal solid solution behaviour (from the structural point of view) of $(U,Am)O_2$ provided a perfect defectless and stoichiometric compound could be obtained. Using two approaches, (SQS and a parametric one), we show with satisfactory agreement between both approaches that there is no demixing in $(U,Am)O_2$ in the whole range of Am content at low temperature. This study is the first assessment of the mixing enthalpy of Am-bearing oxides, the minimum value being about -0.45 eV which (in

absolute value) is 100 times higher than the value obtained for (U,Pu)O_2. Moreover, we show that a larger number of Am cations in the first coordination shell is associated to a energetically more stable oxygen vacancy. (U,Am)O_2 is thus found to form more easily oxygen vacancies than UO_2 and thus, forms more easily hypo-stoichiometric compounds.

The results obtained in this chapter support the experimental studies and also, can be useful for a refined implementation of the thermodynamic computational methods like CALPHAD for the U-Pu-Am-O system.

Summary on the effect of Am content on UO_2 properties. We show that Am induces a decrease of the U-O crystallographic distance of about 4% whatever the Am content less than 50%. The lattice parameter of Am-bearing UO_2 decreases linearly as a function of the Am content in the case of stoichiometric compounds. Moreover, our results indicate that the presence of Am in UO_2 facilitates the formation of neutral oxygen vacancies. In addition, the presence of Am leads to the oxidation of U^{4+} to U^{5+} in such a manner that the concentrations $[U^{5+}]=[Am^{3+}]$. These results on the effect of Am on UO_2 properties pave the way toward the investigation of the effect of Am on (U,Pu)O_2 material properties.

In the last chapter devoted to the results, the goal was to qualify and quantify the effect of low americium content on electronic, structural, elastic, energetic and defect properties of uranium and plutonium mixed oxides.

We first propose an approximation to model (U,Pu,Am)O_2 containing a few percent of americium (less than 10%). We show in agreement with Chap 3 that the more U atoms around the Am atoms, the more stable the configuration is. The electron charge transfer known to occur between U and Am cations can explain why an Am cation is more stable near an U cation. Concerning the valence state of cations, we show that Am(+IV) cations in (U,Pu)O_2 mixed oxides tend to easily reduce to Am(+III): (i) in stoichiometric compounds, the reduction of Am(+IV) is compensated by the oxidation of U(+IV) to U(+V). (ii) hypostoichiometry in americium-bearing uranium-plutonium oxides is accommodated by the reduction of all U(+V) cations (which result from the the presence of Am (+III) cation) before any reduction of the Pu cations. This allows us to highlight that americium exhibits a higher oxygen potential than Pu and U, and thus induces an increase in the oxygen potential in uranium-plutonium mixed oxides.

In addition, these results allow us to conclude that the relative stability as a function of the number of U cations around the Am atom could likely result from the difference in Am(+III)-U(+IV) and Am(+III)-Pu(+IV) electrostatic interactions. Indeed, depending on the number of Pu and U atoms surrounding a given Am atom, the local electrostatic interactions can be strongly affected, which lead to a difference in the total energy of the system.

We point out a decrease in the lattice parameters of $U_{0.75-z}Pu_{0.25}Am_zO_2$ with increasing Am content, in agreement with early studies [41]. Moreover, the evolution of the lattice parameter as a function of Am content (for the three compositions assessed) is not linear as in $U_{1-y}Pu_yO_2$. However, it would be important to extend this study to higher Am contents in order to unequivocally conclude on the evolution of the lattice parameter. We can observe that the presence of Am (for the contents evaluated) has no noticeable effect on the M-M bond length (M= U or Pu) compared to the M-M ones

in $U_{0.75}Pu_{0.25}O_2$ (∼3.90 Å). On the other hand, one observes a very slight decrease in U-O bond lengths of the first oxygen atoms surrounding the U cations of about 0.01 Å for 6.25% of Am. This result could be expected since we showed that the presence of Am leads to a slight decrease in the lattice parameter of $U_{0.75}Pu_{0.25}O_2$ mixed oxides.In addition, we show that the presence of Am in (U,Pu)O_2 has no noticeable effcet on the bulk modulus. In contrast, the mixing enthalpy of (U,Pu)O_2 is strongly affected by the presence the Am. Indeed the presence of Am leads to an important increase of the mixing enthalpy (absolute value) from -4.0 meV for %Am= 0 to -87 meV for %Am= 6.25.

As regards point defect properties, we show that the oxygen vacancies in (U,Pu,Am)O_2 are insensitive to chemical environment in terms of the U and Pu cations surrounding the vacancy, which is in contrast to what was observed in (U,Pu)O_2. Indeed, in U,Pu)O_2, the chemical environment containing at least 2 Pu are the most energetically favorable, the energy difference between the most stable chemical environment and the less stable on being 0.5 eV. However, from our study, we cannot propose an evolution of the formation energy with respect to the americium content since we only considered two americium contents (3.125% and 6.25%).

This manuscript highlights the capability of electronic structure calculations within the DFT method to support the separate-effect experiments and also to feed the higher scale modelling techniques (mentioned in Table 6.7 below) in order to increase the predictivity of the fuel performance codes. Moreover, this study shows the capability of the DFT calculations to efficiently deal with complex materials such as americium-bearing oxide, especially quaternary systems like uranium-americium-plutonium mixed oxides which exhibit a chemical disorder, a spontaneous change in valence state coupled to the strongly correlated effects. The methodology proposed in this study can be applied to other minor actinide-bearing oxides such as Np and Cm-bearing oxides since material properties of these oxides are poorly known. Indeed, although Np and Cm are less abundant than Am within the (U,Pu)O_2 spent fuel, it is not excluded to expect a non negligeable effect on SFR-Na nuclear fuel properties. Despite this maturity of the DFT calculations, it is important to highlight that some improvements still remain to be made. For instance, a 96-atom supercell (used is this study) limits the number of configurations (in term of U and Pu atoms) around an Am (in (U,Pu)O_2) atom and also makes impossible the study of the effect of the second and third cation neighbours on the stability of cation point defects. Extending the supercell size from 96-atom to a larger size could be an alternative but this solution is however very time consuming using the DFT+U calculations. Indeed, we are currently carrying out an investigation coupling the DFT calculations and methods based on empirical interatomic potentials. One of the aims of this study is to use methods based on empirical potentials to explore numerous chemical configurations around a given point defect and also numerous migration mechanisms in order to identify the most likely ones. Then, the DFT calculation will be applied considering the most likely configurations/mechanisms to calculate with higher accuracy defect and atomic transport energetic properties.

In a near future, overcoming as much as possible the size issues of the simulation supercell and a rapid development of computational resources would be a tremendous progress for electronic structure calculations. This could allow us to evaluate through

ab initio calculations defect clusters such as nano-voids, fission gas clusters, dislocations and also to analyse their effect on the material properties. Such progress would enable an *ab initio* prediction of a large set of properties in direct link to the mesoscopic evolution of nuclear fuel properties and thus, a better link to various higher scale models mentioned is Table 6.7. With a rapid development of computational resources, a long-term perspective could be to apply the promising computational methods such as Dynamical Mean-Field Theory (DMFT) and Random Phase Approximation (RPA) in order to increase the accuracy of the *ab initio* calculations, especially for complex materials like actinide oxide-based compounds largely used for nuclear applications.

Table 6.7: Valorisation of the results obtained in this thesis through the multi-scale modelling scheme developed in CEA. We also display experimental techniques complementary to the DFT method. EELS=Electron Energy Loss Spectroscopy, SIMS=Secondary Ion Mass Spectrometry. DSC= Differential Scanning Calorimetry. KineCluE= Kinetic Cluster expansion.

Properties from DFT		Experimental techniques	Codes, model or techniques to feed
Elastic	Elastic constants	Brillouin zone measurements	Thermermechanic Empirical potentials
Structural	Thermal, expansion	XRD	Thermomechanic, empirical potentials
	Phase stability	XRD	CALPHAD
Electronic	Valence state	XANES	CALPHAD
Energetic	Mixing enthalpy		CALPHAD,
	Formation enthalpy	Oxygen calorimetry	KinecluE, Empirical potentials,
	Point defects properties	For identification: PAS, RAMAN EELS coupled to DFT	Cluster dynamics
Transport	Migration energy	SIMS, TDS (inderect method)	DICTRA, thermokinetic
Thermodynamic	Heat capacity	Drop calorimetry, DSC	Thermomechanic CALPHAD

Bibliography

[1] James T. Pegg, Xavier Aparicio-Angles, Mark Storr, and Nora H. de Leeuw. DFT+**U** study of the structures and properties of the actinide dioxides. *Journal of Nuclear Materials*, **492**:269–278, 2017.

[2] J.P. Dancausse, R.G. Haire, S. Heathman, and U. Benedict. High-pressure X-ray diffraction studies of americium and curium dioxides. *Journal of Nuclear Science and Technology*, **39**(sup3):136–139, 2002.

[3] C. Hurtgen and J. Fuger. Self-irradiation effects in americium oxides. *Inorg. Nucl. Chem. Lett.*, **13**(3-4):179–188, 1977.

[4] T.D. Chikalla and L. Eyring. Phase relationships in the americium-oxygen system. *Journal of Inorganic and Nuclear Chemistry*, **30**(1):133–145, 1968.

[5] Prieur Damien, Jankowiak Aurélien, Delahaye Thibaud, Herlet Nathalie, Dehaudt Philippe, and Blanchart Philippe. Fabrication and characterisation of $U_{0.85}Am_{0.15}O_{2-x}$ discs for MARIOS irradiation program. *Journal. Nuclear. materials*, **414**(3):503–507, 2011.

[6] Florent Lebreton, Renaud C. Belin, Thibaud Delahaye, and Philippe Blanchart. In-situ X-ray diffraction study of phase transformations in the Am–O system. *Journal of Solid State and Chemistry*, **196**:217–224, 2012.

[7] Yong Lu, Yu Yang, Fawei Zheng, Bao-Tian Wang, and Ping Zhang. Electronic, mechanical, and thermodynamic properties of americium dioxide. *Journal of Nuclear materials*, **441**(1-3):411–420, 2013.

[8] J.A. Fahey, R.P. Turcotte, and T.D. Chikalla. Thermal expansion of the actinide dioxides. *Inorg. Nucl. Chem. Lett.*, **10**(6):459–465, 1974.

[9] Kazuo Minato, Masahide Takano, Haruyoshi Otobe, Tsuyoshi Nishi, Mitsuo Akabori, and Yasuo Arai. Thermochemical and thermophysical properties of minor actinide compounds. *Journal Nuclear Materials*, **389**(1):23–28, 2009.

[10] D. Taylor. Thermal expansion data. *Transactions and Journal of the British Ceramic Society*, **83**(2):32–37, 1984.

[11] D.G. Martin. The thermal expansion of solid UO_2 and (U,Pu) mixed oxides—a review and recommendations. *Journal of Nuclear Materials*, **152**(2-3):94–101, 1988.

[12] C. Sari and E. Zamorani. An investigation in the americium oxide system. *Journal of Nuclear Materials*, **37**(3):324–330, 1970.

[13] P. Gotcu-Freis, J-Y. Colle, C. Guéneau, N. Dupin, B. Sundman, and R.J.M. Konings. A thermodynamic study of the Pu–Am–O system. *Journal of Nuclear Materials*, **414**(3):408–421, 2011.

[14] Chikashi Suzuki, Tsuyoshi Nishi, Masami Nakada, Mitsuo Akabori, Masaru Hirata, and Yoshiyuki Kaji. Core-hole effect on XANES and electronic structure of minor actinide dioxides with fluorite structure. *Journal of Physics and Chemistry of Solids*, **73**(2):209–216, 2012.

[15] Florent Lebreton. *Synthèse et caractérisation d'oxydes mixtes d'uranium et d'américium.* PhD thesis, Université de Limoges, 2014.

[16] Enrica Epifano. *Study of the U-Am-O ternary phase diagram.* PhD thesis, Paris Saclay university, 2017.

[17] Denis Horlait, Florent Lebreton, Pascal Roussel, and Thibaud Delahaye. XRD monitoring of α self-irradiation in Uranium–Americium Mixed Oxides. *Inorg. Chem.*, 52(24):14196–14204, 2013.

[18] Kyoichi Morimoto, Masato Kato, Masahiro Ogasawara, Motoaki Kashimura, and Tomoyuki Abe. Thermal conductivities of (U,Pu,Am)O_2 solid solutions. *Journal of Alloys and Compounds*, **452**(1):54–60, 2008.

[19] Enrica Epifano, Christine Gueneau, Renaud C. Belin, Romain Vauchy, Florent Lebreton, Jean-Christophe Richaud, Alexis Joly, Christophe Valot, and Philippe M. Martin. Insight into the Am-O phase equilibria: a thermodynamic study coupling high-temperature XRD and CALPHAD modeling. *Inorganic chemistry*, **56**(13):7416–7432, 2017.

[20] Tsuyoshi Nishi, Akinori Itoh, Kenichi Ichise, and Yasuo Arai. Heat capacities and thermal conductivities of AmO_2 and $AmO_{1.5}$. *Journal Nuclear Materials*, **414**(2):109–113, 2011.

[21] Rudy J.M. Konings, Ondrej Beneš, Attila Kovács, Dario Manara, David Sedmidubskỳ, Lev Gorokhov, Vladimir S. Iorish, Vladimir Yungman, E. Shenyavskaya, and E. Osina. The thermodynamic properties of the f-elements and their compounds. part 2. the lanthanide and actinide oxides. *J. Phys. Chem. Ref. Data*, **43**(1):013101, 2014.

[22] Grégory Geneste, Bernard Amadon, Marc Torrent, and Guilhem Dezanneau. DFT+U study of self-trapping, trapping, and mobility of oxygen-type hole polarons in barium stannate. *Physical Review B*, **96**(13):134123, 2017.

[23] Akio Kotani and Haruhiko Ogasawara. Theory of core-level spectroscopy in actinide systems. *Physica B: Condensed Matter*, **186**:16–20, 1993.

[24] Damien Prieur, Philippe M. Martin, Aurelien Jankowiak, Elisabeth Gavilan, Andreas C. Scheinost, Nathalie Herlet, Philippe Dehaudt, and Philippe Blanchart. Local structure and charge distribution in mixed uranium–americium oxides: effects of oxygen potential and Am content. *Inorganic Chemistry*, **50**(24):12437–12445, 2011.

[25] Jean-Francois Vigier, Philippe M. Martin, Laura Martel, Damien Prieur, Andreas C. Scheinost, and Joseph Somers. Structural investigation of $(U_{0.7}Pu_{0.3})O_{2-x}$ mixed oxides. *Inorganic Chemistry*, **54**(11):5358–5365, 2015.

[26] D. Prieur, F. Lebreton, M. Caisso, P.M. Martin, A.C. Scheinost, T. Delahaye, and D. Manara. Melting behaviour of americium-doped uranium dioxide. *The Journal of Chemical Thermodynamics*, **97**:244–252, 2016.

[27] OECD. State-of-the-art report on innovative fuels. *https://www.oecd-nea.org/science/pubs/2014/6895-report-innovative-fuels,NuclearScience,NEA6895*, **397**, 2014.

[28] Vladimir I. Anisimov, Jan Zaanen, and Ole K. Andersen. Band theory and Mott insulators: Hubbard U instead of Stoner I. *Physical Review B*, **44**(3):943, 1991.

[29] I. Cheik Njifon. *Modélisation des modifications structurales, électroniques et thermodynamiques induites par les défauts ponctuels dans les oxydes mixtes à base d'actinides (U,Pu)O_2*. PhD thesis, Aix Marseille Université, 2018.

[30] M. Freyss and I. Cheik Nijfon. *Calculs de structure électronique des propriétés de transport et thermodynamiques de combustibles oxydes mixtes*, Note Technique CEA DEN/DEC/SESC/LLCC NT 16-010. 2016.

[31] Gérald Jomard, Bernard Amadon, François Bottin, and Marc Torrent. Structural, thermodynamic, and electronic properties of plutonium oxides from first principles. *Physical Review B*, **78**(7):075125, 2008.

[32] Boris Dorado, Bernard Amadon, Michel Freyss, and Marjorie Bertolus. DFT+U calculations of the ground state and metastable states of uranium dioxide. *Physical Review B*, **79**(23):235125, 2009.

[33] Martin S. Talla Noutack, Grégory Geneste, Gérald Jomard, and Michel Freyss. First-principles investigation of the bulk properties of americium dioxide and sesquioxides. *Physical Review Materials*, **3**(3):035001, 2019.

[34] A. Jankowiak, C. Maillard, and L. Donnet. Structural study of $Pu_{1-x}Am_xO_2$ (x= 0.2; 0.5; 0.8) obtained by oxalate co-conversion. *Journal of Nuclear Materials*, **393**(1):87–91, 2009.

[35] Masahide Takano, Mitsuo Akabori, Yasuo Arai, and Kazuo Minato. Lattice thermal expansions of NpN, PuN and AmN. *Journal of Nuclear Materials*, **376**(1):114–118, 2008.

[36] C. Hurtgen and J. Fuger. Self-irradiation effects in americium oxides. *Inorganic and Nuclear Chemistry Letters*, **13**:179–188, 1977.

[37] R.C. Ewing, W.J. Weber, and F.W. Clinard Jr. Radiation effects in nuclear waste forms for high-level radioactive waste. *Progress in nuclear energy*, **29**(2):63–127, 1995.

[38] Johann von Pezold, Alexey Dick, Martin Friák, and Jörg Neugebauer. Generation and performance of special quasirandom structures for studying the elastic properties of random alloys: Application to Al−Ti. *Physical Review B*, **81**(9):094203, 2010.

[39] Emerson Vathonne. *Étude par calcul de structure électronique des dégâts d'irradiation dans le combustible nucléaire UO_2: comportement des défauts ponctuels et gaz de fission.* PhD thesis, Université Aix Marseille, 2014.

[40] Lei Shi. *Theoretical study using electronic structure calculations of uranium and cerium dioxides containing defects and impurities.* PhD thesis, Aix Marseille University, 2016.

[41] Ph Martin, S Grandjean, C Valot, G Carlot, M Ripert, P Blanc, and C Hennig. XAS study of $(U_{1-y}Pu_y)O_2$ solid solutions. *Journal of Alloys and Compounds*, **444**:410–414, 2007.

[42] Pierre Hohenberg and Walter Kohn. Inhomogeneous electron gas. *Physical Review*, **136**(3B):B864, 1964.

[43] Walter Kohn and Lu Jeu Sham. Self-consistent equations including exchange and correlation effects. *Physical Review*, **140**(4A):A1133, 1965.

[44] P.M. Martin, E. Vathonne, G. Carlot, R. Delorme, C. Sabathier, M. Freyss, P. Garcia, M. Bertolus, P. Glatzel, and O. Proux. Behavior of fission gases in nuclear fuel: XAS characterization of Kr in UO_2. *Journal of Nuclear Materials*, **466**:379–392, 2015.

[45] Julia Wiktor, Marie-France Barthe, Gérald Jomard, Marc Torrent, Michel Freyss, and Marjorie Bertolus. Coupled experimental and DFT+U investigation of positron lifetimes in UO_2. *Physical Review B*, **90**(18):184101, 2014.

[46] René Bès, Philippe Martin, Emerson Vathonne, Rémy Delorme, Catherine Sabathier, Michel Freyss, Marjorie Bertolus, and Pieter Glatzel. Experimental evidence of Xe incorporation in Schottky defects in UO_2. *Appl. Phys. Lett.*, **106**(11):114102, 2015.

[47] Boris Dorado. *Electronic structure calculations of atomic transport properties in uranium dioxide: influence of strong correlations.* PhD thesis, Aix Marseille University, 2010.

[48] John P. Perdew and Alex Zunger. Self-interaction correction to density-functional approximations for many-electron systems. *Physical Review B*, **23**(10):5048, 1981.

[49] Gabriel Kotliar, Sergej Y. Savrasov, Kristjan Haule, Viktor S. Oudovenko, O. Parcollet, and C.A. Marianetti. Electronic structure calculations with dynamical mean-field theory. *Reviews of Modern Physics*, **78**(3):865, 2006.

[50] Antoine Georges, Gabriel Kotliar, Werner Krauth, and Marcelo J. Rozenberg. Dynamical mean-field theory of strongly correlated fermion systems and the limit of infinite dimensions. *Reviews of Modern Physics*, **68**(1):13, 1996.

[51] Carlo Adamo and Vincenzo Barone. Toward reliable density functional methods without adjustable parameters: The PBE0 model. *The Journal of chemical physics*, **110**(13):6158–6170, 1999.

[52] Jochen Heyd, Gustavo E. Scuseria, and Matthias Ernzerhof. Hybrid functionals based on a screened coulomb potential. *The Journal of chemical physics*, **118**(18):8207–8215, 2003.

[53] A.I. Lichtenstein and M.I. Katsnelson. Ab initio calculations of quasiparticle band structure in correlated systems: LDA++ approach. *Physical Review B*, **57**(12):6884, 1998.

[54] S.L. Dudarev, G.A. Botton, S.Y. Savrasov, C.J. Humphreys, and A.P. Sutton. Electron-energy-loss spectra and the structural stability of nickel oxide: An LSDA+U study. *Physical Review B*, **57**(3):1505, 1998.

[55] F. Aryasetiawan, M. Imada, A. Georges, G. Kotliar, S. Biermann, and A.I. Lichtenstein. Frequency-dependent local interactions and low-energy effective models from electronic structure calculations. *Physical Review B*, **70**(19):195104, 2004.

[56] F. Aryasetiawan, Krister Karlsson, O. Jepsen, and U Schönberger. Calculations of Hubbard U from first-principles. *Physical Review B*, **74**(12):125106, 2006.

[57] Matteo Cococcioni and Stefano De Gironcoli. Linear response approach to the calculation of the effective interaction parameters in the LDA+U method. *Physical Review B*, **71**(3):035105, 2005.

[58] Bernard Amadon, Thomas Applencourt, and Fabien Bruneval. Screened coulomb interaction calculations: cRPA implementation and applications to dynamical screening and self-consistency in uranium dioxide and cerium. *Physical Review B*, **89**(12):125110, 2014.

[59] B. Amadon, F. Jollet, and M. Torrent. γ and β cerium: LDA+U calculations of ground-state parameters. *Physical Review B*, **77**(15):155104, 2008.

[60] B. Meredig, A. Thompson, H.A. Hansen, C. Wolverton, and A. Van de Walle. Method for locating low-energy solutions within DFT+U. *Physical Review B*, **82**(19):195128, 2010.

[61] Hua Y. Geng, Ying Chen, Yasunori Kaneta, Motoyasu Kinoshita, and Q. Wu. Interplay of defect cluster and the stability of xenon in uranium dioxide from density functional calculations. *Physical Review B*, **82**(9):094106, 2010.

[62] Denis Gryaznov, Eugene Heifets, and Eugene Kotomin. The first-principles treatment of the electron-correlation and spin–orbital effects in uranium mononitride nuclear fuels. *Phys. Chem. Chem. Phys.*, **14**(13):4482–4490, 2012.

[63] Ping Zhang, Bao-Tian Wang, and Xian-Geng Zhao. Ground-state properties and high-pressure behavior of plutonium dioxide: Density functional theory calculations. *Physical Review B*, **82**(14):144110, 2010.

[64] Erik R. Ylvisaker, Warren E. Pickett, and Klaus Koepernik. Anisotropy and magnetism in the LSDA+U method. *Physical Review B*, **79**(3):035103, 2009.

[65] G. Kresse and D. Joubert. From ultrasoft pseudopotentials to the projector augmented-wave method. *Physical Review B*, **59**(3):1758, 1999.

[66] Peter E. Blöchl. Projector augmented-wave method. *Physical Review B*, **50**(24):17953, 1994.

[67] Lawrence R. Pratt. A statistical method for identifying transition states in high dimensional problems. *The Journal of chemical physics*, **85**(9):5045–5048, 1986.

[68] R. Elber and M. Karplus. A method for determining reaction paths in large molecules: Application to myoglobin. *Chemical Physics Letters*, **139**(5):375–380, 1987.

[69] E. Weinan, Weiqing Ren, and Eric Vanden-Eijnden. String method for the study of rare events. *Physical Review B*, **66**(5):052301, 2002.

[70] Daniel Sheppard, Rye Terrell, and Graeme Henkelman. Optimization methods for finding minimum energy paths. *The Journal of chemical physics*, **128**(13):134106, 2008.

[71] Xavier Gonze and Changyol Lee. Dynamical matrices, born effective charges, dielectric permittivity tensors, and interatomic force constants from density-functional perturbation theory. *Physical Review B*, **55**(16):10355, 1997.

[72] Xavier Gonze. First-principles responses of solids to atomic displacements and homogeneous electric fields: Implementation of a conjugate-gradient algorithm. *Physical Review B*, **55**(16):10337, 1997.

[73] Richard Car and Mark Parrinello. Unified approach for molecular dynamics and density-functional theory. *Phys. Rev. Lett.*, **55**(22):2471, 1985.

[74] W.H. Zachariasen. Crystal chemical studies of the *5f*-series of elements. xii. new compounds representing known structure types. *Acta Crystallographica*, **2**(6):388–390, 1949.

[75] Damien Prieur, Jean-François Vigier, Thierry Wiss, Arne Janssen, Jörg Rothe, Andrea Cambriani, and Joseph Somers. Structural investigation of self-irradiation damaged AmO_2. *J. Solid State Chem.*, **212**:7–12, 2014.

[76] D.H. Templeton and Carol H. Dauben. Crystal structures of americium compounds1. *J. Am. Chem. Soc.*, **75**(18):4560–4562, 1953.

[77] A. Bœuf, J.M. Fournier, Jean-François Gueugnon, L. Manes, J. Rebizant, and F. Rustichelli. Neutron diffraction study of $^{243}AmO_2$. *Journal de Physique Lettres*, **40**(14):335–338, 1979.

[78] A. Bendjedid, T. Seddik, R. Khenata, H. Baltache, G. Murtaza, A. Bouhemadou, S. Bin Omran, Sikander Azam, and Saleem Ayaz Khan. GGA+U study on phase transition, optoelectronic and magnetic properties of AmO_2 with spin–orbit coupling. *Journal of Magnetism and Magnetic Materials*, **396**:190–197, 2015.

[79] Xiao-Dong Wen, Richard L. Martin, Lindsay E. Roy, Gustavo E. Scuseria, Sven P. Rudin, Enrique R. Batista, Thomas M. McCleskey, Brian L. Scott, Eve Bauer, John J. Joyce, et al. Effect of spin-orbit coupling on the actinide dioxides AnO_2 (An= Th, Pa, U, Np, Pu, and Am): A screened hybrid density functional study. *The Journal of Chemical Physics*, **137**(15):154707, 2012.

[80] Leon Petit, Axel Svane, Zdzislawa Szotek, Walter M. Temmerman, and George Malcolm Stocks. Electronic structure and ionicity of actinide oxides from first principles. *Physical Review B*, **81**(4):045108, 2010.

[81] M. Idiri, T. Le Bihan, S. Heathman, and J. Rebizant. Behavior of actinide dioxides under pressure: UO_2 and ThO_2. *Physical Review B*, **70**(1):014113, 2004.

[82] JM. Friedt, R. Poinsot, J. Rebizant, and W. Müller. ^{237}Np mössbauer study of the after effects of the ^{241}Am α-decay in some metallic and insulating hosts. *J. Phys. Chem. Solids*, **40**(4):279–287, 1979.

[83] D.G. Karraker. Magnetic susceptibility of $^{243}AmO_2$. *J. Chem. Phys.*, **63**(7):3174–3175, 1975.

[84] Darrel W. Osborne and Edgar F. Westrum J.r. The heat capacity of thorium dioxide from 10 to 305 K. the heat capacity anomalies in uranium dioxide and neptunium dioxide. *The Journal of Chemical Physics*, **21**(10):1884–1887, 1953.

[85] J.W. Ross and D.J. Lam. The magnetic susceptibility of neptunium oxide and carbide between 4.2 and 350 K. *Journal of Applied Physics*, **38**(3):1451–1453, 1967.

[86] Yo Tokunaga, Masahiko Osaka, Shinsaku Kambe, Shuhei Miwa, Hironori Sakai, Hiroyuki Chudo, Yoshiya Homma, and Yoshinobu Shiokawa. ^{17}O NMR study in $(Pu_{0.91}Am_{0.09})O_2$. *Journal of Nuclear Materials*, **396**(1):107–111, 2010.

[87] Yo Tokunaga, Tsuyoshi Nishi, Shinsaku Kambe, Masami Nakada, Akinori Itoh, Yoshiya Homma, Hironori Sakai, and Hiroyuki Chudo. NMR evidence for the 8.5 k phase transition in americium dioxide. *Journal of the Physical Society of Japan*, **79**(5):053705, 2010.

[88] H. Schmidt. , in: Proceedings of the 4th journées d'actinides, UK (june 26, 1974): Atomic energy research establishment.

[89] R.L. Gibby. The effect of plutonium content on the thermal conductivity of $(U,Pu)O_2$ solid solutions. *Journal of Nuclear Materials*, **38**(2):163–177, 1971.

[90] Y. Philipponneau. Thermal conductivity of $(U,Pu)O_{2-x}$ mixed oxide fuel. *Journal of nuclear materials*, **188**:194–197, 1992.

[91] Teppei Uchida, Tatsumi Arima, Kazuya Idemitsu, and Yaohiro Inagaki. Thermal conductivities of americium dioxide and sesquioxide by molecular dynamics simulations. *Comput. Mater. Sci.*, **45**(2):229–234, 2009.

[92] Ken Kurosaki, Mitsuhiro Imamura, Isamu Sato, Takashi Namekawa, Masayoshi Uno, and Shinsuke Yamanaka. Molecular dynamics studies of minor actinide dioxides. *J. Nucl. Sci. Techn.*, **41**(8):827–831, 2004.

[93] C. Thiriet and R.J.M. Konings. Chemical thermodynamic representation of AmO_{2-x}. *Journal of Nuclear Materials*, **320**(3):292–298, 2003.

[94] Tsuyoshi Nishi, Masami Nakada, Chikashi Suzuki, Hiroki Shibata, Akinori Itoh, Mitsuo Akabori, and Masaru Hirata. Local and electronic structure of Am_2O_3 and AmO_2 with XAFS spectroscopy. *Journal of Nuclear Materials*, **401**(1-3):138–142, 2010.

[95] Mehdi Baichi, Christian Chatillon, Gérard Ducros, and Karine Froment. Thermodynamics of the O–U system: III-critical assessment of phase diagram data in the U$-$UO$_{2+x}$ composition range. *Journal of Nuclear Materials*, **349**(1-2):57–82, 2006.

[96] Florent Lebreton. *Synthesis and characterization of uranium-americium mixed oxides,*. PhD thesis, Université de Limoges, 2014.

[97] O.S. Vălu, D. Staicu, O. Beneš, R.J.M. Konings, and P. Lajarge. Heat capacity, thermal conductivity and thermal diffusivity of uranium–americium mixed oxides. *Journal of Alloys and Compounds*, **614**:144–150, 2014.

[98] Chas G. Maier and KK. Kelley. An equation for the representation of high-temperature heat content data1. *J. Am. Chem. Soc.*, **54**(8):3243–3246, 1932.

[99] W. Bartscher and C. Sari. A thermodynamic study of the uranium-americium oxide U$_{0.5}$Am$_{0.5}$O$_{2\pm x}$. *Journal of nuclear materials*, **118**(2-3):220–223, 1983.

[100] W. Bartscher. Determination of the oxygen-metal-ratio of uranium-americium mixed oxides. *Fresenius' Z. Anal. Chem*, 310(**5**):413–414, 1982.

[101] K. Mayer, B. Kanellakopoulos, J. Naegele, and L. Koch. On the valency state of americium in U$_{0.5}$Am$_{0.5}$O$_{2\pm x}$. *Journal of Alloys and Compounds*, **213**:456–459, 1994.

[102] Florent Lebreton, Denis Horlait, Richard Caraballo, Philippe M. Martin, Andreas C. Scheinost, Andre Rossberg, Christophe Jegou, and Thibaud Delahaye. Peculiar behavior of (U,Am)O$_{2-\delta}$ compounds for high americium contents evidenced by XRD, XAS, and Raman Spectroscopy. *Inorganic Chemistry*, **54**(20):9749–9760, 2015.

[103] Tsuyoshi Nishi, Masami Nakada, Akinori Itoh, Chikashi Suzuki, Masaru Hirata, and Mitsuo Akabori. EXAFS and XANES studies of americium dioxide with fluorite structure. *Journal of Nuclear Materials*, **374**(3):339–343, 2008.

[104] RE. McHenry. Melting points of curium and americium oxides. *Transactions of the American Nuclear Society (US)*, **8**, 1965.

[105] M. Kurata. Thermodynamic database on U-Pu-Zr-Np-Am-Fe alloy system ii—evaluation of Np, Am, and Fe containing systems. In *IOP Conference Series: Materials Science and Engineering*, volume **9**, page 012023. IOP Publishing, 2010.

[106] Toru Ogawa. Alloying behaviour among U, Np, Pu and Am predicted with the brewer valence bond model. *J. Alloys Compd.*, **194**(1):1–7, 1993.

[107] Masahiko Osaka, Isamu Sato, Takashi Namekawa, Ken Kurosaki, and Shinsuke Yamanaka. Oxygen potentials of (U$_{0.685}$Pu$_{0.270}$Am$_{0.045}$)O$_{2-x}$ solid solution. *Journal of Alloys and Compounds*, **397**(1-2):110–114, 2005.

[108] Weiwei Li, Jiangjiang Ma, Jiguang Du, and Gang Jiang. Molecular dynamics study of thermal conductivities of (U$_{0.7-x}$Pu$_{0.3}$Am$_x$)O$_2$. *Journal of Nuclear Materials*, **480**:47–51, 2016.

[109] Masato Kato and Kenji Konashi. Lattice parameters of (U,Pu,Am,Np)O_{2-x}. *Journal of Nuclear Materials*, **385**(1):117–121, 2009.

[110] S.B. Wilkins, R. Caciuffo, C. Detlefs, J. Rebizant, E. Colineau, F. Wastin, and G.H. Lander. Direct observation of electric-quadrupolar order in UO_2. *Physical Review B*, **73**(6):060406, 2006.

[111] Boris Dorado, Gérald Jomard, Michel Freyss, and Marjorie Bertolus. Stability of oxygen point defects in UO_2 by first-principles DFT+U calculations: Occupation matrix control and Jahn-Teller distortion. *Physical Review B*, 82(3):035114, 2010.

[112] John P. Perdew, Kieron Burke, and Matthias Ernzerhof. Generalized gradient approximation made simple. *Physical Review Letters*, **77**(18):3865, 1996.

[113] Liechtenstein A.I., Vladimir I. Anisimov, Jan Zaanen, and Andersen. Density-functional theory and strong interactions: Orbital ordering in Mott-Hubbard insulators. *Physical Review B*, **52**(8):R5467, 1995.

[114] Hendrik J. Monkhorst and James D. Pack. Special points for brillouin-zone integrations. *Physical Review B*, **13**(12):5188, 1976.

[115] Miguel A. Blanco, Manuel Flórez, and Margarita Bermejo. Evaluation of the rotation matrices in the basis of real spherical harmonics. *Journal of Molecular Structure: THEOCHEM*, **419**(1-3):19–27, 1997.

[116] Robert Laskowski, Georg K.H. Madsen, Peter Blaha, and Karlheinz Schwarz. Magnetic structure and electric-field gradients of uranium dioxide: An ab initio study. *Physical Review B*, **69**(14):140408, 2004.

[117] B.C. Frazer, G. Shirane, D.E. Cox, and C.E. Olsen. Neutron-Diffraction Study of Antiferromagnetism in UO_2. *Physical Review*, **140**(4A):A1448, 1965.

[118] Eric Cockayne and Benjamin P. Burton. Phonons and static dielectric constant in $CaTiO_3$ from first principles. *Physical Review B*, **62**(6):3735, 2000.

[119] N. Hampton, G.A. Saunders, J.H. Harding, and A.M. Stoneham. The dielectric constant of UO_2 below the Néel point. *Journal of Nuclear Materials*, **149**(1):18–20, 1987.

[120] L. Manes and A. Barisich. Dielectric response and infrared spectrum of stoichiometric plutonium dioxide by optical reflection and absorption spectroscopy. *Physica Status Solidi (a)*, **3**(4):971–981, 1970.

[121] Malcolm W. Chase Jr., C.A. Davies, JR Downey Jr., D.J. Frurip, R.A. McDonald, and A.N. Syverud. NIST JANAF thermochemical tables 1985. *National Institute of Standards and Technology, Gaithersburg, MD*, 1986.

[122] Ibrahim Cheik Njifon, Marjorie Bertolus, Roland Hayn, and Michel Freyss. Electronic structure investigation of the bulk properties of uranium–plutonium mixed oxides (U,Pu)O_2. *Inorganic Chemistry*, **57**(17):10974–10983, 2018.

[123] I.J. Fritz. Elastic properties of UO_2 at high pressure. *Journal of Applied Physics*, **47**(10):4353–4358, 1976.

[124] Loup Verlet. Computer "experiments" on classical fluids. i. thermodynamical properties of lennard-jones molecules. *Physical Review*, **159**(1):98, 1967.

[125] Hans Lukas, Suzana G. Fries, and Bo. Sundman. *Computational thermodynamics: the Calphad method*. Cambridge university press, 2007.

[126] D. Staicu, T. Wiss, V.V. Rondinella, J.P. Hiernaut, R.J.M. Konings, and C. Ronchi. Impact of auto-irradiation on the thermophysical properties of oxide nuclear reactor fuels. *Journal of Nuclear Materials*, **397**(1-3):8–18, 2010.

[127] Samuel E. Taylor and Fabien Bruneval. Understanding and correcting the spurious interactions in charged supercells. *Physical Review B*, **84**(7):075155, 2011.

[128] M.W. Chase, Jr. C. A. Davies, J. R. Downey, R. A. McDonald, and A.N. Syverud. NIST JANAF *Thermochemical Tables 1985* (national institute of standards and technology, gaithersburg, MD, 1986). 1986.

[129] Tula R. Paudel, Sitaram S. Jaswal, and Evgeny Y. Tsymbal. Intrinsic defects in multiferroic $BiFeO_3$ and their effect on magnetism. *Physical Review B*, **85**(10):104409, 2012.

[130] G. Makov and M.C. Payne. Periodic boundary conditions in *ab initio* calculations. *Physical Review B*, **51**(7):4014, 1995.

[131] A. Zywietz, J. Furthmüller, and F. Bechstedt. Vacancies in sic: Influence of jahn-teller distortions, spin effects, and crystal structure. *Physical Review B*, **59**(23):15166, 1999.

[132] Yanpeng Yao and Huaxiang Fu. Charged vacancies in ferroelectric $PbTiO_3$: Formation energies, optimal Fermi region, and influence on local polarization. *Physical Review B*, **84**(6):064112, 2011.

[133] Per G Sundell, Mårten E Björketun, and Göran Wahnström. Thermodynamics of doping and vacancy formation in $BaZrO_3$ perovskite oxide from density functional calculations. *Physical Review B*, **73**(10):104112, 2006.

[134] Xavier Gonze, J-M. Beuken, R. Caracas, F. Detraux, M. Fuchs, G-M. Rignanese, Luc Sindic, Matthieu Verstraete, G. Zerah, F. Jollet, et al. First-principles computation of material properties: the ABINIT software project. *Computational Materials Science*, **25**(3):478–492, 2002.

[135] X. Gonze, G.M. Rignanese, M. Verstraete, J.M. Beuken, Y. Pouillon, R. Caracas, F. Jollet, M. Torrent, G. Zerah, and M. Mikami. *Z. Kristallogr.*, **220**:558–562, 2005.

[136] C. G. Van de Walle and A. Janotti. *"Advances in electronic structure methods for defects and impurities in solids", in "Advanced Calculations for Defects in Materials", A. Alkauskas, P. Deák, J. Neugebauer, A. Pasquarello, C. G. Van de Walle (Eds.), Wiley.*

[137] A.L. Shluger and A.M. Stoneham. Small polarons in real crystals: concepts and problems. *Journal of Physics: Condensed Matter*, **5**(19):3049, 1993.

[138] L. Bjaalie, DG. Ouellette, P. Moetakef, T.A. Cain, A. Janotti, B. Himmetoglu, S.J. Allen, S. Stemmer, and C.G. Van de Walle. Small hole polarons in rare-earth titanates. *Applied Physics Letters*, 106(**23**):232103, 2015.

[139] Michael Swift, Anderson Janotti, and Chris G. Van de Walle. Small polarons and point defects in barium cerate. *Physical Review B*, **92**(21):214114, 2015.

[140] Lu Sun, Xiaowei Huang, Ligen Wang, and Anderson Janotti. Disentangling the role of small polarons and oxygen vacancies in CeO_2. *Physical Review B*, **95**(24):245101, 2017.

[141] M. Veronica Ganduglia-Pirovano, Juarez L.F. Da Silva, and Joachim Sauer. Density-functional calculations of the structure of near-surface oxygen vacancies and electron localization on CeO_2 (111). *Physical review letters*, **102**(2):026101, 2009.

[142] Hui-Ying Li, Hai-Feng Wang, Xue-Qing Gong, Yang-Long Guo, Yun Guo, Guanzhong Lu, and P. Hu. Multiple configurations of the two excess *4f* electrons on defective CeO_2 (111): origin and implications. *Physical Review B*, **79**(19):193401, 2009.

[143] Anders Lindman, Paul Erhart, and Göran Wahnström. Polaronic contributions to oxidation and hole conductivity in acceptor-doped $bazrO_3$. *Physical Review B*, **94**(7):075204, 2016.

[144] José J. Plata, Antonio M. Marquez, and Javier Fdez Sanz. Transport properties in the CeO_{2-x} (111) surface: From charge distribution to ion-electron collaborative migration. *The Journal of Physical Chemistry C*, **117**(48):25497–25503, 2013.

[145] N. Aaron Deskins and Michel Dupuis. Electron transport via polaron hopping in bulk TiO_2: A density functional theory characterization. *Physical Review B*, **75**(19):195212, 2007.

[146] Shyue Ping Ong, Vincent L. Chevrier, and Gerbrand Ceder. Comparison of small polaron migration and phase separation in olivine $LiMnPO_4$ and $LiFePO_4$ using hybrid density functional theory. *Physical Review B*, **83**(7):075112, 2011.

[147] M.D. Johannes, Khang Hoang, J.L. Allen, and K. Gaskell. Hole polaron formation and migration in olivine phosphate materials. *Physical Review B*, **85**(11):115106, 2012.

[148] Thomas Maxisch, Fei Zhou, and Gerbrand Ceder. Ab initio study of the migration of small polarons in olivine Li_xFePO_4 and their association with lithium ions and vacancies. *Physical Review B*, 7**3**(10):104301, 2006.

[149] Khang Hoang and Michelle Johannes. Tailoring native defects in LiFePO4: insights from first-principles calculations. *Chemistry of Materials*, **23**(11):3003–3013, 2011.

[150] N. Aaron Deskins, Roger Rousseau, and Michel Dupuis. Localized electronic states from surface hydroxyls and polarons in TiO_2 (110). *The Journal of Physical Chemistry C*, **113**(33):14583–14586, 2009.

[151] V. Kosyak, N.B. Mortazavi Amiri, A.V. Postnikov, and M.A. Scarpulla. Model of native point defect equilibrium in Cu_2ZnSnS_4 and application to one-zone annealing. *Journal of Applied Physics*, **114**(12):124501, 2013.

[152] Paul Soven. Coherent-potential model of substitutional disordered alloys. *Physical Review*, **156**(3):809, 1967.

[153] Arnold Sommerfeld and Hans Bethe. Elektronentheorie der metalle. In *Aufbau der zusammenhängenden Materie*, pages 333–622. Springer, 1933.

[154] Alex Zunger, S-H. Wei, L.G. Ferreira, and James E. Bernard. Special quasirandom structures. *Physical Review Letters*, **65**(3):353, 1990.

[155] Mahesh Chandran, P.R. Subramanian, and Michael F. Gigliotti. First principles calculation of mixing enthalpy of β-Ti with transition elements. *Journal of Alloys and Compounds*, **550**:501–508, 2013.

[156] Florent Lebreton, Denis Horlait, Thibaud Delahaye, and Philippe Blanchart. Fabrication and characterization of $U_{1-x}Am_xO_{2\pm\delta}$ compounds with high americium contents (x= 0.3, 0.4 and 0.5). *Journal of Nuclear Materials*, **439**(1-3):99–102, 2013.

[157] B. Sundman, H.L. Lukas, and S.G. Fries. *Cambridge University Press, New York*, 2007.

[158] Christine Guéneau, Nathalie Dupin, Bo Sundman, Chantal Martial, Jean-Christophe Dumas, Stéphane Gossé, Sylvie Chatain, Franck De Bruycker, Dario Manara, and Rudy J.M. Konings. Thermodynamic modelling of advanced oxide and carbide nuclear fuels: Description of the U–Pu–O–C systems. *Journal of Nuclear Materials*, **419**(1-3):145–167, 2011.

[159] Fabien Bruneval, Céline Varvenne, Jean-Paul Crocombette, and Emmanuel Clouet. Pressure, relaxation volume, and elastic interactions in charged simulation cells. *Physical Review B*, **91**(2):024107, 2015.

[160] Takeo Fujino, Toshiyuki Yamashita, Kinji Ohuchi, Keiji Naito, and Toshihide Tsuji. High temperature electrical conductivity and conduction mechanism of $(U,Pu)O_{2\pm x}$ at low oxygen partial pressures. *Journal of Nuclear Materials*, **202**(1-2):154–162, 1993.

[161] D. Prieur, P.M. Martin, F. Lebreton, T. Delahaye, A. Jankowiak, J-P. Laval, A.C. Scheinost, P. Dehaudt, and P. Blanchart. Alpha self-irradiation effect on the local structure of the $U_{0.85}Am_{0.15}O_{2\pm x}$ solid solution. *Journal of Solid State Chemistry*, **194**:206–211, 2012.

[162] Marcel H.F. Sluiter and Y. Kawazoe. Prediction of the mixing enthalpy of alloys. *Europhysics Letters*, **57**(4):526, 2002.

[163] M. Sluiter, P.E.A. Turchi, F.J. Pinski, and G.M. Stocks. A first-principles study of phase stability in Ni–Al and Ni–Ti alloys. In *High Temperature Aluminides and Intermetallics*, pages 1–8. Elsevier, 1992.

[164] Romain Vauchy, Renaud C Belin, Anne-Charlotte Robisson, Florent Lebreton, Laurence Aufore, Andreas C Scheinost, and Philippe M Martin. Actinide Oxidation State and O/M Ratio in hypostoichiometric uranium–plutonium–americium $U_{0.750}Pu_{0.246}Am_{0.004}O_{2-x}$ mixed oxides. *Inorganic Chemistry*, **55**(5):2123–2132, 2016.

Appendix A

Appendix

A.1 Volume correction in *ab initio* dynamics

In our *ab initio* dynamics simulations the average pressure was not exactly equal to 0 kbar despite the use of the barostat. This could result from the size of our system (96-atom supercell) and from the rather short trajectory (a few picoseconds). Indeed, *ab initio* MD is very time consuming especially for the strongly correlated materials and thus are still limited to a few hundred atoms. Therefore, it is necessary to perform a small correction on the average volume and energy of the system in order to cancel the contribution related to the non-zero pressure.

At T = 0 K, the evolution of pressure for slight variations of volume (we will note $P = f(V)$) can be easily calculated for a given system using static DFT (see Fig.A.1). Based on the Birch-Murnaghan equation of state, we assume that the shape of $P = f(V)$ function is preserved when temperature changes. In other words we consider that the $P = f(V)$ function at a given temperature T_i can be obtained by translating $P = f(V)$ at T= 0 along V axis.

Let note V_0 and V_{oi} the equilibrium volumes (i.e. at P=0) at $T = 0$ and $T = T_i$ respectively. For a given pressure P' slightly different from zero, the corresponding volume at $T = 0$ and $T = T_i$ are respectively V'_0 and V'_{0i}. We purpose to find V_{oi} knowing V'_{0i} which is the average volume obtained in the *ab initio* DM simulations (i.e. for $T \neq 0$).
Thus,

$$V'_0 - V_0 = V'_{0i} - V_{0i} = C(P') \tag{A.1}$$

where C(P') is a constant depending on the pressure. From Eq. A.1,

$$V_{0i} = V'_{oi} - C(P') \tag{A.2}$$

C(P') can be easily calculated from :

$$C(P) = V'_0(P') - V_0 \tag{A.3}$$

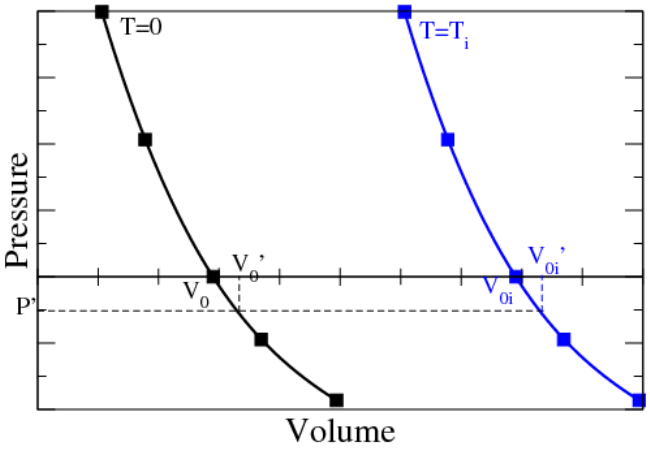

Figure A.1: Schematic representation of pressure as a function of volume. The points of this curve are obtained on the basis of static DFT+U calculation. The blue curve is obtained by translating the black one along volume axis.

Table A.1: Corrected volumes and enthalpies. V'_{0i} and H'_{0i} are the average volumes and enthalpies obtained by *ab initio* MD and V_{0i} and H_{0i} are the corrected volumes and enthalpies.

T_i(K)	V'_{0i}(Å^3)	V_{0i}(Å^3)	$H'_{0i}(kJ.mol^{-1})$x10^6	$H_{0i}(kJ.mol^{-1})$x10^6
286.51	1298.62	1297.58	-3.164	-3.159
381.74	1302.90	1301.07	-3.164	-3.153
566.21	1307.69	1304.62	-3.153	-3.141
761.79	1326.42	1312.32	-3.145	-3.128
951.94	1338.70	1331.08	-3.139	-3.115
1140.39	1353.85	1342.98	-3.135	-3.102
1334.04	1365.73	1356.50	-3.116	-3.088
1501.29	1380.83	1371.35	-3.103	-3.073

V'_0 is calculated for each pressure using the analytical function V=f(P). We report in Tab. A.1 corrected values obtained using this scheme.

A.2 Energy correction in *ab initio* dynamics

The enthalpy of a system is defined as:

$$H = U + PV \tag{A.4}$$

were U is the internal energy directly obtained in *ab initio* DM simulations. The objective here is also to find the enthalpy H corresponding to P=0. We used the same methodology as for the volume correction to cancel the enthalpy contribution related to the non-zero pressure. We note H_{0i} and H'_{0i} the enthalpy for $P = 0$ and $P \neq 0$ respectively at a given temperature $T = T_i$.

$$H_{0i} = H'_{0i} - K(P') \tag{A.5}$$

where K(P') is a constant depending on the pressure and calculated through $K(P') = H'_0 - H_0$, H'_0 being the enthalpy at T=0 and H_0 the enthalpy at T=0 and P=0. The corrected enthalpies values are reported in Tab. A.1 .

Modélisation par calcul de structure électronique de l'influence de l'américium dans les combustibles nucléaires oxydes

L'oxyde mixte d'uranium-plutonium (MOX) avec une teneur en plutonium d'environ 25% est le combustible de référence des futurs réacteurs nucléaires Français de Génération IV. Ce combustible nucléaire sera fabriqué à partir du combustible usé provenant des réacteurs à eau pressurisée (REP), et par conséquent, contiendra de l'américium en faible pourcentage. La question qui émerge est celle de savoir si la présence de l'américium affectera les performances et la sûreté du combustible MOX. Il faut noter que le multirecyclage étant envisagé dans le cas des REP utilisant le MOX (%Pu $\sim$ 10) comme combustible, la même problématique se pose également pour les REP. Ainsi, une meilleure mise en évidence des effets induits par la présence de l'américium sur les propriétés de l'oxyde mixte d'uranium-plutonium est donc nécessaire pour maîtriser les conséquences de la présence de cet élément sur la sûreté et la performance des combustibles. Cette étude consiste à déterminer l'influence d'une faible teneur en américium sur les propriétés structurales, électroniques, élastiques, énergetiques en température finie et de défauts ponctuels des oxydes mixtes $(U,Pu)O_2$ par calculs de structure électronique, à l'aide de la méthode DFT+U. Pour cela, nous avons commencé par l'étude des oxydes purs d'américium (AmO_2 et Am_2O_3) afin d'adapter la méthode DFT+U aux oxydes contenant de l'américium, puis de prédire certaines propriétés d'intérêt manquantes ou mal connues de AmO_2 et Am_2O_3. Une fois la méthode DFT+U mise en œuvre dans les oxydes purs d'américium, l'étape suivante était de l'appliquer à $(U,Pu,Am)O_2$ afin de déterminer l'effet de Am. Cependant, étant donné la complexité du système quaternaire U-Pu-Am-O et les données très rares sur ce composé, nous avons choisi d'abord d'étudier $(U, Am)O_2$. Nous montrons que la présence d'américium facilite la formation de lacunes d'oxygène dans $(U, Am)O_2$. Par ailleurs, l'américium induit une légère diminution du paramètre de maille de $(U,Pu,Am)O_2$. Enfin, nous montrons que l'Am induit un état de valence particulier des cations, en particulier une oxydation partielle de U(+IV) en U(+V).

Mots clés: Calculs de struture électronique, DFT+U, combustible nucléaire oxyde, américium.

First-principles study of the effect of americium content in mixed oxide fuels

Uranium-plutonium mixed oxide (MOX) with a plutonium content of about 25% is the reference fuel for the Generation IV nuclear reactors in France. This nuclear fuel will be fabricated from spent fuel coming out of pressurized water reactors (PWR) currently in operation in France and, as a consequence, will contain a few percent of americium. The emerging question is whether the presence of americium will affect the performance and safety of the MOX fuel. Note that the multirecycling of spent fuel is envisaged for PWR using MOX (%Pu $\sim$10) and thus, the same issue is raised for PWR since recycled fuel will contain a few percent of americium. A better evidence of the effects induced by the presence of americium on the uranium-plutonium mixed oxide properties is thus necessary to monitor the consequences of the presence of this element on the safety and the performance of the nuclear fuels. This study consists in determining the influence of a low americium content on structural, electronic, elastic, energetic, finite temperature and point defects properties of $(U,Pu)O_2$ mixed oxides by appropriate electronic structure calculations i.e. using DFT+U. For this, we began by studying the pure americium oxides (AmO_2 and Am_2O_3) in order to adapt the DFT+U method to americium-bearing oxides and then to provide some missing properties of interest of AmO_2 and Am_2O_3. Once the DFT+U method implemented in pure americium oxides, the next step was to apply it to $(U,Pu,Am)O_2$ in order to determine the effect of Am. But, given the complexity of the U-Pu-Am-O quaternary system and the very rare data on this compound, we made the choice to first study $(U,Am)O_2$. We show that the presence of Am facilitates the formation of oxygen vacancies in $(U,Am)O_2$. We also show that the presence of americium induces a slight decrease in lattice parameter of $(U,Pu,Am)O_2$. Finally, we show that americium induces a particular valence state of cations, especially a partial oxidation of U (+IV) to U(+V).

Keywords: First-principles, DFT+U, mixed oxide fuels, americium.

Laboratoire de Modélisation Multi-échelle du Combustible-CEA/DEN/DEC/SESC
13108 Saint-Paul-Lez-Durance, France